

This item was submitted to [Loughborough's Research Repository](#) by the author.
Items in Figshare are protected by copyright, with all rights reserved, unless otherwise indicated.

Novel polyurethane/graphene nanocomposite coatings

PLEASE CITE THE PUBLISHED VERSION

PUBLISHER

Loughborough University

PUBLISHER STATEMENT

This work is made available according to the conditions of the Creative Commons Attribution-NonCommercial-NoDerivatives 4.0 International (CC BY-NC-ND 4.0) licence. Full details of this licence are available at:
<https://creativecommons.org/licenses/by-nc-nd/4.0/>

LICENCE

CC BY-NC-ND 4.0

REPOSITORY RECORD

Tong, Yao. 2016. "Novel Polyurethane/graphene Nanocomposite Coatings". figshare.
<https://hdl.handle.net/2134/23223>.

Department of Materials

Novel Polyurethane/Graphene Nanocomposite Coatings

by

Yao Tong

Doctoral Thesis to be inserted

Submitted in partial fulfilment of the requirements for the award of

Doctor of Philosophy of Loughborough University

10-08-2016

Project Supervisor: Professor Mo Song

Sponsoring Company: TATA Steel

Company Supervisor: Dr. Siva Bohm

Acknowledgement

I would like to thank my supervisor, Professor Mo Song, for his consistent support and supervision through my entire project. I have been benefited from his help, guidance and inspiration throughout my PhD period. He had taught me and led me into the world of graphene and shared with me his precious experience and knowledge. Moreover, I would be graceful for his help in my life and thoughtful advice for my future.

I would also like to express my gratitude to Dr Jie Jin who had taught me and trained me everything in the lab. I could not do my experiments correctly and adapt to my PhD career quickly without her. She also provided advice on my literature writing and paper writing which had helped me a lot in my academic path.

My gratitude also goes to Dr Siva Bohm for his help on the arrangement of the resources and training in TATA Steel UK. In addition, he also helped me a lot to understand EIS and how to make good coating. I would like to thank the staff in the advanced coating group of TATA Steel R&D. They are very nice and always answer my question professionally. Their help had helped me to get into the coating area quickly.

I appreciate all the help and training from the staff and research students in the department of materials. They had given me a lot of useful advice in characterisation techniques and my experiments.

At last, I would like to thank my family and my friends who had support me and encourage me along my PhD life.

Abstract

A series of graphene based conductive and anticorrosion coatings were developed in this project. Multi-layer coating consists of EPD pristine graphene coating, PU/graphene primer and PU/graphene topcoat was developed. A simple mechanical-chemical approach was suggested to fabricate graphene with low cost and high efficiency. XRD was used to characterize the exfoliation efficiency of graphite. TEM was used to examine the size of the graphene sheets. SEM was used to characterize the surface morphology of the coatings. The particle size of all the carbon materials used was characterised by Malvern particle sizer. FTIR and XPS were used to characterize the chemical composition of the graphene powder and the coatings fabricated. MDSC and FTIR were used to monitor the cure dynamic of PU.

The proposed mechanical-chemical approach was cost effective and suitable for large-scale production of graphene. XRD results indicated that the graphite layers were exfoliated efficiently and TEM results confirmed the existence of graphene. EPD was used to deposit graphene and PP10 graphite on steel substrates. With fine control of the EPD conditions and thermal treatment, electrical conductive coatings on steel substrates were produced successfully. The best electrical conductivity was 10 times higher than the electrical conductivity than steel substrate. The anticorrosion properties of the EPD coatings were not good due to their porous nature. Therefore, a polymeric protective coating is needed to improve the anti-corrosion properties. Hybrid filler was adopted in the PU nanocomposites and the performance of the nanocomposites reinforced by hybrid filler was the best. The conductive mechanism of the nanocomposites was proposed. From the results of FTIR and MDSC, graphene had catalytic effect and steric hindrance effect on the cure of PU where catalytic effect was more obvious at high cure temperature and steric hindrance effect was more dominated with high graphene loading. GO also showed catalytic effect and steric hindrance effect. In addition, the functional groups on the GO surface can participate

in the reaction with PU. Therefore, the reaction mechanism was altered. From the results, the addition of excessive amount of filler can significantly affect the cure behaviour of two-part PU and even reduce the crosslink density and weaken its mechanical properties.

Content List

Chapter 1 Introduction.....	1
References	3
Chapter 2 Literature Review	5
2.1 Introduction	5
2.2 Graphene based materials: Synthesis methods and functionalization	6
2.2.1 Synthesis methods	6
2.2.2 Functionalization of graphene	10
2.3. Applications of graphene in coating.....	12
2.3.1 Pristine graphene based materials coating.....	12
2.3.2 Graphene based nanocomposites coating.....	23
2.4. Polyurethane based coatings.....	30
2.4. 1 Building blocks and synthesis of polyurethane	30
2.4.1.1 Isocyanates	31
2.4.1.2 Polyols	32
2.4.1.3 Catalysts	32
2.4.1.4 Chain extenders (CEs).....	33
2.4.1.5 Stoichiometry for PUs reactions.....	34
2.4.2 PU based coatings.....	35
2.4.2.1 Thermoplastic PU based coatings.....	37
2.4.2.2 Thermoset PU based coatings and coating selection.....	39
2.4.2.3 Why we use PU/graphene based coatings for protective coating.....	40
2.5. Coating methods.....	42
2.6. Conclusions and future perspectives	49
References	50
Chapter 3 Experimental.....	68
3.1 Materials.....	68
3.1.1 Carbon based particles.....	68

3.1.2 PU topcoat, primer and reactants.....	68
3.1.3 Steel substrates	70
3.1.4 Other chemicals	70
3.2 Graphene fabrication	70
3.3 Carbon based conductive coating	72
3.4 PU nanocomposite coatings	75
3.5 PU cure dynamic	79
3.6 Introduction of the characterisation techniques.....	82
3.6.1 Four point probe method	82
3.6.2 EIS	83
3.6.3 MDSC.....	84
3.6.4 FTIR	85
3.6.5 SEM.....	86
3.6.6 TEM.....	87
3.6.7 Particle size measurement	88
3.6.8 XRD.....	88
3.6.9 XPS.....	89
References	90
Chapter 4 Graphene Fabrication.....	94
4.1. Introduction	94
4.2. The investigation of the efficiency of the exfoliation method.....	96
4.2.1 XRD analysis.....	97
4.2.2 TEM analysis.....	99
4.2.3 Particle size analysis.....	103
4.2.4 XPS analysis.....	105
4.2.5 FTIR analysis.....	110
4.3 Conclusions	113
References	113
Chapter 5 Carbon based coatings on steel with improved electrical conductivity	117

5.1 Introduction	117
5.2 Theories about the oxidation of steel.....	118
5.3 Carbon based coatings on steel.....	121
5.3.1 The surface characteristic and electrical conductivity of the initial heat treated samples	121
5.3.2 Optimization of EPD conditions.....	134
5.3.3 Comparison of the electrical conductivity of the coating on different steel substrates	141
5.4 Conclusions	150
References	151
Chapter 6 Electrical conductivity and anti-corrosion capacity of PU/graphene nanocomposite coatings.....	156
6.1. Introduction	156
6.2. Application of EIS in coating evaluation	158
6.2.1 Fundamentals of EIS	158
6.2.1 Application of EIS in coatings	160
6.3. The electrical conductivity of the nanocomposite coatings.....	163
6.3.1 PU conductivity	163
6.3.2 Primer conductivity	166
6.3.3 Hybrid filler system and multi-layer coating.....	167
6.3.4 The Mechanisms of electrical conductivity	172
6.4 The anti-corrosion property of the nanocomposite coatings	174
Hybrid filler system.....	181
6.5 The surface characterisation of the coated surfaces	185
6.6. Conclusions	186
References	186
Chapter 7 Cure dynamics of PU/graphene nanocomposites.....	189
7.1 Introduction	189
7.2 Theories of the cure dynamic monitored by MDSC and FTIR	191
7.2.1 MDSC.....	191
7.2.2 FTIR	194

7.3 Results of cure dynamic from FTIR and MDSC	195
7.3.1 MDSC characterisation	195
7.3.2 FTIR characterisation	210
7.4 Conclusions	213
References	213
Chapter 8 Conclusions and Future Work	217
8.1 Conclusions	217
8.2 Future work	218
Publications	220

Figures and Tables

Figure 2.1 The procedure to prepare GO and reduced GO using BPO.....	10
Figure 2.2 Procedure to graft PP chains on graphene via in situ Ziegler-Natta polymerization	11
Table 2.1 Pristine graphene based coatings used in electrical applications	14
Figure 2.3 OTR versus number of bi layers.....	16
Figure 2.4 Schemes of anti-corrosion mechanism of CVD graphene coating on copper [67]	17
Table 2.2 Performance of graphene produced by CVD as anti-corrosion and anti-oxidation coating.....	18
Figure 2.5 Humidity sensing mechanism of graphene oxide/silicon bilayer.....	20
Table 2.3 Graphene based coatings used in SPME application.....	21
Figure 2.6 Preparation procedure of G/PAA-AgNps/RGO sandwich structure.....	22
Table 2.4 Comparison of pure PBT and PBT/Graphene coatings.....	26
Figure 2.7 SEM images of GO/PU nanocomposites (a) 1 wt% of GO (b) 4 wt% of GO.....	27
Table 2.5 Comparison of PANI coating, Steel and composite coatings.....	27
Figure 2.8 The basic reactions of isocyanate group with other functional group.....	30
Figure 2.9 The chemical structures of some commercial diisocyanates.....	31
Figure 2.10 Reaction mechanism for the polyurethanes reaction due to: (a) and (b) organometallic catalysts, and(c) and (d) tertiary amine.....	33
Table 2.6 Six different types of PUs in ASTM standard.....	36
Figure 3.1 The electrodes arrangement of the linear array four point probe.....	82
Figure 3.2 Principle of XPS [35].....	90
Table 4.1 Description of the specimens.....	98
Figure 4.1 XRD spectrum of the specimens and pristine graphite (a) whole scan range (b) 2 θ from 20 ° to 30 °.....	98
Figure 4.2 TEM images of Specimen A with different scale (a) 0.5 μ m (b) 0.5 μ m (c) 200nm	

(red arrow indicates the folded edges in the figures).....	99
Figure 4.3 TEM images of Specimen F with different scales (a) 2 μm (b) 0.5 μm (red arrow indicates the wrinkles of graphene sheets) (c) 200 nm (red arrow indicates the impurities).....	100
Figure 4.4 Plot of volume base particle size distribution of different specimens.....	104
Figure 4.5 Plot of accumulated volume versus particle diameter of different specimen.....	105
Table 4.2 Summary of the particle size distribution of the specimens.....	105
Figure 4.6 Survey scan XPS spectrum of specimen A.....	106
Table 4.3 The summary of relative elements atomic ratio of different specimens.....	107
Figure 4.7 C1s XPS spectrum of (a) specimen A and (b) specimen B from high resolution scan.....	108
Figure 4.8 FTIR spectrum of (a) specimen A and (b) specimen B.....	111
Figure 4.9 The armchair and zigzag configurations of graphene edges [32].....	112
Figure 5.1 the mechanism of high temperature oxidation of steel [20].....	118
Figure 5.2: (a) TEM image of PP10; (b) X-ray diffraction pattern of the sheet in (a); (c) TEM image of G; (d) X-ray diffraction pattern of the graphene sheet in (c); (e) TEM image of G graphene with smaller magnification; (f) X-ray diffraction of the stacking graphene sheets in (e).....	121
Figure 5.3: Schemes of nanoscale electron diffraction patterns of (a) a single-layer graphene membrane and (b) a two-layer membrane.....	122
Figure 5.4: SEM images of the carbon based particles coated sample by EPD; (a) The PP10 coated sample with initial EDP conditions (b) The PP10 coated sample with lower voltage; (c) The PP 10 coated sample with longer deposition time; (d) G coated sample with longer deposition time.....	123
Figure 5.5: SEM image of the post heat treated samples (a) Graphene coated 540°C treated for 5 minutes (b) PP10 coated 540°C treated for 5 minutes (c) Graphene coated 580°C treated for 5 minutes (d) PP10 coated 580°C treated for 5 minutes (e) Graphene coated 600°C treated for 5 minutes (f) PP10 coated 600°C treated for 5 minutes (g) An iron oxide scale bound	

particle.....	126
Figure 5.6 EDX analysis of the coating drop-off site of a graphene coated sample.....	126
Figure 5.7: XPS spectrum of graphite coated sample treated at 580 ⁰ C for 5 minutes (a) survey scan (b) Iron element high resolution scan (c) Carbon element high resolution scan (d) Oxygen element high resolution scan.....	127
Table 5.1: XPS data of graphite coated sample treated at 580 ⁰ C for 5 minutes.....	128
Figure 5.8: SEM image of graphite coated sample to review its surface structure.....	129
Figure 5.9: SEM image of the steel-coating interface of (a) graphite coated sample treated at 630 for 5minutes (b) graphene coated sample treated at 630 for 5minutes	130
Figure 5.10: Plot of relative conductivity versus thermal treatment temperatures of the oxide layers on BP steel.....	130
Figure 5.11: Plot of relative conductivity versus thermal treatment temperatures of graphite coated samples.....	130
Figure 5.12: Plot of relative conductivity versus thermal treatment temperatures of graphene coated samples.....	132
Figure 5.13: Plot of relative conductivity versus thermal treatment times of graphite coated samples at 600 °C.....	133
Figure 5.14 Schematic of particles binding process during heat treatment.....	133
Figure 5.15 SEM images of iodine concentrations variation trials (a) DP1061 (0.175mg/ml) (b) DP1062 (0.44mg/ml) (c) DP1063 (0.74mg/ml) (d) DP1064 (0.99mg/ml) (e) DP1065 (1.23mg/ml) (scale bar:200µm).....	134
Figure 5.16 SEM images of deposition times variation trials (a) DP1066 (0.5 min) (b) DP1067 (1 min) (c) DP1068 (1.5 mins) (d) DP1069 (2 mins) (e) DP10610 (2.5 mins) (scale bar: 200 µm).....	135
Figure 5.17 SEM images of SEM images of voltage variation trials (a) DP1866 (20V) (b) DP1867 (30V) (c) DP1868 (40V) (d) DP1869 (50V) (e) DP18610 (60V) (scale bar:200µm)	137
Figure 5.18: Plot of electrical conductivity ratios versus iodine concentrations.....	138

Figure 5.19: Plot of electrical conductivity ratios versus deposition times.....	139
Figure 5.20: Plot of electrical conductivity ratios versus voltages.....	140
Figure 5.21 Images of 13KE008 (a) graphene coated (b) graphite coated.....	141
Figure 5.22 Images of 13KE005 (a) graphite coated (b) graphene coated.....	141
Figure 5.23 Images of 13KE009 (a) graphene coated (b) graphite coated.....	142
Figure 5.24 Images of 13KE21 (a) graphene coated (b) graphite coated.....	143
Figure 5.25 SEM images of (a)(b) graphite coated 13KE21 samples and (c)(d) graphene coated 13 KE21 samples.....	143
Table 5.2 Electrical conductivity of coated 13KE21 samples.....	143
Figure 5.26 XPS surface scan of PP10 coated sample (a) Carbon element scan (b) Oxygen element scan (c) Nickel element scan (d) Iron element scan.....	144
Table 5.3 XPS data of the PP10 coated sample treated at 580 ⁰ C for 5 minutes.....	145
Figure 5.27 XPS surface scan of the PPG coated sample (a) Nickel element scan (b) Iron element scan (c) Oxygen element scan (d) Carbon element scan.....	146
Table 5.4 XPS data of the PPG coated sample treated at 580 ⁰ C for 5 minutes.....	146
Figure 5.27 XPS surface scan of the graphene coated sample (a) Nickel element scan (b) Oxygen element scan (c) Carbon element scan (d) Iron element scan.....	147
Table 5.4 XPS data of the graphene coated sample treated at 580 ⁰ C for 5 minutes.....	148
Figure 5.28 XPS depth profiling of (a) PP10 coated sample (b) PPG coated sample (c) the graphene coated sample.....	149
Figure 6.1 Images of (a) impedance vector (b) example Bode plot (c) example Bode plot with phase angle as Y axis (d) example Nyquist plot.....	160
Figure 6.2 Images of equivalent circuits (a) simple Randles Circuit (b) coatings in the middle or at the end of degradation (c) coatings contain defects.....	162
Figure 6.3 Plot of electrical conductivity versus stirring rate (topcoat trials).....	163
Figure 6.4 Plot of electrical conductivity versus PP10 weight percent for PPPU trials.....	164
Table 6.1 Electrical conductivity values of PPPU system.....	164
Figure 6.5 Plot of electrical conductivity versus PP10 weight percent for EPPPU trials.....	165

Table 6.2 Table 2 Electrical conductivity values of EPPPU system.....	165
Table 6.3 Electrical conductivity of PPPU topcoat.....	166
Figure 6.6 Plot of electrical conductivity versus PP10 weight percent for EPP primer trials	166
Table 6.4 Electrical conductivity EPP system.....	167
Table 6.5 Electrical conductivity of hybrid filler PU topcoat system.....	167
Table 6.6 Electrical conductivity of hybrid filler primer system.....	168
Table 6.6 Electrical conductivity of hybrid filler primer system.....	168
Table 6.7 Electrical conductivity of second set of hybrid filler primer system.....	169
Figure 6.7 Plot of electrical conductivity versus hybrid filler weight percent of HIVE samples primer system.....	170
Table 6.8 Electrical conductivity, resistance, conductivity ratios of hybrid filler filled primer samples primer system.....	170
Table 6.9 Electrical conductivity comparison of the samples with and without slat addition..	171
Figure 6.8 Plots of (a) particle size distribution of three different fillers (b) Accumulated volume versus particle diameter of three different fillers.....	172
Figure 6.9 Scheme of the filler reinforced coating (a) PP10 (b) PP10 + MWCNT (c) TEG + MWCNT.....	173
Figure 6.10 Bode plot of the samples with EPD coating (after heat treatment).....	174
Figure 6.11 EIS results of PPPU trial (a) Bode plot (b) Bode phase angle plot (c) Nyquist plot.....	174
Figure 6.12 EIS results of EPP trials (a) Bode plot (b) Bode phase angle plot (c) Nyquist plot.....	176
Figure 6.13 EIS results of EPPU trials (a) Bode plot (b) Bode phase angle plot (c) Nyquist plot.....	179
Figure 6.14 EIS results of HIVE hybrid filler trials (a) Bode plot (b) Bode phase angle plot (c) Nyquist plot.....	180

Table 6.10	Fit result of hybrid filler series from Randel cell.....	182
Figure 6.15	EIS results of multi-layer coating trials (a) Bode plot (b) Bode phase angle plot (c) Nyquist plot.....	184
Figure 6.16	Example FEGSEM images of (a) PPPU 6500 (b) PPPU 10500 (c) PPU14500	185
Figure 7.1	Non-isothermal DSC curves of (a) pure PU resin with different modulation amplitude and PU nanocomposites with different filler loadings (b) G (c) GO (d) TEG	195
Figure 7.2	Isothermal DSC curves of PU/G nanocomposites with different G loadings (a) 0 wt% (b) 0.5wt% (c) 1 wt% (d) 4 wt%	196
Figure 7.3	Isothermal DSC curves of PU/GO nanocomposites with different GO loadings (a) 0 wt% (b) 0.5wt% (c) 1 wt% (d) 4 wt%	197
Figure 7.4	Isothermal DSC curves of PU/TEG nanocomposites with different TEG loadings (a) 0 wt% (b) 0.5wt% (c) 1 wt% (d) 4 wt%	198
Figure 7.5	Plots of conversion (a) against reaction time of PU/G nanocomposites with different G loadings (a) 0 wt% (b) 0.5wt% (c) 1 wt% (d) 4 wt%.....	199
Figure 7.6	Plots of conversion (a) against reaction time of PU/GO nanocomposites with different GO loadings (a) 0 wt% (b) 0.5wt% (c) 1 wt% (d) 4 wt%.....	199
Figure 7.7	Plots of conversion (a) against reaction time of PU/TEG nanocomposites with different TEG loadings (a) 0 wt% (b) 0.5wt% (c) 1 wt% (d) 4 wt%.....	200
Figure 7.8	Plots of conversion rate (da/dt) against conversion (a) of PU/G nanocomposites with different G loadings (a) 0 wt% (b) 0.5wt% (c) 1 wt% (d) 4 wt%.....	201
Figure 7.9	Plots of conversion rate (da/dt) against conversion (a) of PU/GO nanocomposites with different GO loadings (a) 0 wt% (b) 0.5wt% (c) 1 wt% (d) 4 wt%	203
Figure 7.10	Plots of conversion rate (da/dt) against conversion (a) of PU/TEG nanocomposites with different TEG loadings (a) 0 wt% (b) 0.5wt% (c) 1 wt% (d) 4 wt%	204
Figure 7.11	Plots of activation energy versus conversion of PU nanocomposites with different	

filler loadings (a) G (b) GO (c) TEG.....	205
Figure 7.12 Plots of pre-exponential factor versus conversion of PU nanocomposites with different filler loadings (a) G (b) GO (c) TEG.....	207
Table 7.1 The reaction parameters obtained from the modelling of the MDSC results.....	208
Figure 7.12 Example FTIR spectrums of PU nanocomposites (PU/G) cured with different time (without calibration).....	210
Figure 7.13 Plots of conversion versus reaction time of PU/G nanocomposites with different G loadings obtained from FTIR characterisation (a) 0 wt% (b) 0.5wt% (c) 1 wt% (d) 4 wt%	210
Figure 7.14 Plots of conversion versus reaction time of PU/GO nanocomposites with different GO loadings obtained from FTIR characterisation (a) 0 wt% (b) 0.5wt% (c) 1 wt% (d) 4 wt%	211
Figure 7.15 Plots of conversion versus reaction time of PU/TEG nanocomposites with different TEG loadings obtained from FTIR characterisation (a) 0 wt% (b) 0.5wt% (c) 1 wt% (d) 4 wt%	213

Chapter 1 Introduction

Polymer nanocomposites are polymer matrices reinforced by nanofillers. Nanocomposites can be classified into three categories according to the dimensions of dispersed particle in nanoscale: such as spherical silica nanoparticles [1], carbon nanotube [2] and nano-clay [3]. Nanofillers have been widely used in the polymer industry for reinforcement of polymers. For example, the rubber used for engineering applications usually contains nanofillers for improving performance. Polyurethane (PU) is an extremely versatile material for engineering applications because the wide range of formulations and types of PU available. PU can find a broad range of industrial applications include: coating, elastomers, adhesives, medical devices, foam products and sealants [4]. The versatility of PU in different applications is due to the enormous selection of isocyanate, polyol and chain extenders. PU coatings can be found on different materials to improve their lifetime and appearance. Formulations and processing techniques were developed continuously according to the modern requirements of coating. PU coating consists of one-part and two-part systems in general. In terms of automotive applications, PU coating provide exterior high gloss, improves starch resistance, improved colour retention and excellent corrosion resistance. In the case of construction area, PU coatings are applied by spray coating method on building floors, concrete supports and steel trusses for improving durability, reducing maintenance cost and improving weathering resistance [5]. Although the properties of PU coatings are excellent, the requirements of different application are increased with the technology developed. Hence, the utilisation of filler in PU coating for superior properties is good way to develop the products that meet the high standards.

The properties of fillers are important to the performance of nanocomposites. With application of appropriate fillers, the performance of a polymer matrix can be

enhanced dramatically. Graphene has received more and more attention since its discovery. Owing to the unique tightly packed sp^2 bonded two dimensional honeycomb lattice, graphene possesses many extraordinary properties such as electron transportation properties [6,7], mechanical properties [7–9], thermal properties [10], and barrier properties [11]. The potential applications of graphene are broad, including energy storage devices [12], coating applications [13], nanocomposites [14] and so on. As a result of the extraordinary properties of graphene, it is an attractive filler to reinforce different polymeric matrices. PU has wide applications in industry and, therefore, the researches on incorporating graphene in PU had been conducted widely in the world. Graphene can be incorporated into PU coating to produce electrical conductive coating [15], anti-corrosion coating [16], scratch resistance coating [17] and other functional coatings. Graphene oxide (GO) can react with PU to form a dense thermoset network which improves the mechanical properties of PU based materials significantly [18]. The works of utilising graphene in PU were generally lab based. There are several problems that need to be solved before large scale commercialisation: 1. the large-scale production of graphene is expensive; 2. suitable dispersion methods and procedures are needed to disperse graphene in coating uniformly; 3. a suitable coating method to apply coating on steel substrate. In terms of electrical conductive coating, a low percolation threshold to make the polymer conductive was achieved, but the conductivity values were not high. In addition, the anti-corrosion properties of the conductive nanocomposites which relate to commercial application closely did not report a lot.

In this project, graphene based fillers were incorporated in some in-line products supplied by TATA steel to investigate the possibility of utilising graphene in a commercial scale. Several objectives were set to achieve the expectations:

1. Investigation of the possibility of applying pristine graphene/graphite coating on steel substrates *via* electrophoresis deposition;

2. Development of a suitable method to produce pristine graphene from graphite;
3. Suggestion on suitable procedures to incorporate graphene based fillers in PU topcoat and primers;
4. Understanding of the effect of fillers on electrical conductivity and anti-corrosion properties;
5. Investigation of the surface morphology and properties of the nanocomposite coatings;
6. Understanding of the effect of graphene based fillers on the cure dynamics of PU;

References

- [1] Mark E. Ceramic-Reinforced Polymers and Polymer-Modified Ceramics. *Polym Eng Sci* 1996;36:2905–20.
- [2] Ebbesen TW. Carbon nanotubes: preparation and properties. London, NewYork, Tokyo, Boca Raton :CRC press; 1996.
- [3] Xia H, Song M, Zhang Z, Richardson M. Institutional Repository Microphase separation, stress relaxation and creep behavior of polyurethane nanocomposites. *J Appl Polym Sci* 2007;103:2992–3002.
- [4] Kim JT, Kim BK, Kim EY, Park HC, Jeong HM. Synthesis and shape memory performance of polyurethane/graphene nanocomposites. *React Funct Polym* 2014;74:16–21.
- [5] Chattopadhyay DK, Raju KVS. Structural engineering of polyurethane coatings for high performance applications. *Prog Polym Sci* 2007;32:352–418.
- [6] Geim AK, Novoselov KS. The rise of graphene. *Nat Mater* 2007;6:183–91.
- [7] Singh V, Joung D, Zhai L, Das S, Khondaker SI, Seal S. Graphene based materials: Past, present and future. *Prog Mater Sci* 2011;56:1178–271.
- [8] Lee C, Wei X, Kysar JW, Hone J. Measurement of the elastic properties and intrinsic strength of monolayer graphene. *Science* 2008;321:385–8.
- [9] Lee C, Wei X, Li Q, Carpick R, Kysar JW, Hone J. Elastic and frictional

- properties of graphene. *Phys Status Solidi* 2009;246:2562–7.
- [10] Balandin AA, Ghosh S, Bao W, Calizo I, Teweldebrhan D, Miao F, Lau CN, Superior thermal conductivity of single-layer graphene. *Nano Lett* 2008;8:902–7.
- [11] Hu J, Ji Y, Shi Y. A Review on the use of graphene as a protective coating against corrosion. *Ann J Mater Sci Eng* 2014;1:1–16.
- [12] Sanjinés R, Abad MD, Vâju C, Smajda R, Mionić M, Magrez A. Electrical properties and applications of carbon based nanocomposite materials: An overview. *Surf Coatings Technol* 2011;206:727–33.
- [13] Dennis R V, Patil V, Andrews JL, Aldinger JP, Yadav GD, Banerjee S. Hybrid nanostructured coatings for corrosion protection of base metals: a sustainability perspective. *Mater Res Express* 2015;2:032001.
- [14] Young RJ, Kinloch IA, Gong L, Novoselov KS. The mechanics of graphene nanocomposites: A review. *Compos Sci Technol* 2012;72:1459–76.
- [15] Pang B, Yu L, Dong H, Dong L. Preparation and properties of graphene/polyurethane conductive polymer composite films. *ECS Trans* 2015;66:31–7.
- [16] Mo M, Zhao W, Chen Z, Yu Q, Zeng Z, Wu X, et al. Excellent tribological and anti-corrosion performance of polyurethane composite coatings reinforced with functionalized graphene and graphene oxide nanosheets. *RSC Adv* 2015;5:56486–97.
- [17] Cai D, Yusoh K, Song M. The mechanical properties and morphology of a graphite oxide nanoplatelet/polyurethane composite. *Nanotechnology* 2009;20:085712(1–5).
- [18] Cai D, Jin J, Yusoh K, Rafiq R, Song M. High performance polyurethane/functionalized graphene nanocomposites with improved mechanical and thermal properties. *Compos Sci Technol* 2012;72:702–7.

Chapter 2 Literature Review

2.1 Introduction

A coating is usually employed to improve the surface properties of a substrate, wettability, corrosion resistance and adhesion, for example. The coating industry has been driven by economic benefits and growing environmental concerns to seek new technologies and materials to improve the efficiency of coatings. There are several factors affect the effectiveness of a coating against all the possible damaging sources: they are the quality of the coating, the substrate characteristics, the properties of the coating/substrate interface, and the corrosiveness of the environment [1]. In order to satisfy the industrial requirements nowadays, polymer nanocomposites have been increasing investigated and applied in coatings because nanocomposites provide superior properties at a relatively low cost. Additionally, the processing procedure can be much less complicated than multi-layer coatings [1,2].

Graphene, a new generation material, is an allotrope of the carbon, which was first isolated by simple mechanical exfoliation in 2004 [3]. It is a two dimensional honeycomb single layer crystal lattice formed by the tightly packed sp^2 bonded carbon atoms. Owing to the unique structure of graphene, these carbon atoms form an excellent electronic carrier space. Therefore, graphene has extraordinary electrical properties such as high electron mobility at room temperature ($250,000 \text{ cm}^2/\text{V}$) [4,5] and ballistic transport and quantum hall effect at room temperature [6]. In addition, graphene also has excellent optical properties [5]. Excellent mechanical properties of graphene (*i.e.* 1TPa Young's Modulus and 130GPa tensile strength) have also been reported and the mechanical properties relate to the number of graphene layers and the internal defects of the graphene layers [5,7,8]. It is possible that the energy band gap of graphene can be changed by applying a uniaxial strain on graphene which is in turn able to affect the electronic properties of graphene [9,10]. In terms of thermal properties, the highest thermal conductivity at room temperature has been reported as $5000 \text{ Wm}^{-1}\text{K}^{-1}$ [11]. Some potential applications of graphene have been suggested by researchers such as gas detection [12], transistors [13], nanocomposites [14], energy storage devices [6], barrier applications [15] and so on. However, graphene is still a giant gold mine that can be dug deeper.

Owing to the excellent properties of graphene, it is believed that it can be used to enhance the performance of coatings significantly. Graphene is very ideal to be efficient filler for high quality polymer matrix nanocomposite coating. In addition, it can be used as a sole high quality coating or with nano-particles to form graphene-nanoparticles composites coating. Graphene is identified as a high water and oil repellent material while graphene oxide (GO) is hydrophilic [16]. This property can make graphene suitable for the coating that provides water and oil resistance. An analysis of frictional properties and wear resistance of a film made up of multi graphene layer films was performed using an AFM by Lin and his co-workers [17]. Superb frictional properties and high wear resistance were reported. These results mean that graphene is able to become a protective coating against scratch or other physical damage toward a substrate. Graphene was also proved to be an effective corrosion barrier material because it was considered inert under the conditions where chemical reactions of other substrates will take place [18]. As a result, it is also promising in improving the anti-corrosion properties of a coating system.

In coating applications, graphene is believed to be promising, but the articles designated for coating applications are limited. In this review, the synthesis methods and functionalization of graphene were described briefly. The articles about utilization of graphene in coating published in recent years were reviewed. The conclusions summarized the published researches and suggested the future research perspectives.

2.2 Graphene based materials: Synthesis methods and functionalization

2.2.1 Synthesis methods

Different methods have been developed to synthesize graphene, but, not all of them can be used to synthesize good quality graphene efficiently. Three major routes: mechanical exfoliation, reduction from graphene oxide, and chemical vapour deposition (CVD), are regarded as the most promising routes to synthesize graphene and they have the potential to be used for large scale graphene production in the future. Among them, the chemical route, graphene reduced from graphene oxide have frequently been used to study the utilization of graphene based materials in different applications.

Mechanical exfoliation The first graphene sheet was produced by simple mechanical exfoliation [3]. Therefore, initially mechanical exfoliation became a very attractive method for the researchers to produce graphene initially. The very first mechanical exfoliation method was a simple peeling process where pre-treated graphite was fixed on a photoresist and graphene layers were peeled off by a scotch tape [3]. Although this simple method can produce graphene with extraordinary properties, it is limited by its low efficiency. Many efforts have been made to improve mechanical exfoliation method. Ultrasonic devices, solvent and surfactants were used to modify this process to produce high quality graphene on larger scales. The solvents and the surfactants can be intercalated into the atomic layers of graphite to form graphite intercalation compounds to prevent agglomeration and assist further separation of graphene single layer [5,19,20]. The influence of ultrasonic power, time and solvent used on the volume of graphite intercalation compounds was also investigated [5]. Although the use of solvent and surfactants can help to produce good quality graphene in larger scale, their major drawbacks are high solvent cost and the difficulties in following graphene deposition caused by high solvent boiling point [5,19]. Graphite oxides produced by chemical methods were also used in mechanical exfoliation. However, the subsequent produced graphene had inevitable structure defects which could disrupt the electronic structure of graphene. These structural defects could not be restored by chemical reduction or thermal annealing [21–23]. Hence, physical exfoliated graphene is preferred when graphene structure is required in most applications. However, it is still extremely challenging to scale up mechanical exfoliation process to produce large amount of graphene in a cost effective way with commercial available technologies and devices.

Chemical vapour deposition (CVD) Chemical vapour deposition was first reported in 2006. Ni foil was used as a substrate and camphor was used as precursor [24]. Since then, the chemical vapour deposition method has received more and more attention for being regarded as a new promising route to produce graphene on a large scale [5]. In addition, this method was able to control the number of graphene layers and minimize the folding of graphene, and this meant controlled

thickness graphene film could be synthesized [5,23,25,26]. Medium-high carbon solubility (>0.1 atomic%) substrates like Ni and low carbon solubility (<0.1 atomic%) substrates like Cu have different graphene growth mechanisms [5]. For a high carbon solubility substrate, a graphene layer is grown from the precipitation of carbon on the substrate, which is dissolved into the substrate earlier, after cooling. A typical CVD process generally has three steps [26,27]:

1. The substrate is put into a chemical vapour deposition chamber at a setting vacuum and temperature with a diluted hydrocarbon gas.
2. The dissolution of the carbon atoms into the substrate starts at a relatively low temperature.
3. Graphene layers are formed from the out-diffused dissolved carbon atoms in the followed rapid quenching.

The type and concentration of the hydrocarbon gas and the thickness of the substrate determine the concentration of dissolved carbon atoms. Both cooling rate and the concentration of dissolved carbon atoms control the thickness and the crystal structure of the graphene layers [26,27]. For the low carbon solubility substrate, the growth of graphene does not company with a diffusion process. The graphene layers are grown on the surface of the substrate and this process is a four-step process [28]:

1. Methane is deposited on the substrate to form C_xH_y with exposing the substrate to hydrogen.
2. Nuclei start to form from the local supersaturation of C_xH_y on the substrate.
3. Graphene islands are grown from the nuclei on the substrate surface.
4. Graphene covers the substrate surface.

Whether graphene can cover the whole substrate surface depends on the amount of C_xH_y on the substrate. Some modifications of the chemical vapour deposition method have been carried out in recent years. For example, plasma can be used to enhance chemical vapour deposition process that provides a route to synthesize graphene with lower temperature and shorter deposition time [29]. Although CVD is believed to be an ideal route to synthesize large area graphene sheet, the graphene

produced from this technique still has intrinsic defects which allow the transportation of some molecules. Therefore, detrimental effect on the barrier properties of graphene sheet is resulted [30]. In addition, the cost of equipment and the time required to synthesise large amount of graphene are the key limitations.

Reduction and synthesis of graphene oxide Although mechanical exfoliation and CVD can produce high quality graphene, it is still extremely challenging to enlarge the synthesise scale cost effectively with commercial available technologies and devices. Researchers focus more on the reduction and synthesis of graphene oxide because graphene oxide and reduced graphene oxide can be synthesized easier than pristine graphene. Graphene oxide is usually synthesized from the oxidation of graphite by strong oxidants based on Brodie [31], Staudenmaier [32], Hummers' method [33] or some other modification of these methods. Hummers' method was more widely used and many modifications had been made to synthesize graphene oxide for designated applications [5,13,34]. GO can be easily dispersed in many solvents and especially well in water which facilitate any subsequent processing [35]. The reduction of GO to is basically a chemical route to produce graphene with compromised properties induced by the chemical process. GO can be reduced in either chemical routes or thermal routes. Various chemicals had been reported to reduce GO such as hydrazine [23], hydroquinone [36], sodium borohydride (NaBH_4) [37] and ascorbic acid [38]. Hydrazine hydrate reductant was found to be the best one to produce thin and fine RGO. However, NaBH_4 exhibited the best efficient to reduce graphene oxide although it can react slowly with water [5]. Thermal reduction of GO utilizes heat treatment to remove oxide functional group on GO to produce reduced graphene oxide (RGO) [5,13]. A simple and low temperature one-step solvothermal method was reported by Dubin *et al.* [39]. The reduction of GO was resulted from thermal reduction at 200 and the reaction with *N*-methyl-2-pyrrolidinone (NMP) molecules. The detailed chemistry of reduction and the study toward synthesizing ROG with better properties will grow rapidly as the research in graphene moving forward.

2.2.2 Functionalization of graphene

The functionalization of graphene is the major route to stabilise graphene suspensions in a complex environment without agglomeration takes place. For composites based coatings, functionalization of graphene plays a very important role to achieve good interfacial bonding between matrices and graphene sheets. Graphene functionalization can be achieved *via* physical or chemical approaches and there are three major categories of functionalization: functionalization *via* organic species, functionalization *via* macromolecules and functionalization *via* nanoparticles [40].

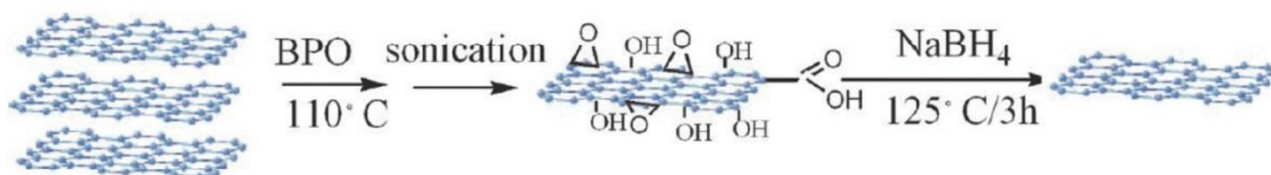


Figure 2.1 The procedure to prepare GO and reduced GO using BPO [44]

Many organic substances can react with the π bonds of graphene and, therefore, different functional groups can be introduced for different purposes. The oxidation of graphite can generate oxidised functional groups on graphene layers which gives the opportunity to produce stable graphene suspension in water or some organic solvents. Graphene oxide (GO) is easy to disperse in water because of its hydrophilic nature. However, it is not soluble in every organic solvent and, therefore, functionalization of graphene is necessary to enable formation of stable graphene suspension with different organic solvent [40,41]. Further treatments of the oxidised groups of GO by organic species can also introduce functional groups such as carboxylic groups, enabling graphene to be available for more applications [42,43]. According to literature, radical reactions can be used as the second route to synthesize graphene oxide and further functionalization. One example is the utilization of benzoyl peroxide to synthesize graphene oxide [44]. The preparation procedure is shown in Figure 2.1. The functionalization of graphene *via* macromolecules is achieved by grafting macromolecules on to graphene sheets. There are two kinds of methods for this type of functionalization: “Graft from” method and “Graft to” method [40]. For “Graft from” method, initiators are immobilized on graphene network for further reaction to take place. One example of this method is the grafting of polypropylene chains onto graphene network by *in situ* Ziegler-Natta polymerization (Figure 2.2) [45]. In terms of “Graft to” method, the key point is incorporating

graphene into polymer matrixes to form composites with the presence of functional groups on graphene sheet which able to form covalent bonds with polymer matrixes. One example for this kind of method is the formation of nanocomposites by ring opening reaction between epoxide and graphene pre-functionalized by amines [46]. Comparing “Graft to” and “Graft from” methods, “Graft from” method is more likely to improve the compatibility of graphene with organic solvents and polymer matrixes whilst “Graft to” method is to fabricate graphene-polymer nanocomposites by covalently bonding functional groups on graphene network to polymer matrices [40].

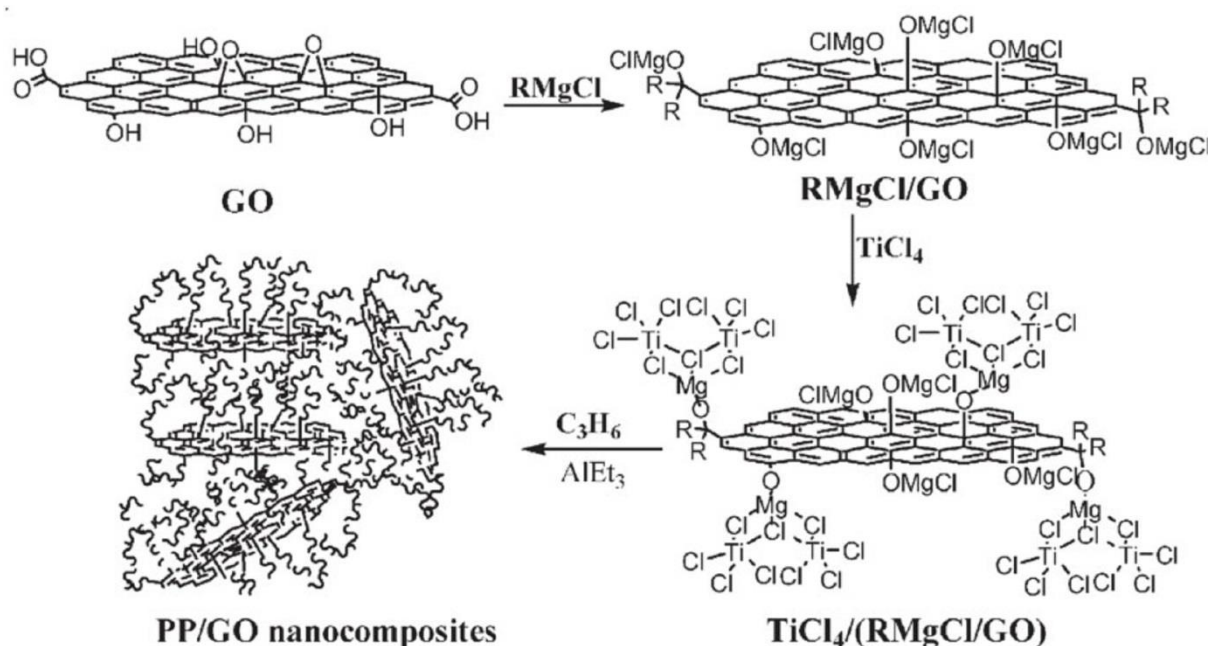


Figure 2.2 Procedure to graft PP chains on graphene *via in situ* Ziegler-Natta polymerization [45]

The third route to functionalize graphene is essentially the route to fabricate graphene-nanoparticles (G-NPs) composites. The nanoparticles are well investigated in these years and they are widely regarded as providing profound property enhancement in many applications. The combination of graphene and nano-particles is to achieve the synergistic effects of both materials with the goal of developing excellent properties composites. There are three main strategies to synthesize graphene-nanoparticles composites: pre-graphenization, post-graphenization and syn-graphenization [5]. For pre-graphenization, reduced graphene oxide is synthesized first and then mixed with nanoparticles to form composites. One example for this strategy is the synthesis of Pd nanoparticles on graphene oxide sheets *via* electrochemical method [47]. The solubility of reduced graphene oxide in different organic solvent and the addition of second phase nano-particles are the major

consideration in this strategy. In post-graphenization, nanoparticles are prepared first and, then, nanoparticles and appropriate metal salt precursors are mixed with graphene oxide suspension followed by reduction. The synthesis of RGO/TSCuPc Composite is an example for post-graphenization. RGO solution was prepared first and then it was mixed with TSCuPc aqueous solution for subsequent processes which deposited NPs on RGO network [48]. Syn-graphenization is a one-step approach in which the second component of the composites functions as a stabilizer to improve the composites' properties. A good example for syn-graphenization can be the study of synthesizing graphene-CdS quantum dot nanocomposites by a one-step facial method. In this one-step facial method, solvothermal reduction of GO and deposition of CdS on GO network took place simultaneously [49].

2.3. Applications of graphene in coating

2.3.1 Pristine graphene based materials coating

It may be convenience and cost effective to use pristine graphene based materials directly without further processing such as synthesize graphene on a substrate to form a coating layer with commercial available technique. The published papers indicated that this concept was possible and the coated substrates showed improved properties. However, some problems still need to be resolved before commercialization.

Coatings for electrical applications: For the utilization of graphene, the electrical properties of graphene are often the most favourable because they are the most promising and attractive properties in industry. A potential transparent conductive coating suitable for the practical touch panel application was fabricated on copper substrate *via* the combination of plasma CVD and roll-to-roll process [50]. Improved electrical conductivity and highly uniform transmittance and haze were reported. Although the electrical conductivity was improved, the measured sheet resistance was still so high that could not meet the requirements in electrical applications. A large conductive transparent chemical converted graphene film was fabricated *via* spray coating method [51]. Graphene oxide was synthesized from expandable graphite according to modified Hummer's method and mixed with hydrazine monohydrate afterward. The substrate used for coating was

quartz. The conductive film exhibited low sheet resistance of $2200 \Omega \text{sq}^{-1}$ and high transmittance of 84%. However, the stabilization time of GO-hydrazine suspension is a few weeks long and this limits the conductive film to be used in commercial applications. The success of electrophoresis deposited graphene film on glass substrate was reported by Ishikawa *et al.* [52]. Graphene was reduced from GO, which was produced by modified Hummers' method, after being electrical deposited on glass substrates. The lowest sheet resistant and highest transmittance measured were $4.59 \times 10^4 \Omega \text{sq}^{-1}$ and 83.8%, respectively. The sheet resistant measured here was lower than the CVD fabricated graphene film mentioned previously, but it is still too high to be used in a commercial product. Uniform reduced GO film for soft touch screen was able to be fabricated on polyethylene terephthalate substrate *via* large scale rod-coating [53]. The reduced GO film reported has even lower sheet resistance which is up to $1,800 \Omega \text{sq}^{-1}$ and high transparency and high flexibility were also reported.

Although the most attractive property of graphene is electrical conductivity, other outstanding electrical properties such as fast electron mobility make it promising in improving other electrical properties other than electrical conductivity. A hierarchical graphene oxide/ MnO_2 nanostructure sponge was fabricated by dipping commercial available macroporous sponge into graphene oxide and MnO_2 solutions in a sequence [54]. The graphene oxide used was produced by modified Hummer's method. The results showed that this coated sponge could be used as super capacitor or be used in batteries because of high specific capacitance, wide operation range, good energy and power density, and excellent cycling stability. Its outstanding properties included about 10% degradation after 10,000 cycles at a charge–discharge, specific current of 10 A/g, retaining 90% of its capacitance after 10,000 cycles under a scan rate of 10 V/s, maximum E of 2.08 Wh/kg and highest P of 94 kW/kg at the operate voltage of 0.8 V. For the utilization of electron mobility of graphene, Jeon *et al.* reported that moderately reduced graphene oxide could be used as the hole transporting layer (HTL) in polymer solar cells (PSCs) [55]. The reduction of graphene oxide was performed *via* the thermal treatment of solution processed graphene film at about 250°C under air atmosphere. The reduced graphene oxide layer was coated on to indium tin oxide (ITO) coated glass substrate by spin coating method. Compared to poly(3, 4-ethylenedioxythiophene): poly

(styrene-sulfonate) HTL, the transportation efficiency of moderately reduced graphene oxide HTL was improved slightly, but it was much more stable after exposing the HTL into air. In terms of transmittance properties, an example is the attempt to use reduced graphene oxide coating on aluminium film for an effective optoacoustic transmitter used high pressure and high frequency ultrasound generation [56]. Graphene oxide was synthesized by modified Hummer's method and then it was reduced to form RGO. RGO was spin coated on glass substrate before the aluminium film deposition on the RGO. The RGO coated aluminium transmitter generated enhanced optoacoustic pressure of 64 times the aluminium-alone transmitter under a pulsed laser excitation. As a result, this RGO coated aluminium film was very ideal for laser-induced ultrasound application. In addition, graphene based materials could be used to improve the photocatalytic activity of TiO_2 film [57]. Graphene oxide was synthesized through a modified Hummers' method and it was coated on TiO_2 film by spin coating method. The graphene oxide coated TiO_2 film exhibited better photocatalytic activity, due to the giant π -conjugation system and two dimensions planar structure. However, the photocatalytic activity decreased on higher graphene oxide loading as a result of absorbance and scattering of photons *via* excess carbon in the system. There are still a lot of studies related to utilize graphene based materials as coatings in electrical applications and some of them are listed in Table 2.1.

Table 2.1 Pristine graphene based coatings used in electrical applications

Coating types	Substrates	Applications	Improved properties	Coating methods	Ref
Graphene	$\text{Li}[\text{Li}_{0.2}\text{Mn}_{0.54}\text{Ni}_{0.13}\text{Co}_{0.13}]\text{O}_2$	Cathod materials	Cycling performance and rate capacity	Spray drying	[58]
Graphene	Carbon coated LiFePO_4	Cathod of Li-ion battery	Discharge capacity	Rapid, one-pot, microwave-assisted hydrothermal	[59]

				method	
Few layers graphene	Porous $\text{Li}_4\text{Ti}_5\text{O}_{12}$	Energy storage	Capacities, cyclic performance and capacity retention	Direct pyrolysis of $\text{C}_{28}\text{H}_{16}\text{Br}_2$	[60]
Graphene	Al_2O_3	Dye-sensitised solar cells	Energy conversion efficiency	Doctor-blading	[61]
Graphene	PtRh electrodes	Electrochemical sensitivity	Electron transfer	Dip coating	[62]
Few layers graphene	Iron oxide nanoparticles	Units of hyperthermia therapeutics	Magnetic properties	<i>In situ</i> polymerization with precursor	[63]
Graphene oxide	Core-shell structure Polystyrene	Electrorheological smart materials	Electrorheological properties	Strong $\pi-\pi$ stacking interaction	[64]
Graphene oxide saturable absorbers	ITO glass	Passively Q-switched operation	Pulse width and peak power	Spin coating	[65]
Graphene	Al_2O_3	Photoanodes	Superior photoelectrochemical responses	Direct synthesis	[66]
Graphene oxide	FTO glass	Electrode for battery	High open circuit voltage ($\sim 250\text{mV}$) and short circuit current (0.31mA)	Spin coating	[67]

Coatings for protection purposes: The extraordinary properties of graphene make it become an effective barrier toward oxidation and corrosion of a substrate (mention the properties of the sheet for permeability). In terms of barrier properties, a graphene oxide/poly (ethylene imide) (PEI) oxygen barrier coating was studied [68]. Graphene oxide was produced by oxidizing and exfoliating graphite according to modified Hummers' method. The coating was deposited onto a PET film through layer-by-layer method to form graphene oxide/PEI bilayer. The oxygen barrier properties were measured by MOCON and the OTR values indicated that OTR of a deposited coating decreased with the increasing numbers of graphene oxide/PEI bilayers (Figure 2.3). However, the water vapour barrier properties were not improved. For water barrier properties, a superhydrophobic structures was fabricated by coating multi-walled carbon nanotubes (MWCNTs) and ROG on to silica colloids [69]. Graphene oxide was produced by modified Hummer's method and then it was reduced to form RGO. RGO and MWCNTs were coated on to the colloids by LBL in which RGO sheets were negatively charged and MWCNTS were positively charged. The

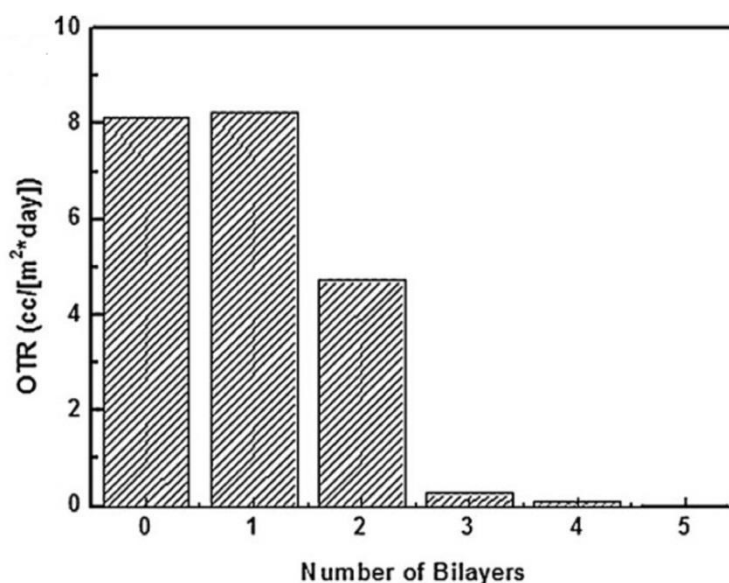


Figure 2.3 OTR versus number of bi layers [70]

fabricated composites exhibited controllable surface hydrophobicity which could be readily controlled from 119 to 151 °C by controlling the number of the bilayers deposited on to the colloidal particles. In addition, graphene fluoride was adopted as transparent hydrophobic coating innovatively by Zhang et al. [70]. Graphene fluoride was produced from liquid phase exfoliation of graphite fluoride and graphene fluoride coating was spin coated on glass substrate for further

characterization. The measured contact angle was 123° and the light transmittance was up to 92% both indicated that a good candidate for transparent hydrophobic coating was produced. Moreover, long service life of graphene fluoride coating was detected in water erosion experiments and ultraviolet aging tests.

The efficiency of graphene based materials as anti-corrosion and anti-oxidation coating on different substrates with different coating methods was reported [71–77]. Most of reported graphene coating layer was fabricated by CVD and their results were summarized in Table 2.2. Nilsson and his co-workers suggested the limitations of graphene coating for corrosion inhibition on metal surfaces where graphene coated by CVD could only function as corrosion inhibitors at low gas pressure [73]. Nayak *et al.* indicated that graphene was a good protective coating due to its inertness to oxidizing gas and liquid solutions, but its oxidation resistance was limited below 500°C [74]. An anti-corrosion mechanism of CVD graphene coating on copper substrate was proposed by Singh

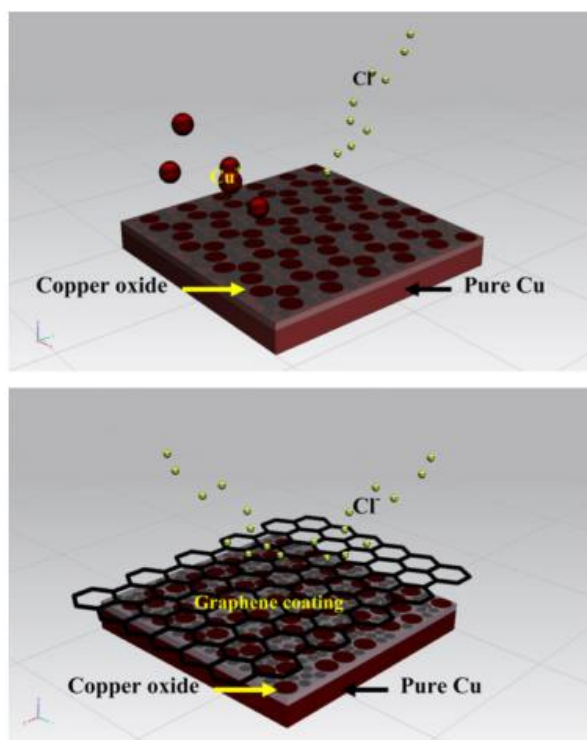


Figure 2.4 Schemes of anti-corrosion mechanism of CVD graphene coating on copper [75]

Raman *et al.* and this mechanism may be used to explain the anti-corrosion behaviour of graphene film on different metal substrates (Figure 2.4) [75]. Apart from CVD, spray coating was used to

coat graphene on gold coated cuprous substrates by Noel *et al.* [77]. Graphene solution was purchased from market directly. The coated substrates had less weight gain during corrosion test than pure gold coated substrates and low contact resistance and low friction coefficient were also identified. The spray coated graphene was not only be used as anti-corrosion coating but also be used as surface protection coating resulted from its low friction coefficient. Dry contact sliding was carried out by Won and his co-workers to test the durability and degradation mechanisms of graphene coating on copper substrates [78]. The graphene coating was grown on Cu substrates by CVD. The friction coefficient of graphene was obtained as about 0.18 and remained stable up to several thousand cycles. As a result of the formation of amorphous carbon layer on the wear crack, an increase of friction coefficient after a certain time was detected. From these results, pristine graphene can be a good candidate as surface protection coating.

Table 2.2 Performance of graphene produced by CVD as anti-corrosion and anti-oxidation coating

Substrates	The performance of graphene coating	Ref
Cu and Cu/Ni alloy	Metal surfaces were well protected from oxidation even after heating at 200°C in air for up to 4 h	[71]
Cu	Deterioration was not detected under vigorous flow boiling conditions for long exposure	[72]
Pt	Reconstruction of Pt could be preserved in O ₂ pressures as high as 10 ⁻⁴ mbar and CO pressures below 10 ⁻⁶ mbar	[73]
Ni	Oxidation resistance of the coating was effective up to post annealing of 500°C	[74]
Cu	Corrosion resistance of coating is 1.5 orders of higher magnitude than uncoted substrates	[75]
Cu and Ni	In an aerated Na ₂ SO ₄ solution: Direct coated copper films were corroded 7 times slower than bare copper. Direct coated nickel substrates were corroded 20 times slower than bare nickel.	[76]

Coatings for sensing and absorbent applications: The unique structure of graphene based materials makes it a promising candidate in sensing and absorbent applications [4]. A superhydrophobic and superoleophilic sponge was fabricated by coating graphene on melamine sponge *via* dip coating [79]. This graphene coated sponge exhibited high absorption capacities up to 165 times of its weight, high selectivity, good recyclability, lightweight, robustness, and inertness to corrosive environments. Biochar, a attractive material has potential applications in many environmental areas, could be coated by graphene to enhance thermal stability and absorption properties [80]. Graphene was produced by mechanical exfoliation from graphite powder and it was coated onto cotton wood by dip coating before pyrolysis into biochar. Thermal decomposition temperature of graphene coated biochar was 64°C higher than pure biochar and enhanced absorption ability to aqueous methylene blue was also identified.

Compared to absorbent applications, graphene based materials had attracted more attention of the researchers in sensing applications. Graphene was coated on quartz crystal microbalance (QCM) by solution drop-coating method for the detection of formaldehyde [81]. The QCM-type sensor showed frequency change when exposed to different concentrations of formaldehyde. Perfect linear correlation between frequency shifts versus concentration change of HCHO was achieved during the analysis. A potential bio-sensor was produced *via* coating reduced graphene oxide nano ribbons (rGONRs) on Si/SiO₂ substrates by spray coating [82]. GONRs were fabricated through chemically unzipping multi-walled carbon nanotubes and they were deposited on Si/SiO₂ substrates before reduction. High on/off ratio and ability of detecting adenosine triphosphate (ATP) molecules were identified in this rGONRs network. Graphene based materials can also be used in water sensing applications. Yao *et al.* developed a graphene oxide/silicon bilayers for humidity sensing applications [83]. The ultimate sensitivity could reach 79μV/%RH with a wide detection range of 10–98%RH and the humidity sensibility could be enhanced by increasing the thickness of the graphene oxide coating. A humidity sensing mechanism was also proposed (Figure 2.5). Graphene oxide coated quartz crystal microbalance was also used for humidity detection [84]. Graphene oxide was synthesized by the modified Hummers method and spin coated on quartz crystal substrates. The GO coated quartz crystal substrates showed excellent humidity sensing properties and a linear

frequency response versus RH in the wide detection range of 6.4–93.5% RH was obtained.

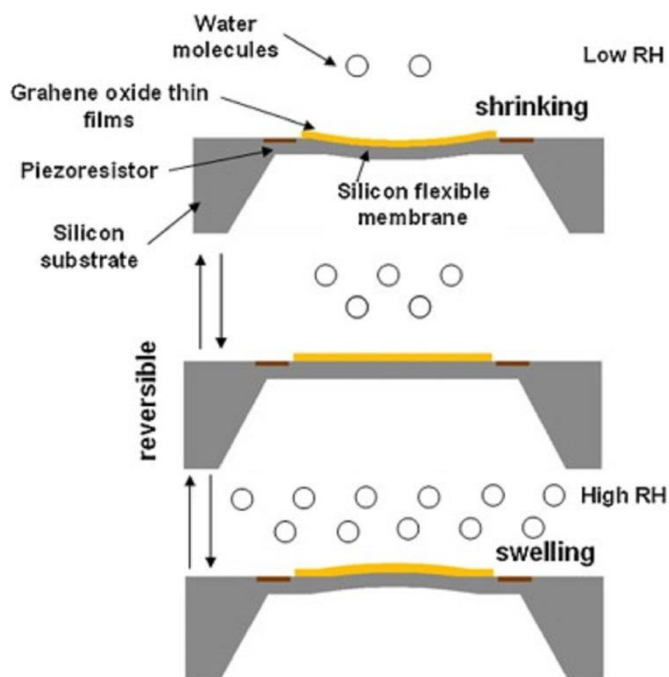


Figure 2.5 Humidity sensing mechanism of graphene oxide/silicon bilayer [84]

Apart from using graphene based materials to develop new sensing structure, graphene based materials can also be coated onto commercial available equipments such as probes to improve their performance. As reported by Zhang *et.al.*, graphene can be coated onto a plunger-in-needle microsyringe for solid-phase microextraction (SPME) device as a sorbent material toward UV filters [85]. The graphene was coated on the microsyringe by sol-gel method. Compared to other commercial available SPME fibres, graphene coated microsyringe exhibited different selectivity and showed high extraction efficiency for light polar salicylates and 4-MBC. There are a lot of related reports about the utilization of graphene based materials in SPME and they were summarized in Table 2.3. The performance of graphene and graphene oxide coated columns as stationary phase for capillary electrochromatography and capillary liquid chromatography was investigated by Qu *et al.* [86]. Graphene oxide was synthesized by the modified Hummers method and then was coated on a capillary column via 3-aminopropyltriethoxymethyl silane as coupling agent. Graphene coated column was reduced from GO coated capillary. Effective separation of natural, basic and proteins were observed on the GO coated column. However, graphene coated column had poor separation performance. Graphene coated Fe_3O_4 nanoparticles could also be used as adsorbent material for

high-performance liquid chromatography [87]. Graphene was synthesized *via* the reduction of graphene oxide obtained by modified Hummer's method. Graphene was coated on Fe_3O_4 nanoparticles by *in situ* chemical coprecipitation of Fe^{2+} and Fe^{3+} in an alkaline solution in the presence of graphene. Compared to other methods (e.g. SPME), the type of magnetic nanoparticles exhibited high adsorption capacity, rapid adsorption rates, low amount of sorbents can be used and short equilibrium time to extract triazine herbicides. Similar study was conducted for gas chromatography using graphene oxide [88]. GO was synthesized by a modified Hummer's method. The capillary column was pretreated with 3-AMDS toluene solution and it was then dipped into GO solution to form GO coated column. Separation of various organic compounds with good separation efficiencies was achieved.

Table 2.3 Graphene based coatings used in SPME application

Coating type	Synthesis method	Substrates	Coating methods	Materials detected	Ref
Graphene	Reduction of graphene oxide	Stainless steel wire	Dip coating	Six selected pyrethroid pesticides	[89]
Graphene	-	Stainless steel wire	Sol-gel	Organochlorine pesticides (OCPs)	[90]
Graphene nano sheets	Microwave assisted reduction of graphene oxide	Stainless steel wire	Dip coating	OCPs	[91]
Graphene	Their previous work	Stainless steel wire	Dip coating	Triazines herbicides	[92]
Graphene	Reduction of graphene oxide	Stainless steel wire	Dip coating	Carbamates	[93]

C18 functionalized graphene oxide	-	Stainless steel wire	LBL	Polycyclic aromatic hydrocarbons (PAHs)	[94]
-----------------------------------	---	----------------------	-----	---	------

Signal enhancement is also an area that can be benefited from graphene based materials. According to Hao and his coworkers, graphene can also be coated onto conventional metallic surface-enhanced Raman scattering (SERS) substrates to improve the sensitivity of SERS detection [95]. Graphene was synthesized by CVD on copper foil and then was transferred to gold nanostructures (nanoparticles or nanohole arrays). The graphene coated substrates exhibited 3-fold or 9-fold enhancement in Raman signal of methylene blue compared to bare nanohole or nanoparticle substrates, respectively. Kim *et al.* developed a GO/polyallylamine hydrochloride (PAA) – Ag nanoparticles (AgNPs)/PAA-RGO three layers films for SERS enhancer and anti-corrosion coating [96]. The preparation procedure is shown in Figure 2.6. Graphene oxide was synthesized by their method and graphene oxide was reduced by hydrazine monohydrate. Raman signal on R6G on was enhanced by 6 fold on GO/PAA-AgNPs/PAA-RGO whilst AgNPs/PAA-RGO film was 1.67 fold. The GO/PAA-AgNPs/PAA-RGO films exhibited prolonged lifetime up to 72 days against oxidation under ambient conditions. Cobalt nanoparticles coated by graphene surface functionalized with benzylamine groups were nanomagnets that were able to broaden the range of analytes for surface-assisted laser desorption/ionization mass spectrometry (SALDI-MS) analysis [97]. This G coated CoNPs was prepared using flame spray pyrolysis with metal containing organic precursors. The nanomagnets were also able to extract perfluorooctanesulfonate from large volumes of aqueous solutions by magnetic separation.

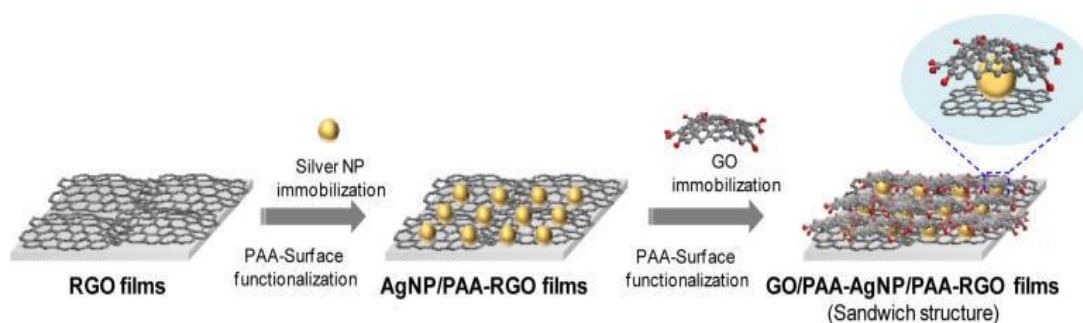


Figure 2.6 Preparation procedure of G/PAA-AgNPs/RGO sandwich structure [96]

2.3.2 Graphene based nanocomposites coating

As reported previously, pristine graphene based materials coating exhibited excellent properties in different applications. However, it is still challenging when proceeds to large scale commercialization. Adhesion is the critical factor of coating durability and applicability. Some surface treatments and graphene functionalization routes can help to achieve good adhesion but these may not good enough for long term durability. In addition, the pristine graphene based coating layer may not dense and many micro channels may exist between graphene sheets. The existence of micro channels is detrimental to long term durability as these micro channels allow erosion and corrosion to take place easily. A porous coating layer is impossible to be commercialized. The technologies nowadays are difficult to produce perfect defect free graphene based materials. Therefore, the development of graphene based nanocomposites is an alternative route to trigger the commercialization of graphene based materials. In coating applications, researchers mainly focus on polymeric graphene based nanocomposites and graphene-nanoparticles composites (G-NPs).

Graphene-nanoparticles composites as coatings: In G-NPs, graphene based particles are usually coated on to nanoparticles first and then the coated nanoparticles can be used as coating materials. There are some published articles related to electrical properties improvement by G-NPs. Wang *et al.* reported that graphene oxide wrapped sulphur particles could be used to modify the capacity and cycling stability of rechargeable Lithium-sulfur battery cathode material [98]. The resulting composites exhibited high and stable specific capacities up to about 600 mAhg^{-1} over more than 100 cycles. Another example is the attempt to adopt $\text{SnO}_2\text{-SiC/G}$ nanocomposite for high performance lithium-ion storage [99]. $\text{SnO}_2\text{-SiC/G}$ nanocomposite was in situ generated by simple ball milling method and it was graphene coated on to $\text{SnO}_2\text{-SiC}$ core-shell structure in which SnO_2 nanoparticles were uniformly deposited onto SiC core. Graphene was produced from reduction of graphene oxide. The nanocomposite exhibited a high reversible capacity of 810 mA h g^{-1} and 83% capacity retention over 150 charge/discharge cycles between 1.5 and 0.01 V at a rate of 0.1 A g^{-1} . A high reversible capacity of 425 mA h g^{-1} was obtained at a rate of 2 A g^{-1} as well. A reversible capacity of 1451 mA h g^{-1} and good cyclability were measured when discharged to a higher potential at 3.0 V. G-NPs were also used to improve photo-activity in their related applications. A

graphene- TiO_2 nanoparticles composite coating was prepared and coated on to a conducting support medium for enhanced photoelectrocatalytic activity [100]. Graphene was reduced from graphene oxide produced from modified Hummers' method. The composite coating was applied on to F-doped tin oxide (FTO) via dip coating method to form a film electrode. Compared to pure TiO_2 film electrode, graphene- TiO_2 composite exhibited better photoelectrocatalytic capacity. In addition, a TiO_2 -dextran-graphene oxide nanocomposite, which was prepared by an environmental friendly strategy, could be used to enhanced photocatalytic activity [101]. This composite coating was applied onto the substrates *via* spin-coating method. The results showed that TiO_2 -dextran-graphene oxide composite exhibited excellent photocatalytic activity and photovoltaic response than pure TiO_2 because the electron-hole pairs in the composite had longer life time. Graphene based TiO_2 nanocomposites were mostly studied in photocatalytic activity, but there were many other systems could be used as potential coating on a substrate to improve photocatalytic activity as suggested by Zhang *et al.* and Yang *et al.* [102,103]. In their group, the utilization of G-NPs in both 'selective' and 'non-selective' processes were studied extensively [104–106], and the effect of different carbon based materials for photocatalytic activity was investigated as well [107].

In terms of barrier properties, there is only one related report. Kou *et al.* have developed a facial strategy to synthesize GO- SiO_2 nanohybrids as general building blocks for large area super hydrophilic coating [108]. GO was synthesized according to their own method and SiO_2 nanoparticles were deposited on to GO nanosheets *via in situ* hydrolysis of TEOS. Ceramic, PP and lotus leaf were used as substrates. Compared to bare substrates, all the coated substrates had much smaller contact angles which indicated excellent wettability of water was achieved. In addition, GO- SiO_2 sheets could be made into paper film by a filtering technique and exhibited high conductivity of 10^3 – 10^4 Sm^{-1} after reduction by hydrazine vapour. G-NPs can also be used in SPME application to improve extraction performance. ZnO/graphene nanocomposite for SPME silica fibre coating was developed by Zhang *et al.* [109]. Graphene was produced by reduction from graphene oxide obtained according to modified Hummers' method. The SPME fibres coated by ZnO/graphene nanocomposite exhibited enhanced durability, enlarged surface area, higher extraction selectivity and sensitivity toward sulphur compounds.

The challenges of G-NPs commercialization are similar to pristine graphene based materials coatings. A dense layer G-NPs coating layer without any pores is difficult to achieve. The process of coating graphene based materials on nanoparticles is complicated and is not cost-effective. G-NPs may have better properties but the cost to produce this type of composites is much higher than using pristine graphene based materials.

Polymeric graphene based nanocomposites as coatings: The incorporation of graphene based materials into polymer not only can improve one property of a polymer, but also enhance several properties at the same time such as electrical properties and mechanical properties. Polyurethane acrylate (PUA) coating reinforced by graphene was synthesized by Liao *et al.* using *in-situ* polymerization on a TEFLON plate [110]. The graphene used was thermal reduced graphene received from a company. Their results showed that the electrical conductivity of the composite increased with increasing graphene loading. The cured composites exhibited lower percolation concentration than uncured composite and the addition of graphene could reinforce the mechanical properties of PUA coating in rubbery region. A graphene reinforced poly(butylene terephthalate) (PBT) composite was synthesized by Fabbri *et al.* and they suggested that this composite could be a potential conductive coating [111]. The graphene nanoplatelets used were purchased from a company. The key results of this study are shown in Table 2.4. The decomposition temperature under oxygen atmosphere exhibited optimum value at 0.75 wt% graphene loading while the melting temperature decreased with the increase of graphene loading. The Percolation threshold appears between 0.5 wt% and 0.75 wt% graphene loading. The composite with 0.5 wt% graphene loading had optimum hardness but the hardness decreased with the increase of graphene loading. The performance of DSSCs could also be improved by using Graphene/Nafion[®] composites as counter electrode [112]. Graphene was reduced from the GO synthesized according to Staudenmaier's method and graphene/ Nafion[®] was coated on ITO glass by drop coating method. A solar-to-electricity conversion efficiency (η) of 8.19% was achieved by using this type of composite. Although it was only a little smaller the η of s-Pt film (8.89%), the cost is much lower. A transparent conductive graphene oxide/ poly (ethylene glycol) diacrylate coating was developed for magnetic shielding and anti-static applications [113]. The coating was applied on to glass substrates

and cured by UV light. The percolation threshold was 0.02 wt% and the lowest sheet resistance measured was $6300 \Omega \text{ sq}^{-1}$.

Table 2.4 Comparison of pure PBT and PBT/Graphene coatings

Samples	$T_{i.ox}$ (°C)	T_m (°C)	Electrical resistance (M Ω)	Hardness (HV)
PBT	389	228.4	-	15.1 ± 1.2
PBT/G 0.5 wt%	388	223.6	760	26.6 ± 1.8
PBT/G 0.75 wt%	404	214.2	200	23.1 ± 1.7
PBT/G 1.0 wt%	390	212.3	50	9.5 ± 2.6

In terms of protective coatings, there are a few researches published in recent years. An anti-corrosion polyaniline/graphene composite coating for steel has been prepared by Chang and his co-workers [114]. The graphite powders were exfoliated and functionalized with 4-aminobenzonic acid (ABA), and the graphene and graphene-like sheet were obtained from a direct electrophilic substitution reaction in a PPA/P₂O₅ medium. Compared to bare steel, PANI coating and clay reinforced PANI coating, graphene reinforced PANI coatings exhibited the best electrochemical corrosion resistance, oxygen barrier efficiency and water barrier efficiency (Table 2.5). Graphene reinforced poly(phenylene sulphide) (PPS) was reported that exhibited seven times higher wear life than pure PPS coating [115]. Graphene oxide was synthesized by the Hummer's method and it was functionalized to yield organophilic graphene. The as-produced solution was coated on steel substrates through spray coating. The major wear form was identified as abrasive wear for graphene reinforced PPS coating whilst the wear form of pure PPs coating was adhesive wear. In addition, polyamide 11 (PA11)/graphene coating could also be used to improve tribological properties of PA11 [116]. Graphene oxide was prepared through the Hummer's method and it was functionalized to produce organophilic graphene. The PA 11 and organophilic graphene composites were spray coated on to steel substrates. The wear life of the composite coating increased by 460%–880% compared with that of pure PA 11 coating, but the values of friction coefficients had hardly changed.

Higher performance polyurethane (PU)/functionalized graphene nanocomposites was developed by Cai and his co-workers for mechanical and thermal stability improvement and it could be a potential surface protection coating [117]. The GO used was prepared by their method. The morphology of resulted composites is shown in Figure 2.7 and a good dispersion of GO was observed. Improved scratch resistant, thermal stability, hardness indentation and Young's modulus were reported. A study suggested that graphene could be used as nano-additives in galvanic corrosion protection coating [118]. Graphene was purchased from a company and ITO and graphene were used as additives of primer epoxy coating which spray coated on the surfaces of carbon fibre composites. The results showed that both ITO and graphene could be used for lightning strike protection, but ITO had better protection efficient.

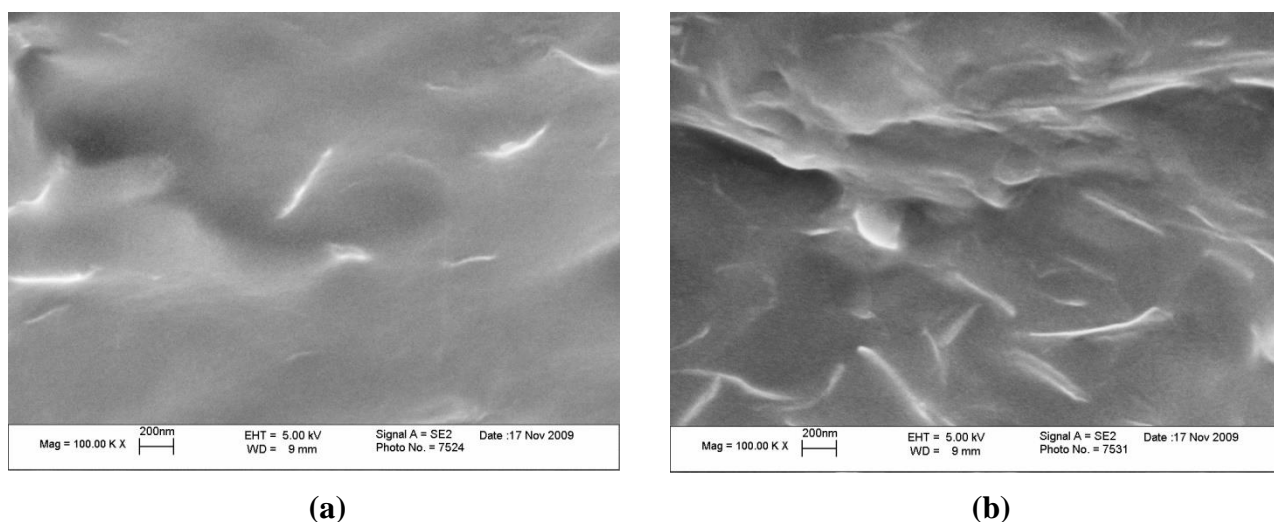


Figure 2.7 SEM images of GO/PU nanocomposites (a) 1 wt% of GO (b) 4 wt% of GO [117]

Table 2.5 Comparison of PANI coating, Steel and composite coatings

Samples	Electrochemical corrosion measurements		Oxygen Permeability (barrer)	Vapour Permeability Rate (g/hr.m ²)
	E _{corr} (mV)	I _{corr} (μA/cm ²)		
Steel	-789	14.71	N/A	N/A
PANI	-647	307	0.75	170
0.5 wt% Graphene reinforced PANI	-537	0.38	0.13	20

0.5 wt% Clay reinforced PANI	-584	1.38	0.35	60
---------------------------------	------	------	------	----

Conductive coatings and protective coatings receive a lot of attraction, but the study toward mechanical properties and thermal stability of a coating is important as well. A graphene-reinforced waterborne polyurethane nanocomposite coating was fabricated by the sol-gel method using silane-functionalized graphene nanosheets [119]. The graphene oxide powder was synthesized according to Hummer's method and the graphene oxide powder was chemically reduced to form graphene nanosheets suspension. With increasing the weight percent of graphene in the coating (from 0 to 5 wt%), the tensile strength increased from 11.8 MPa to 20.2MPa, the Young's modulus increased from 69.8 MPa to about 118 MPa and the elongation at break reduced from 324% to 138%. In addition, the thermal properties of the waterborne coating were improved by graphene where the decomposition temperature increased from about 258°C to about 270°C. PUA coating could be reinforced by functionalized GO to obtain improved thermal stability and mechanical properties according to Yu *et al.* [120]. GO was synthesized according to Hummer's method and it was functionalized to be UV curable with PUA. The initial degradation temperature of the PUA composite with 1.0 wt% functionalized graphene oxide was increased to 316 °C from 299 °C (pure PUA). The storage modulus and tensile strength of the PUA composite with 1.0 wt% functionalized graphene oxide were increased by 37% and 73%, respectively, compared with those of neat PUA. A functionalized graphene sheets/UV cured epoxy nanocomposite coating was developed to seek better mechanical properties by Martin-Gallego *et al.* [121]. The coating was coated on glass substrates and cured by UV-light for subsequent characterizations. Compared to pure epoxy resin, graphene reinforced epoxy nanocomposite exhibited higher glass transition temperature, higher stiffness and higher storage modulus for high temperature. The toughening effect of graphene platelets toward epoxy resin, which is widely used in coating application, was investigated [122]. The graphene platelets were produced from direct mechanical exfoliation and chemical modified for interfacial strength study. The glass transition temperature (T_g) had a 14.7% increase compared to pure Bisphenol A diglycidyl ether (DGEBA) and the highest fracture energy release rate G_{1c} obtained was 613.4 Jm⁻². The toughening mechanisms were identified as voiding, micro-cracking

and breakage of graphene platelets. The possibility of polymeric graphene based composites being used in SPME application was studied by Zou *et al.* [123]. Graphene/Polypyrrole composite was coated on to stainless steel wire by *in situ* polymerization. The prepared graphene/polypyrrole coated fibre showed the highest extraction efficiency toward five phenols compared to a number of commercial fibres and polypyrrole or GO/polypyrrole coated fibres. The graphene/polypyrrole composite coating on fibre also exhibited good thermal and mechanical stability, excellent adhesion and long lifetime.

The published papers about graphene based materials reinforced composites are numerous and they may be used in coating applications if proper processing techniques are used. Yoo *et al.* summarized a list of graphene based materials reinforced polymers nanocomposites which could be used in all sorts of applications. Corrosion resistance and erosion resistance are vital for the commercialization of a coating because they relate to the life time of a coating system. It is worthwhile to commercialize a coating system only when it process both good properties and long life time. Orientation, particle size, aspect ratios, number and wrinkles of graphene based materials in polymer matrix are the major factors that affect the corrosion and erosion resistance. The process of corrosion and erosion is basically a process that corrosive substances diffuse through the coating layer and damage the substrate. The utilization of fillers and produce defect free composites is to diminish or lengthen the diffusion paths of these substances. In order to achieve maximized barrier efficiency of the graphene based materials: 1) good dispersion of graphene based materials must be achieved; 2) the orientation of graphene sheets should be parallel to coating layer; 3) the aspect ratios of graphene sheets are high and the particle size of graphene particles is large; 4) aggregation and wrinkles of graphene sheets should be prevented; and 5) larger numbers of graphene sheets presented in the polymer matrix can help to increase the diffusion paths [15]. The most attractive property of graphene is its electrical conductivity. Although the graphene based materials can improve the electrical properties of a polymer, the achieved electrical properties still cannot meet the requirements of electrical applications. In general, the resistant of a filler reinforced polymer composite is determined by the tunnelling resistant between the particles and the contact resistant between fillers [124]. The electrical conductivity of polymers is generally low. Although graphene

can improve their electrical conductivity, it is still not high enough to fulfil the industrial requirements. The combination of small particle size and large particle size conductive fillers is a way to further improve the electrical conductivity of polymer nanocomposites because small particle size fillers can act as bridges between two large sized particle to reduce the tunnelling resistance between them [124].

2.4. Polyurethane based coatings

2.4. 1 Building blocks and synthesis of polyurethane

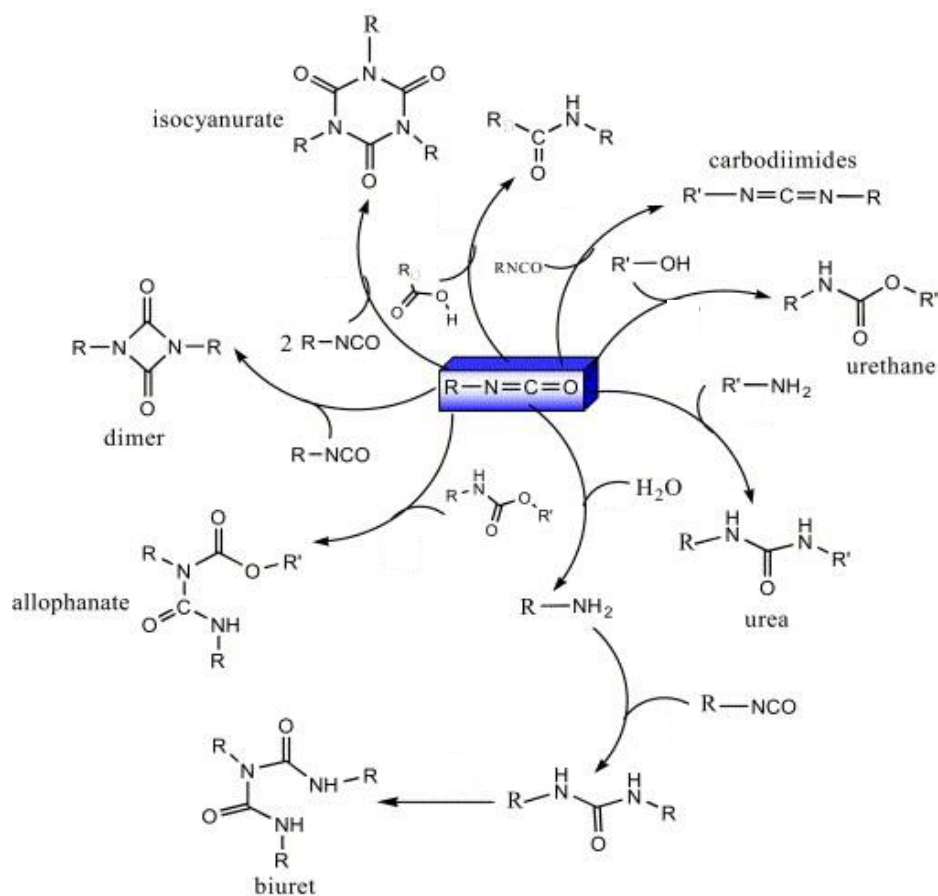


Figure 2.8 The basic reactions of isocyanate group with other functional groups

The key reaction to produce PU is the reaction between isocyanate group and active hydroxyl group. Apart from this reaction, the isocyanate group can also react with other functional groups because it is very reactive. Its reactions can be divided into two main categories: (1) the reactions of isocyanates with compounds containing active hydrogen, (2) the reactions of between isocyanate groups (self-condensation). The basic reactions of isocyanates with other substances are shown in Figure 2.8 [1,125]. The pronounced positive electro character of the C atom in $-N=C=O$ is the

main reason for the high reactivity of isocyanate groups towards nucleophilic agents. The large electrophilic character of the carbon atom is imparted from the electronegativity of the oxygen and the nitrogen in --N=C=O . In the reaction systems to produce PUs, diisocyanates, polyols, catalysts and even chain extenders are usually be used. Therefore, the final structure and properties of a PU polymer are highly dependent on the structure and properties of the components used to synthesize PUs.

2.4.1.1 Isocyanates

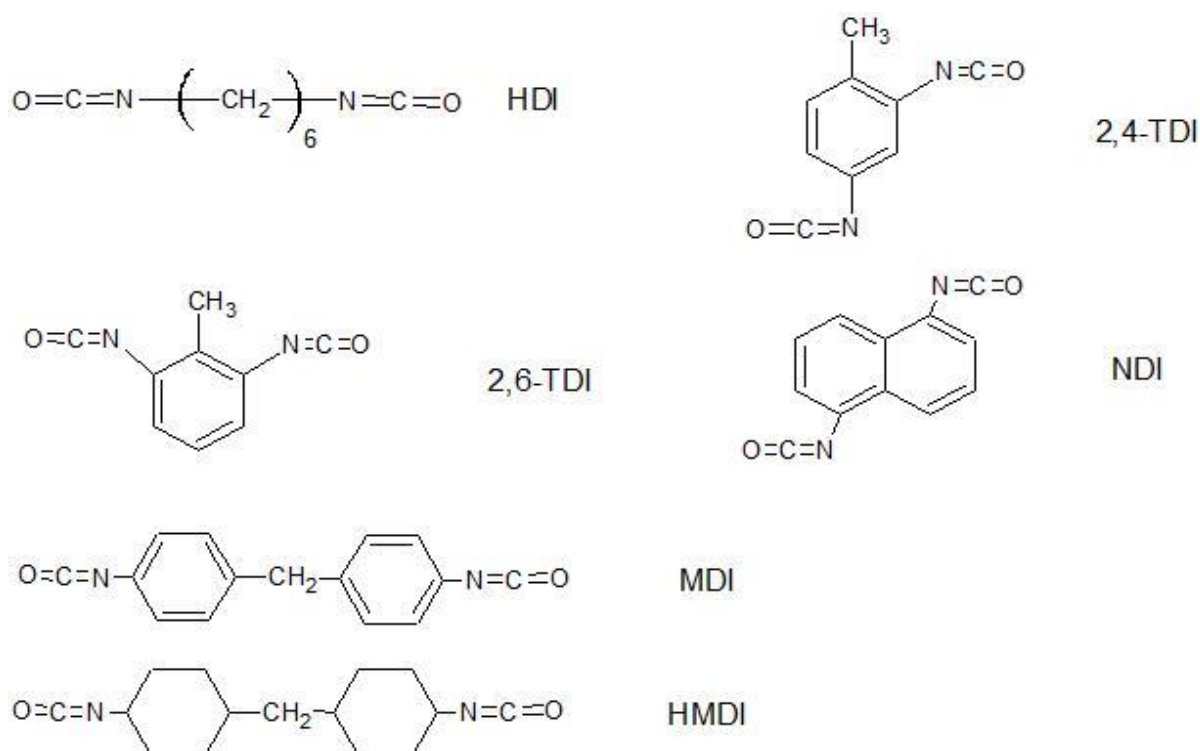


Figure 2.9 The chemical structures of some commercial diisocyanates

Aromatic, aliphatic, cycloaliphatic or polycyclic multifunctional isocyanates can be used to manufacture PU coatings. The multifunctional isocyanates commonly used in industry are toluene diisocyanate (TDI), methylene diphenyl diisocyanate (MDI), xylene diisocyanates (XDI), tetramethyl xylene diisocyanates (TMXDI), hydrogenated xylene diisocyanate (HXDI), hexamethylene diisocyanate (HDI), isophorone diisocyanate (IPDI), 4, 4-dibenzyl diisocyanates (DBDI) *etc* [1]. The chemical structures of some diisocyanates are shown in Figure 2.9. Compared to other types of diisocyanates, the PUs produced from aromatic diisocyanates have greater rigidity, higher oxidation resistance and lower ultraviolet resistance [126]. As mentioned before, the

properties of final PU products have high dependent on the structures of the reactants

2.4.1.2 Polyols

The polyols used for polymerizing PUs can be a multifunctional polyether *e.g.*, poly(ethylene glycol) and poly(propylene glycol), polyether polyol (PEPO), acrylic polyol (ACPO), polycarbonate polyol *etc.* and a mixture of different polyols. Different kinds of crosslinked or branched polymers can be achieved with adopting different molecular weight and functionalities hydroxyl-containing reactants or isocyanates. For example, utilizing low molecular weight reactants such as ethylene glycols and 1, 4-butane diol can give hard and stiff polymers as a result from a high concentration of urethane groups. On the other hand, more flexible polymer chains can be achieved by utilizing high molecular weight polyols. Soft and elastomeric PU can be obtained from long-chain polyols with low functionality (1.8-3.0) while more rigid, crosslinked product can be obtained from short-chain polyols of high functionality (>3) [1]. In industrial applications, polyesters are usually prepared from a mixture of two or more diacids reacted with two or more polyols which result in a range of very complex product [127,128]. PEPO- and ACPO- derived PUs have good resistance against normal weathering, but the hydrolysis of ester groups lead to deterioration of mechanical properties under prolonged exposure to humid atmosphere. In order to slow down the hydrolysis process, polycarboimides can be added as acid scavengers and suppress the autocatalytic effect [129,130]. PEPO-based PU coatings have superior heat stability, adhesive properties and oil resistance. In addition, this type of coating also has low manufacturing cost which is favoured by a wide range of commercial applications.

2.4.1.3 Catalysts

With the addition of catalysts, the reactions to produce PUs can be carried out at lower temperatures and at a more rapid rate. The most often used catalysts used in the reaction between isocyanates and alcohols are tertiary amines [131](*i.e.* 1,4-diazabicyclo [2.2.2] octane (DABCO)), triethyl amine (TEA), and organo tin compounds [132](*i.e.* stannous octoate). The catalytic effect of organometallic compound is resulted from their complex forming ability with isocyanate and hydroxyl groups [133]. The proposed mechanisms of organometallic catalysts and tertiary amines

are shown in Figure 2.10 [134,135]. The interaction of metal cation with isocyanate and alcohol leads to an intermediate complex which can readily rearrange to yield the urethane product (Figure 2.10 (a) and (b)). The catalytic mechanisms of tertiary amines contain the complexation of the amine and isocyanate group (Figure 2.10(c)). Afterward, the complex formed react with alcohol to form urethane product (Figure 2.10(d)).

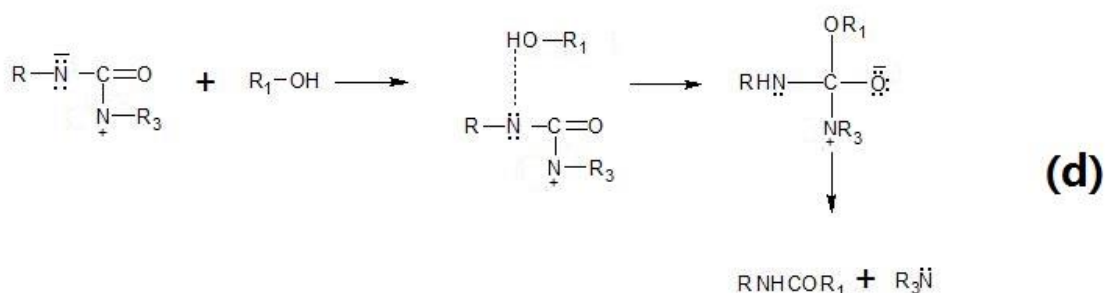
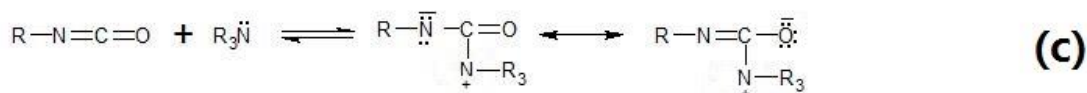
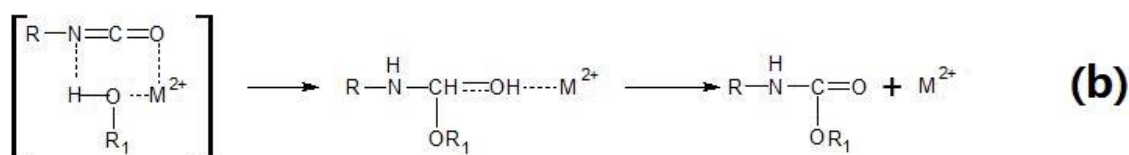
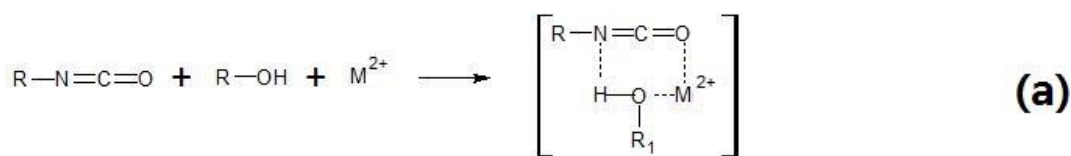


Figure 2.10 Reaction mechanism for the reaction of polyurethanes due to: (a) and (b) organometallic catalysts, and (c) and (d) tertiary amine catalysts

2.4.1.4 Chain extenders (CEs)

Chain extenders are low molecular weight reactants that can extend the chain length in PUs formulas in order to produce elastomeric properties. These reactants are commonly hydroxyl or amine terminated and their molecular weight usually ranges from 40 to 300. The chain extenders should be difunctional to act as chain extending elements in the systems. If the functionality of the chain extenders greater than three, they will be regarded as cross-linkers. The chain length,

molecular weight, functionality and conformation of CEs can influence the mechanical properties and thermal and hydrolytic stability via influencing the packing of hard segments in thermoplastics PUs [136–138]. 1, 4 butane diol, ethylene diamine and trimethylol propane are three commonly used chain extenders [1]. The CEs containing amine groups react faster but the reaction rates sometimes too fast to control and the final product may have bad smell. The reactions between isocyanate groups and hydroxyl based CEs usually have slow reaction rates and even require catalyst. In addition, hydroxyl based CEs have poor solubility in polyols which profoundly limit their adoption in PUs formulas [139].

2.4.1.5 Stoichiometry for PUs reactions

The structure and properties of reactants are important to the properties of PUs but the stoichiometry and formulations of the reactants are important as well. The amount of reactants used is crucial to the properties of the final products. Therefore, the calculations of the PUs formulae need to be strict and concise. The terms and equations needed for PUs formulae calculations are listed below [140]:

(1). *Functionality*: It represents the number of active functional groups in a molecule. For polyols, their functionality depends on the number of active hydroxyl groups. For example, the functionality of 1, 4 butane diol is 2.

(2). *Hydroxyl value (OHV)*. The value of OHV is determined by the how many miligrammes of potassium hydroxide needed to neutralize the acetic acid which combines on acetylation of one gram of sample and is usually supplied by the manufacturers for a given glycol. It is affected by acid value (AV).

(3). *Weight percentage of hydroxyl (OH%)*. When OHV is not supplied, OH% is used to evaluate the hydroxyl content of a polyol. The relationship between OHV and OH% is:

$$\text{OHV} = \text{OH\%} \times 33$$

(4) *Molecular weight of polyols*. Molecular weight of polyols can be calculated according to the equation below (56.1 is the molecular weight of KOH):

$$M_w = \frac{56.1 \times \text{functionality} \times 1000}{OHV}$$

(5) *NCO content (NCO%)*. NCO% can be calculated according the equation below and one example calculations are shown as examples:

$$NCO\% = \frac{42 \times \text{functionality}}{\text{Molecular weight of isocyanates}}$$

$$\text{For TDI, } NCO\% = \frac{42 \times 2}{174} = 48\%$$

(6) *Equivalent weight*. This term represents the molecular weight of each unit of functionality. For example, 1 mol NCO reacts with 1 mol OH and then 1g equivalent isocyanate needs 1g equivalent polyol to react. The equations to calculate equivalent weight of reactants for PU formulations are listed below:

$$\text{Equivalent weight of isocyanate} = \frac{\text{molecular weight}}{\text{functionality}} = \frac{42 \times 100}{NCO\%}$$

$$\text{Equivalent weight of polyol} = \frac{56100}{OHV}$$

$$\text{Equivalent weight of water} = \frac{18}{2} = 9$$

$$\text{Equivalent weight of acid} = \frac{56100}{AV}$$

$$\text{Equivalent weight of primary amine} = \frac{\text{molecular weight}}{2}$$

$$\text{Equivalent weight of secondary amine} = \text{molecular weight}$$

(7) *Isocyanate index*. The equation shown below show the definition of this term:

$$\text{Isocyanate index} = \frac{\text{Actual quantity of isocyanate}}{\text{Calculated quantity of isocyanate}} \times 100\%$$

2.4.2 PU based coatings

ASTM has summarized six different PU coating types in the ASTM standard D16 and they are shown in Table 2.6 [141]. Apart from the classification from ASTM, PU based coatings can be

classified into thermoplastic and the thermoset coatings in general. A brief introduction to these two kinds of coatings will be given.

Table 2.6 Six different types of PUs in ASTM standard

	Type I	Type II	Type III	Type IV	Type V	Type VI
ASTM description	One-package Pretreated	One-package moisture cured	One-package heat cured	Two-package catalyst	Two-package polyol	One-package non-reactive lacquer
Characteristics	Unsaturated drying oil modified; no free isocyanate	Contains free isocyanate	Blocked isocyanate	Isocyanate prepolymer plus catalyst	Part A – isocyanate rich; Part B – Polyols or amines	Fully polymerized polyurethane dissolved in solvents
Main curing mechanism	Oxidation of drying oil; Solvent evaporation	Reaction with atmospheric moisture	Thermal release of blocking agents and then reaction	Reaction of isocyanate with moisture and/or components in catalysts	Reaction between Part A and B; instant curing possible	Solvent evaporation
Polymer	Alcoholysis products of drying oils reacted with isocyanate	Higher molecular weight diols and triols	Prepolymer forms to an adduct with blocking agents such as phenol	Prepolymer similar to Type II but catalysts could contain polyol/amine	Relatively lower molecular weight	Thermoplastic polymer with relatively high molecular weight
Chemical resistance	Fair	Fair to good	Good to excellent	Fair to excellent	Good to excellent	Fair
Corrosion	Poor	Poor to good	Fair to good	Fair to	Fair to	Poor to fair

resistance				excellent	excellent	
Corrosion protective applications	Exterior or interior; non-immersion services; Wood; Concrete; Metal	Exterior or interior; non-immersion services; Wood; Concrete; Metal	Not used for anticorrosive coatings in the field; Automotive and product finishes	Similar to Type I but the design of catalyst may change the properties; Some suitable for immersion	Used for many substrates; Elastomer for concrete; Rigid for metals	Not normally used for corrosion protection; Automotive and product finishes
Special considerations	Better abrasion than most oil paints	Properties and curing affected by humidity	Heat required for cure	Similar to Type II but with speed of curing	Special equipment may be required	VOC limitation

2.4.2.1 Thermoplastic PU based coatings

The effect of HSs and SSs play dominated role in the properties of thermoplastic PU coatings because thermoplastics PUs can be regarded as a linear structural block copolymer of hard segments (HSs) and soft segments (SSs) [1]. The properties of HS and SS vary significantly and, therefore, phase separation may be observed in the final product. Phase separation takes place due to the incompatibility or thermodynamic immiscibility between HSs and SSs. The HSs usually consist of polar materials and they tend to form cluster or aggregate into ordered hard domains due to carbonyl or amino hydrogen bonds. Meanwhile, SSs form amorphous domains [142]. Schollenberger first studied these segmented PUs in 1959 [143]. Cooper and Tobolsky further investigated these segmented PUs and found out that the hard segments acted as filler particles as well as crosslinkers which lead to the restriction of the motion of the amorphous soft segments [144]. Composition variables and processing conditions such as properties and structure of HSs and SSs, synthesis methods and thermal history of the PUs are very important for the properties of the

final product [1].

The structure, length and distribution of HS can strongly affect morphology, thermal behaviour and performance of PU coatings [145,146]. In polyether based PU coatings, their mechanical properties depend mainly on the HS content. The presence of hydrogen bonding in the hard segments domains leads to strong domain cohesion. A morphological change from interconnecting to isolated hard segments domains takes place when the HS content is increased [147]. By measuring the T_g of the SS, the effect of HS content on the phase separation can be investigated [148]. The T_g of SS is influenced by the restrict movement induced at the HS junctions or phase boundaries where HS acts as a filler particle [149]. In addition, the variation in mechanical properties was regarded as the result from the morphology change induced by the variation of HS content [150]. Models containing MDI/BDO repeating units were used to investigate the melting behaviours of PUs and those studies indicated that the melting of model compounds increases with the number of HS units, which are MDI units, and an extrapolated value of homopolymer accounting for the chain end effects was also investigated [151–155]. The model compounds $R-(MDI-HQE)_p-MDI-R'$ (where $p=1,2,3$; R,R' is ethanol and/or 2-phenoxyethanol; and HQE is *bis*(2-hydroxyethyl) ether) had been utilized to indicate the relationship between melting points and oligomer length and the results showed that the melting point increases with increasing the oligomer length [156]. A limiting value for melting points for infinite molecular weight was also calculated from the model compounds [157].

The properties of the final coatings are affected by the chemical composition and molecular weight distribution of the incorporated soft segment (*i.e.* multifunctional polyols). The thermal deformation and thermal properties of the PUs are strongly affected by the molecular weight of SS. In addition, the chemical structure of SS influences the solubility parameter of SS and, therefore, the compatibility between SSs and HSs in PU coatings [158]. When HS length is fixed, increasing the molecular weight of SS raise the tendency of the isolation of HS domains in the SS matrix. This phenomenon results in a higher degree of phase separation between SSs and HSs and a lower T_g will be resulted as well [159,160]. When the functionality of SS is fixed, increasing the molecular

weight of SS has similar effect which leads to increased thermodynamic incompatibility between hard and soft segments [161]. If the functionality of SS is increased, the strength of PUs will be increased and the overall degree of phase separation will be reduced as well as a result from the increased domain boundary mixing [162].

The effect of hydrogen bonding in thermoplastic PUs plays a major role in their macroscopic properties. The high electronegativity of nitrogen atom in urethane attracts N-H bonded electron and partial positive charge on the hydrogen is developed. Therefore, hydrogen bonding can be formed between N-H and the neighbouring oxygen atoms. In polyurethanes, the N-H group is the donor group and the acceptor group can be carbonyl of the imide groups, C=O in the PUs or the oxygen atom of the ester or ether linkage when polyester or a polyether are used as the SSs. The hydrogen bonding presented in PUs develops physical crosslinks and, therefore, can provide enhanced strength and stiffness [163,164]. Pimentel and Sederholm suggested a linear relationship between the length of the hydrogen bonding and phase separation behaviour in PUs. The shorter the hydrogen bonding, the stronger the bonding [165].

2.4.2.2 Thermoset PU based coatings and coating selection

Although thermoplastic PUs have excellent properties as coatings, their poor resistance towards mechanical strains and higher temperature deformation/ degradation are the major drawbacks. In general, their working temperatures are below 100 °C [166]. Thermoset PU coatings provide superior tensile strength, scratch resistance and chemicals resistant than thermoplastic PU coatings as a result from the presented crosslinks. In order to improve the performances of thermoset PU coatings, the effect of different crosslinkers in PU structure was evaluated. Utilizing the soft segments with functionalities greater than two, isocyanates with functionalities greater than two, peroxides and tri-functional chain extenders are common methods to produce thermoset PU coatings. A careful calculation of the amount of reactants used to produce thermoset PU coating is needed to produce a product with desired properties [1]. There are ten different kinds of thermoset PU coatings included: high solid coatings, moisture-cured polyurethanes (MCPUs), polyurethane imide, polyurea coatings, UV-curable coatings and waterborne coatings. Each kind of coating has

its own advantages and major drawbacks. The selection of PU coatings should be considered carefully according to specific applications and modifications of backbone structure of PU coatings can be adopted if necessary with the consideration of the end use of the coating and the cost of modification. There are several factors need to be considered when selecting a PU coating to a specific application [1,167].

1. The properties of the modified PU coating such as mechanical properties, thermal stability and corrosion resistance.
2. The resistance of the coating against environmental damage.
3. The compatibility of the coating and the targeted substrate within the expected environment and working temperature. Good coating-substrate adhesion must be guaranteed.
4. When an application is critical and the consequences of failure are disastrous, a particular coating must be used even the cost is very high, particularly when there is no other option.
5. For better protection of substrate, knowledge of the following parameters is very important: coating application method, composition, thickness, mechanical properties, coating-substrate adhesion, friction coefficient, thermal expansion coefficient, heat conductivity, density, specific heat and the overall stress level exhibited by the coated body.

2.4.2.3 Why we use PU/graphene based coatings for protective coating

With careful tailoring of PU formulation, PU can be an excellent choice for protection coating. Compared to other polymers as coating, PU has better mechanical properties and the adhesion between PU and steel is excellent without any surface treatment which allows PU to be a perfect choice of protective coating for steel substrates [1,168,169]. Although PU based coatings have been widely adopted, the application of PU is limited by its thermal stability, stiffness, scratch resistance, tensile strength, friction resistance, wear resistance and anti-corrosion properties [170,171]. Therefore, modification of PU is necessary to enhance its performance. The widely accepted method of modification is to produce PU nanocomposites *via* adding nanofillers such as graphene, nano-clay and carbon nanotube *etc.* Since the discovery of 2004, graphene is regarded as the miracle materials in the world and it is believed that it can significantly improve the performance of

a polymer by acting as a reinforcement. The extraordinary properties make it an excellent choice for performance enhancement of PU. The excellent mechanical properties of graphene make it a good reinforcement for the stiffness and thermal stability of PUs. In addition, the high aspect ratios and low gas and water permissibility of graphene indicates that graphene has outstanding barrier properties. Graphene was also reported as a potential anti-corrosion coating which block the electrochemical corrosion in electrolytes [18]. Although graphene can act as corrosion protective coating, it can only work as a short term measure because researchers had found out that graphene might facilitate corrosion in long term. The graphene produced in labs or industries so far is not perfect. The corrosion media can penetrate through the defects of graphene and react with the metal substrates in long term experiments [172]. In addition, the cost of producing graphene is still very high using current technology and it is difficult to obtain defect-free graphene. Therefore, pristine graphene as corrosion protective coating is not suitable for long-term cost-effective application. In order to develop a protective coating with desired durability and good corrosion resistance, an effective route is to produce PU/graphene nanocomposite coating.

Ramezanzadeh and his co-workers developed a PU/graphene coating with improved barrier and anti-corrosion properties for steel substrates [173]. Graphene oxide was produced by modified Hummer's method. In order to improve the interfacial bonding between PU and graphene oxide, graphene oxide sheets were functionalized by polyisocyanate first and then mixed with polyol and isocyanate to produce PU/graphene nanocomposite coatings. The effect of GO and functionalized GO on the performance of PU was compared. The EIS results and salt-spray (5wt% NaCl solution) indicated that the functionalized GO reinforced PU had the best barrier properties and anti-corrosion properties. The addition of GO and functionalized GO can block the diffusion of corrosive substances (water, oxygen and alkaline solution etc.) which improve the barrier properties of the PU. In addition, the ionic resistance of the PU will be improved as well. Owing to the excellent electrical properties of GO, the GO sheets were negatively charged, which improves the ionic resistance of PU because the charged GO sheets prevented the anions from diffusing into the coating-substrate interface. The tribological and anti-corrosion properties of PU nanocomposite coatings reinforced with functionalized graphene and GO were investigated by Mo *et al.* [170]. The

graphene and GO were functionalized with 3-amino-propyltriethoxysilane (APTES). After APTES functionalization, the dispersions of G and GO were more uniform in the PU matrix. The enhancement of tribological and anti-corrosion properties was attributed to the lubricant effect and excellent barrier properties of graphene as GO because GO had worse chemical stability than graphene owing the functional groups on GO surface. The optimised filler loading was between 0.25% and 0.5%. Compared to PU/functionalized graphene coating, the coating reinforced by functionalized GO had better tribological performance but the anti-corrosion property was worse. Apart from anti-corrosion property, the electrical properties of PU can be improved by adding graphene. The investigation of the effect of graphene on electrical conductivity, rheology and crystallinity on PU was conducted by Canales and his colleagues [174]. The graphene used was thermal reduced graphene produced in their lab. Crystallisation during cooling affected the distribution of graphene in PU matrix and the electrical conductivity decreased first and then increased; the highest electrical conductivity achieved was 6.1×10^{-4} S/cm.

From the literature, graphene can improve the anti-corrosion and electrical properties of PU significantly even in low filler content. The reported PU/graphene nanocomposites had excellent anti-corrosion properties and electrical properties which indicated that the advantages of PU and graphene could be combined effectively. However, the preparation of graphene and the mixing of graphene with PU are complicated, which limits the commercialisation of PU/graphene nanocomposite coatings. A low cost and efficient way to disperse graphene in PU is necessary for large scale coating production.

2.5. Coating methods

Different coating methods have been used by recent studies and they were summarized in this section. Their possible advantages and limitations are discussed and their availability for different types of graphene based coatings is suggested.

CVD. Chemical vapour deposition method is a method to synthesize graphene layers on a substrate and transfer to other substrates. When utilizing this method in coating, graphene can be deposited

on to the target substrates without the transfer process. More detailed graphene growth mechanisms were stated in the former graphene synthesis method section. CVD is a method with great potential to produce graphene in large scale and this also suggests that large scale coating is also foreseeable. In addition, pure and dense coating can be produced by CVD method, and the CVD parameters can be adjusted to produce coatings with different surface morphology, thickness and even crystal structure. The major disadvantages of CVD are safety and hazard issues caused by the precursor gases, difficulty of depositing multicomponent materials and high equipment cost [175]. In general, CVD is suitable to apply highly dense and pure graphene based coatings such as pristine graphene on a substrate. The coating structure can be controlled at the atomic level or nanometre level.

Dip coating. Dip coating is a convenient method to coat thin film on a substrate and it is very frequently used for research purposes. However, it is not suitable for industrial processes due to the inconsistent coating quality. Compared to dip coating, spin coating is often used in industrial processes. The dip coating process generally has five steps [176]:

1. The substrate is dipped into the solution of the coating material at a constant speed. Before this step, pre-treatment process may be conducted according to different substrates.
2. The substrate remains in the solution for a designated time and is starting to be pulling up.
3. The coating thin film begins to deposit on the substrate while the substrate is pulled up. The thickness of the coating depends on the speed used in pulling up process. Slower pulling up gives thinner coating layer.
4. Excess liquid will be drained from the substrate surface.
5. Solvent evaporates from substrate surface to form a thin film. The evaporation may begin in step 3 if the solvent is volatile.

In research, dip coating is more convenient and feasible than other methods because it is a very simple method and does not require sophisticated equipment. Because of its simplicity, the coating layer produced by this method may not have good quality. For graphene based composite coating, the thickness distribution can be a problem. In terms of pristine graphene based materials coating,

the coating layer produced may not be dense enough to provide extraordinary properties. In addition, the substrate cannot be too large and complicated. However, the biggest advantage of dip coating is simplicity. Although dip coating is more suitable in lab, it still can be a potential large scale coating method to produce products that can satisfy the applications for low standard requirements with a competitive price. This approach is possibly more suitable to produce graphene based composite coating than pristine graphene based coating because the viscosity of the graphene based composite coating is much higher. Therefore, it can develop a better interfacial adhesion toward a substrate and a more uniform coating layer. A subsequent treatment process may need to form a solid coating layer.

Spin coating. Spin coating is a process widely used for applying uniform thin film on a flat substrate. The applied materials are usually polymeric coatings and they are applied onto flat substrates in the form of solution. The solvents used are usually volatile. The driving force that drives the solution rapidly off the substrate is centrifugal force and a machine used for spin coating is called spin rotator spinner. The centrifugal force is applied continuously until desired film thickness is achieved [176,177]. Several factors can affect the final film thickness: 1. kinematic viscosity; 2. coefficient of solvent diffusion; 3. the critical shear rate for onset of shear thinning of the viscosity; 4. the rotational speed; 5. the radius of the substrate; 6. the coating solution concentration. The two major influenced factors are the rotational speed and the coating solution concentration [176–178]. A typical spin coating process is a four steps process [176,178,179]:

1. Polymer solution is deposited on the substrate with an excess amount to cover the substrate completely.
2. The substrate spins rapidly to displace the polymer solution with centrifugal force.
3. Laminar radial flow of the liquid layer of uniform thickness remaining on the substrate.
4. Removal of solvent via evaporation until the film stops flowing and is dried completely.

Some treatments were used to assist the coating process. For example, N₂ gas was used to blow the graphene oxide coated silicon chip to accelerate the evaporation of water during the process of spin

coating [83]. All the assisted treatments during or after the spin coating process are to obtain uniform continuous graphene based materials thin film. Compared to dip coating, the coating layer produced by this approach is denser and more uniform. The substrate shape and size is limited by the spin coating apparatus. Only flat surface can be spin coated. The spin coating method is not suitable for complicate shape product. In addition, this method is more suitable to coat pristine graphene based coatings or graphene-nanoparticles composite coatings on a substrate.

Layer by layer self-assembling (LBL). In multi-film production, layer-by-layer self-assembling method is very ideal. This method utilize the attraction between positive and negative charges to make the films self-assemble on a substrate and the this method is also called layer-by-layer deposition method [180,181]. In layer-by-layer self-assembling process, the films are deposited onto a substrate by immersing the pre-treated substrate into graphene solutions and polymer solution cyclically to form multi-layers films [180]. The substrate is pre-treated into positively charged by introducing positive charged functionalities such as amine functionalities [181]. The graphene solution can be directly used as negatively charged dipping particles but the polymer solution may need to be changed the pH to for subsequent dipping process [180,181]. This method is a method suitable for producing two components multi-layers coating. However, only some research papers investigated its applicability for graphene based materials. There is no direct indication of utilizing this method for coating applications. This method is similar to dip coating method where the substrates are dipped into the coating solution and are withdrawn to form coating layer, but the coating layer produced by LBL is denser due to the compact force originated from the attractive force between negative and positive charges.

Sol-gel approach. The sol-gel process is a widely used wet-chemical process and it has been studied extensively since its discovery. Sol refers to the colloidal solution which acts as the precursor and it will evolve to gel which refers to the integrated network. The precursor sol can be deposited onto a substrate (e.g. via dip coating), casted into a mould with the designated shape or used to synthesize powders. The gel is generally a gel-like biphasic system containing both solid

and liquid phases. Large quantity of liquid needs to be removed for sol turn into gel and the simplest method is pour off the liquid after sedimentation which requires a certain amount of time to take place. Drying process is required in sol-gel method to remove the liquid phase in the system. Severe densification and shrinkage always accompany the drying process. After the drying process, a thermal treatment is usually necessary for further polycondensation, mechanical properties enhancement and structural stability. The advantages of sol-gel process are cheap, low temperature and fine control of the final product's chemical composition [182,183]. The coating film produced by sol-gel method tends to crack and there is a thickness limitation of each layer (about 1 micron) [175]. This method is suitable to apply graphene based composite coating onto a substrate and the substrate can have complicate shape.

Direct apply and curing. This method is a very simple coating method that a coating mixture is coated onto a substrate directly and cured under ambient conditions. The coatings that can be cured under ambient conditions such as curing at room temperature are suitable to use this method, UV curable nanocomposite coatings, for example. The interfacial bonding between the substrate and the coating may be weak because this method is applying a coating directly without any treatments or subsequent processes. The substrate shape and size are not limited and coating can be applied onto some vital parts of a component directly. This method is more suitable to apply graphene based composite coatings.

Spray drying. Spray drying is a technique to produce dry powder from solution or suspension by rapid drying with the aid of a hot gas. The heating gas used in spray drying unique is usually air. However, nitrogen is used when the liquid is flammable solvent or the product is oxygen sensitive [184]. The liquid dried is dispersed into a controlled drop size spray by atomizer or spray nozzle. The drop size ranges from 10 μm to 500 μm according to different process needs [185]. Spray drying technique is only suitable to produce powder form product and one vital requirement to produce graphene coated powder is that the particle size of graphene must be much smaller than the target powder. The graphene is coated onto a powder form substrate during the spraying process. Powder

agglomeration and uneven coating may be problems when using this method. This method is more suitable to process pristine graphene based materials and graphene-nanoparticles composite coating.

Spray coating. Spray coating is a technique for depositing thin film on a substrate. This technique is widely used in industrial coating, painting and graphic art [186]. This large output technique is able to deposit a broad range of materials on various substrates with different morphologies and it is usually used in in-line production. In addition, it can be easily scaled to larger substrates or roll-to-roll manufacturing. The substrates with different shape can be processed and the fluids with different characteristics can be used. As a result, solutions with different properties can be readily deposited onto different shapes' substrates to obtain films with desired properties [186,187]. The apparatuses for spray coating employ compressed gas (airbrush gun) to plasma torch (plasma spray coating) to fulfil different product requirements. Different apparatuses should be selective carefully to process graphene based coatings. Both pristine graphene based coatings and graphene based composites coatings can be processed by this method.

In-situ polymerization. The in-situ polymerization method is suitable for the unstable reactants that must be synthesized in-situ. The polymerization happens in a continuous phase to make all the unstable reactants in the reaction mixture but not isolated on their own. The reaction mixture can be applied onto a substrate as coating before the viscosity of the mixture becomes too high. However, there still no study about applying the mixture on a substrate as coating right after the mixture is in-situ polymerized. This method may not suitable to be used in coating industries.

Electrophoretic deposition (EPD). EPD is a technique that attracts lot of attentions because of its high versatility usage with different materials and their combinations. It is also a cost-effective process and requires very simple equipment. This method was first widely used in ceramic coating and it began to be used in other materials when more and more interests were received. This process is a colloidal process and its advantages are short deposition time, simple apparatus, low cost, little restriction of the shape of substrate and easy control of deposited layer thickness and surface morphology. The film produced also exhibited good microstructure homogeneity and high packing

density. The only intrinsic limitation of EPD compared to other colloidal process is that water cannot be used as its liquid medium because the applied voltage in water triggers the generation of hydrogen and oxygen gases at the electrodes which have negative effects on the quality of the deposited films and potential safety threats [188].

In this process, the solid particles are charged under electric field. Then, the charged particles are attracted to move toward the substrates with opposite charge to form deposited layer via particle coagulation[188,189]. There are two types of EPD process: cathodic and anodic. When the particles are positively charged, they are attracted to deposition onto negative electrode (cathode). The reason for anodic EPD is similar where the particles are negatively charged. The substrates used in EPD must be conductive and the required conductance of liquid medium is lower than electroplating [190]. The principle driving force of EPD process is the charge on the particles and the electrophoretic mobility of the particles in the solvent under applied voltage. There are two major groups of parameters can influence film quality and film characteristics: (1) those parameters related to the suspension and (2) those parameters related to the process. In terms of the parameters relate to the suspension, many of them must be considered. However, particle size, dielectric constant of liquid, conductivity of suspension, viscosity of suspension, zeta potential and stability of suspension are more influencing among those suspension parameters. Regarding the parameters relate to the process, deposition time, applied voltage, concentration of solid suspension and conductivity of substrate [188]. To ensure a successful EPD process, powder washing, which removes any impurities on the powder, is very vital because it contribute to the careful control of a defined chemistry of particle suspension [191]. One problem must be prevented in EPD process is the formation of drying cracking. Several approaches have been published such as careful control of the EPD process with moderate control of subsequent drying [188,192].

EPD has been adopted to fabricate carbon nanotube coatings [193]. The carbon nanotube coatings produced via EPD can be used in biomedical, structural and functional applications [189,193]. For carbon nanotubes coatings, the suspension for EPD is usually prepared by adding carbon nanotubes,

Triton X100 as an ionic surfactant and iodine 99.9% as a charger to an aqueous solution. The resulted suspension mixture is centrifuged to remove large carbon nanotubes agglomerations [189]. EPD has been widely used to coat graphene based materials on different substrates [194]. It is believed to be a promising method to produce high quality graphene based coatings. There are still a lot of works needed to be done to find out suitable conditions for different coating applications. This method is more suitable to produce pristine graphene based coatings and graphene-nanoparticles composite coatings

2.6. Conclusions and future perspectives

It is evidenced that graphene exhibit many extraordinary properties from many published characterization results. Graphene based materials have wide range of potential applications such as flexible transparent electrode, sensors and electronic components. Graphene based polymeric nanocomposites also show very low percolation threshold of electrical conductivity, and improved mechanical, thermal, and barrier properties. However, there are still lots of challenges lie on the path toward mature graphene utilization. Defect-free graphene is the perfect materials for being used in all kinds of applications but the fabrication techniques are still not mature. Moreover, the scale-up of fabricating graphene based materials with acceptable cost is still extremely challenging. Essentially, the potential health risks of graphene based materials need to be evaluated before large scale utilization.

The potential electrical properties, barrier properties, mechanical properties and thermal properties were identified when coated pristine graphene based materials and graphene based composites on a substrate. In addition, other properties were also identified such as catalytic activity, sensing sensitivity, and barrier efficiency. However, most of the published articles on utilizing graphene in coating focus on electrical properties. Much more efforts need to be given in for fully understand the potential applications of graphene based coatings. The influence of graphene coated surface morphology on improvement efficiency needs to be investigated as well. No matter how the graphene is synthesized, the ease for subsequent coating processing needs to be considered. If the

synthesized graphene can be readily used without any treatment, the cost can be lowered and a good quality coating may be produced as well. In order to optimize the properties of polymer graphene based composites, the control of graphene based materials orientation and dispersion during processing is critical. Much more effort in nano-engineering is needed to understand the behaviour of graphene based materials in polymer processing. In coating applications, coating methods have a profound effect on the properties and morphology of the resulted coating. Two or more coating techniques may be used at the same time to produce a multilayer graphene based coating system to meet the industrial requirements as the current techniques are difficult to satisfy industrial standards when they are used separately. The development of new technologies for graphene based materials fabrication and processing is still essential to face the demands and challenges in industries nowadays.

References

- [1] Chattopadhyay DK, Raju KVS. Structural engineering of polyurethane coatings for high performance applications. *Prog Polym Sci* 2007;32:352–418.
- [2] Liao B, Song M, Liang H, Pang Y. Polymer-layered silicate nanocomposites . 1 . A study of poly (ethylene oxide)/ Na⁺ -montmorillonite nanocomposites as polyelectrolytes and polyethylene-block-poly (ethylene glycol) copolymer / Na⁺ -montmorillonite nanocomposites as fillers for reinf. *Polymer (Guildf)* 2001;42:10007–11.
- [3] Novoselov KS, Geim AK, Morozov S V., Jiang D, Zhang Y, Dubonos S V., et al. Electric field effect in atomically thin carbon films. *Science* (80-) 2004;306:666–9.
- [4] Geim AK, Novoselov KS. The rise of graphene. *Nat Mater* 2007;6:183–91.
- [5] Singh V, Joung D, Zhai L, Das S, Khondaker SI, Seal S. Graphene based materials: Past, present and future. *Prog Mater Sci* 2011;56:1178–271.
- [6] Sanjinés R, Abad MD, Vâju C, Smajda R, Mionić M, Magrez A. Electrical properties and applications of carbon based nanocomposite materials: An overview. *Surf Coatings Technol* 2011;206:727–33.

- [7] Lee C, Wei X, Kysar JW, Hone J. Measurement of the elastic properties and intrinsic strength of monolayer graphene. *Science* 2008;321:385–8.
- [8] Lee C, Wei X, Li Q, Carpick R, Kysar JW, Hone J. Elastic and frictional properties of graphene. *Phys Status Solidi* 2009;246:2562–7.
- [9] Ni Z, Yu T, Lu Y, Wang Y, Feng Y, Shen Z. Uniaxial strain on graphene: raman spectroscopy study and band-gap opening. *ACS Nano* 2008;2:2301–5.
- [10] Mohiuddin TMG, Lombardo A, Nair RR, Bonetti A, Savini G, Jalil R, et al. Uniaxial strain in graphene by Raman spectroscopy: G peak splitting, Grüneisen parameters, and sample orientation. *Phys Rev B Condens Matter Mater Phys* 2009;79:205433(1–8).
- [11] Balandin AA, Ghosh S, Bao W, Calizo I, Teweldebrhan D, Miao F, et al. Superior thermal conductivity of single-layer graphene. *Nano Lett* 2008;8:902–7.
- [12] Zhang H, Lee HK. Plunger-in-needle solid-phase microextraction with graphene-based sol-gel coating as sorbent for determination of polybrominated diphenyl ethers. *J Chromatogr A* 2011;1218:4509–16.
- [13] Zhu Y, Murali S, Cai W, Li X, Suk JW, Potts JR, et al. Graphene and graphene oxide: synthesis, properties, and applications. *Adv Mater* 2010;22:3906–24.
- [14] Young RJ, Kinloch IA, Gong L, Novoselov KS. The mechanics of graphene nanocomposites: A review. *Compos Sci Technol* 2012;72:1459–76.
- [15] Yoo BM, Shin HJ, Yoon HW, Park HB. Graphene and graphene oxide and their uses in barrier polymers. *J Appl Polym Sci* 2014;131:39628(1–23).
- [16] Hsieh C Te, Chen W. Water/oil repellency and work of adhesion of liquid droplets on graphene oxide and graphene surfaces. *Surf Coatings Technol* 2011;205:4554–61.
- [17] Lin L, Kim DE, Kim WK, Jun SC. Friction and wear characteristics of multi-layer graphene films investigated by atomic force microscopy. *Surf Coatings Technol* 2011;205:4864–9.
- [18] Kirkland NT, Schiller T, Medhekar N, Birbilis N. Exploring graphene as a corrosion protection barrier. *Corros Sci* 2012;56:1–4.
- [19] Hernandez Y, Nicolosi V, Lotya M, Blighe FM, Sun Z, De S, et al. High-yield production of

- graphene by liquid-phase exfoliation of graphite. *Nat Nanotechnol* 2008;3:563–8.
- [20] Green AA, Hersam MC. Solution phase production of graphene with controlled thickness via density differentiation. *Nano Lett* 2009;9:4031–6.
- [21] Eda1 G, Fanchini1 G, Chhowalla1 M. Large-area ultrathin films of reduced graphene oxide as a transparent and flexible electronic material. *Nat Nanotechnol* 2008;3:270–4.
- [22] Becerril HA, Mao J, Liu Z, Stoltenber RM, Bao Z, Chen Y. Evaluation of solution-processed reduced graphene oxide films as transparent conductors. *ACS Nano* 2008;2:463–70.
- [23] Stankovich S, Dikin DA, Piner RD, Kohlhaas KA, Kleinhammes A, Jia Y, et al. Synthesis of graphene-based nanosheets via chemical reduction of exfoliated graphite oxide. *Carbon N Y* 2007;45:1558–65.
- [24] Somani PR, Somani SP, Umeno M. Planer nano-graphenes from camphor by CVD. *Chem Phys Lett* 2006;430:56–9.
- [25] Cao H, Yu Q, Colby R, Pandey D, Park CS, Lian J, et al. Large-scale graphitic thin films synthesized on Ni and transferred to insulators: Structural and electronic properties. *J Appl Phys* 2010;107:044310 (1–7).
- [26] Kim KS, Zhao Y, Jang H, Lee SY, Kim JM, Kim KS, et al. Large-scale pattern growth of graphene films for stretchable transparent electrodes. *Nature* 2009;457:706–10.
- [27] Reina A, Jia X, Ho J, Nezich D, Son H, Bulovic V, et al. Large area, few-layer graphene films on arbitrary substrates by chemical vapor deposition. *Nano Lett* 2009;9:30–5.
- [28] Li X, Cai W, Colombo L, Ruoff RS. Evolution of graphene growth on Ni and Cu by carbon isotope labeling. *Nano Lett* 2009;9:4268–72.
- [29] Malesevic A, Vitchev R, Schouteden K, Volodin A, Zhang L, Tendeloo G Van, et al. Synthesis of few-layer graphene via microwave plasma-enhanced chemical vapour deposition. *Nanotechnology* 2008;19:305604.
- [30] O'Hern SC, Stewart C a, Boutilier MSH, Idrobo JC, Bhaviripudi S, Das SK, et al. Selective molecular transport through intrinsic defects in a single layer of CVD graphene. *ACS Nano*

2012;6:10130–8.

- [31] Brodie BC. Sur le poids atomique du graphite. *Ann Chim Phys* 1860;59:466.
- [32] Staudenmaier L. Verfahren zur darstellung der graphits äure. *Berichte Der Dtsch Chem Gesellschaft* 1898;31:1481–7.
- [33] Hummers Jr WS, Offeman RE. Preparation of graphitic oxide. *J Am Chem Soc* 1958;80:1339–1339.
- [34] Potts JR, Dreyer DR, Bielawski CW, Ruoff RS. Graphene-based polymer nanocomposites. *Polymer* 2011;52:5–25.
- [35] Paredes JI, Villar-Rodil S, Martínez-Alonso A, Tascón JMD. Graphene oxide dispersions in organic solvents. *Langmuir* 2008;24:10560–4.
- [36] Wang G, Yang J, Park J, Gou X, Wang B, Liu H, et al. Facile synthesis and characterization of graphene nanosheets. *J Phys Chem C* 2008;112:8192–5.
- [37] Si Y, Samulski ET, Hill C, Carolina N. Synthesis of water soluble graphene. *Nano Lett* 2008;8:1679–82.
- [38] Dua V, Surwade SP, Ammu S, Agnihotra SR, Jain S, Roberts KE, et al. All-organic vapor sensor using inkjet-printed reduced graphene oxide. *Angew Chem Int Ed Engl* 2010;49:2154–7.
- [39] Dubin S, Gilje S, Wang K, Tung VC, Cha K, Hall AS, et al. A one-step, solvothermal reduction method for producing reduced graphene oxide dispersions in organic solvents. *ACS Nano* 2010;4:3845–52.
- [40] Song M, Cai D. Graphene functionalization: A Review. In: Mittal V, editor. *Polym. Nanocomposites*, Royal Society of Chemistry; 2012, p. 1–51.
- [41] Titelman GI, Gelman V, Bron S, Khalfin RL, Cohen Y, Bianco-Peled H. Characteristics and microstructure of aqueous colloidal dispersions of graphite oxide. *Carbon N Y* 2005;43:641–9.
- [42] Veca LM, Lu F, Mezziani MJ, Cao L, Zhang P, Qi G, et al. Polymer functionalization and solubilization of carbon nanosheets. *Chem Commun (Camb)* 2009:2565–7.

- [43] Salavagione HJ, Martínez G, Gómez MA. Synthesis of poly(vinyl alcohol)/reduced graphite oxide nanocomposites with improved thermal and electrical properties. *J Mater Chem* 2009;19:5027–32.
- [44] Shen J, Hu Y, Shi M, Lu X, Qin C, Li C, et al. Fast and Facile Preparation of Graphene Oxide and Reduced Graphene Oxide Nanoplatelets. *Chem Mater* 2009;21:3514–20.
- [45] Huang Y, Qin Y, Zhou Y, Niu H, Yu Z, Dong J. Polypropylene/Graphene Oxide Nanocomposites Prepared by in Situ Ziegler–Natta Polymerization. *Chem Mater* 2010;22:4096–102.
- [46] Fang M, Zhang Z, Li J, Zhang H, Lu H, Yang Y. Constructing hierarchically structured interphases for strong and tough epoxy nanocomposites by amine-rich graphene surfaces. *J Mater Chem* 2010;20:9635–43.
- [47] Sundaram RS, Gómez-Navarro C, Balasubramanian K, Burghard M, Kern K. Electrochemical modification of graphene. *Adv Mater* 2008;20:3050–3.
- [48] Chunder A, Pal T, Khondaker SI, Zhai L. Reduced graphene oxide/copper phthalocyanine composite and its optoelectrical properties. *J Phys Chem C* 2010;114:15129–35.
- [49] Cao A, Liu Z, Chu S, Wu M, Ye Z, Cai Z, et al. A facile one-step method to produce graphene-CdS quantum dot nanocomposites as promising optoelectronic materials. *Adv Mater* 2010;22:103–6.
- [50] Yamada T, Ishihara M, Hasegawa M. Large area coating of graphene at low temperature using a roll-to-roll microwave plasma chemical vapor deposition. *Thin Solid Films* 2013.
- [51] Pham VH, Cuong TV, Hur SH, Shin EW, Kim JS, Chung JS, et al. Fast and simple fabrication of a large transparent chemically-converted graphene film by spray-coating. *Carbon N Y* 2010;48:1945–51.
- [52] Singh BP, Jena BK, Bhattacharjee S, Besra L. Development of oxidation and corrosion resistance hydrophobic graphene oxide-polymer composite coating on copper. *Surf Coatings Technol* 2013;232:475–81.
- [53] Wang J, Liang M, Fang Y, Qiu T, Zhang J, Zhi L. Rod-coating: towards large-area

- fabrication of uniform reduced graphene oxide films for flexible touch screens. *Adv Mater* 2012;24:2874–8.
- [54] Ge J, Yao H, Hu W, Yu X, Yan Y, Mao L, et al. Facile dip coating processed graphene/MnO₂ nanostructured sponges as high performance supercapacitor electrodes. *Nano Energy* 2012;1–8.
- [55] Jeon YJ, Yun JM, Kim DY, Na SI, Kim SS. High-performance polymer solar cells with moderately reduced graphene oxide as an efficient hole transporting layer. *Sol Energy Mater Sol Cells* 2012;105:96–102.
- [56] Lee SH, Park M, Yoh JJ, Song H, Jang EY, Kim YH, et al. Reduced graphene oxide coated thin aluminum film as an optoacoustic transmitter for high pressure and high frequency ultrasound generation. *Appl Phys Lett* 2012;101:2419091–4.
- [57] Yoo DH, Cuong TV, Pham VH, Chung JS, Khoa NT, Kim EJ, et al. Enhanced photocatalytic activity of graphene oxide decorated on TiO₂ films under UV and visible irradiation. *Curr Appl Phys* 2011;11:805–8.
- [58] He Z, Wang Z, Guo H, Li X, Wu X, Yue P, et al. A simple method of preparing graphene-coated $\text{Li}[\text{Li}_{0.2}\text{Mn}_{0.54}\text{Ni}_{0.13}\text{Co}_{0.13}]\text{O}_2$ for lithium-ion batteries. *Mater Lett* 2012;91:261–4.
- [59] Shi Y, Chou S, Wang J, Wexler D, Li H, Liu H, et al. Graphene wrapped LiFePO_4/C composites as cathode materials for Li-ion batteries with enhanced rate capability. *J Mater Chem* 2012;22:16465–70.
- [60] Jian Z, Zhao L, Wang R, Hu Y, Li H, Chen W, et al. The low-temperature (400 °C) coating of few-layer graphene on porous $\text{Li}_4\text{Ti}_5\text{O}_{12}$ via $\text{C}_{28}\text{H}_{16}\text{Br}_2$ pyrolysis for lithium-ion batteries. *RSC Adv* 2012;2:1751–4.
- [61] Park JH, Seo SW, Kim JH, Choi CJ, Kim H, Lee DK, et al. Improved Efficiency of Dye-Sensitized Solar Cell Using Graphene-Coated Al_2O_3 -TiO₂ Nanocomposite Photoanode. *Mol Cryst Liq Cryst* 2011;538:285–91.
- [62] Wang D, Gentle IR, Lu GQ. Enhanced electrochemical sensitivity of PtRh electrodes coated

- with nitrogen-doped graphene. *Electrochem Commun* 2010;12:1423–7.
- [63] Mendes RG, Bachmatiuk A, Melkhanova S, Klingeler R, Bu B, Ru MH. A facile route to coat iron oxide nanoparticles with few-layer graphene. *J Phys Chem C* 2012;116:23749–56.
- [64] Zhang WL, Liu YD, Choi HJ. Graphene oxide coated core–shell structured polystyrene microspheres and their electrorheological characteristics under applied electric field. *J Mater Chem* 2011;21:6916–21.
- [65] Li X, Li GQ, Zhao SZ, Wang XM, Yin L, Huang H, et al. Diode-pumped Nd:YVO₄ laser passively Q-switched with graphene oxide spin coated on ITO substrate. *Laser Phys* 2012;22:673–7.
- [66] Jung SW, Park JH, Seo SW, Kim JH, Choi CJ, Kim H, et al. Enhanced Photoelectrochemical Response of Graphene-Coated Al₂O₃-TiO₂ Nanocomposite Photoanodes. *Mol Cryst Liq Cryst* 2011;538:272–7.
- [67] Gupta RK, Alahmed ZA, Yakuphanoglu F. Graphene oxide based low cost battery. *Mater Lett* 2013;112:75–7.
- [68] Yu L, Lim YS, Han JH, Kim K yun, Kim JY, Choi SY, et al. A graphene oxide oxygen barrier film deposited via a self-assembly coating method. *Synth Met* 2012;162:710–4.
- [69] Hong J, Kang SW. Hydrophobic properties of colloidal films coated with multi-wall carbon nanotubes/reduced graphene oxide multilayers. *Colloids Surfaces A Physicochem Eng Asp* 2011;374:54–7.
- [70] Zhang M, Ma Y, Zhu Y, Che J, Xiao Y. Two-dimensional transparent hydrophobic coating based on liquid-phase exfoliated graphene fluoride. *Carbon N Y* 2013;63:149–56.
- [71] Chen S, Brown L, Levendorf M, Cai W, Ju S, Edgeworth J, et al. Oxidation resistance of graphene-coated Cu and Cu/Ni alloy. *ACS Nano* 2011;5:1321–7.
- [72] Kousalya AS, Kumar A, Paul R, Zemlyanov D, Fisher TS. Graphene: an effective oxidation barrier coating for liquid and two-phase cooling systems. *Corros Sci* 2012:10–5.
- [73] Nilsson L, Andersen M, Balog R, Lægsgaard E, Hofmann P, Besenbacher F, et al. Graphene coatings: probing the limits of the one atom thick protection layer. *ACS Nano* 2012;6:10258–

66.

- [74] Nayak PK, Hsu CJ, Wang SC, Sung JC, Huang JL. Graphene coated Ni films: a protective coating. *Thin Solid Films* 2012;0–4.
- [75] Singh Raman RK, Chakraborty Banerjee P, Lobo DE, Gullapalli H, Sumandasa M, Kumar A, et al. Protecting copper from electrochemical degradation by graphene coating. *Carbon* 2012;50:4040–5.
- [76] Prasai D, Tuberquia JC, Harl RR, Jennings GK, Rogers BR, Bolotin KI. Graphene: corrosion-inhibiting coating. *ACS Nano* 2012;6:1102–8.
- [77] Noel S, Baraton L, Alamarguy D, Jaffre A, Hauquier F, Viel P, et al. Graphene films for corrosion protection of gold coated cuprous substrates in view of an application to electrical contacts. *Inst Electr Electron Eng* 2012.
- [78] Won MS, Penkov O V., Kim DE. Durability and degradation mechanism of graphene coatings deposited on Cu substrates under dry contact sliding. *Carbon* 2012:1–10.
- [79] Nguyen DD, Tai NH, Lee SB, Kuo WS. Superhydrophobic and superoleophilic properties of graphene-based sponges fabricated using a facile dip coating method. *Energy Environ Sci* 2012;5:7908–12.
- [80] Zhang M, Gao B, Yao Y, Xue Y, Inyang M. Synthesis, characterization, and environmental implications of graphene-coated biochar. *Sci Total Environ* 2012;435-436:567–72.
- [81] Ying Z, Zheng L, Song K, Hu W. Characterization of quartz crystal microbalance sensors coated with graphene films. *Procedia Eng* 2012;29:2448–52.
- [82] Dong X, Long Q, Wang J, Chan-Park MB, Huang Y, Huang W, et al. A graphene nanoribbon network and its biosensing application. *Nanoscale* 2011;3:5156–60.
- [83] Yao Y, Chen X, Guo H, Wu Z, Li X. Humidity sensing behaviors of graphene oxide-silicon bi-layer flexible structure. *Sensors Actuators B Chem* 2012;161:1053–8.
- [84] Yao Y, Chen X, Guo H, Wu Z. Graphene oxide thin film coated quartz crystal microbalance for humidity detection. *Appl Surf Sci* 2011;257:7778–82.
- [85] Zhang H, Lee HK. Simultaneous determination of ultraviolet filters in aqueous samples by

- plunger-in-needle solid-phase microextraction with graphene-based sol-gel coating as sorbent coupled with gas chromatography-mass spectrometry. *Anal Chim Acta* 2012;742:67–73.
- [86] Qu Q, Gu C, Hu X. Capillary coated with graphene and graphene oxide sheets as stationary phase for capillary electrochromatography and capillary liquid chromatography. *Anal Chem* 2012;84:8880–90.
- [87] Zhao G, Song S, Wang C, Wu Q, Wang Z. Determination of triazine herbicides in environmental water samples by high-performance liquid chromatography using graphene-coated magnetic nanoparticles as adsorbent. *Anal Chim Acta* 2011;708:155–9.
- [88] Qu Q, Shen Y, Gu C, Gu Z, Gu Q, Wang C, et al. Capillary column coated with graphene oxide as stationary phase for gas chromatography. *Anal Chim Acta* 2012;757:83–7.
- [89] Chen J, Zou J, Zeng J, Song X, Ji J, Wang Y, et al. Preparation and evaluation of graphene-coated solid-phase microextraction fiber. *Anal Chim Acta* 2010;678:44–9.
- [90] Ke Y, Zhu F, Zeng F, Luan T, Su C, Ouyang G. Preparation of graphene-coated solid-phase microextraction fiber and its application on organochlorine pesticides determination. *J Chromatogr A* 2012.
- [91] Ponnusamy VK, Jen JF. A novel graphene nanosheets coated stainless steel fiber for microwave assisted headspace solid phase microextraction of organochlorine pesticides in aqueous samples followed by gas chromatography with electron capture detection. *J Chromatogr A* 2011;1218:6861–8.
- [92] Wu Q, Feng C, Zhao G, Wang C, Wang Z. Graphene-coated fiber for solid-phase microextraction of triazine herbicides in water samples. *J Sep Sci* 2011:193–9.
- [93] Zhao G, Song S, Wang C, Wu Q, Wang Z. Solid-phase microextraction with a novel graphene-coated fiber coupled with high-performance liquid chromatography for the determination of some carbamates in water samples. *Anal Methods* 2011;3:2929–35.
- [94] Xu L, Feng J, Liang X, Li J, Jiang S. C18 functionalized graphene oxide as a novel coating for solid-phase microextraction. *J Sep Sci* 2012;35:1531–7.
- [95] Hao Q, Wang B, Bossard JA, Kiraly B, Zeng Y, Chiang IK, et al. Surface-Enhanced Raman

- Scattering Study on Graphene-Coated Metallic Nanostructure Substrates. *J Phys Chem C* 2012;116:7249–54.
- [96] Kim YK, Han SW, Min DH. Graphene oxide sheath on ag nanoparticle/graphene hybrid films as an antioxidative coating and enhancer of surface-enhanced Raman scattering. *ACS Appl Mater Interfaces* 2012;4:6545–51.
- [97] Kawasaki H, Nakai K, Arakawa R, Athanassiou EK, Grass RN, Stark WJ. Functionalized graphene-coated cobalt nanoparticles for highly efficient surface-assisted laser desorption/ionization mass spectrometry analysis. *Anal Chem* 2012;84:9268–75.
- [98] Wang H, Yang Y, Liang Y, Robinson JT, Li Y, Jackson A, et al. Graphene-wrapped sulfur particles as a rechargeable lithium-sulfur battery cathode material with high capacity and cycling stability. *Nano Lett* 2011;11:2644–7.
- [99] Chen Z, Zhou M, Cao Y, Ai X, Yang H, Liu J. In situ generation of few-layer graphene coatings on SnO₂-SiC core-shell nanoparticles for high-performance lithium-ion storage. *Adv Energy Mater* 2012;2:95–102.
- [100] Wang P, Ao Y, Wang C, Hou J, Qian J. Enhanced photoelectrocatalytic activity for dye degradation by graphene-titania composite film electrodes. *J Hazard Mater* 2012;223-224:79–83.
- [101] Shi M, Shen J, Ma H, Li Z, Lu X, Li N, et al. Preparation of graphene–TiO₂ composite by hydrothermal method from peroxotitanium acid and its photocatalytic properties. *Colloids Surfaces A Physicochem Eng Asp* 2012;405:30–7.
- [102] Zhang N, Zhang Y, Xu Y. Recent progress on graphene-based photocatalysts: current status and future perspectives. *Nanoscale* 2012;4:5792–813.
- [103] Yang M, Xu Y. Selective photoredox using graphene-based composite photocatalysts. *Phys Chem Chem Phys* 2013;15:19102–18.
- [104] Zhang N, Zhang Y, Pan X, Yang M, Xu Y. Constructing ternary CdS – graphene – TiO₂ hybrids on the flatland of graphene oxide with enhanced visible-light photoactivity for selective transformation. *J Phys Chem C* 2012;116:18023–31.

- [105] Zhang Y, Zhang N, Tang Z, Xu Y. Graphene transforms wide band gap ZnS to a visible light photocatalyst . The New Role of Graphene as a Macromolecular Photosensitizer. *ACS Nano* 2012;6:9777–89.
- [106] Zhang Y, Tang Z, Fu X, Xu Y. TiO₂ -Graphene nanocomposites for gas-phase photocatalytic degradation of volatile aromatic pollutant: is TiO₂ - graphene truly different from other TiO₂-carbon composite materials? *ACS Nano* 2010;4:7303–14.
- [107] Zhang Y, Tang Z, Fu X, Xu Y. Engineering the unique 2D mat of graphene to achieve graphene-TiO₂ nanocomposite for photocatalytic selective transformation: what advantage does graphene have over its forebear carbon nanotube? *ACS Nano* 2011;5:7426–35.
- [108] Kou L, Gao C. Making silica nanoparticle-covered graphene oxide nanohybrids as general building blocks for large-area superhydrophilic coatings. *Nanoscale* 2011;3:519–28.
- [109] Zhang S, Du Z, Li G. Graphene-supported zinc oxide solid-phase microextraction coating with enhanced selectivity and sensitivity for the determination of sulfur volatiles in *Allium* species. *J Chromatogr* 2012;1260:1–8.
- [110] Liao K, Qian Y, Macosko CW. Ultralow percolation graphene/polyurethane acrylate nanocomposites. *Polymer (Guildf)* 2012;53:3756–61.
- [111] Fabbri P, Bassoli E, Bon SB, Valentini L. Preparation and characterization of poly (butylene terephthalate)/graphene composites by in-situ polymerization of cyclic butylene terephthalate. *Polymer* 2012;53:897–902.
- [112] Yeh MH, Sun CL, Su JS, Lin LY, Lee CP, Chen CY, et al. A low-cost counter electrode of ITO glass coated with a graphene/Nafion® composite film for use in dye-sensitized solar cells. *Carbon* 2012;50:4192–202.
- [113] Sangermano M, Marchi S, Valentini L, Bon SB, Fabbri P. Transparent and conductive graphene oxide/Poly(ethylene glycol) diacrylate coatings obtained by photopolymerization. *Macromol Mater Eng* 2011;296:401–7.
- [114] Chang CH, Huang TC, Peng CW, Yeh TC, Lu HI, Hung WI, et al. Novel anticorrosion coatings prepared from polyaniline/graphene composites. *Carbon* 2012;50:5044–51.

- [115] Pan B, Zhao J, Zhang Y, Zhang Y. Wear performance and mechanisms of polyphenylene sulfide/polytetrafluoroethylene wax composite coatings reinforced by graphene. *J Macromol Sci Part B* 2012;51:1218–27.
- [116] Pan B, Xu G, Zhang B, Ma X, Li H, Zhang Y. Preparation and tribological properties of polyamide 11/graphene coatings. *Polym Plast Technol Eng* 2012;51:1163–6.
- [117] Cai D, Jin J, Yusoh K, Rafiq R, Song M. High performance polyurethane/functionalized graphene nanocomposites with improved mechanical and thermal properties. *Compos Sci Technol* 2012;72:702–7.
- [118] Zhang B, Patlolla VR, Chiao D, Kalla DK, Misak H, Asmatulu R. Galvanic corrosion of Al/Cu meshes with carbon fibers and graphene and ITO-based nanocomposite coatings as alternative approaches for lightning strikes. *Int J Adv Manuf Technol* 2012.
- [119] Wang X, Xing W, Song L, Yang H, Hu Y, Yeoh GH. Fabrication and characterization of graphene-reinforced waterborne polyurethane nanocomposite coatings by the sol–gel method. *Surf Coatings Technol* 2012;206:4778–84.
- [120] Yu B, Wang X, Xing W, Yang H, Song L, Hu Y. UV-curable functionalized graphene oxide/polyurethane acrylate nanocomposite coatings with enhanced thermal stability and mechanical properties. *Ind Eng Chem Res* 2012;51:14629–36.
- [121] Martin-Gallego M, Verdejo R, Lopez-Manchado M A., Sangermano M. Epoxy-graphene UV-cured nanocomposites. *Polymer* 2011;52:4664–9.
- [122] Zaman I, Phan TT, Kuan H-C, Meng Q, Bao La LT, Luong L, et al. Epoxy/graphene platelets nanocomposites with two levels of interface strength. *Polymer* 2011;52:1603–11.
- [123] Zou J, Song X, Ji J, Xu W, Chen J, Jiang Y, et al. Polypyrrole/graphene composite-coated fiber for the solid-phase microextraction of phenols. *J Sep Sci* 2011;34:2765–72.
- [124] Jin J, Lin Y, Song M, Gui C, Leesirisan S. Enhancing the electrical conductivity of polymer composites. *Eur Polym J* 2013;49:1066–72.
- [125] Narayan R, Chattopadhyay DK, Sreedhar B, Raju KVS, Mallikarjuna NN, Aminabhavi TM. Synthesis and characterization of crosslinked polyurethane dispersions based on

- hydroxylated polyesters. *J Appl Polym Sci* 2006;99:368–80.
- [126] Saunders JH, Frisch KC. *Polyurethanes: chemistry and technology*. Interscience Publishers New York; 1964.
- [127] Santos D, Manuel A. Polyester polyols and their use as the polyol component in two-component polyurethane paints. U.S. Patent US 6,184,332, 2001.
- [128] Wamprecht C, Sonntag M. Polyester polyols and their use as a binder component in two-component polyurethane coating compositions. U.S. Patent US 6,423,816, 2002.
- [129] Brown DW, Lowry RE, Smith LE. Kinetics of hydrolytic aging of polyester urethane elastomers. *Macromolecules* 1980;13:248–52.
- [130] Pegoretti A, Fambri L, Penati A, Kolarik J. Hydrolytic resistance of model poly(ether urethane ureas) and poly(ester urethane ureas). *J Appl Polym Sci* 1998;70:577–86.
- [131] Buredeniuc JJ, Kamzelski AZ. Blowing catalyst compositions containing hydroxyl and surface active groups for the production of polyurethane foams. U.S. Patent 1702913, 2006.
- [132] Roy S, Majumdar K. Preparation of organo-tin catalyst useful for preparation of polyurethanes. U.S. Patent 194604, 2004.
- [133] Dzierza W. Mechanical properties of crosslinked polyurethanes. *J Appl Polym Sci* 1978;22:1331–42.
- [134] Britain JW, Gemeinhardt PG. Catalysis of the isocyanate-hydroxyl reaction. *J Appl Polym Sci* 1960;IV:207–11.
- [135] Lenz RW. *Organic chemistry of synthetic high polymers*. New York: Interscience; 1967.
- [136] Liaw D. The relative physical and thermal properties of polyurethane elastomers :effect of chain extenders of bisphenols, diisocyanate, and polyol structures. *J Appl Polym Sci* 1997;66:1251–65.
- [137] Petrovic ZS, Javni I, Divjakovic V. Structure and physical properties of segmented polyurethane elastomers containing chemical crosslinks in the hard segment. *J Polym Sci Part B Polym Phys* 1998;36:221–35.

- [138] Petrovic ZS, Ferguson J. Polyurethane elastomers. *Prog Polym Sci* 1991;16:695–836.
- [139] The DoW Chemical Company. A guide to glycols 2003.
- [140] Oertel G, Abele L. Polyurethane hand book. 2nd ed. Munich; New York; Cincinnati; Hanser; 1993.
- [141] ASTM Standard D16-00. Technology of paint, related coatings, materials, and applications n.d.
- [142] Seymour RW, Cooper SL. Thermal analysis of polyurethane block polymers. *Macromolecules* 1972;6:48–53.
- [143] Schollenberger CS. Simulated vulcanizates of polyurethane elastomers. U.S. Patent 2,871,213, 1959.
- [144] Cooper SL, Tobolsky A V. Properties of linear elastomeric polyurethanes. *J Appl Polym Sci* 1966;10:1837–44.
- [145] Schneider N., Paik Sung C., Matton RW, Illinger J. Thermal transition behavior of polyurethanes based on toluene diisocyanate. *Macromolecules* 1975;8:62–7.
- [146] Pandya M V., Deshpande DD, Hundiware DG. Effect of diisocyanate structure on viscoelastic, thermal, mechanical and electrical properties of cast polyurethanes. *J Appl Polym Sci* 1986;32:4959–69.
- [147] Wang CB, Cooper SL. Morphology and properties of segmented polyether polyurethaneureas. *Macromolecules* 1983;16:775–86.
- [148] Speckhard TA, Strate GVER, Gibson PE, Cooper SL. Properties of polyisobutylene-polyurethane block copolymers: I. Macroglycols from ozonolysis of isobutylene-isoprene copolymer. *Polym Eng Sci* 1983;23:337–49.
- [149] Chang SL, Yu TL, Huang CC, Chen WC, Linliu K, Lin TL. Effect of polyester side-chains on the phase segregation of polyurethanes using small-angle X-ray scattering. *Polymer (Guildf)* 1998;39:3479–89.
- [150] Bengtson B, Feger C, Macknight WJ, Schneider NS. Thermal and mechanical properties of solution polymerized segmented polyurethanes with butadiene soft segments. *Polymer*

(Guildf) 1985;26:895–900.

- [151] Miller JA, Lin SB, Hwang KKS, Wu KS, Gibson PE, Cooper SL. Properties of polyether-polyurethane block copolymers: effects of hard segment length distribution. *Macromolecules* 1985;18:32–44.
- [152] Briber RM, Thomas EL. The structure of MDI/BDO-based polyurethanes: Diffraction studies on model compounds and oriented thin films. *J Polym Sci Polym Phys Ed* 1985;23:1915–32.
- [153] Hwang KKS, Wu G, Lin SB, Cooper SL. Synthesis and characterization of MDI-butanediol urethane model compounds. *J Polym Sci Polym Chem Ed* 1984;22:1677–97.
- [154] Camberlin Y, Pascault JP, Letoffe JM, Claudy P. Synthesis and DSC study of model hard segments from diphenyl methane diisocyanate and butane diol. *J Polym Sci Polym Chem Ed* 1982;20:383–92.
- [155] Camberlin Y, Pascault JP, Letoffe M, Claudy P. Model Hard segments from diphenyl methane diisocyanate and different chain extenders, and corresponding linear block polyurethanes. *J Polym Sci Polym Chem Ed* 1982;20:1445–56.
- [156] Tonelli C, Trombetta T, Maccone P. Synthesis and physical characterization of model hard segments based on diphenyl methane diisocyanate and hydroquinone bis(2-hydroxyethyl) ether. *J Polym Sci Part A Polym Chem* 1999;37:1473–87.
- [157] Tonelli C, Trombetta T, Scicchitano M, Simeone G, Ajroldi G. New Fluorinated Thermoplastic Elastomers. *J Appl Polym Sci* 1996;59:311–27.
- [158] Yoo SR, Lee HS, Seo SW. Orientation and phase separated structure of polyurethanes having various chemical structures. *Polymer-Korea* 1997;21:467–79.
- [159] Frontini PM, Rink M, Pavan A. Development of polyurethane engineering thermoplastics. II. Structure and properties. *J Appl Polym Sci* 1993;48:2023–32.
- [160] Hartmann B, Duffy J V., Lee GF, Balizer E. Thermal and dynamic mechanical properties of polyurethaneureas. *J Appl Polym Sci* 1988;35:1829–52.
- [161] Stanford JL, Still RH, Wilkinson AN. Effects of soft-segment prepolymer functionality on

- structure–property relations in RIM copolyurethanes. *Polymer* (Guildf) 2003;44:3985–94.
- [162] Stanford JL, Still RH, Wilkinson AN. Effectts of soft segment prepolymer functionality on structure development in RIM copolymers. *Polymer* (Guildf) 1995;36:3555–64.
- [163] Christenson CP, Harthcock MA, Meadows MD, Guerra RE, Howard WL, Creswick MW, et al. Model MDU/butanediol polyurethanes : molecular structure , morphology , physical and mechanical properties. *J Polym Sci Part B Polym Phys* 1986;24:1401–39.
- [164] Mishra AK, Chattopadhyay DK, Sreedhar B, Raju KVSN. FT-IR and XPS studies of polyurethane-urea-imide coatings. *Prog Org Coatings* 2006;55:231–43.
- [165] Pimentel GC, Sederholm CH. Correlation of infrared stretching frequencies and hydrogen bond distances in crystals. *J Chem Phys* 1956;24:639.
- [166] Masiulanis B, Zielinski R. Mechanical, thermal, and electric properties of polyurethaneimide elastomers. *J Appl Polym Sci* 1985;30:2731–41.
- [167] Dahotre NB, Kadolkar P, Shah S. Refractory ceramic coatings: processes, systems and wettability/adhesion. *Surf Interface Anal* 2001;31:659–72.
- [168] González-García Y, González S, Souto RM. Electrochemical and structural properties of a polyurethane coating on steel substrates for corrosion protection. *Corros Sci* 2007;49:3514–26.
- [169] Gasem ZM. *Protective Coatings*. Dhahran, Saudi Arabia: n.d.
- [170] Mo M, Zhao W, Chen Z, Yu Q, Zeng Z, Wu X, et al. Excellent tribological and anti-corrosion performance of polyurethane composite coatings reinforced with functionalized graphene and graphene oxide nanosheets. *RSC Adv* 2015;5:56486–97.
- [171] Cai D, Yusoh K, Song M. The mechanical properties and morphology of a graphite oxide nanoplatelet / polyurethane composite. *Nanotechnology* 2009;20:085712–6.
- [172] Schriver M, Regan W, Gannett W, Zaniwski A, Crommie M, Zettl A. Graphene as a long-term metal oxidation barrier: worse than nothing. *ACS Nano* 2013;7:5763–8.
- [173] Ramezanzadeh B, Ghasemi E, Mahdavian M, Changizi E, Mohamadzadeh Moghadam MH. Covalently-grafted graphene oxide nanosheets to improve barrier and corrosion protection

- properties of polyurethane coatings. *Carbon* 2015;93:555–73.
- [174] Canales J, Muñoz ME, Fernández M, Santamaría A. Rheology, electrical conductivity and crystallinity of a polyurethane/graphene composite: implications for its use as a hot-melt adhesive. *Compos Part A Appl Sci Manuf* 2016;84:9–16.
- [175] Choy KL. Chemical vapour deposition of coatings. *Prog Mater Sci* 2003;48:57–170.
- [176] Scriven LE. Physics and applications of dip coating and spin coating. *MRS Proc* 1988;121:717–29.
- [177] Lawrence CJ, Zhou W. Spin coating of non-newtonian fluids. *J Nonnewton Fluid Mech* 1991;39:137–87.
- [178] Le Roux JD, Paul DR. Preparation process of composite membranes by a spin coating. *J Memb Sci* 1992;74:233–52.
- [179] Bornside DE, Macosko CW, Scriven LE. On the modeling of spin coating. *J Imaging Technol* 1987;13:122–30.
- [180] Szabó T, Szeri A, Dékány I. Composite graphitic nanolayers prepared by self-assembly between finely dispersed graphite oxide and a cationic polymer. *Carbon* 2005;43:87–94.
- [181] Sheng K, Bai H, Sun Y, Li C, Shi G. Layer-by-layer assembly of graphene/polyaniline multilayer films and their application for electrochromic devices. *Polymer* 2011;52:5567–72.
- [182] Brinker CJ, Scherer GW. *Sol-gel science: the physics and chemistry of sol-gel processing*. Academic Press; 1990.
- [183] Hench LL, West JK. The sol-gel process. *Chem Rev* 1990;90:33–72.
- [184] Mujumdar AS. *Handbook of industrial drying*. 3rd ed. CRC Press, Taylor & Francis Group; 2007.
- [185] Niessen WR. *Combustion and incineration processes*. 3rd ed. CRC Press, Taylor & Francis Group; 2002.
- [186] Girotto C, Rand BP, Genoe J, Heremans P. Exploring spray coating as a deposition technique for the fabrication of solution-processed solar cells. *Sol Energy Mater Sol Cells*

2009;93:454–8.

- [187] Maa YF, Ameri M, Rigney R, Payne LG, Chen D. Spray-coating for biopharmaceutical powder formulations: beyond the conventional scale and its application. *Pharm Res* 2004;21:515–23.
- [188] Besra L, Liu M. A review on fundamentals and applications of electrophoretic deposition (EPD). *Prog Mater Sci* 2007;52:1–61.
- [189] Li X, Liu X, Huang J, Fan Y, Cui F. Biomedical investigation of CNT based coatings. *Surf Coatings Technol* 2011;206:759–66.
- [190] Binner JJGP. Advanced ceramic processing and technology Vol.1. Noyes da corporation/Noyes Publications; 1990.
- [191] Basu RN, Randall CA, Mayo MJ. Fabrication of dense zirconia electrolyte films for tubular solid oxide fuel cells by electrophoretic deposition. *J Am Ceram Soc* 2001;84:33–40.
- [192] Sarkar P, De D, RHO H. Synthesis and microstructural manipulation of ceramics by electrophoretic deposition. *J Mater Sci* 2004;39:819–23.
- [193] Boccaccini AR, Cho J, Roether JA, Thomas BJC, Jane Minay E, Shaffer MSP. Electrophoretic deposition of carbon nanotubes. *Carbon N Y* 2006;44:3149–60.
- [194] Chavez-Valdez A, Shaffer MSP, Boccaccini AR. Applications of graphene electrophoretic deposition.:A review. *J Phys Chem B* 2013;117:1502–15.

Chapter 3 Experimental

3.1 Materials

3.1.1 Carbon based particles

TIMREX PP10 natural graphite (PP10) which supplied by TATA steel was purchased from TIMCAL Ltd (100% graphite). The expandable graphite was purchased from China Qing Dao Graphite Company (100% expandable graphite). MWCNT was purchased from a company in China (100% CNT).

3.1.2 PU topcoat, primer and reactants

In the case of producing PU nanocomposite conductive coatings, matured PU topcoat and primer were supplied by TATA steel. The pigments and the corrosion inhibitor were removed from the coating. The information of the coating is as followed:

Topcoat

Product name: Chocolate Brown HMPU

Product No.: 301/M07363

Contains: 1,6-diisocynatohexane Homopolymer, Methylethylketone oxim-blocked (PU >80%), hydrocarbons, C₁₀, aromatics, >1% naphthalene

Primer

Product name: P21PR00/CF79 BPRIM 266 WHITE PR

Product No.: 330/0068

Contains: EPOXY RESIN (Number average $M_w \leq 700$, >80%), hydrocarbons, C₁₀, aromatics, >1% naphthalene

For the investigation of cure dynamic of PU, model PU was used. The selection of the reactants based on the feasibility of cure dynamic investigation. The reaction rate of the model PU is moderate and fillers can be mixed with the PU with ease. The information of the reactants with chemical structures is shown below:

Isocyanate

4,4'-methylenebis (cyclohexyl isocyanate) (HMDI) (purchased from Sigma Aldrich, >90% isomer)

Molecular weight: 262.35

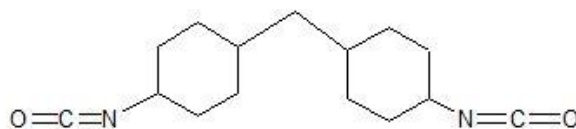
Equivalent weight: $262/2=131$

Appearance: colourless liquid

Density (at 20 °C): 1.066 g/ml

Flash point: >110 °C

NCO content: 32%

**Polyol**

Lupranol 2090 (>99.5%)

Molecular weight: 6000

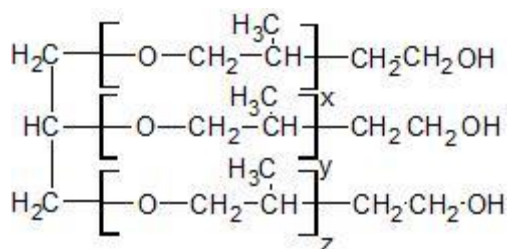
Equivalent weight: 2,000

Appearance: colourless liquid

Density (at 20 °C): 1 g/ml

Flash point: N/A

OHV: 28.05

**Chain extender**

1,4 – Butandiol (purchased from Sigma Aldrich, >99.5%))

Molecular weight: 90.12

Equivalent weight: 45.06

Appearance: colourless liquid

Density: 1.017g/ml at 25 °C

Flash point: N/A



Catalyst

The catalyst used for this system is DABCO-33LV supplied by Air Products and Chemicals, Inc. It is a mixture of triethylenediamine and di (propylene glycol).

3.1.3 Steel substrates

Cold rolled steel ‘Black Plate’, which was used as substrates, was provided by TATA Steel R&D. The BP steel was a 0.2mm thick steel sheet initially and it was cut into 20mm by 50mm steel sheets for subsequent coating processes. Apart from BP, there are other steel substrates will be used for comparison test in EPD graphene coating sections which will be described in detail later.

Code	Description
13KE005	316 stainless steel
13KE008	Black plate with better roughness
13KE009	Carbon steel nickel plated
13KE21	Special treatment steel

3.1.4 Other chemicals

Acetone (99.5% purity) and iodine (>99%) were purchased from Sigma Aldrich. Melamine which was used for graphene exfoliation was purchased from Sigma Aldrich. H_2SO_4 (>95%), HNO_3 (70%), HCl (38 wt% concentration), KMnO_4 (>99%), 30% H_2O_2 solution, NaCl (>99.5%) and BaCl_2 (>99.5%) were purchased from Fisher Ltd (UK).

3.2 Graphene fabrication

Sample preparation

Graphene (G) was produced by mechanochemical method from expandable graphite in the lab [1]. Expandable graphite was mixed with melamine in volume ratios of 1:1

and 1:3 to produce powder mixtures. The mixtures were then mixed with de-ionised water to form suspensions and the concentrations were 1g/100ml. The suspensions were then kept at 80 °C for 1 hour with constant magnetic stirring around 200 rpm to allow the melamine to fully penetrate the expandable graphite galleries. After stirring, the suspensions were filtrated and dried at 80 °C for 5 hours. The dried powder mixtures were then underwent ball-milling for graphene exfoliation. The ball milling machine ran for 500 rounds and 1000 rounds. The milled mixtures were then washed by de-ionized water and the second exfoliation process would be performed. The initial exfoliated mixtures were then exfoliated by 1 hour ultrasonication (Fisher Scientific Sonic Dismembrator Model 500, 300 W), 1 hour mechanical stirring or 4 hours mechanical stirring. After second exfoliation process, the mixtures were washed by hot water to remove melamine completely. The washed particles were put into a drying cabinet overnight for water removal. The table below summarized the graphene produced by the above methods.

Code name	Graphite to Melamine Volume Ratio	Ball-milling Revolutions	Exfoliation Method	Exfoliation Time (hours)
A	1:1	1000	Ultrasonic	1
B	1:1	1000	Mechanical	4
C	1:3	1000	Mechanical	4
D	1:3	1000	Ultrasonic	1
E	1:3	1000	Mechanical	1
F	1:3	500	Mechanical	4

Characterisation

The effectiveness of the exfoliation procedures of flake graphite was determined by

x-ray diffraction (XRD) scans on the D2 phaser (Brunker Corporation) from 1° to 30° (2theta) with a step size of 0.02° . The morphologies of the graphene flakes were observed under the JEM-2000FX transmission electron microscope (TEM) (JEOL Limited.). XPS testing was carried out on the Thermo Scientific K-Alpha XPS system (Thermo Fisher Scientific Inc.) with an Al K- α X-ray source with a power of 200 W and under 10^{-7} Torr vacuum. The Fourier transform infrared (FTIR) spectra were done on the FTIR-8400S Fourier Transform Infrared Spectrophotometer (Shimadzu Corporation) with 4 cm^{-1} resolution over 64 scans. The graphene EPD coating was done on steel substrates with 40 V and 2 mA for 5 minutes. The conductance of the graphene coating was measured by the four-point conductivity test, on the multi-height microposition probing system (Jandel Engineering Limited). The basic introduction of the techniques used would be covered in 3.6.

3.3 Carbon based conductive coating

Sample preparation

Graphene (G) or graphite (PP10) was mixed with acetone to form a suspension. Iodine was then added into the suspension and stirred until fully dissolved. The resulted mixture was ultrasonicated for 30 minutes by using Fisher Scientific Sonic Dismembrator Model 500 at room temperature. The BP substrates were cleaned by acetone and then it was degreased in 5% alkaline solution at 70°C for 3 minutes. The distance between two electrodes was 10mm and a voltage of 40V was applied for 30 seconds initially. The DC source used in EPD was Consort EV265. EPD coated samples were thermal treated in a furnace (Carbolite RHF 16/8) with different temperatures for different times. Different EPD conditions were used as well to investigate the optimized EPD conditions for the best conductivity. The materials, heat treatment temperature and time, and EPD conditions are shown in the tables below.

Heat treatment temperature trials

Materials	Heat treatment temperature (°C)	Treatment time (mins)
PP10	520, 540, 560, 580, 600, 610, 620, 630, 660, 700	5
Graphene		

Heat treatment time trials

Materials	Heat treatment temperature (°C)	Treatment time (mins)
PP10	600	1, 2, 3, 4, 5

EPD conditions trials*Iodine amount change*

Sample Name	Voltage (V)	Current (mA)	Time (mins)	Iodine weight in 80 ml acetone (mg)
DP1061	40	12	2	14
DP1062	40	25	2	35.5
DP1063	40	40	2	59.3
DP1064	40	51	2	79.1
DP1065	40	53	2	100.7

Deposition time change

Sample Name	Voltage (V)	Current (mA)	Time (mins)
DP1066	40	20	0.5
DP1067	40	20	1
DP1068	40	20	1.5

DP1069	40	20	2
DP10610	40	20	2.5

Voltage change

Sample Name	Voltage (V)	Current (mA)	Time (mins)
DP1866	20	7	2
DP1867	30	13	2
DP1868	40	17	2
DP1869	50	20	2
DP18610	60	24	2

In the EPD conditions test, all the samples were heat treated at 580 °C for 5 minutes

Characterisation

Carl Zeis (Leo) 1530VP Field Emission Gun Scanning Electron Microscope (FEG-SEM) and Thermo Scientific K-Alpha X-ray Photoelectron Spectroscopy (XPS) were used to characterize the surface morphology and surface composition of the coated samples respectively. The electrical conductivity of the coated samples was measured by using a FLUKE PM6306 programmable automatic RCL meter with a four point probe. Relative electrical conductivity C_c/C_s was used show the electrical conductivity enhancement, where C_c represents the measured electrical conductivity of the coated samples and C_s represents the measured electrical conductivity of bare steel. Electrochemical impedance spectroscopy (EIS) was used to characterize the corrosion resistance of the coatings. The basic introduction of the techniques used would be covered in 3.6.

3.4 PU nanocomposite coatings

Sample preparation

For the fabrication of nanocomposite coatings PP10, G, MWCNT and TEG were used. Initially, topcoat was stirred by a glass rod to let the polymer particles disperse uniformly in the suspension and then a calculated amount of PU topcoat was poured into a glass bottle for latter mechanical stirring. The total weight of the composite was 6g. A calculated amount of filler was added into the PU topcoat during mechanically stirring. The duration of mechanical stirring was 4 hours. In the single filler trials, only G and PP10 were used. The stirring time was set according to the results obtained from 3.2.

For hybrid filler filled coating, the total weight of the composite was 6g. According to the filler ratio, calculated amount of TEG, G or PP10 and MWCNTs were added into a glass bottle and a suitable amount of acetone was added as well. The resulted suspension was ultrasonicated for 30 minutes. After ultrasonication, the glass bottle was put into a fume cupboard to evaporate the acetone until a filler paste was resulted. Calculated amount of topcoat was added into the glass bottle and the mixture was mechanical stirred at 1000 rpm for 4 hours. The preparation procedure of primer based nanocomposite coatings was similar.

All the resulted mixtures were coated on to the BP steel by hand draw bar which performed with a glass rod. Before coating, The BP substrates were cleaned by acetone and then they were degreased in 5% alkaline solution at 70 °C for 3 minutes. The coated samples were put into an oven at 290 °C for 4 minutes 40s for fully cured. For EPD + topcoat system, topcoat was directly coated on to EPD deposited layer by hand draw bar. The as-prepared sample was cured at the same conditions as other samples. For multi-layer system, epoxy primer was directly coated on to EPD deposited layer by hand draw bar and cured in the oven at 290 °C for 3 minutes. PU

top coat was subsequently coated on to the coated sample by hand draw bar and the resulting multi-layer coating was put into the oven for 4 minutes 40s.

Single filler weight percent trial

PP10 was incorporated into topcoat primarily. G filler and primer was used as comparison. The weight percent used was shown below.

Primer codename	PP10 loading (wt%)
EPP6	6
EPP8	8
EPP10	10
Topcoat codename	PP10 loading (wt%)
PPPU1	1
PPPU2	2
PPPU3	3
PPPU5	5
PPPU6	6
PPPU7	7
PPPU8	8
PPPU10	10
PPPU12	12
PPPU14	14
PPPU17	17.39
Topcoat codename	G loading (wt%)
GPU1	1
GPU3	3
GPU5	5
GPU8	8

Stirring rate trial

The effect of stirring rate on the electrical conductivity of the topcoat was examined and the stirring rates used were shown below.

Topcoat codename	PPPU8500	PPPU8750	PPPU81000	PPPU81500
Stirring rate (rpm)	500	750	1000	1500

Primer + topcoat initial trial

1 wt% Primer/PP10 composite was coated onto the steel substrate and cured in an oven for under-cure. Topcoat was coated on to the primer coated substrates at room temperature and then the topcoat and primer were fully cured in an oven.

Code name	PP10 loading (wt%)
EPPPU7	7
EPPPU8	8
EPPPU10	10
EPPPU12	12
EPPPU14	14
EPPPU17	17.39

Hybrid filler trials

In the first hybrid filler trial, the effects of adding MWCNT and G were evaluated.

Code name	HIPU8	HIIPU8	HIIPU8
Filler ratio in weight	PP10:MWCNT:G = 1:1	PP10:MWCNT= 1:1	PP10:G = 1:1

After the investigation, the hybrid filler system with best electrical conductivity was used in primer system from comparison.

Code name	HIIEPP4	HIIEPP8
Filler ratio in weight	PP10:MWCNT = 1:1	PP10:MWCNT= 1:1

Weight percent	4 wt%	8 wt%
-----------------------	-------	-------

In order to improve the electrical conductivity of the coating further, TEG was used. TEG was prepared from heat treatment of expandable graphite. The expandable graphite was put into an oven under 900 °C for about 90s. Afterwards, the heat treated expandable graphite was obtained. The electrical conductivities of epoxy primer loaded with the fillers with different ratios were tested. The filler ratios and corresponded code name was shown below.

Code name	HIVE21000	HVE21000	HVIE21000
Filler ratio in weight	TEG:MWCNT = 1:1	TEG:MWCNT = 2:1	TEG:MWCNT = 1:2
Weight percent (%)	2	2	2

After comparing the effect of hybrid filler ratios, the effect of weight percent on the conductivity of primer was investigated.

Code name	TEG loading (wt%)
HIVE21000	2
HIVE41000	4
HIVE51000	5
HIVE61000	6
HIVE71000	7
HIVE81000	8

Multi-layer coating trial

The electrical conductivity and anti-corrosion resistance of multi-layers coatings were investigated. The tri-layers coating systems and bi-layers coating systems were prepared with the coating below:

Code name	Coating system
MI(1)	EPD+HIIIEPP8+HIIPU8

MI(2)	EPD+HIIIEPP4+HIIPU8
MII(1)	HIIIEPP8+HIIPU8
MII(2)	HIIIEPP4+HIIPU8

Slat addition

Sodium chloride was added into the HIVE61000 mixture before mechanical stirring. The electrical conductivity values after and before salt addition were compared.

Characterization

The electrical conductivity of the coated samples was measured by using a FLUKE PM6306 programmable automatic RCL meter with a four point probe. Relative electrical conductivity C_c/C_s was used show the electrical conductivity enhancement, where C_c represents the measured electrical conductivity of the coated samples and C_s represents the measured electrical conductivity of bare steel. Optical microscopy (Leica DFC480) and FEGSEM (Carl Zeis (Leo) 1530VP) were used to characterize the surface of the coated samples. EIS was used to characterize the corrosion resistance of the coatings. The basic introduction of the techniques used would be covered in 3.6.

3.5 PU cure dynamic

Stoichiometry

Equivalent weight of isocyanates = 131 g/mol

Equivalent weight of polyol = 2000 g/mol

For theoretical reactions, 1 unit isocyanate needs to react with 1 unit polyol

5g of polyol is used in the experiment.

The molar value of OH group in 5g poly (propylene glycol) = $\frac{5}{2000} = 0.0025 \text{ mol}$

If there are three batches where 26 wt%, 30 wt% and 34 wt% hard segment content (HS%) are used,

$$\text{HS wt\%} = \frac{\text{Weight of HMDI} + \text{Weight of BDO}}{\text{Weight of the whole PU system}}$$

The required HMDI and BDO for 26 wt% hard segment content = $\frac{5 \times 0.26}{0.74} = 1.76g$

The required HMDI and BDO for 30 wt% hard segment content = $\frac{5 \times 0.3}{0.7} = 2.14g$

The required HMDI and BDO for 34 wt% hard segment content = $\frac{5 \times 0.34}{0.66} = 2.57g$

Chain extender 1,4-butanediol will be used as well and the hard segment content includes the weight of chain extender and the weight of isocyanate needed. Took 26wt% hard segment content as example and assumed x g BDO, y g HMDI were used and the isocyanate index was n. Therefore, two equations could be obtained:

$$x + y = 1.76 \quad (1)$$

$$\frac{5}{2000} + \frac{x}{45.06} = \frac{1}{n} \times \frac{y}{131} \quad (2)$$

When the isocyanate index was fixed, the required amount of BDO and HMDI could be obtained from equation (1) and (2). The calculation results were listed as followed.

26 wt% HS%			30 wt% HS%			34% HS%		
Index	HMDI (g)	BDO(g)	Index	HMDI (g)	BDO (g)	Index	HMDI (g)	BDO (g)
1	1.39	0.37	1	1.68	0.46	1	2.00	0.57
1.05	1.41	0.35	1.05	1.70	0.44	1.05	2.02	0.55
1.1	1.43	0.33	1.1	1.72	0.42	1.1	2.04	0.53
1.15	1.44	0.32	1.15	1.73	0.41	1.15	2.07	0.50
1.2	1.46	0.30	1.2	1.75	0.39	1.2	2.09	0.48
1.25	1.47	0.29	1.25	1.77	0.37	1.25	2.10	0.47
1.3	1.48	0.28	1.3	1.78	0.36	1.3	2.12	0.45
1.35	1.49	0.27	1.35	1.80	0.34	1.35	2.14	0.43
1.4	1.50	0.26	1.4	1.81	0.33	1.4	2.15	0.42

1.45	1.51	0.25	1.45	1.82	0.32	1.45	2.17	0.40
1.5	1.52	0.24	1.5	1.83	0.31	1.5	2.18	0.391

The amounts of filler needed in each system are listed in the table below

HS content (wt%)	26	30	34
0.5 wt% filler (g)	0.0338	0.0357	0.0379
1 wt% filler (g)	0.067	0.072	0.0757
2 wt% filler (g)	0.137	0.146	0.1514
4 wt% filler (g)	0.280	0.298	0.3028

Procedure of sample preparation

In this cure dynamic study, 26wt% HS content PU, 1.05 isocyanate index for G and PP10, and 1.1 isocyanate index for GO was adopted. In order to disperse graphene oxide, calculated amount of GO was added in to acetone first and magnetically stirred for 48 hour to break the GO sheets into small flakes. The mixture was then ultrasonicated 30mins. After mixing with polyol by mechanical stirring for 30 minutes, the resulted mixture was put into a vacuum oven under 80 °C for 2 hours to remove the water and acetone in the polyol. After that, the resulted mixture was mixed with calculated amount of isocyanate at room temperature and stirred for 10 minutes to achieve a uniform mixture. Calculated amount of graphene was added into acetone and ultrasonicated 30mins. After mixing with polyol by mechanical stirring for 30 minutes, the mixture was put into a vacuum oven under 80 °C for 2 hours to exclude the water in the polyol. After that, the resulted mixture was mixed with calculated amount of isocyanate at room temperature and stirred for 10 minutes to achieve a uniform mixture. The preparation procedure of PP10 filled PU was similar to the preparation procedure of graphene filled PU.

Characterization

TA Instruments Differential Scanning Calorimetry (DSC) 2920 calorimeter was used for non-isothermal and quasi-isothermal cure dynamic test. Nitrogen gas rate was set at 50 ml/min. All the tests were carried out in modulated temperature DSC mode. For non-isothermal test, the samples were tested from room temperature to 250 °C with a heat rate of 10 °C/min. The modulation amplitudes were ± 0.2 °C, ± 0.4 °C and ± 1 °C and a modulated period of 60s. The results obtained from different modulation amplitudes were compared. The cure temperatures for isothermal tests were selected according to the non-isothermal tests. For quasi-isothermal tests, the samples were put into the MDSC at a certain cure temperature for 300 minutes with modulation amplitude of ± 0.4 °C and a modulated period of 60s. The FTIR spectra from 4000⁻¹ cm to 600⁻¹ cm of the samples with different cure times at different cure temperature were obtained *via* Shimadzu FTIR-8400s spectrophotometer with a 2 cm⁻¹ resolution over 64 scans. The samples were coated on to a KBr disk and then the coated disk was put into an oven for curing. The basic introduction of the techniques used would be covered in 3.6.

3.6 Introduction of the characterisation techniques

3.6.1 Four point probe method

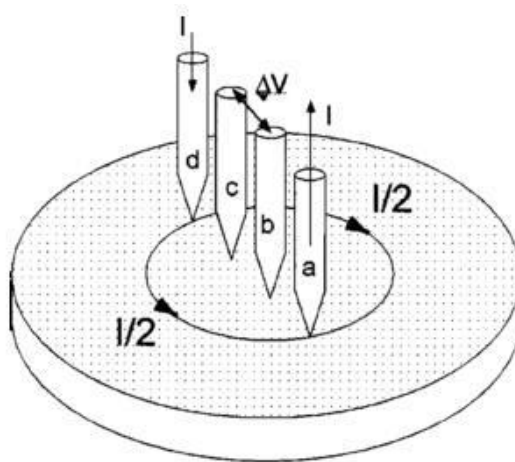


Figure 3.1 The electrodes arrangement of the linear array four point probe [2]

Four point probe method is a common methods to measure resistivity and it can be readily coupled with computer to perform rapid and automatic testing [2,3]. There are two types of probe arrangement: linear array and square array [4]. Linear array probe is adopted in the project. The classical arrangement of linear four point probe consists of four equal length needle-like electrodes and the distance of adjacent electrodes is the same (Figure 3.1) [2]. The current is injected into the material *via* the outer two electrodes and the inner electrodes were used to measure the resultant electric potential distribution. The contact resistance between the probe and the materials can be neglected by using the separate electrodes for the current injection and electric potential measurement [5]. Inhomogeneity, shape and dimensions of the sample will affect the results of four point probe test [3,6,7]. In this project, the resistivity of the coated sample is calculated by the equation below [2,8]:

$$\rho = \frac{\pi w}{\ln 2} \left(\frac{V}{I} \right) = 4.5342 \times w \times \left(\frac{V}{I} \right)$$

Where w is the thickness of the sample, V is the voltage and I is the current. Relative electrical conductivity C_c/C_s was used show the electrical conductivity enhancement, where C_c represents the measured electrical conductivity of the coated samples and C_s represents the measured electrical conductivity of bare steel. The thickness of the steel substrate is 0.1mm. In order to reduce the experimental error, the thickness of the coated sample is assumed to be nearly the same as the steel substrate.

3.6.2 EIS

Electrochemical impedance spectroscopy is a convenient and powerful technique to investigate the mechanisms of electrochemical reactions, the properties of porous electrodes, passive surfaces and transport properties of materials [9,10]. The advantages of using EIS include: (1) the results can be interpreted by linear systems theory because EIS is a linear technique; (2) *via* linear electrical response techniques, the impedance (or admittance) can be obtained from EIS when the measurement is done over infinite frequency range; (3) the efficiency of this technique is very high; (4)

the data obtained is determined by integral transform techniques (the Kramers – Kronig transform) which is not affected by the physical process involved during measurement (5) it is non-destructive and does not accelerate corrosion reactions [11]. Owing to the power of EIS, it is frequently to evaluate the performance of coated metal system (organic coating and inorganic coating *etc.*). In terms of organic coatings coated metals, the corrosion mechanism, the defects, the degradation and the lifetime of the organic coating can be investigated by EIS [10,12,13]. The information acquired from EIS would be very useful for coating development. The electrical resistance of the coating some time can be a general indicator of its anti-corrosion performance where coatings have over $10^8 \Omega\text{cm}^{-2}$ resistance can provide good corrosion protection while that with under $10^6 \Omega\text{cm}^{-2}$ has poorer corrosion protection [14]. During EIS measurement, voltage with a small-amplitude sinusoidal variation (E_t) is applied onto the polymer in the range from mini-Hz to million Hz. The resulted current waveform (I_t) at each frequency is measured. The value of impedance is the ratios between E_t and I_t and it can be expressed as a complex number. The results of EIS are usually presented in three plots: (1) Bode plot where the impedance in logarithm is plotted against the frequencies in logarithm (2) Nyquist plot where the real component of the impedance is plotted against the complex component of the impedance. (3) The plot of phase angle (the difference in the phase between voltage and current) against frequency in logarithm.

3.6.3 MDSC

DSC is a thermal technique that measures the differences in heat flow between a sample and a reference as a function of sample temperature when the two are underwent a controlled temperature changing condition. It is a calorimetric method which can measure the differences in energy between the references and the samples. In addition, DSC was developed to avoid the difficulties when using DTA or quantitatively compensate to those difficulties such as the temperature dependences of

thermal transport and sensor sensitivity [15,16]. There are two types of DSC instruments: power compensation and heat flux mode. The DSC used in this experiment is heat flux DSC. In this type of DSC, heat flows into both the sample and the reference material through electrically heated constant thermoelectric disk. Then heat is transferred into the sample and the reference via the two pans [15]. Heat flux DSC has a similar operative mechanism to a conventional DTA, except the quantitative compensation for the problems' areas mentioned above. DSC can determine specific heat, glass transition temperature, melting and crystallization points, heats of fusion and crystallization and heat of reaction. Only small amount of specimen (5mg - 40mg) is required for each run. Modulated temperature DSC (MTDSC) was developed to increase the sensitivity for polymer transitions. The simultaneous measurement of the amplitude (modulus) of the complex heat capacity, the heat flow and the phase angle between heat flow and heating rate (heat flow phase) enables a more detailed study of complicated materials systems, both in quasi-isothermal and non-isothermal conditions. In other thermal analysis techniques that use an oscillating excitation of the materials, dynamic mechanical analysis, dielectric thermal analysis and dynamic rheometry, for example, a phase angle is defined between the modulated input and the resulting output signal. MDSC can help to characterize the reaction of thermosetting materials and facilitate the cure dynamic study of PU nanocomposites.

3.6.4 FTIR

Infrared spectroscopy is one of the most important analytical techniques that can identify the composition of matter. The most significant advantage of infrared spectroscopy is that it can study states of the substance. Solid surface, solutions, liquids, pastes, powders, films, gases and other states can be examined through appropriate sampling techniques and many samples that hard to be examined before can be studied now because of the development of technology. The instrument for this

experiment is Fourier-transform infrared (FTIR) spectroscopy. It is an advance instrument that quality of infrared spectra is improved and the time of obtaining the data is minimized as well. The principle for Infrared spectroscopy to identify different substance is identifying the vibrations of the atoms of a molecule. In term of polymer, infrared spectroscopy examines different groups according to the six different vibration of the atomic bonding. The peak, which stands for the energy absorbed, in an infrared absorption spectrum corresponds to the frequency of a vibration of specific part of a sample molecule [17]. Some specific interactions (hydrogen bonding and chemical reactions) in PU nanocomposites can be detected by FTIR. The hydrogen bonding can be detected by the shifting in frequency of the absorption peak for the hydrogen bonded unit. The reaction kinetics between isocyanate and polyol can be identified via monitoring the peak of NCO group because the peak of NCO in the FTIR spectrum shrinks due to the reaction between NCO group and OH group.

3.6.5 SEM

SEM is a frequently used technique to characterize the surface of materials. When the electron beam hit the specimen, secondary electrons are produced from the release of valance electrons from the atom of the specimen [18]. The secondary electrons are detected and amplified to form image. The energy of the secondary electrons is very weak and, therefore, only the electrons generated from the surface can be detected clearly. Hence, SEM is a surface-specific technique. The accelerating voltage ranges from 1kV to 40kV. A low accelerating voltage is recommended to observe the surface structure clearly. In addition, high accelerating voltage will melt the polymer which results damaged surface. The sample for SEM should be conductive so that the electrons can pass through the sample stage without causing charging which leads to distorted image. A thin conductive layer (gold or platinum) is usually deposited onto the surface of the polymeric sample. In order to increase the contrast, staining and etching process may be adopted. For the observation of the cross-section of the

sample, cutting by ultramicrotome or razor blade can be used for soft materials. In terms of hard materials, the cross section is prepared via fracturing and freeze fracture if adopted for the materials soft at room temperature but hard at low temperature. Compared to TEM, the resolution is lower but the detail of the surface is clearer. With the aid of SEM, the surface finish and the surface morphology of the coatings can be evaluated with ease.

3.6.6 TEM

TEM is one of the major techniques to characterize nanofillers. Electron beam is employed and high resolution down to 0.2 nm can be achieved. Smaller morphological details can be obtained compared to SEM and optical microscopy. For polymer blends and nanocomposites, the sample for TEM must be very thin (1-100nm) to allow electron penetration. The sample is usually prepared by ultramicroscopy and diamond or glass blade cutting in cryogenic temperature. In terms of nanofillers characterization, the particle suspension must be dilute. Water and acetone is the most widely used suspension medium because of their very low level of reactivity. Copper grid is used to dip in the suspension and capture the nanofillers for imaging [19]. High degree of vacuum is required for TEM because the quality of image will be distorted with the presence of air [20]. When electron beam passes through the sample, the electrons are either scattered or un-scattered by the nuclei or the electrons of the atom. The intensity distribution of the electrons is shown on the fluorescent screen [20,21]. Low atomic number atoms have limited scattering ability which leads to poor phase contrast TEM image. Owing to the resolution of TEM, graphene sheets can be seen clearly with the aid of TEM. Numerous research papers adopted TEM as the major characterization technique to identify the existence and the layers of graphene [22–26].

3.6.7 Particle size measurement

Particle size measurement can be performed *via* different methods including: chemisorption, X-ray diffraction, electron microscopy, sieving, sedimentation, light scattering and acoustic methods [27]. In this project, the particle sizes of the graphite, graphene and MWCNT will be characterized by Malvern Instruments Mastersizer. The measurement of the machine is based on the laser scattering pattern of the particle. The samples are dispersed in deionised water. The dispersed sample is poured into the sample holding chamber which has a stirrer to keep the particles suspending. During the measurement, the optical bench in the mastersizer captures the actual scattering pattern from the laser scattered by the particle suspension. The optical bench is made up of many detectors which responsible for capturing the scattering light from a particular range of angles. After the scattering pattern, the sizes of the particles can be calculated according to Mie theory. Mie theory is the widely accepted theory that can be used to predict light scattering behaviour of all materials under all conditions. The particle with a defined size have its characteristic scattering pattern [28].

3.6.8 XRD

X-rays are generated whenever a beam of high-speed electrons hit a metal target and this usually happens in a vacuum tube [29,30]. In addition, the metal target is always water cooled to prevent melting because most of the dynamic energy generated by the electrons is converted into heat. Nickel-filtered CuK_α radiation (1.54718 \AA) is generally used in polymer studies [31]. X-ray diffraction is a very effective method to investigate the orderly arrangement of atoms. The information of the arrangement is obtained via the interaction of electromagnetic radiation to interference with structures whilst the sizes of structures compares to the wavelength of the radiation. If the structure is in order, the interferences can be sharpen, and, hence, the radiation can be scattered or diffracted under some specific conditions [29]. The reason why diffraction happens is that there are some certain phase relations between two or more

waves. The definition of a diffracted beam may be a beam which is formed by a large number of scattered rays that can reinforce each another. Therefore, diffraction is a scattering phenomenon which is caused by the cooperation of a large number of atoms without any new interaction between x-rays and atoms appears [30]. Phases identification, orientation of phases, habit plane of interfaces, crystallography of defects, order/disorder information are usually obtained via electron diffraction [32]. There are some essential conditions must be met to let diffraction happens, and Bragg's law describes these conditions. The equation of Bragg's law is: $n\lambda = 2d \sin \theta$, where n is the order of diffraction, λ is the wavelength of the radiation, d is the perpendicular distance between the planes that diffraction occur, and θ is the angle between the incident beam and the plane [30,32]. In this project, XRD was used to evaluate the efficiency of graphene exfoliation. Graphite is the stacking version of graphene sheets. With higher degree of exfoliation, the signature XRD peaks of graphite will become lower.

3.6.9 XPS

XPS is highly sensitive equipment for surface analysis of materials. The chemical structure, surface composition, chemical state and electronic state can be obtained from the XPS spectrum. The principle of XPS is shown in Figure 3.2. The x-ray spectrum can be the intensities of photoelectron *versus* binding energy or kinetic energy. When the sample is bombarded by x-ray, the electrons in the core levels of the atoms will be ejected to form photoelectron. The ejected photoelectrons will be captured and analysed by the electron spectrometer after which the plots of photoelectron intensities versus binding energy can be obtained [33]. According to the equation binding energy (E_{binding}) = $h\nu$ (energy of x-ray photon) – kinetic energy (E_{kinetic}) – ϕ (work function), the binding energy can be obtained and it is the characteristic feature of electrons ejected from a certain energy level. The XPS spectrum can be used to reproduce the electronic structure of an atom accurately. The

electrons ejected without energy loss contribute to the featuring peaks while those with inelastic scattering and energy loss contribute to the back ground of the spectrum [34]. The elements on the surface can be identified easily according to the featuring peaks' position and area in the XPS spectrum.

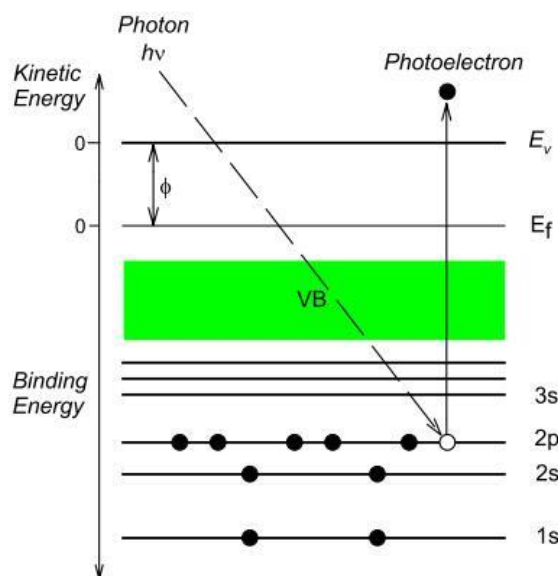


Figure 3.2 Principle of XPS [35]

References

- [1] Zhao W, Fang M, Wu F, Wu H, Wang L, Chen G. Preparation of graphene by exfoliation of graphite using wet ball milling. *J Mater Chem* 2010;20:5817–9.
- [2] Schuetze AP, Lewis W, Brown C, Geerts WJ. A laboratory on the four-point probe technique. *Am J Phys* 2004;72:149.
- [3] Mironov VS, Kim JK, Park M, Lim S, Cho WK. Comparison of electrical conductivity data obtained by four-electrode and four-point probe methods for graphite-based polymer composites. *Polym Test* 2007;26:547–55.
- [4] Swartzendruber LJ. Four-point probe measurement of non-uniformities in semiconductor sheet resistivity. *Solid State Electron* 1964;7:413–22.
- [5] Smits FM. Measurement of sheet resistivities with the four-point probe. *Bell Syst Tech J* 1958;37:711–8.
- [6] Rymaszewski R. Relationship between the correction factor of the four-point probe value and the selection of potential and current electrodes. *J Phys E*

- 1969;2:170–4.
- [7] Yoshimoto S, Murata Y, Kubo K, Tomita K, Motoyoshi K, Kimura T, et al. Four-point probe resistance measurements using PtIr-coated carbon nanotube tips. *Nano Lett* 2007;7:956–9.
- [8] Singh S. Study the temperature dependence of resistance of a semiconductor (four probe method). *Www.sardarsinghsir.com* 2012:2012.
- [9] Macdonald DD. Review of mechanistic analysis by electrochemical impedance spectroscopy. *Electrochim Acta* 1990;35:1509–25.
- [10] Lasia A. Electrochemical impedance spectroscopy and its applications. *Mod Asp Electrochem* 1999;32:143–248.
- [11] Macdonald DD. Reflections on the history of electrochemical impedance spectroscopy. *Electrochim Acta* 2006;51:1376–88.
- [12] Kendig M, Scully J. Basic aspects of electrochemical impedance application for the life prediction of organic coatings on metals. *Corrosion* 1990;41:22–9.
- [13] Zhao M, Wu M, Dong Y. The application of EIS in evaluating anti-corrosion coating. *Oil Gas Storage Transp* 2007;26:39–42.
- [14] Bonora PL, Deflorian F, Fedrizzi L. Electrochemical impedance spectroscopy as a tool for investigating underpaint corrosion. *Electrochim Acta* 1996;41:1073–82.
- [15] Skoog DA, Holler FJ, Nieman TA. Principles of instrumental analysis. 5th ed. Thomson Learningm Inc.; 1997.
- [16] Gallagher PK. Thermoanalytical Instrumentation, Techniques, and methodology. In: Turi EA, editor. *Therm. Charact. Polym. Mater.*, New York ; London : Academic Press; 1997.
- [17] S. Barbara. *Infrared Spectroscopy: Fundamentals and applications, analytical techniques in the science*. John Wiley & Sons; 2004.
- [18] JEOL Ltd. *Scanning electron microscope A To Z - basic knowledge for using the SEM*.

- [19] Williams DB, Carter CB. Transmission electron microscopy: a textbook for materials science. Springer US; 2009.
- [20] Robeson LM. Polymer blends : a comprehensive review. Munich ; Cincinnati: Hanser; 2007.
- [21] Reifer D, Windeit R, Kumpf RJ, Karbach a., Fuchs H. AFM and TEM investigations of polypropylene/polyurethane blends. Thin Solid Films 1995;264:148–52.
- [22] Ferrari AC, Bonaccorso F, Falko V, Novoselov KS, Roche S, Bøggild P, et al. Science and technology roadmap for graphene, related two-dimensional crystals, and hybrid systems. Nanoscale 2014.
- [23] Lee C, Wei X, Li Q, Carpick R, Kysar JW, Hone J. Elastic and frictional properties of graphene. Phys Status Solidi 2009;246:2562–7.
- [24] Meyer JC, Geim AK, Katsnelson MI, Novoselov KS, Booth TJ, Roth S. The structure of suspended graphene sheets. Nature 2007;446:60–3.
- [25] Song M, Cai D. Graphene functionalization : a review. In: Mittal V, editor. Polym. Nanocomposites, Royal Society of Chemistry; 2012, p. 1–51.
- [26] Wu T-T, Ting J-M. Preparation and characteristics of graphene oxide and its thin films. Surf Coatings Technol 2012:1–5.
- [27] Trunschke A. Particle size measurement 2006;1.
- [28] Malvern Instruments Ltd. Mastersizer 2000 User Manual 2007.
- [29] Billmeyer FW. Textbook of polymer science. 3rd ed. New York ; Chichester : Wiley; 1984.
- [30] Cullity BD. Elements of X-ray diffraction. 3rd ed. Upper Saddle River, N.J. : Prentice Hall ; London : Prentice-Hall International; 2001.
- [31] Alexander LE. X-Ray diffraction methods in polymer science. Wiley-Interscience; 1969.
- [32] Dyson DJ. X-ray and electron diffraction studies in materials science. London : Maney for the Institute of Materials, Minerals, and Mining; 2004.

- [33] Hofmann S. Practical surface analysis: state of the art and recent developments in AES, XPS, ISS and SIMS 1986;9:3–20.
- [34] Watts JF, Wolstenholme J. An introduction to surface analysis by XPS and AES. An Introduction to Surface Analysis by XPS and AES. Wiley-VCH; 2003.
- [35] Smart R, McIntyre S, Bello I. X - ray Photoelectron Spectroscopy.

Chapter 4 Graphene Fabrication

4.1. Introduction

Since the discovery of graphene by Geim and Novoselov, it was considered as the miracle materials in this decade which can be applied in every industry. It is considered as the basic element of other carbon allotropes (carbon nanotube, graphite and fullerene etc.) [1]. Defect-free graphene sheet is an ideal 2D single crystal structure which possesses the form of a honeycomb lattice with sp^2 hybridised carbon atoms packed together. The carbon atoms are joined tightly by σ covalent bonds. Each carbon atom in graphene sheet can contribute one unbounded electron to form π bonds above the honeycomb sheet. This unique structure grants graphene with many extraordinary properties especially electrical and thermal conductivity [2]. The properties were summarised in Chapter 2. Graphene based materials are expected to play a key role in several fields such as electronic applications include touch screens, flexible devices, sensor, photonic devices *etc.* In terms of energy area, batteries and supercapacitors are the major applications. During the research of graphene, it was found that the photonic properties were also fascinating which enabled the application in light emitting diodes, ultrafast laser, photodetector and so on [3]. The extraordinary properties only appear in single layer graphene and few layers (<10) graphene. The main obstacle of graphene commercialisation is the advance method to produce cheap graphene based materials.

Numerous methods had been proposed by researchers to prepare graphene which were summarised in Chapter 2. These methods can be classified into two categories: the top-down methods and the bottom-up methods. The top-down methods adopt pristine graphite or other graphite related materials to start with and graphene is produced by trying to reduce the number of layers via different exfoliation methods. In terms of bottom-up methods, the graphene is generally synthesized from various

sources. The dilemma now is how to maintain the properties and performance of graphene upon scaling up as well as reducing the cost of graphene preparation. The quality of graphene is also very important for the future applications. However, the quality of graphene cannot be defined in an absolute term because the requirements of graphene are different according to various applications. For example, the graphene sheets with defects, voids and cavities are more favourable in batteries and supercapacitors applications while the high performance electronic applications require defect free, large area and flat graphene sheets. The development of graphene preparation method is application based [4]. A general route can be proposed: 1. Find out the key properties of the application; 2. Search the suitable methods to prepare graphene; 3. Minimise cost of producing perfect graphene; 4. Scale up. In terms of electrical conductive and anti-corrosion composite coating, graphene sheets act as electrical conductance and the barrier against corrosive substances. Therefore, the graphene sheets used should be defect free and has large lateral size which allows the current pass through the composite coatings. The graphene sheets do not necessary to be large area flat sheet and, hence, exfoliation route is adopted to prepare the graphene for the project.

Simple start-up materials and equipments are the key to minimise the cost. A chemical-mechanical approach was suggested as a suitable method to produce graphene for composite applications. This chemical-mechanical method is also a top-down method. Graphite was used as starting material. Graphene was exfoliated with the aid of melamine. The graphite layers are held together by Van der Waals forces. In order to exfoliate the layers, some chemicals are used to penetrate the gap and expand the layers. Melamine is one of the effective chemical that can assist the exfoliation of graphene [5]. Owing to the high affinity of graphite layers in aminotriazines, melamine can penetrate the gap between graphite layers and expand them [6]. In this method, melamine powder was first mixed with graphite powder in a

certain ratios. Afterward, the mixed powder was poured into a dry ball-milling machine. The strong shear forces created during ball-milling allowed the graphite to be exfoliated initially. Final exfoliation of graphene was achieved by either ultrasonication or mechanical stirring. The melamine in the system was removed by repeated washing of hot water to make sure the prepared graphene was pure. U this method, high quality graphene for composite coating can be produced.

In this chapter, the graphenes produced by modifying the conditions of the chemical-mechanical method was examined. The efficiency of exfoliation and the size and the purity of graphene were evaluated.

4.2. The investigation of the efficiency of the exfoliation method

The experimental procedures are summarised in Chapter 3. Table 4.1 shows the specimens from different exfoliation procedure. The code names used in the discussion below can be referred from Table 4.1.

Table 4.1 Description of the specimens

Code name	Graphite to Melamine Volume Ratio	Ball-milling Revolutions	Exfoliation Method	Exfoliation Time (hours)
A	1:1	1000	Ultrasonic	1
B	1:1	1000	Mechanical	4
C	1:3	1000	Mechanical	4
D	1:3	1000	Ultrasonic	1
E	1:3	1000	Mechanical	1
F	1:3	500	Mechanical	4

4.2.1 XRD analysis

XRD is an effective technique to identify the Figure 4.1 shows the XRD pattern of pristine graphite flakes and the graphene specimens. In can be seen from figure 5.1 (a) that there are two signature peaks of graphite at approximately $2\theta=3^\circ$ and 26° . The strongest signature peak is the one at around 26° and it represents the [002] crystallographic direction of graphite with a theoretical d spacing of 3.354 Å [7]. [002] is the direction of the graphite layers stacking. Although the peak at 26° appears in the XRD patterns of all the specimens, it can still indicate that the graphite have been exfoliated successfully, due to the reduction of intensity. The specimens were prepared without any centrifugation. Therefore, nano-graphite and graphene were co-existed in the specimens. In addition, the exfoliated graphene sheets would be re-stacked together in to [002] direction due to Van der Waals force and the re-stacking resulted in layered structure. The XRD patterns of all the specimens can confirm that the graphite layers were exfoliated.

From Figure 4.1(b), the XRD patterns of specimens A and D have the weakest intensity which means that ultrasonication is the most effective method to exfoliate graphene. The graphite to melamine ratio did not have an obvious effect on the exfoliation efficiency of ultrasonication. Hence, the volume ratio of 1:1 would be sufficient for effective exfoliation in ultrasonication. Excessive melamine may increase the difficulty in the purified stage and cost control. From the figure, specimen C has the highest intensity which means the process is insufficient for graphene exfoliation. It is expected that the prolonged stirring time leads to a more effective exfoliation of graphene. Longer stirring time allows the graphene to be exfoliated completely. However, the obtained results suggest a contrary result when comparing the XRD peaks of specimens C and E. The exfoliation efficiency decreased with higher ball milling revolution as indicated from the results of specimens C and F.

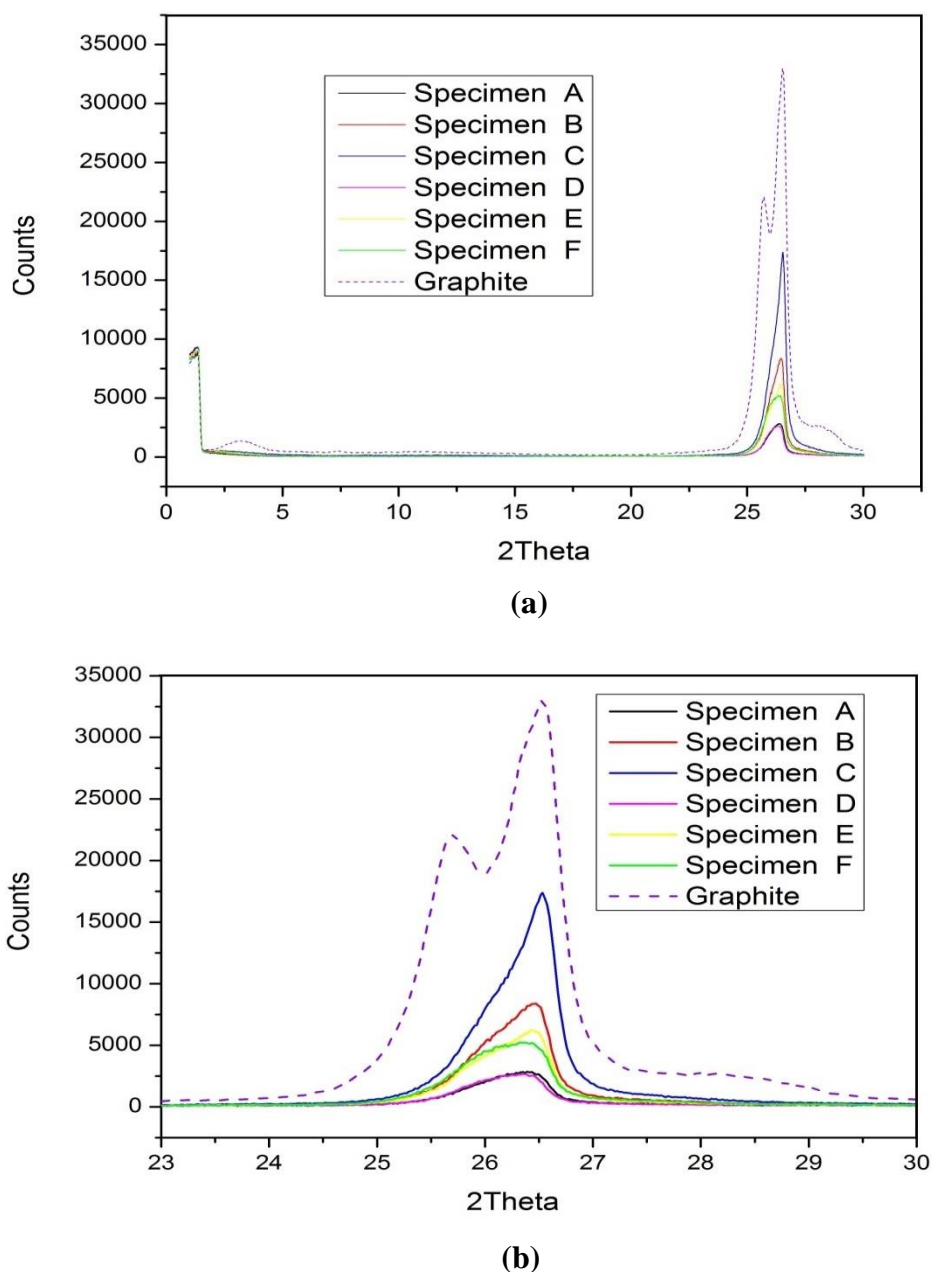


Figure 4.1 XRD spectrum of the specimens and pristine graphite (a) whole scan range (b) 2 θ from 20° to 30°

Therefore, a conclusion can be drawn that longer exfoliation times do not promote the exfoliation of graphene. The experiments were repeated several times and the same conclusion was drawn. As a result, the effect of experimental errors could be minimised. Comparing the results of specimens B and C, excessive melamine had an adverse effect on the efficiency of graphene exfoliation. The possible reason is that the shear force generated from the exfoliation method cannot be transferred to graphite to exfoliate graphene effectively. The excessive melamine may act as lubricant which

weakens the effect of shear force on graphite. The XRD peak intensities of specimens E and F are quite close. A possible reason is that the graphite was underwent a similar extent of exfoliation in these two procedures. Therefore, the number of ball milling revolution has a more profound effect than the time of mechanical stirring as they represent the extent of the graphite is subjected to shear force. Based on the results comparison, an assumption can be made that there is a maximised degree of exfoliation for this mechanical-chemical method.

4.2.2 TEM analysis

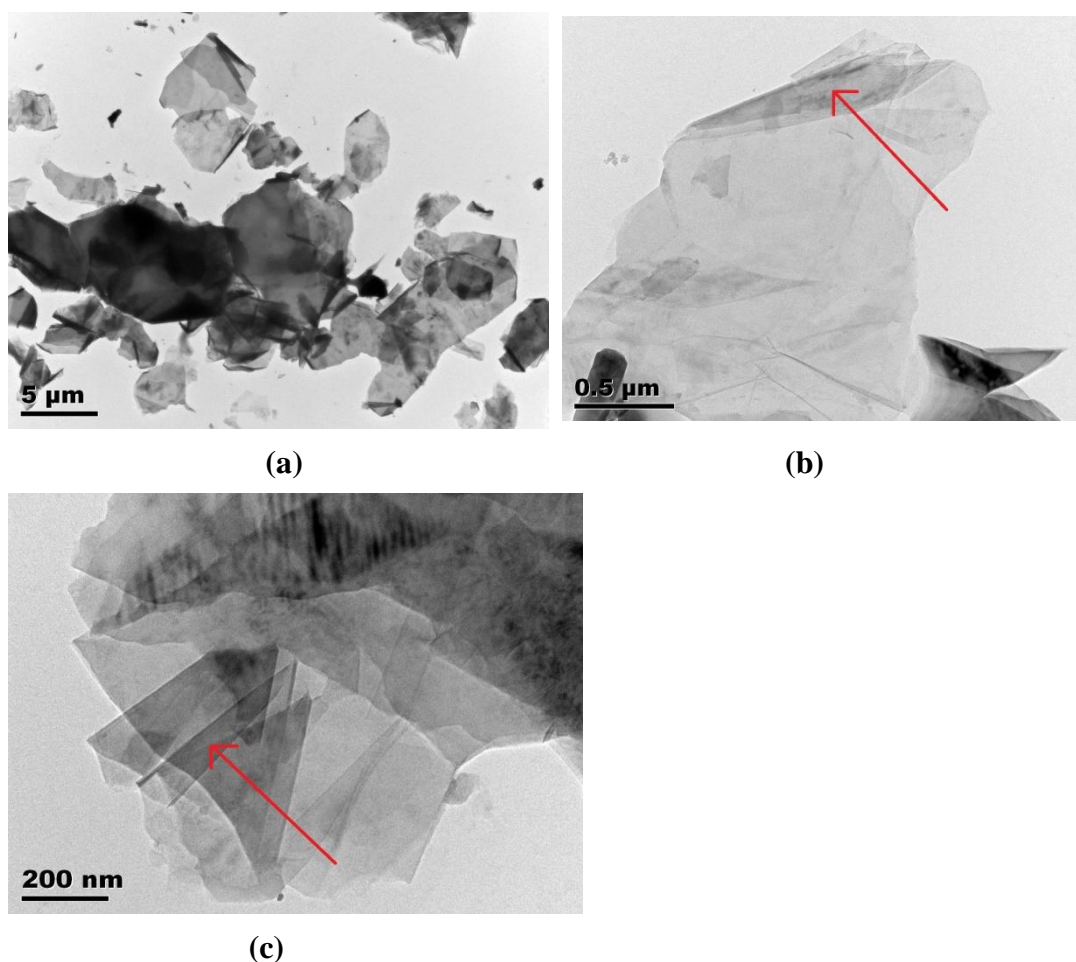


Figure 4.2 TEM images of Specimen A with different scale (a) 0.5 μm (b) 0.5 μm (c) 200nm (red arrow indicates the folded edges in the figures)

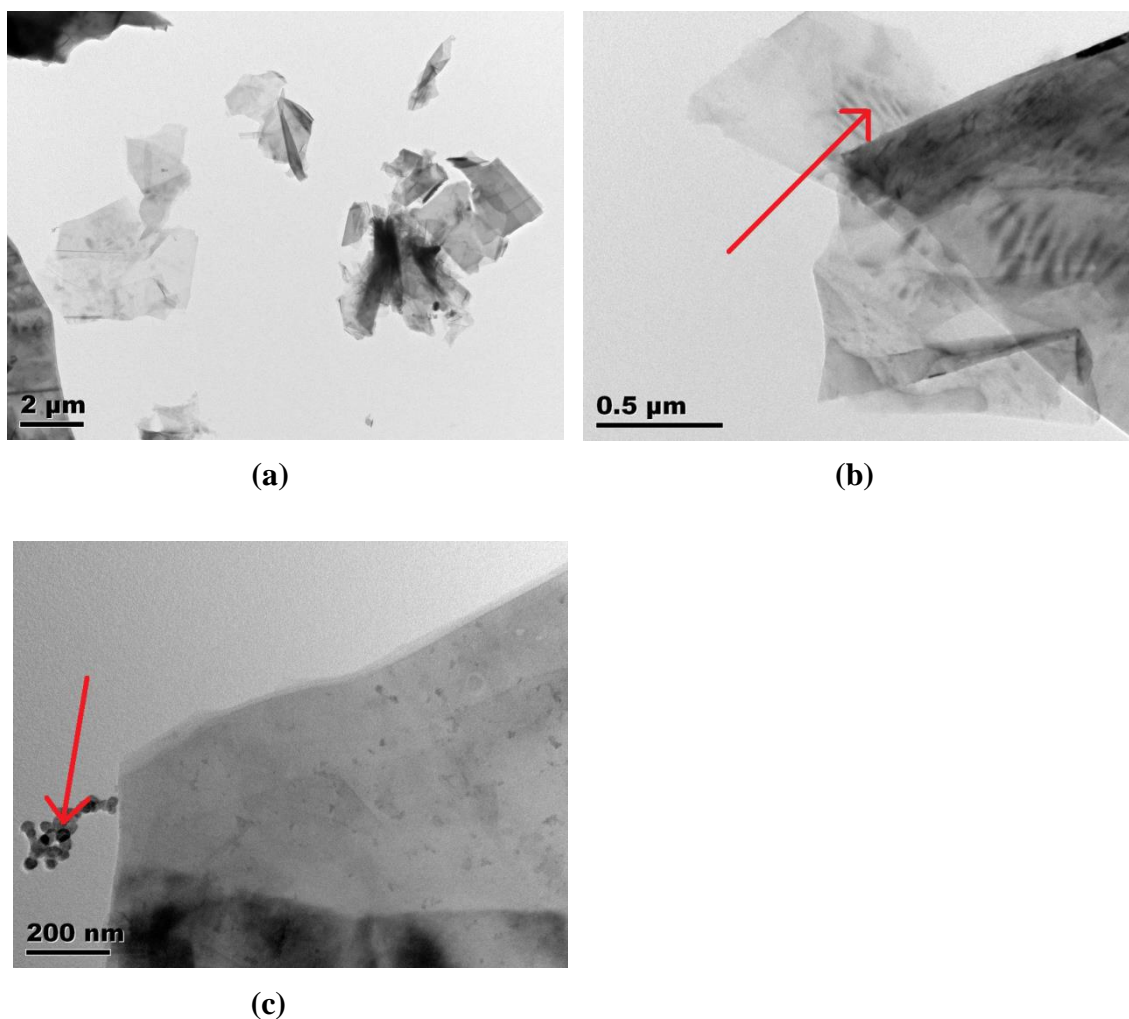


Figure 4.3 TEM images of Specimen F with different scales (a) 2 μm (b) 0.5 μm (red arrow indicates the wrinkles of graphene sheets) (c) 200 nm (red arrow indicates the impurities)

Figure 4.2 and Figure 4.3 are the TEM images of the selected graphene specimens (A and F). These two specimens were selected because they had the lowest and second lowest intensities. Figure 4.2 and figure 4.3 are the low magnification images of specimens A and F showing the overall quality of graphene sheets. It can be seen that the obtained graphene sheets range from one layer to approximately eight layers. The size of the graphene sheets is various ranging from one micron to ten microns. Generally, this method can produce good quality of graphene sheets with large size that suitable for coating applications. It should be noted that while single layer graphene sheets were presented, there were a number of graphene sheets were stacked or overlapped together. The overlapping and re-stacking can partially account for the

peak appears in the XRD patterns of the specimens. Re-stacking or overlapping is not evitable after the drying of specimens. The structure of single-layer graphene ranges from nanometres to microns with the thickness of a single atom and considerably large specific area. Coupling with the strong Van der Waals interactions between the single layers with proximity, the graphene sheets own the tendency of aggregation and re-stacking [8]. The irreversible aggregation or re-stacking generally takes place in dry state. Hence, the re-stacking and aggregation can be regarded as the reverse of the exfoliation process that results in the regaining of the graphitic multi-layer structure, causing the loss in performance [9]. In order to produce graphene based coatings with excellent performance, re-staking and aggregation should be prevented. Considering the compatibility with the current graphene preparation method, the addition of certain spacers would be the most practical method to prevent the aggregation and re-stacking [10]. Platinum nanoparticles can be deposited on the graphene sheets *via* the reduction of chloroplatinic acid to prevent the aggregation of graphene sheets without compromising the electrical properties. This method suggested by Si *et al.* can be compatible with the graphene preparation method readily but the extra cost is a limitation [11]. Carbon nanotubes are another option because they are of a similar nature to graphene and can provide excellent electrical conductivity while preventing aggregation and re-stacking. Cheng and his co-workers adopted ultrasonication in ethanol and vacuum filtration to produce graphene/carbon nanotube film [12]. The carbon nanotubes were positioned between the graphene layers in a direction parallel to the layers. However, this approach increases the complexity and the cost of the current mechanical-chemical approach. Apart from the above two methods, the prepared graphene sheets can be stored in a liquid medium with constant magnetic stirring to keep the suspension uniform. From the discussion above, the mechanical-chemical approach still can be modified to fit in the commercial coating production line.

From Figure 4.2 and Figure 4.3, there are some very small graphene sheets which appear as well. Apart from the original small size graphene sheets, excessive ultrasonication would lead to the size reduction of graphene sheets as pointed out in a previous research [13]. The conclusion that the size of graphene sheets would be broken down by ultrasonication or mechanical stirring is speculated. The solid evident will be provided in the particle sizer analysis. The size of graphene is vital or its physical properties. There is a paper pointed out that the reduction of size led to lower thermal conductivity [14]. The folding of graphene sheets is indicated by red arrows in Figure 4.2 (b) and 4.2 (c). The edge of the graphene sheets had folded back onto the sheet and the folded structure remained. The Van der Waals force helps to stabilize the folded layers against the elastic energies introduced by folding [15]. The folded edges have interesting properties as their structures are similar to carbon nanotube. As indicated by Zhang and his co-workers, the graphene sheets prepared via ultrasonication had the tendency to formed folded structure and they produced folded 10 layers structure via ultrasonication [16]. Their conclusion can explain why so many folded graphene sheets appear in Figure 4.2 (b) and (c).

There are some parallel patterns exist in some of the graphene sheets as shown in Figure 4.3 (b). These parallel patterns may be created by the crumpling of graphene sheets in the direction perpendicular to the surface of the sheets. The wrinkles existed on graphene sheets were widely reported. The formation of wrinkles relates to the natural instability of graphene where thermal fluctuations cause the 2D structure to crumple in 3D structure [17]. This phenomenon is normally seen in the graphene sheets prepared by CVD where the graphene sheets are transferred to another substrate. The thermal stress and the thermal expansion coefficient difference between graphene and metal substrates lead to the formation of wrinkles on the entire film [18]. In terms of mechanical stirring and ultrasonication, wrinkles only exist in some graphene sheets because graphene sheet is very soft and it has the tendency to form

wrinkles due to edge instability and strain induced formation [19]. The presence of wrinkles can affect the electrical, optical, mechanical and chemical properties of graphene [19,20]. How to control wrinkles effectively is still needed to study extensively but some level of control is possible. Reducing the temperature is a way to stabilise the graphene sheets and reduce the wrinkles [20]. In addition, increasing the layer number can restrain the graphene sheets to hinder the formation of wrinkles. However, this approach is detrimental to the properties of graphene and the final composite coatings. Reducing the temperature during graphene preparation is more compatible to the current mechanical-chemical approach. The graphene sheets produced can be dried *via* other drying methods such as freeze drying to reduce the temperature during drying. Ice bath or water bath can be applied during ultrasonication to reduce the heat generated.

There some unknown particles in the specimen as indicated by a red arrow in Figure 4.3 (c). Despite of the contamination induced during preparation, the presence of residue melamine added during the ball milling is also possible. Although hot water was used to wash the graphene, there is a very small amount of melamine still remains in the specimen. The purity of the specimen would be investigated by FTIR and XPS.

4.2.3 Particle size analysis

The particle size of the original graphite ranges from 400 to 700 microns as indicated by the description of the product. Table 4.2, Figure 4.4 and Figure 4.5 show the results of the specimens from particle sizer. Both figures suggest that the specimens exfoliated by ultrasonication had smaller particle sizes. This means ultrasonication can break down the particles effectively. Comparing the results of specimens A and D, the specimen with higher graphite to melamine ratio had smaller particle size and narrower particle size distribution. Hence, the addition of melamine helps to break down the particle as well. This assumption can be further confirmed by the results of specimens B and C. However, the reduction of particle size is not good for the

improvement of electrical conductivity. Therefore, 1:1 graphite to melamine ratio is more favourable. Comparing the results of the specimens produced by mechanical stirring, the mechanical stirring step does not have much effect on breaking down the particles and larger particle size (aggregate or agglomerate) is even resulted in longer mechanical stirring time. Therefore, mechanical stirring is not effective to break down the particle and might be a good way to disperse the graphene sheets in coatings. In terms of uniformity, the specimens produced by mechanical stirring have better uniformity as the shear force generated by ultrasonication is fiercer.

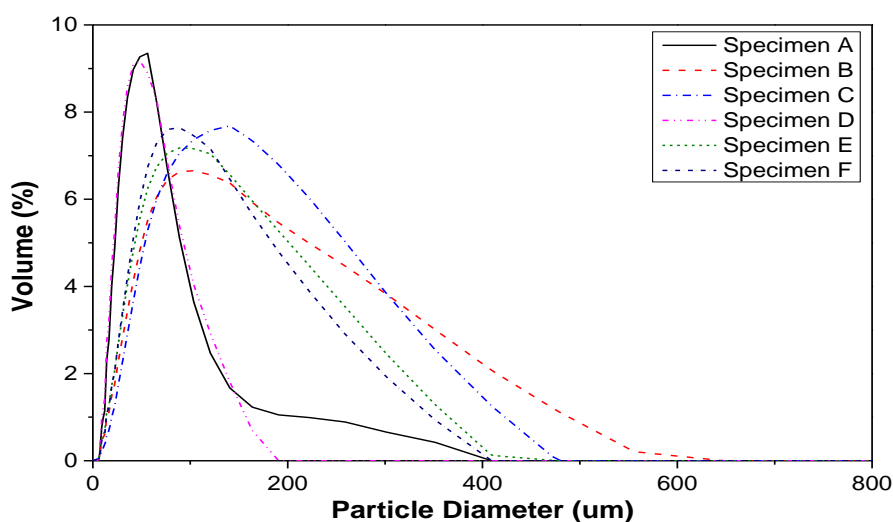


Figure 4.4 Plot of volume base particle size distribution of different

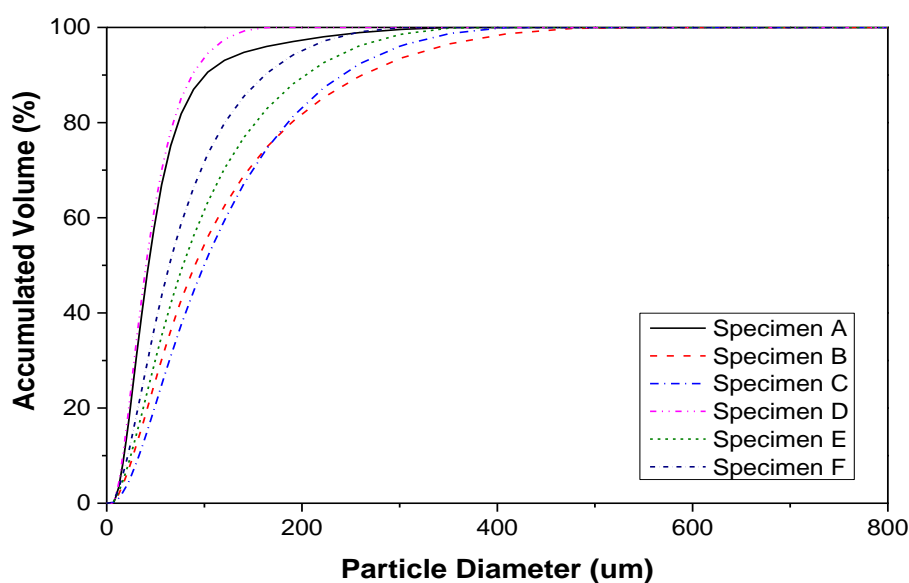


Figure 4.5 Plot of accumulated volume *versus* particle diameter of different specimens

Table 4.2 Summary of the particle size distribution of the specimens

	D(v,0.1)^a (μm)	D(v,0.5) ^a (μm)	D(v,0.9)^a (μm)	D[4,3]^b (μm)	D[3,2]^c (μm)	Uniformity
Specimen A	17.17	42.63	100.49	55.11	33.85	0.668
Specimen B	27.03	90.29	261.32	119.99	57.94	0.786
Specimen C	33.05	99.59	233.95	119.95	66.48	0.638
Specimen D	16.56	40.13	87.40	46.90	31.58	0.545
Specimen E	24.62	78.03	202.64	97.63	50.92	0.695
Specimen F	25.07	74.53	188.46	92.50	50.78	0.669

a: D (v, 0.1/0.5/0.9) is the size of particle at which 10%/50%/90% of the sample is smaller than this size;

b: D [4, 3] is the volume mean diameter;

c: D [3, 2] is the surface area mean diameter.

4.2.4 XPS analysis

Figure 4.6 shows an example survey XPS spectrum of the specimens and the relative amount of elements from the survey scan was summarised in Table 4.3. The elements existed on the surface of the specimens were examined. Apart from the carbon elements, there are a lot of other elements presented in the specimens. The other element may be resulted from residue melamine and contamination.

Small amounts of silicon were found in every specimen and the presence of silicon might relate to the ball milling process. The ball mill jars or balls for ball milling are usually ceramic components that contain silicon. Although they have excellent hardness and abrasion resistance, wearing of the components is inevitable. Therefore,

there may be contamination from the equipment that contains silicon. There are considerable amount of oxygen exist in every specimens. There are several sources of the oxygen impurity: 1. the vapour absorbed by the specimens; 2. the contamination from ball milling process (*e.g.* SiO_2); 3. the oxygen in the atmosphere; 4. the potential oxidation of the graphene specimens. Graphite can be oxidized by strong oxidative chemicals such as the production of graphite oxide *via* Hummer's method. The produced graphite oxide can be exfoliated and reduced to form graphene [21]. However, the oxidation of graphite is not likely in the mechanical-chemical approach because the chemicals used were not aggressive. It has been reported that the graphene sheets less than 3-layers would be oxidized heavily at the temperature higher than $200\text{ }^\circ\text{C}$ [22]. The highest temperature involved with the approach was lower than $100\text{ }^\circ\text{C}$. There was no oxidation took place theoretically. However, a high resolution scan of carbon elements was performed on the specimens to find out whether any oxidation occurred during preparation.

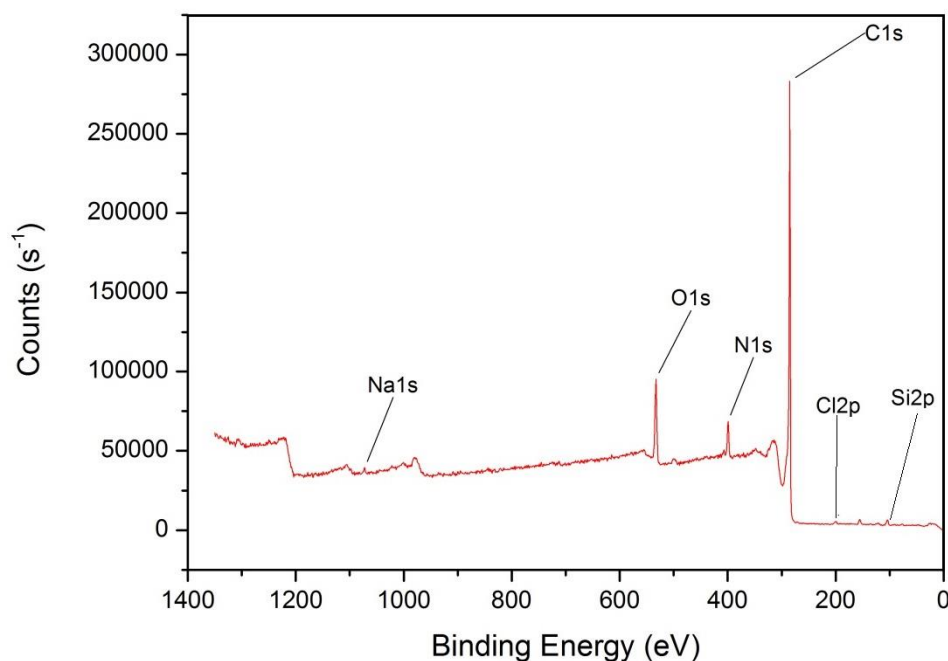


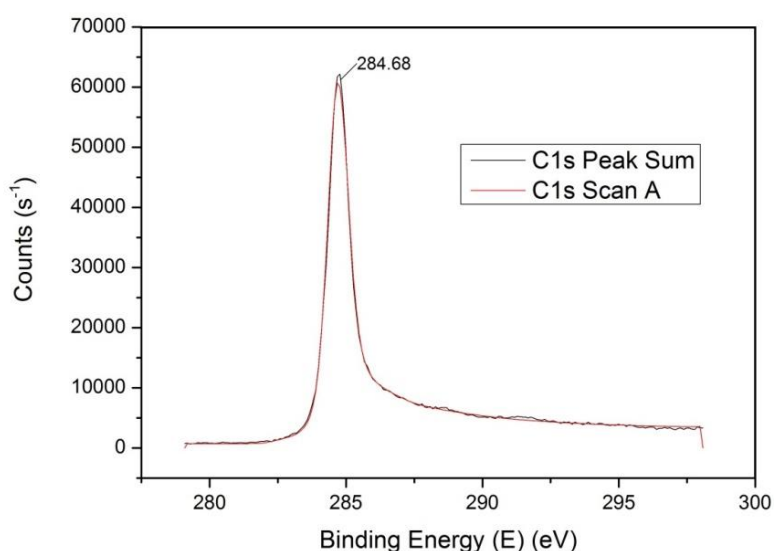
Figure 4.6 Survey scan XPS spectrum of specimen A

Table 4.3 The summary of relative elements atomic ratio of different specimens

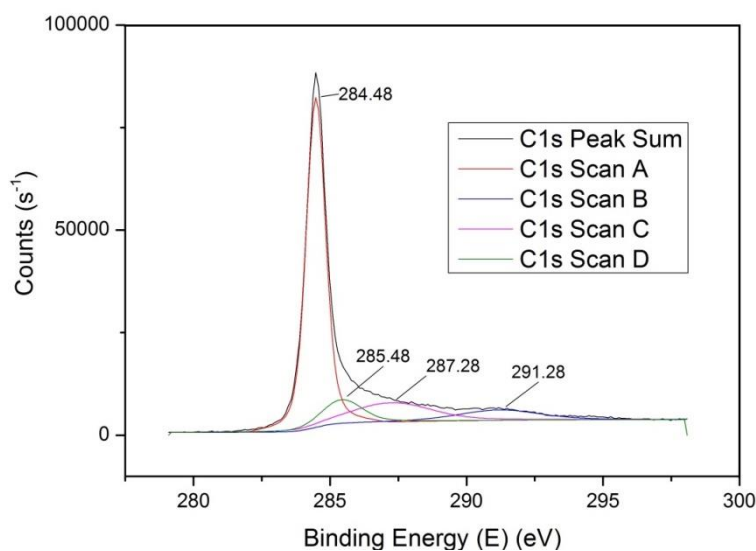
Elements	Atomic ratio (%) for each specimen					
	A	B	C	D	E	F
C	84.33	77.32	81.34	73.55	80.08	83.14
O	8.77	12.11	9.55	12.21	9.62	10.72
N	4.5	6.95	5.93	8.97	6.39	2.59
Si	1.77	2.65	1.3	1.59	1.44	1.4
Na	0.28	0.46	0.18	0.3	0.23	-
Cl	0.35	0.51	0.37	0.5	0.52	0.73
Ca	-	-	0.53	1.15	0.76	0.65
Mg	-	-	0.55	1.34	0.96	0.54
S	-	-	-	0.38	-	-
P	-	-	0.24	-	-	-
Zn	-	-	-	-	-	0.24

The amount of nitrogen in the specimens ranges from 2.59% to 8.97%. Some researchers pointed out that graphene could absorb nitrogen into the graphitic lattice and the only 2 wt% nitrogen could be absorbed in maximum [23]. The amounts of nitrogen presented in specimens were higher than the maximum absorbed value. Taking the nitrogen in the atmosphere into consideration, it is still impossible for the nitrogen element occupies such a high portion of atomic ratio in the specimens. According the TEM results, there were some small particles present in the specimens. As a result, it was highly likely that residual melamine could account for the nitrogen element in the specimens. FTIR was used to further confirm this assumption. Small amounts of metallic elements such as calcium and magnesium were identified in some specimens. These elements are likely to be in the form of chloride salt as chlorine present in every specimen. Calcium chloride and magnesium chloride are commonly found in water. The water used to prepare graphene was tap water because it was

more cost effective. Therefore, the chloride compounds may come from the water itself, the equipment to boil the water and the water containers. Calcium and magnesium ions only appeared in the specimens with higher graphite to melamine ratio because the specimens were washed more times by the boiling water. The source of phosphorous, zinc and sulfur may be environmental contamination.



(a)



(b)

Figure 4.7 C1s XPS spectrum of (a) specimen A and (b) specimen B from high resolution scan

The specimens prepared from ultrasonication and mechanical stirring were selected for carbon element high resolution scan (Figure 4.7). From Figure 4.7 (b), there is only one peak presented in the spectrum and no splitting peaks were detected during

the scan. From Figure 4.7 (a), the peak can be split into four peaks with the binding energy of 284eV, 285eV, 287eV, and 291eV. Although there are four peaks presented in the spectrum of specimen A, the shape of the XPS spectra of specimens A and B are quite similar. This indicates that the specimens were identical in the aspect of electronic state. Apart from the peak at 284eV, the other three peaks in the spectrum of specimen A has very low intensity which mean their contribution to the spectrum is limited. Therefore, the presence of the correspondence bonds is limited as well. The binding energy of the peak around 284.6eV represents the carbon atoms in non-oxidised state which are the carbon atoms in the lattice of graphene [24,25]. The peak at 285eV reveals the presence of C-N bonds which indicates that melamine remains in the specimen. The peak with a binding energy of 287eV stands for the C-O bonds which is an indication of oxidation. The forth peak at 291eV is the sp^2 hybridised carbons in the π to π^* configuration.

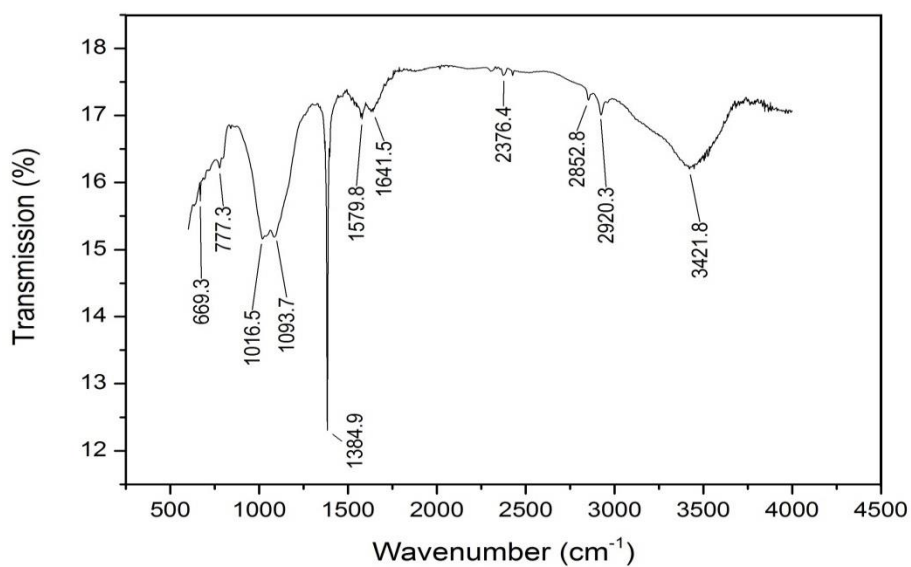
As the contribution of the peaks from 285eV, 287eV and 291eV is very small, they even could not be detected in other specimens because their signals were very weak. Therefore, the graphene specimens were generally pure. However, the existence of oxidation would make the carbon atoms in the graphene sheet to change from sp^2 hybridised to sp^3 hybridised. There sp^3 hybridised carbon atoms would cause disturbance of the carrier transport, forcing carriers to hop over the sp^3 sites instead of near ballistic transport [26]. As a result, the conductivity would be weakened. During the preparation, no oxidising reagents were added. The oxidation might possibly take place during the drying process as the specimens were dried for a long time under 80 °C to remove the moisture completely. The temperature was quite high which might lead to limited level of oxidation. Considering the oxidation and the reduction of wrinkles, freeze drying maybe a suitable method to dry the graphene.

4.2.5 FTIR analysis

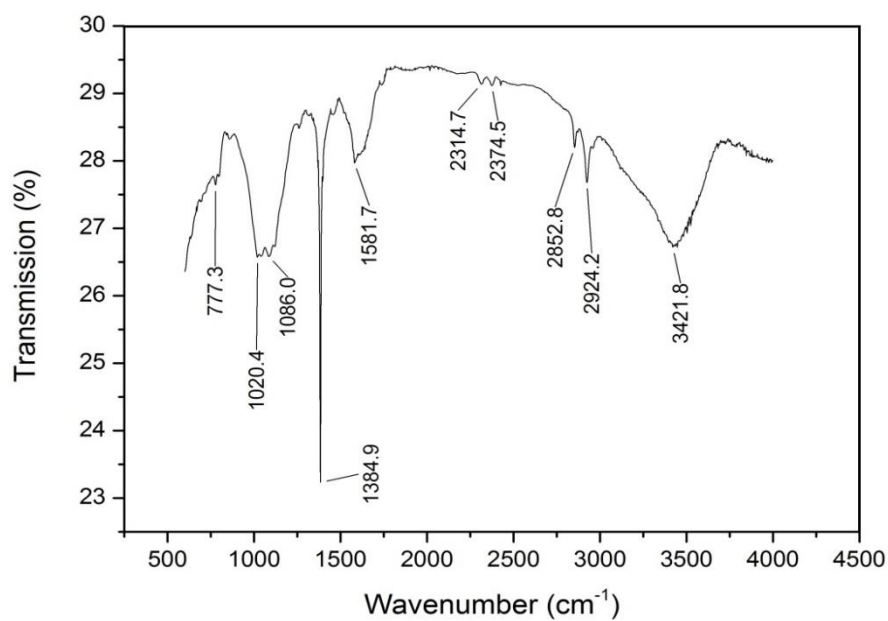
The example FTIR spectra of the specimens are shown in Figure 4.8. The main peaks appeared in the spectra are similar in the spectrum of every specimen. Therefore, the spectrums of specimens A and B were selected as the examples for discussion. Although the peaks' positions of the specimens are the same generally, the intensities of the peaks vary despite the curves were generalised. This might be caused by the operator errors during FTIR sample preparation. The dark powder has a relatively low transmittance for visible light and intra-red which induce the difficulties of sample preparation. Minimum amount of graphene powder was mixed with KBr powder to produce a sample disk. Owing to the nature of graphene powder, it was difficult to fully ground the graphene and create complete homogeneous mixtures with KBr. Therefore, the inhomogeneous nature of all the specimens caused the intensity variation and the noise in the spectrums.

The peaks of the FTIR spectra were analysed and identified *via* a FTIR database [27,28]. A broad peak around 3420.1 cm^{-1} appeared both in Figure 4.8(a) and (b) and it was identified as the characteristic peak of -OH stretching which came from the moisture in the atmosphere or the absorbed water in the sample. The peak in 1641 cm^{-1} also indicated the presence of water as seen in Figure 4.8 (a). The three peaks around 669 cm^{-1} , 2314 cm^{-1} and 2374 cm^{-1} were represented the carbon dioxide fluctuation in the air. The C-C skeleton vibrations of the graphene carbon rings could be identified via the peak around 1580 cm^{-1} . The evident of possible oxidation was found in the peaks around 1020 cm^{-1} and 1060 cm^{-1} as they represented C-O vibrations. The twin peaks identified at 2852 cm^{-1} and 2924 cm^{-1} stood for the stretching of -CH . The trace of residue melamine was spotted in the sample with the peaks around 1385 cm^{-1} and 777 cm^{-1} . The FTIR results well correspond to the XPS results and TEM results regarding the presence of oxidation and residual melamine. Melamine was not completely removed from the specimens. The residue melamine is most likely to be

absorbed by the graphene sheets. The presence of impurities may affect the performance in electrical properties.



(a)



(b)

Figure 4.8 FTIR spectra of (a) specimen A and (b) specimen B

The graphene was a honeycomb structure made up of sp^2 hybridised carbon atoms with one free electron to form π bonds above and below the graphene plane. Therefore, the existence of $-CH$ peaks in the FTIR results was unusual. There was no contamination and chemical used during the preparation had C-H bond. Considering the structure of graphene, the C-H bonds may come from the edge of graphene. There are two kinds of edge configuration with different electronic and magnetic properties, the armchair and zigzag (Figure 4.9) [29]. At the edge of the graphene sheet, the carbon atoms of both configurations only have two C-C bonds. Therefore, there are two free electrons in the carbon atoms. One of the free electrons contributes to the π bonds above or below the graphene layer while the other forms C-H bond. The carrier mobility and the electrical properties of graphene will be deteriorated potentially with the presence of defects [30,31]. Hence, the amount of the carbon atoms at the edge should be kept in a minimum level. A very straightforward approach is to increase the sheet size of the graphene to reduce the relative amount of the carbon atoms at the

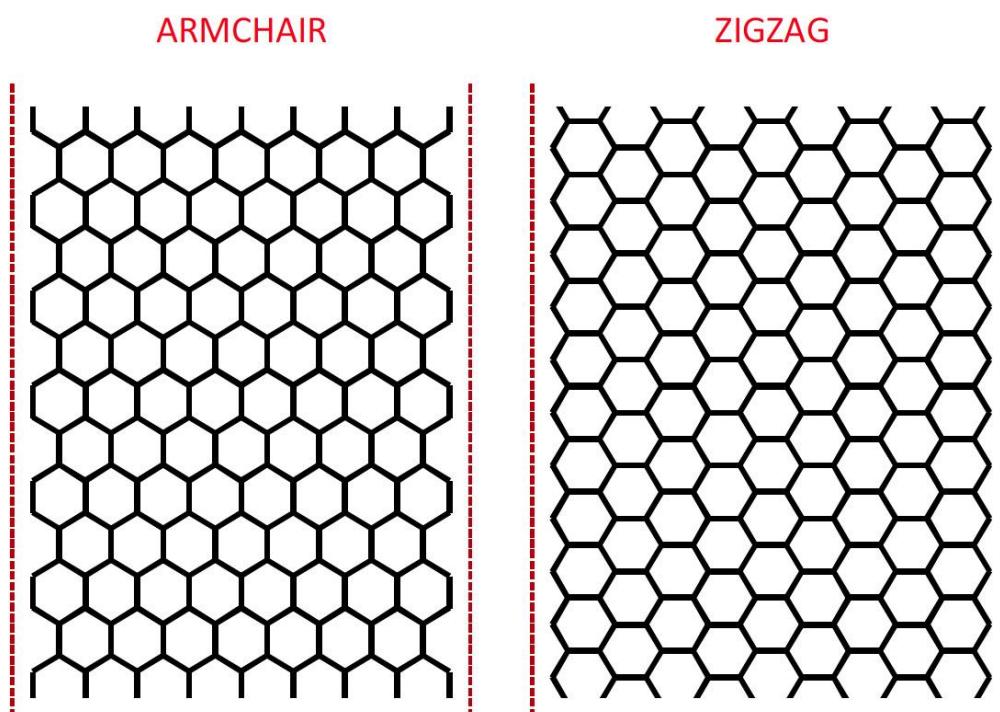


Figure 4.9 The armchair and zigzag configurations of graphene edges [32]

edge. In terms of the mechanical-chemical preparation method, an alternative exfoliated method to produce large size graphene sheets is desired.

4.3 Conclusions

The proposed mechanical-chemical approach to prepare graphene is successful and it is both cost effective and suitable for large scale production. The equipments required are not sophisticated and the procedure does not involve complicated steps. In addition, the raw materials used are not expensive. The most effective exfoliation conditions are: 1:1 graphite to melamine ratios, 1000R ball milling revolutions and 1 hour ultrasonication time. The prepared graphene sheets have 1 to 10 layers, sizing approximately from a few microns to nearly 50 microns. Limited level of oxidation and small amount of residue melamine were identified. Generally, this approach is suitable to produce the graphene sheets for coating applications where the purity is not the priority issue. In addition, the exfoliated graphene in the liquid can be readily mixed with matrix to form composite coatings.

References

- [1] Geim AK, Novoselov KS. The rise of graphene. *Nat Mater* 2007;6:183–91.
- [2] Novoselov KS, Geim AK, Morozov S V., Jiang D, Zhang Y, Dubonos S V., *et al.* Electric field effect in atomically thin carbon films. *Science* (80-) 2004;306:666–9.
- [3] Zhu Y, Murali S, Cai W, Li X, Suk JW, Potts JR, *et al.* Graphene and graphene oxide: synthesis, properties, and applications. *Adv Mater* 2010;22:3906–24.
- [4] Ferrari AC, Bonaccorso F, Falko V, Novoselov KS, Roche S, Bøggild P, *et al.* Science and technology roadmap for graphene, related two-dimensional crystals, and hybrid systems. *Nanoscale* 2014;7:4598–810.
- [5] Zhao W, Fang M, Wu F, Wu H, Wang L, Chen G. Preparation of graphene by exfoliation of graphite using wet ball milling. *J Mater Chem* 2010;20:5817–9.

- [6] WUEST J., ROCHEFORT A. Strong adsorption of aminotriazines on graphene. *Chem Commun* 2010;46:2923–5.
- [7] Mindat.org - the mineral and locality database. Graphite n.d.:1.
- [8] Shen J, Hu Y, Li C, Qin C, Ye M. Synthesis of amphiphilic graphene nanoplatelets. *Small* 2009;5:82–5.
- [9] El-Kady MF, Strong V, Dubin S, Richard BK. Laser scribing of high-performance and flexible graphene-based electrochemical capacitors. *Science* (80) 2012;335:1326–30.
- [10] Li J, Östling M. Prevention of graphene restacking for performance boost of supercapacitors—a review. *Crystals* 2013;3:163–90.
- [11] Si Y, Samulski ET. Exfoliated graphene separated by platinum nanoparticles. *Chem Mater* 2008;20:6792–7.
- [12] Cheng Q, Tang J, Ma J, Zhang H, Shinya N, Qin L-C. Graphene and carbon nanotube composite electrodes for supercapacitors with ultra-high energy density. *Phys Chem Chem Phys* 2011;13:17615–24.
- [13] Hernandez Y, Nicolosi V, Lotya M, Blighe FM, Sun Z, De S, et al. High-yield production of graphene by liquid-phase exfoliation of graphite. *Nat Nanotechnol* 2008;3:563–8.
- [14] Cao H, Guo Z, Xiang H, Gong X. Layer and size dependence of thermal conductivity in multilayer graphene nanoribbons. *Phys Lett A* 2011;376:525–8.
- [15] Rotkin S, Gogotsi Y. Analysis of non-planar graphitic structures: from arched edge planes of graphite crystals to nanotubes. *Mater Res Innov* 2002;5:191–200.
- [16] Zhang J, Xiao J, Meng X, Monroe C, Huang Y, Zuo J-M. Free folding of suspended graphene sheets by random mechanical stimulation. *Phys Rev Lett* 2010;104.
- [17] Fasolino A, Los JH, Katsnelson MI. Intrinsic ripples in graphene. *Nat Mater* 2007;6:858–61.

- [18] Liu N, Pan Z, Fu L, Zhang C, Dai B, Liu Z. The origin of wrinkles on transferred graphene. *Nano Res* 2011;4:996–1004.
- [19] Deng S, Berry V. Wrinkled, rippled and crumpled graphene: an overview of formation mechanism, electronic properties, and applications. *Mater Today* 2015;00.
- [20] Katsnelson MI, Geim AK. Electron scattering on microscopic corrugations in graphene. *Philos Trans R Soc A* 2008;366:195–204.
- [21] Hummers Jr WS, Offeman RE. Preparation of graphitic oxide. *J Am Chem Soc* 1958;80:1339–1339.
- [22] Liu L, Ryu S, Tomasik MR, Stolyarova E, Jung N, Hybertsen MS, et al. Graphene oxidation: thickness-dependent etching and strong chemical doping. *NANO Lett* 2008;8:1965–70.
- [23] Araujo PT, Terrones M, Dresselhaus MS. Defects and impurities in graphene-like materials. *Mater Today* 2012;15:98–109.
- [24] Vadahanambi S, Jung JH, Oh IK. Microwave syntheses of graphene and graphene decorated with metal nanoparticles. *Carbon N Y* 2011;49:4449–57.
- [25] Naumkin A V., Kraut-Vass A, Gaarenstroom SW, Powell CJ. NIST X-ray Photoelectron Spectroscopy Database. Meas Serv Div Natl Inst Stand Technol Mater Meas Lab
- [26] Bagri A, Mattevi C, Acik M, Chabal YJ, Chhowalla M, Shenoy VB. Structural evolution during the reduction of chemically derived graphene oxide. *Nat Chem* 2010;2:581–7.
- [27] Zhao Y, Zhan L, Tian J, Nie S, Ning Z. Enhanced electrocatalytic oxidation of methanol on Pd/polypyrrole-graphene in alkaline medium. *Electrochim Acta* 2011;56:1967–72.
- [28] National Institute of Advanced Industrial Science and Technology (AIST) J. Spectral Database for Organic Compounds (SDBS)
- [29] Tian J, Cao H, Wu W, Yu Q, Chen YP. Direct Imaging of Graphene Edges:

- Atomic Structure and Electronic Scattering. *Nano Lett* 2011;11:3663–8.
- [30] Terrones M, Botello-Mendez, R. A, Campos-Delgad J, Lepez-Ureas F, Vega-Cantu, et al. Graphene and graphite nanoribbons: Morphology, properties, synthesis, defects and applications. *Nano Today* 2010;5:351–72.
- [31] Ritter KA, Lyding JW. The influence of edge structure on the electronic properties of graphene quantum dots and nanoribbons. *Nat Mater* 2009;8:235–42.
- [32] Koester SJ. UltrasMOOTH Graphene Nanoribbon Formation Using Templated Nanoparticle Crystallographic Etching. Univ Minnesota 2011.

Chapter 5 Carbon based coatings on steel with improved electrical conductivity

5.1 Introduction

Steel, an alloy of iron and other elements, is a very important and widely applied material in industry. Various in composition and forms, steel have been applied in many different applications such as automotive shell, supporting column and tableware [1]. It is also an important material that is widely utilized in energy storage applications such as interconnect for solid-oxide fuel cells (SOFC) [2] and bipolar plate for proton exchange membrane fuel cells [3]. For energy storage applications, the electrical conductivity and corrosion resistance of the working environment of the major components are the essential properties. Although some types of steel have good electrical conductivity, their electrical conductivities are still not high enough and they do not possess excellent anti-corrosion properties for the long-term durability of the energy storage device. Hence, different coating systems have been adopted to improve the performance of the steel based components in energy storage applications. For example, polymer based coatings [4–7], multilayer coatings [8,9] and ceramic based coatings [2,10,11] were used as electrical conductivity and corrosion resistant enhancers on steel surface for energy storage applications. However, although the improvement was promising, there is still a long way to go from small scale lab production to large scale commercialisation. Therefore, seeking of new materials and new technologies are still crucial for the future development.

Graphene, a new era material, has many extraordinary properties such as high tensile strength [12], high electrical conductivity [12–14] and barrier properties [15]. It is a very promising material to be utilized as coating to improve a wide range of properties no matter applied as composite or pristine form [16]. Electrophoresis deposition (EPD) has been received increasing interest due to its simplicity and cost effectiveness. The graphene EPD based materials on steel have been adopted by researchers for various applications such as biocompatible materials [17] and transparent conductive materials [18]. Although all the reported results in the electrical conductivity were promising, only few papers mentioned the adhesion between graphene based materials and the substrates in the literature [19]. Pristine graphene is a pure carbon material and it does not form interactions with steel. Hence, the adhesion between steel and graphene is poor and the coated pristine graphene sheets on steel

can be easily started off after EPD. Without improved adhesion between pristine graphene and steel substrates, the graphene coating layer will not be able to satisfy the requirements for long-term durable coating in energy storage applications.

In this chapter, graphene and graphite were applied on to steel as conductive coating by means of electrophoresis deposition (EPD). A simple method, thermal treatment was initially used to improve the adhesion between pristine graphene or graphite and steel substrates. The effects of EPD conditions and thermal treatment on the electrical conductivity were investigated. The composition and the morphology of the coating surface and the coating-steel interface were also assessed.

5.2 Theories about the oxidation of steel

When steel is exposed to oxidation conditions above 570 °C, a multilayer scale forms

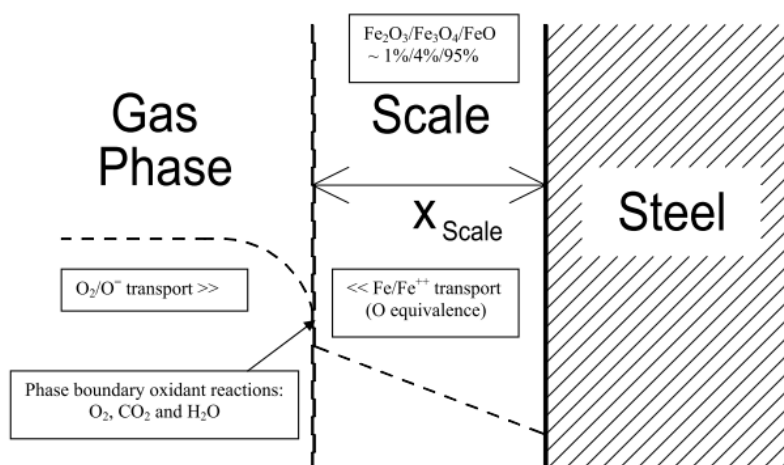


Figure 5.1 the mechanism of high temperature oxidation of steel [20]

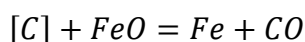
consisting of FeO (wustite), Fe₃O₄ (magnetite) and Fe₂O₃ (hematite) with the wustite layer next to the steel surface and hematite at the gas-scale interface [20]. The mechanism of high temperature oxidation of steel is shown in Figure 5.1. The oxidation mechanism depends on (1) the transport of oxidant gas from the bulk gas phase; (2) phase boundary reaction(s) at the gas - scale interface; or (3) the diffusion of Fe cations to the scale-gas phase interface. If steel oxidation takes place in a reheat furnace, the gas composition temperature, steel surface characteristics and steel composition can be the major factors that affect this process [21–23]. However, according to Poirier *et al.*, the only factor affecting scale habit and intactness is the steel grade, and the stack oxygen and oxygen enrichment levels did not significantly affect these properties [20]. The steel grade was also the most important factor affecting the

adhesion between scale and the steel. The steel grades which contain more Ni, Cu, Cr and/or Mo had a more adherent scale. The microstructure images shown in the literature also indicate that the more adherent samples had a porous scale and/or rough steel-scale interface. The scale also appears to be removed easier with increasing stack oxygen concentrations and the effort for scale removal appears to decrease slightly with increasing oxygen enrichment and sample exposure times. These results indicate that oxygen enrichment has far less effect on the scale properties than the steel grade.

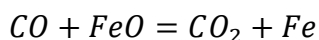
The oxidation behaviour of iron at 570 °C to 700 °C is more complex. The isothermal-oxidation kinetics follows the parabolic law in this temperature range. A detailed study on the effects of sample preparation on oxidation kinetics and scale structure was developed and found that no effect was exhibited at 650 °C, but the effects at 580 and 600 °C were significant. At 580 °C, the scaling rate on the cold-worked sample was much faster than that on the annealed sample [24]. Cold working was introduced by surface polishing. The scale structure developed on the cold-worked sample was uniform in thickness, consisting of a thin surface layer of hematite (about 1/8 of the total thickness), a thick intermediate magnetite layer, and a non-continuous wustite layer at the scale-iron interface. The scale structure developed on the annealed sample at 580 °C was different. Firstly, the thickness varied at different locations. Secondly, the scale was much thinner. Thirdly, the hematite layer was the major component of the scale. At some locations, the hematite layer occupied nearly the entire thickness of the scale. Finally, wustite was not detectable even after oxidation for 20 hours. Increased plastic flow at 650 °C, which took place in the wustite layer primarily, was thought to continually collapse the pores formed during oxidation. Thus, the scale-iron adherence was maintained. In addition, the rapid recrystallization process taking place in the iron substrate at 650 °C would significantly reduce the cold-work effects introduced by mechanical polishing [25]. As in the case of oxidation at 580 °C and 600 °C, the large population of dislocations on the sample surfaces introduced by cold working provided an effective mechanism for vacancy annihilation, thus reducing the tendency of scale-iron separation during oxidation at these temperatures. The magnetite layer developed on cold-worked samples consists of a fine-grain layer forming at the inner region and a coarser columnar-grain layer at the outer region. The fine-grain layer was believed to form via an oxide-dissociation mechanism, associated with void formation at the scale-iron interface and subsequent void migration along grain boundaries through the magnetite layer. The impurity carbon in iron was thought to have assisted in the formation of the fine-grain layer, and

maintaining the adherence between the scale and the iron substrate [26,27].

During steel oxidation, carbon from the steel substrate can be oxidized, causing decarburization of the steel when the rate of carbon oxidation exceeds that of iron. Decarburization is normally observed above 700 °C, particularly for steels containing relatively high levels of carbon [28,29]. Simultaneous scaling and decarburization has been studied, and the general consideration is that during steel oxidation, carbon reacts with the scale via the following reaction [30]:



Where [C] stands for the carbon in solution in steel, further reaction between CO and scale may happen:



These reactions can proceed only when the generated gas can escape through the scale through microchannels such as pores or microcracks [29,31]. If not, the pressure of CO gas would build up and blistering and rupture of scale will be resulted when the pressure exceed a critical value [29]. The carbon-bearing gases generated during steel oxidation can also be transported *via* the outward movement of voids originated at the scale–steel interface [32]. For the temperature lower than 700 °C, the rate of carbon oxidation may be lower than that of iron oxidation. The expelled carbon (still in the steel) due to the more rapid iron oxidation must then either remain at the scale–steel interface or diffuse into the steel, causing enrichment of carbon in the surface layer of the steel substrate. If the enrichment exceeds the solubility of carbon, solid carbon (graphite) may precipitate at the scale–steel interface [33].

For Fe–C alloys containing more than 0.1% of carbon, the effect of carbon on steel oxidation varies at different temperature ranges. Below 570 °C, increased carbon content in steel results in increased oxidation rate, because the scale formed over pearlite (FeC₃+Fe) is finer and the scale is generally more adherent, allowing more rapid iron diffusion through the scale. At 700 °C, higher carbon contents resulted in less adherent scale, lower oxidation rate, and less regular scale structures with more high oxides (hematite and magnetite).

5.3 Carbon based coatings on steel

5.3.1 The surface characteristic and electrical conductivity of the initial heat treated samples

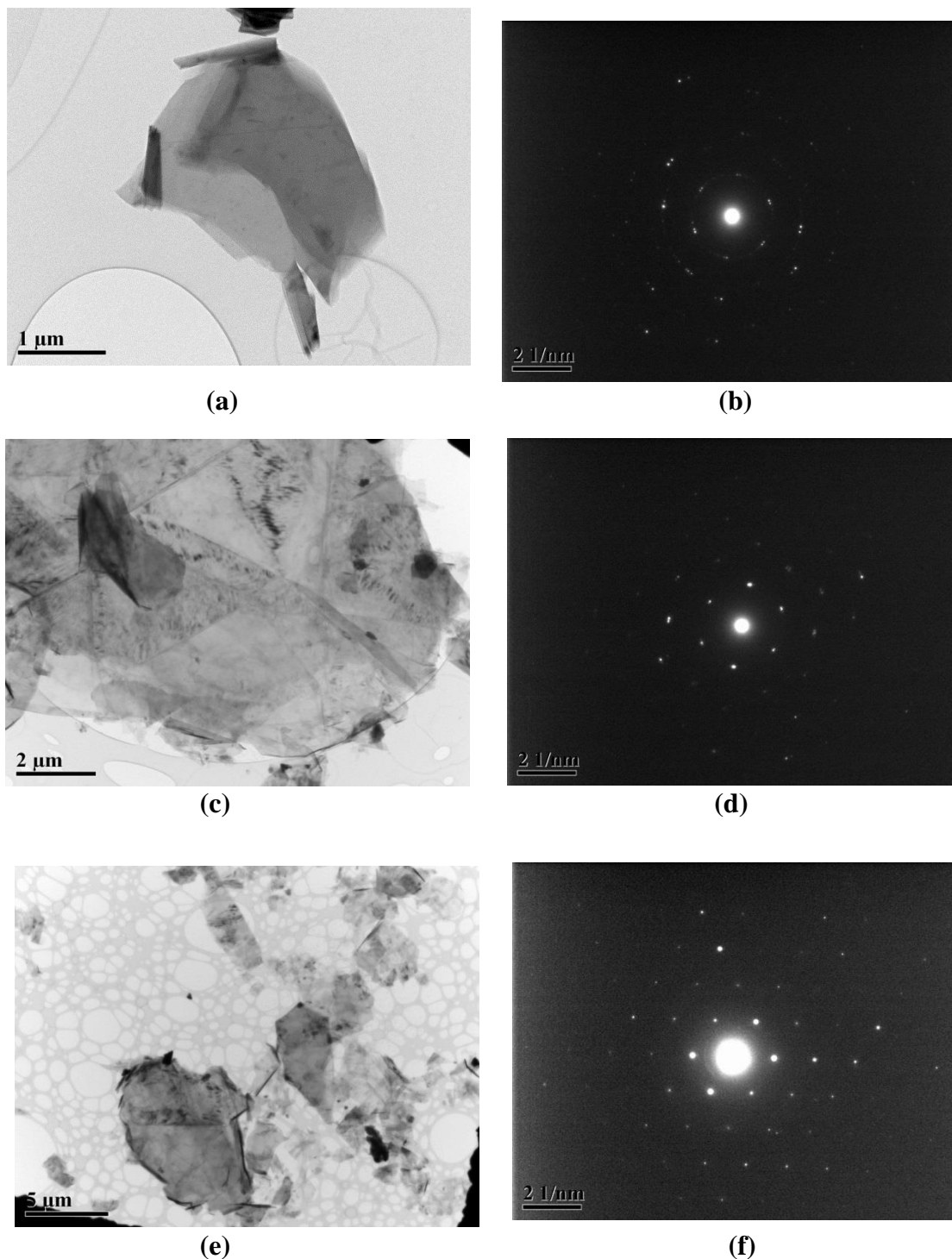


Figure 5.2: (a) TEM image of PP10; (b) X-ray diffraction pattern of the sheet in (a); (c) TEM image of G; (d) X-ray diffraction pattern of the graphene sheet in (c); (e) TEM image of G graphene with smaller magnification; (f) X-ray diffraction of the stacking graphene sheets in (e)

TEM images and diffraction pattern of PP10 graphite and the graphene fabricated from expandable graphite (G) are shown in Figure 5.2. The sampling area of the x-ray diffraction of this TEM is in nano scale. Comparing Figure 5.2 (a) and (c), PP10 has smaller amount of graphene sheets than G and the size of the graphene sheets are smaller as well. Figure 5.2 (e) can further confirm that G has larger amount of graphene sheets with various layers and folding and their size are bigger. In addition, graphite nanoflakes also present in the figure. In the literature, only electron diffraction patterns of graphene sheets with different layers were discussed [34,35]. However, x-ray diffraction pattern and electron diffraction pattern of a substance is similar. The schemes of the electron diffraction pattern of single layer and two layer graphene in literature were redrawn and shown in Figure 5.3. In a diffraction pattern, a triangle is formed around the centre bright spot. For the diffraction pattern of single layer graphene, the two spots in the middle of one side of the triangle have higher intensity than other two spots as indicated by the arrows in Figure 5.3(a). For two layer graphene, the spots in the vertices of the triangle have higher intensity (Figure 2 (b)). The x-ray patterns shown in Figure 5.2 for single layer graphene are similar to the electron diffraction pattern in the literature. As a result, the existence of single layer graphene sheets in PP10 and G can be confirmed. Although G has more graphene sheets, the phenomenon of bigger graphene sheets cover smaller graphene sheets is more serious and this will lead to a ring x-ray diffraction pattern at the stacking site [34,35]. Figure 5.2 (f) indicates that a couple of graphene sheets are stacking at the site. The x-ray pattern will start to grow to be a ring shape if more graphene sheets are stacking in an area.

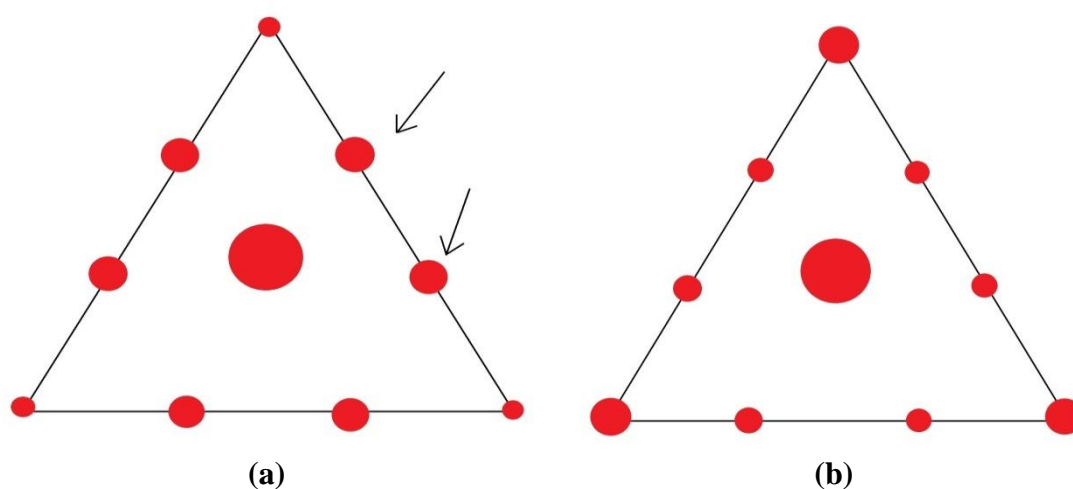


Figure 5.3: Schemes of nanoscale electron diffraction patterns of (a) a single-layer graphene membrane and (b) a two-layer membrane

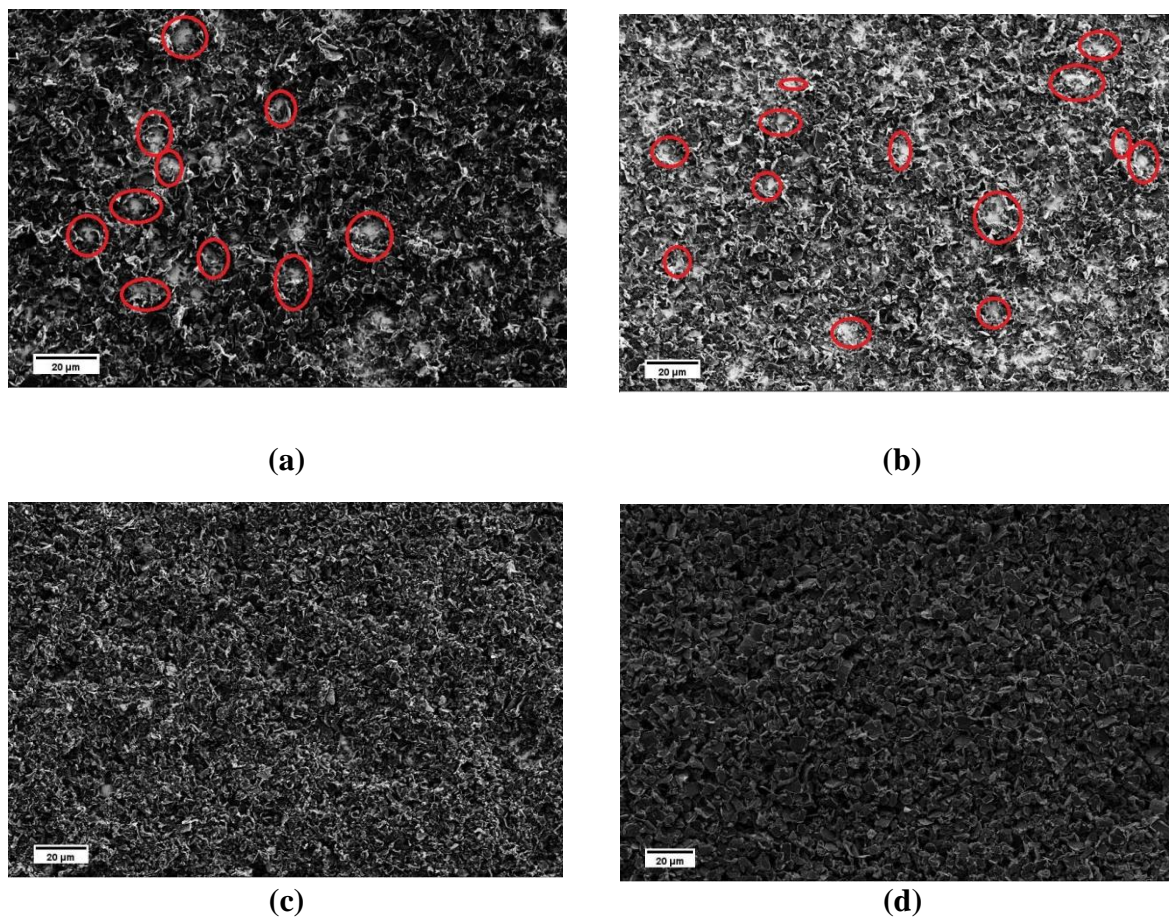


Figure 5.4: SEM images of the carbon based particles coated sample by EPD; (a) The PP10 coated sample with initial EDP conditions (b) The PP10 coated sample with lower voltage; (c) The PP 10 coated sample with longer deposition time; (d) G coated sample with longer deposition time

The SEM images of some samples after EPD are shown in Figure 5.4. From Figure 5.4 (a) and (b), there are pores exist in the coating layer, which are labelled by red circles, between the graphite particles and the pores are resulted from the escape of hydrogen gas. The particle movement carriers, hydrogen ions, are generated from the reaction between acetone and iodine. After moving the particles and let them deposited on to the substrate, the hydrogen ions recombined to form hydrogen gas and escaped from the system into the air. With lower voltage used, the particles in suspension moved slower and the EPD deposited layer was more porous because fewer particles deposited on to the steel surface in the same amount of time (Figure 5.4 (b)). When longer deposition time was adopted, a thick EPD deposited layer was produced and the whole steel surface was covered by the graphite particles. Comparing G coated (Figure 5.4 (d)) and PP10 coated samples, their surface morphologies are distinctive and this is resulted from the morphologies of the two different particles used. The electrical conductivity of the EPD coated samples was difficult to measure because the coating layers

were scratched off easily by the probe. Therefore, thermal treatment was carried out after EPD to improve the adhesion between the EPD coated layer and the steel substrate for electrical conductivity measurement.

All the treated samples exhibit acceptable adhesion that the coating layer cannot be scratched off by tissue papers. The SEM images of some coated samples are shown in Figure 5.5 where black spots or areas represent the carbon based particles and the grey spots or areas represent the oxide scale layer. From Figure 5.5, the carbon based particles do not cover the whole surface of the steel substrate. There are two possible reasons for that. The first possible reason is, as mentioned before, resulted from the diffusion of hydrogen gas out from the substrate surface to the air. Secondly, the oxide scale grew during thermal treatment process were around the carbon based particles and even fully buried the particles with small size (such as graphene and few layer graphene whose thicknesses are nanoscale). Therefore, only large and thick particles can be seen in the SEM images. Comparing G coated and PP10 coated samples, their surface morphologies were quite similar. From Figure 5.5 (a)-(f), only a few carbon based particles could be bound if the thermal treatment temperature was low and most of the carbon based particles were buried by the thick oxide scale when high treatment temperature was used. The adhesion between carbon based particles and steel is improved after the thermal treatment because the iron oxides scale produced can lock the particles on the surface and the adhesion of the coating layer and the Steel/coating adhesion mainly depends on the adhesion between the oxide scale and the steel substrate. Figure 5.5 (g) is the evidence for particles locked by iron oxides. In addition, from Figure 5.5 (g), the thickness of the oxide scale is not uniform and this may result from the thermal treatment process of the steel or the short treatment time did not allow the oxide scale layer to grow completely. The thickness of the oxide scale layer will be discussed later.

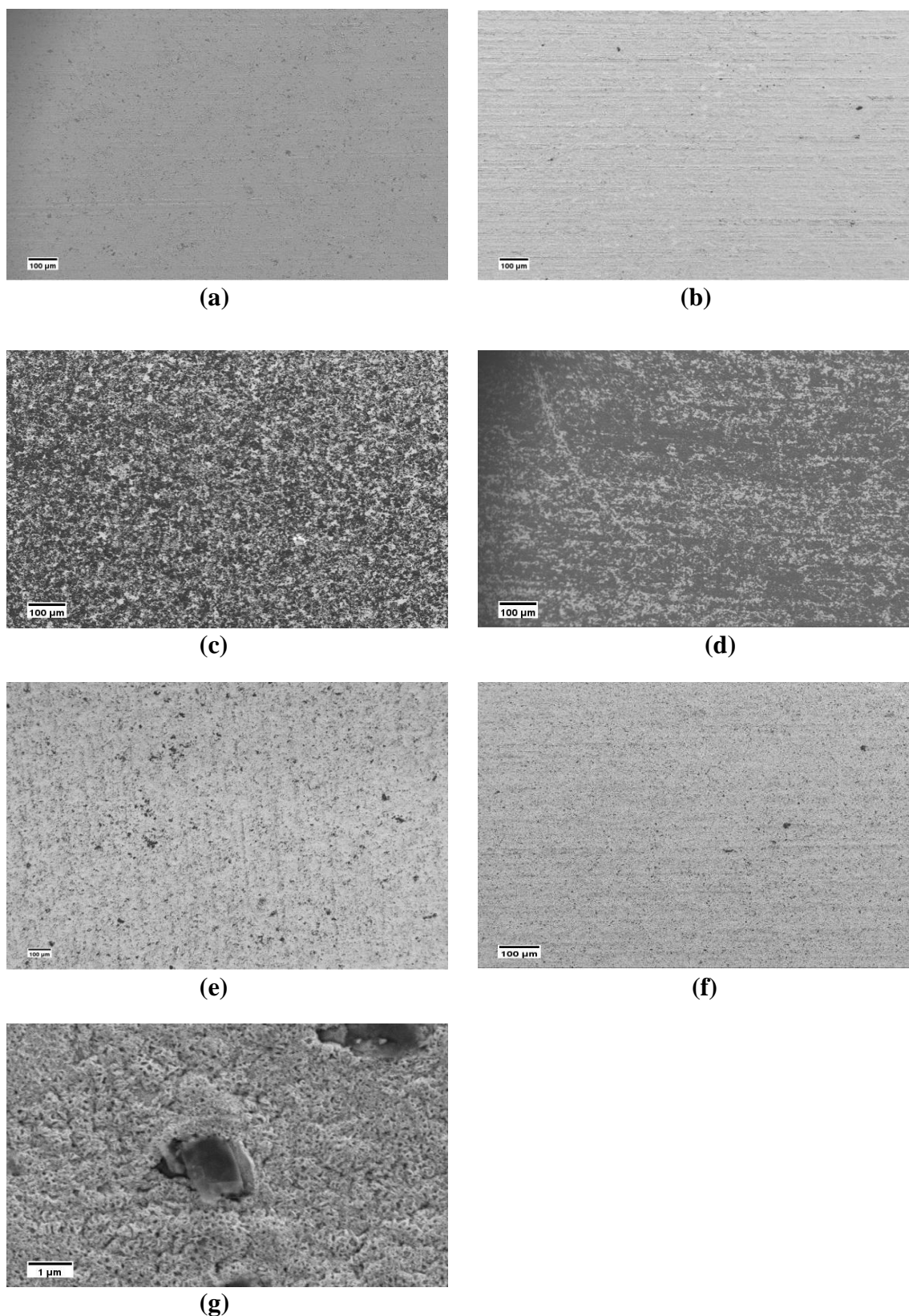


Figure 5.5: SEM image of the post heat treated samples (a) Graphene coated 540°C treated for 5 minutes (b) PP10 coated 540°C treated for 5 minutes (c) Graphene coated 580°C treated for 5 minutes (d) PP10 coated 580°C treated for 5 minutes (e) Graphene coated 600°C treated for 5 minutes (f) PP10 coated 600°C treated for 5 minutes (g) An iron oxide scale bound particle

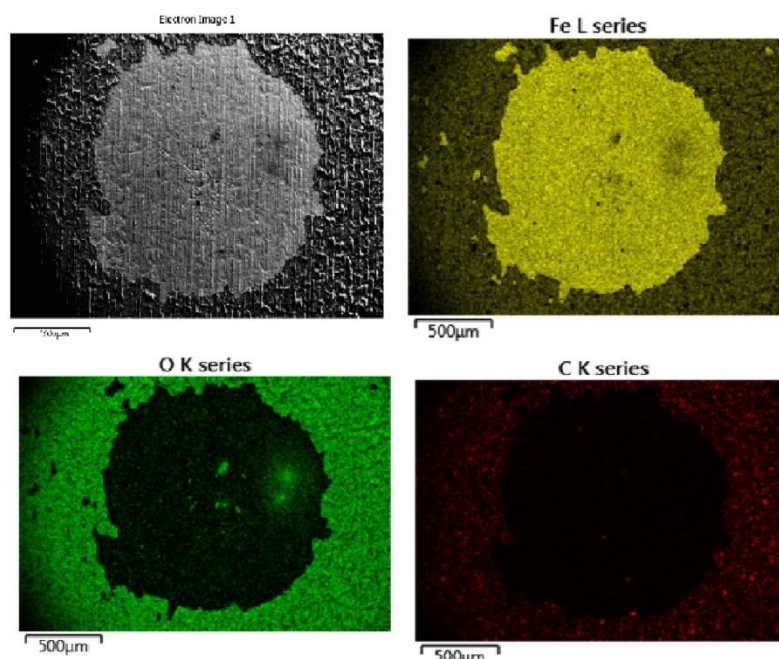
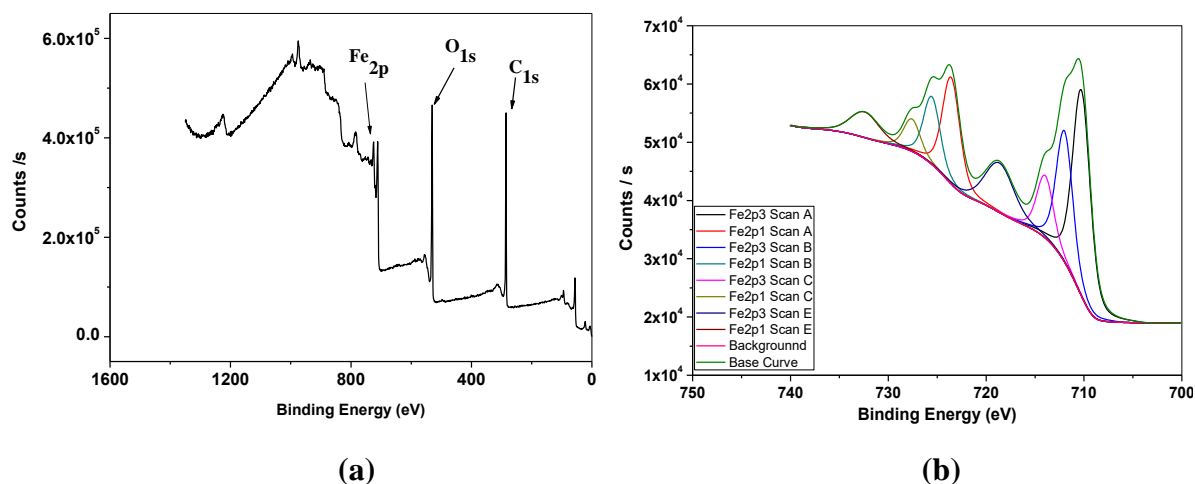


Figure 5.6 EDX analysis of the coating drop-off site of a graphene coated sample

Thermal treatment helps to produce good graphite or graphene coating layer. However, coating layer drop-off was observed in some of the coated samples and this phenomenon is more serious when the thermal treatment temperature is higher. Figure 5.6 shows the elemental profile of the coating drop-off site of graphene coated steel substrate. The bright spots and areas in the elemental profile images indicate the existence of a certain element. The contaminations that have not been fully cleaned in the graphene may be the possible reason for the drop-off of the coating layer because they may decompose at high temperature which leads to coating layer blow off and unbalanced localized heat. In addition, the oxide scale did not grow uniformly and the scale layer could not adhere onto the steel substrate. From Figure 5.6, iron is the only element exists in the drop-off site as shown in the Fe L series image. This also indicates that coating layer was completely removed during thermal treatment because only iron element was detected in the drop-off site. In the coating layer, carbon element and oxygen element are distributed uniformly. Iron element may also exist in the coating layer but its signal is not strong. The signal of oxide element is brighter than the signal of carbon element. This may indicate the amount of oxygen element is greater than carbon element. However, the EDX image offers only qualitative analysis of the elements presented in the surface. The composition of the coating layer cannot be examined accurately.

XPS results of graphite coated sample are shown in Figure 5.7 and Table 5.1. After

comparing with the database, all existing compounds in the coating layer are identified. Comparing the binding energy values in Table 5.1 and database, iron peak binding energy 711.99eV and 713.97eV represent the existence of hematite (Fe_2O_3) and iron peak binding energy 710.26 eV suggest that the existence of magnetite (Fe_3O_4). For oxygen peak binding energy, 529.63 eV can represent the existence of both hematite and magnetite and 531.63 eV represent the existence of hematite. As a result, the iron oxides existed in the coating layer are identified as hematite and magnetite where hematite has much larger quantity. In terms of carbon peak binding energy, 284.7eV represents the carbon without reacting with other substances and 288.45eV may represent the existence of carbon compounds such as carbon dioxide or carbon monoxide. The existence of carbon compounds may result from environmental contamination and do not indicates that graphite was involved in any reactions during thermal treatment. The analysis depth of XPS is limited. The coating layer may consist of several layers that contain different iron oxides and XPS can only analyse the outermost surface. In Figure 5.7, the surface structure of the oxide scale is similar to the hematite structure shown in literature [36]. This can also be the evident of the existence of hematite in the surface of graphite coated samples and hematite is also the major component of the outermost oxide scale. In addition, the oxide scale layer is likely to be a thin hematite layer in the outermost surface with a magnetite layer underneath [25].



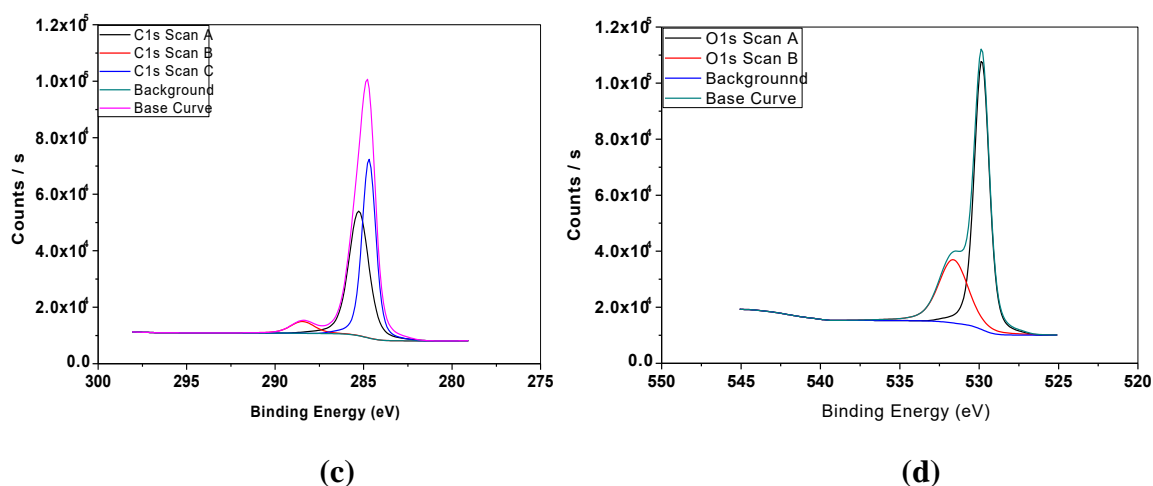


Figure 5.7: XPS spectrum of graphite coated sample treated at 580^o C for 5 minutes (a) survey scan (b) Iron element high resolution scan (c) Carbon element high resolution scan (d) Oxygen element high resolution scan

Table 5.1: XPS data of graphite coated sample treated at 580^o C for 5 minutes

Name	Fe2p3 Scan A	Fe2p3 Scan B	Fe2p3 Scan C	O1s Scan A	O1s Scan B	C1s Scan A	C1s Scan B	C1s Scan C
Peak Binding Energy	710.26	711.99	713.97	529.83	531.63	285.27	288.45	284.7
Atomic %	4.52	2.72	1.3	20.83	9.59	28.97	3.34	28.73

The porosity formed in the oxides scale layer is mainly resulted from the growth stresses and resultant deformation and grain growth. The micro-voids are also formed within the oxide scale layer as a result of the inward diffusion of oxygen and outward diffusion of metal take place during oxidation [31]. In addition, with the contribution of hematite formation, a porous coating layer is highly possible to appear (Figure 5.8). When hematite interacted with each other, it was easy to form porous coating layer. With the oxygen and metal took place, pores and micro-voids were formed in the oxide scale layer. The formation of micro-voids mainly took place in underneath magnetite layer. Magnetite layer consists of a fine-grain layer at the inner region and a coarser columnar-grain layer at the outer region. Voids are formed at the scale-iron interface and subsequent void migration takes place along grain boundaries. Therefore, voids appear in the coating layer and the porous structure is resulted [26,27].

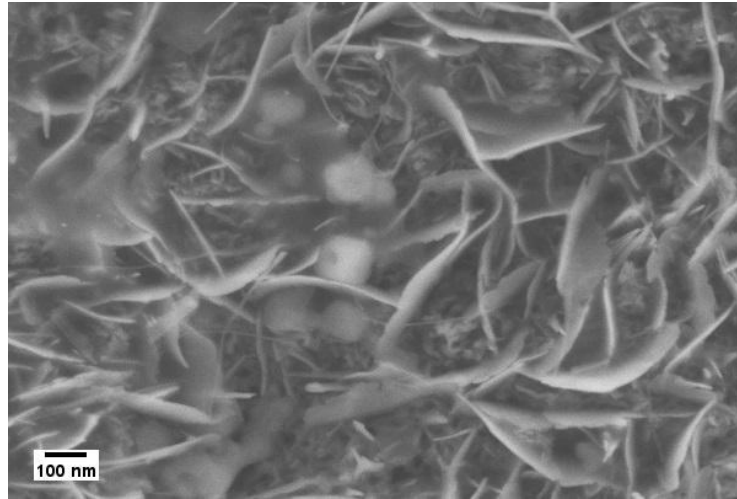


Figure 5.8: SEM image of graphite coated sample to review its surface structure

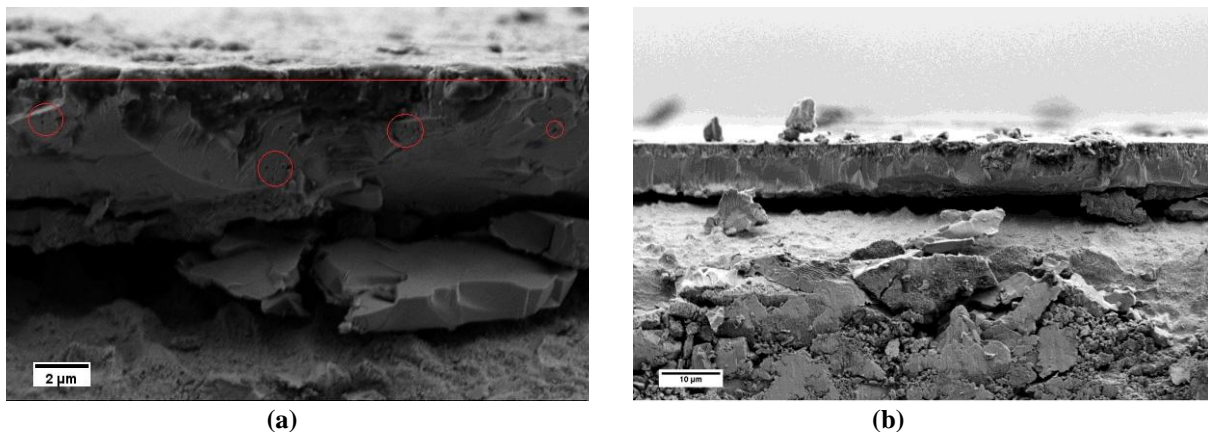


Figure 5.9: SEM image of the steel-coating interface of (a) graphite coated sample treated at 630 for 5 minutes (b) graphene coated sample treated at 630 for 5 minutes

The structure of the interfaces of high temperature treated sample is clearer because the scale layer is thicker and more fully developed. The steel-coating interface was observed clearest in the graphite coated sample heat treated at 630 °C for 5 minutes (Figure 5.9). From Figure 5.9 (a), the scale layer has two layers and the top layer is porous, which is hematite layer. The two layers are separated by a red line. This is the same as the theory mentioned above that the scale layer has a hematite top layer followed by a continuous magnetite layer [25]. But the wustite layer could not be observed clearly. Additionally, large columnar grains can be observed in the scale interphase. Grain boundaries are also visualized in Figure 5.9 (a). Micro-voids were formed during the thermal treatment in the areas labelled by red circles in

the figure. The actual carbon based particles binding layer is hematite layer because the generated magnetite layer is dense and is not able to bind any carbon based particles [29,37]. As a result, no matter how thick the EPD deposited layer is, only the innermost layer of EPD deposited carbon based particles can be bound during thermal treatment process. Figure 5.8 (b) shows the steel-coating interphase of the graphene coated sample which was treated at same condition as the graphite coated sample. Their steel-coating interfaces are similar and this indicates that the presence of different carbon based particles do not have a fundamental effect on the oxidation process of steel.

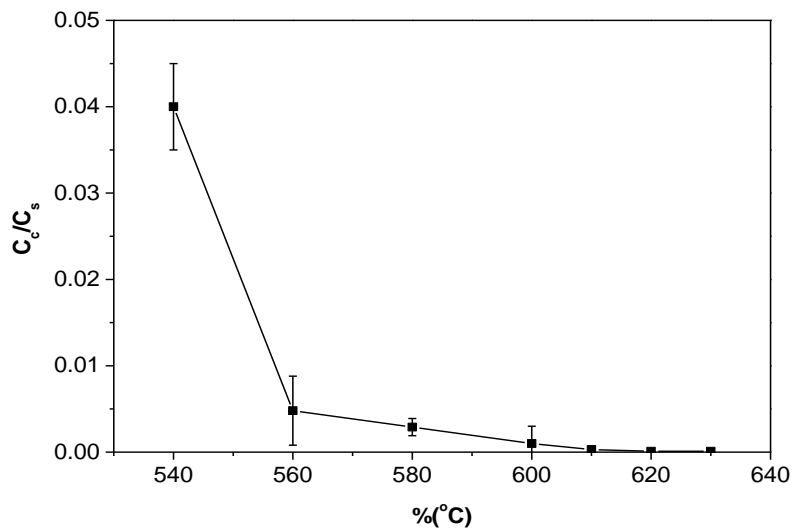


Figure 5.10: Plot of relative conductivity versus thermal treatment temperatures of the oxide layers on BP steel

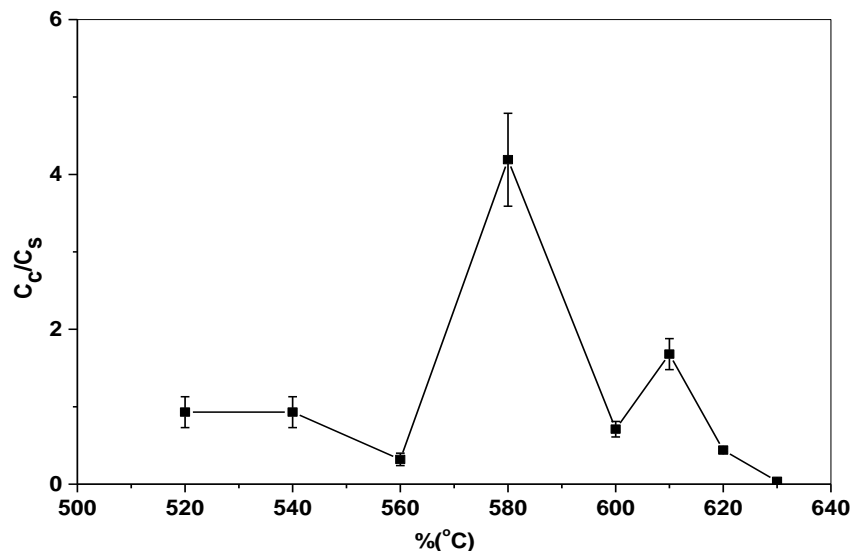


Figure 5.11: Plot of relative conductivity versus thermal treatment temperatures of graphite coated samples

After taking out the samples from the furnace for thermal treatment, all the samples were cleaned by tissue papers to wipe out any particles that not adhere onto the steel substrates. Figure 5.10 shows the relative conductivity of BP steel treated in different temperatures for five minutes. After heat treatment, the conductivity of the steel surface was reduced significantly compared to bare steel substrate. Figure 5.11 and 5.12 show the trend of the electrical conductivity versus treatment temperature. If the value of relative conductivity equals to 1, this means that the conductivity of the coated samples is the same as the steel substrate. From Figure 5.11, the peak relative conductivity was achieved when 580 °C was applied to treat the coating samples. The relative conductivity of the coated samples does not change at 520°C and 540°C and, then, it begins to rise to its peak value at 580°C, after which it begin to fall. Another smaller peak value appears at 610°C. However, considering the standard deviation, the relative conductivity at 610°C may be an inaccurate value. If so, there is only one peak relative conductivity value which appears at 580°C. Compared to graphite coated samples, the graphene coated samples have less serious change of relative conductivity and their relative conductivity values do not have a very high value which range from 1 to 2.5. The relative conductivity drops significantly when thermal treatment temperature is higher than 610°C. Again, when considering the standard deviation, the relative conductivity values from 520°C to 610°C may only vary a little and this can indicates that a more stable conductivity value is exhibited when utilizes graphene. 580°C seems to be the best treatment temperature for both graphite coated samples and graphene coated samples. Compared to the relative conductivity of Figure 5.11 and Figure 5.12 to Figure 5.13, the presence of carbon based particles can improve the conductivity of oxide layer on steel substrate.

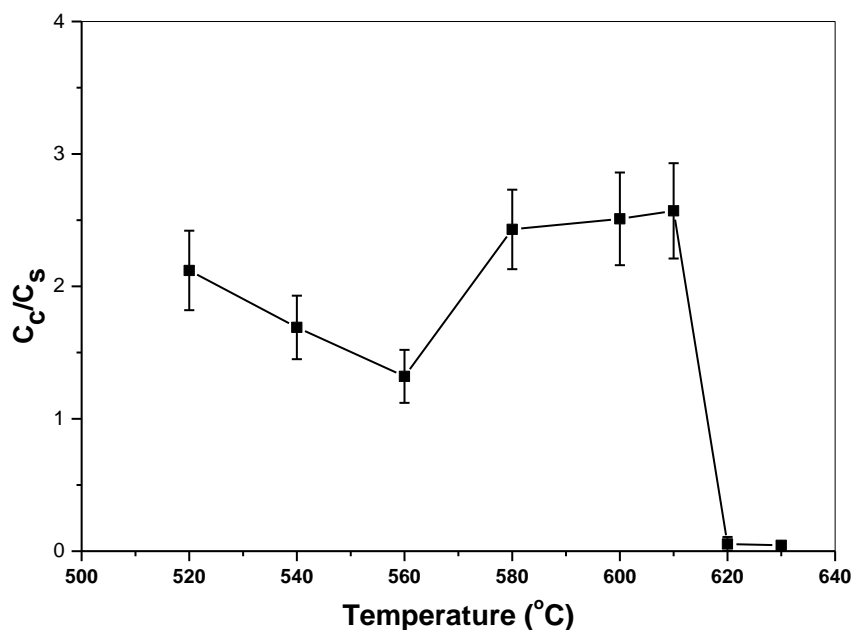


Figure 5.12: Plot of relative conductivity *versus* thermal treatment temperatures of graphene coated samples

The resistance of the coating layer is mainly contributed from the tunnelling resistance between particles and the contact resistance between the probe and the coating when current pass through. The tunnelling resistant is much greater than contact resistant [38]. With higher thermal treatment temperature was used, the hematite layer grew thicker and buried more thin and small particles. Hence, large and thick particles contributed more as the electrical conducted component. With the oxide scale buried more particles, the tunnelling resistant increased when current passed through the coating layer during four point probe test and, therefore, electrical conductivity of the coating layer was reduced. In the case of graphene coated samples, from the SEM images, the residual graphite and exfoliated graphite were the major electrical conducted component. Although the graphene has much more few layers graphene and single layer graphene than PP10, the contact resistant generated between carbon-carbon contact and carbon-iron oxides contact in the graphene coated sample is much greater than PP10 coated sample. In PP10 coated samples, the presence of few layers graphene can act as a bridge to fill the gap between two large particles so as to reduce the tunnelling resistance [39].

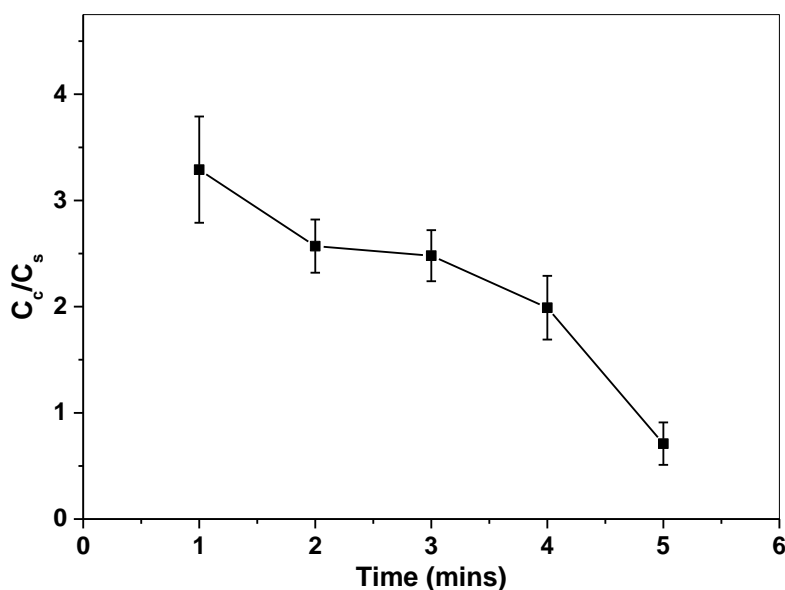


Figure 5.13: Plot of relative conductivity *versus* thermal treatment times of graphite coated samples at 600 °C

Figure 5.13 shows the trend of relative conductivity varies with prolonged treatment time. The relative conductivity values of the graphite coated samples drop significantly with prolonged thermal treatment time. As the samples were treated in the furnace longer, the tunnelling resistant increased significantly and led to reduced electrical conductivity. However, under a certain temperature, carbon based particle cannot be bound onto the steel substrate with inadequate time. For example, if the sample is treated at 520°C, the thermal treatment time should be longer than 5 minutes to bind the carbon based particles.

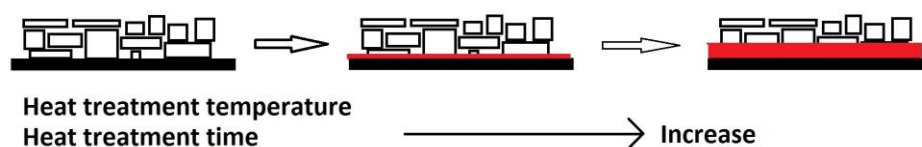
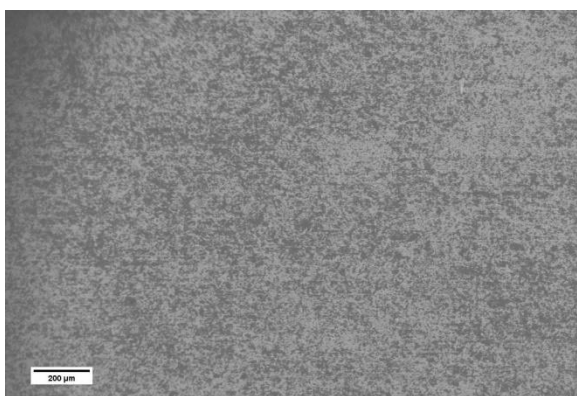


Figure 5.14 Schematic of particles binding process during heat treatment

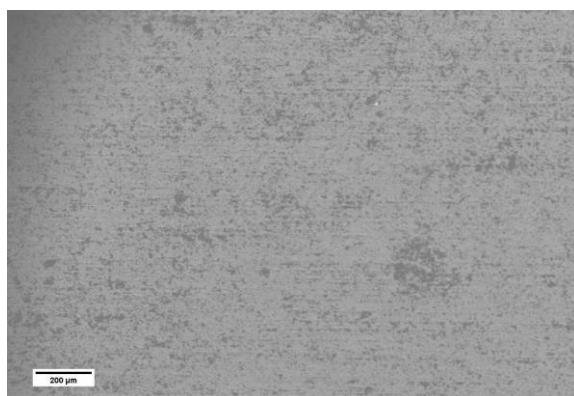
A schematic for the binding mechanism is proposed in Figure 5.14. The binding mechanism resulted from heat treatment is mechanical binding. A layer of oxide scale is generated when the steel substrates contact with air under high temperature. The particles deposited by EPD were bound by the as-generated layer and form a dense coating layer. All the results shown before can be the evidence of the proposed binding mechanism. The binding layer grown during heat treatment is not electrically conductive. As mentioned before, it is crucial that to

control the thickness of the hematite layer to bind as many particles as it can without affecting the coated samples electrical conductivity. If the hematite layer is too thick, most of the EPD deposited particles will be buried inside the hematite layer and are not able to function as electrical conductor. If the hematite layer is too thin, it may be only able to bind very small particles and bigger size particles are not able to be bound. The area of the particles occupied on the coating surface is an important factor that relate to the electrical conductivity of the coated samples. Low particle occupied area has low electrical conductivity. In addition, from the SEM images, the porosity of the compound layer is quite high that it will have detrimental effect on corrosion resistant.

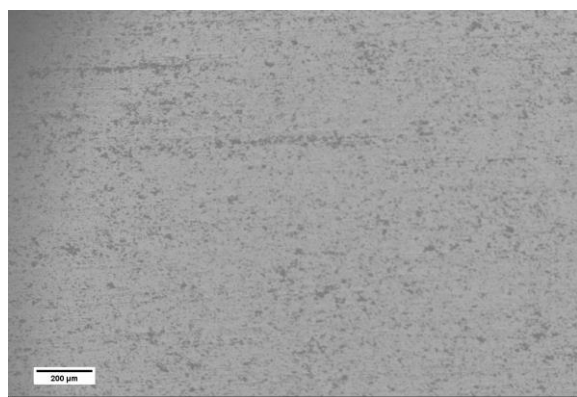
5.3.2 Optimization of EPD conditions



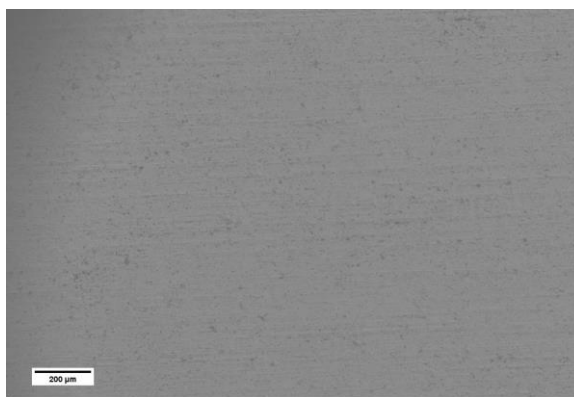
(a)



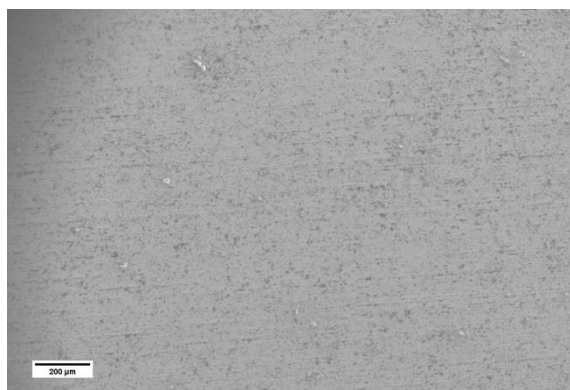
(b)



(c)



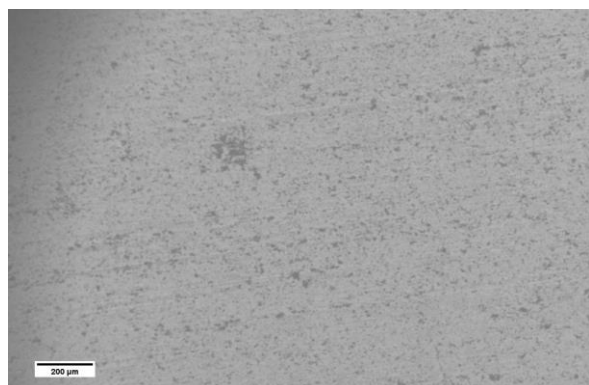
(d)



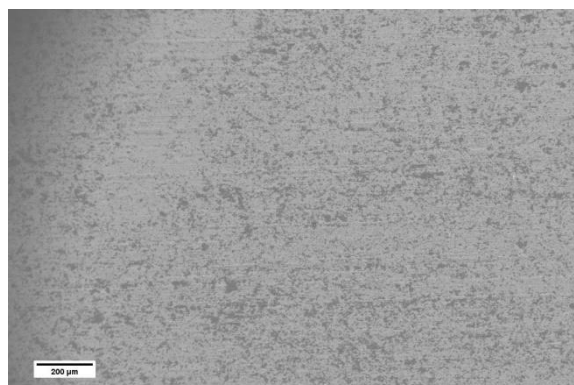
(e)

Figure 5.15 SEM images of iodine concentrations variation trials (a) DP1061 (0.175mg/ml) (b) DP1062 (0.44mg/ml) (c) DP1063 (0.74mg/ml) (d) DP1064 (0.99mg/ml) (e) DP1065 (1.23mg/ml) (scale bar:200μm)

Figure 5.15 shows the SEM image of the samples produced by varying iodine concentration in acetone. It is quite obvious that sample DP1061 has the highest particle coverage and the least unoccupied sites. Iodine concentration in suspension relates to the deposition speed of particle directly and can affect the packing behaviour of the coating layer. When the same voltage is applied, higher iodine concentration means high as-generated current. Higher current may cause turbulence in the suspension and the coating layer may be disturbed during its deposition. Hence, lower iodine concentration is beneficial to produce a coating layer with good quality. The thickness of as-deposited coating layer also increases with the increase of iodine concentration in suspension. However, if the iodine concentration is too low, the particles movement in the suspension is not able to be activated and a coating layer cannot be formed from the particles.



(a)



(b)

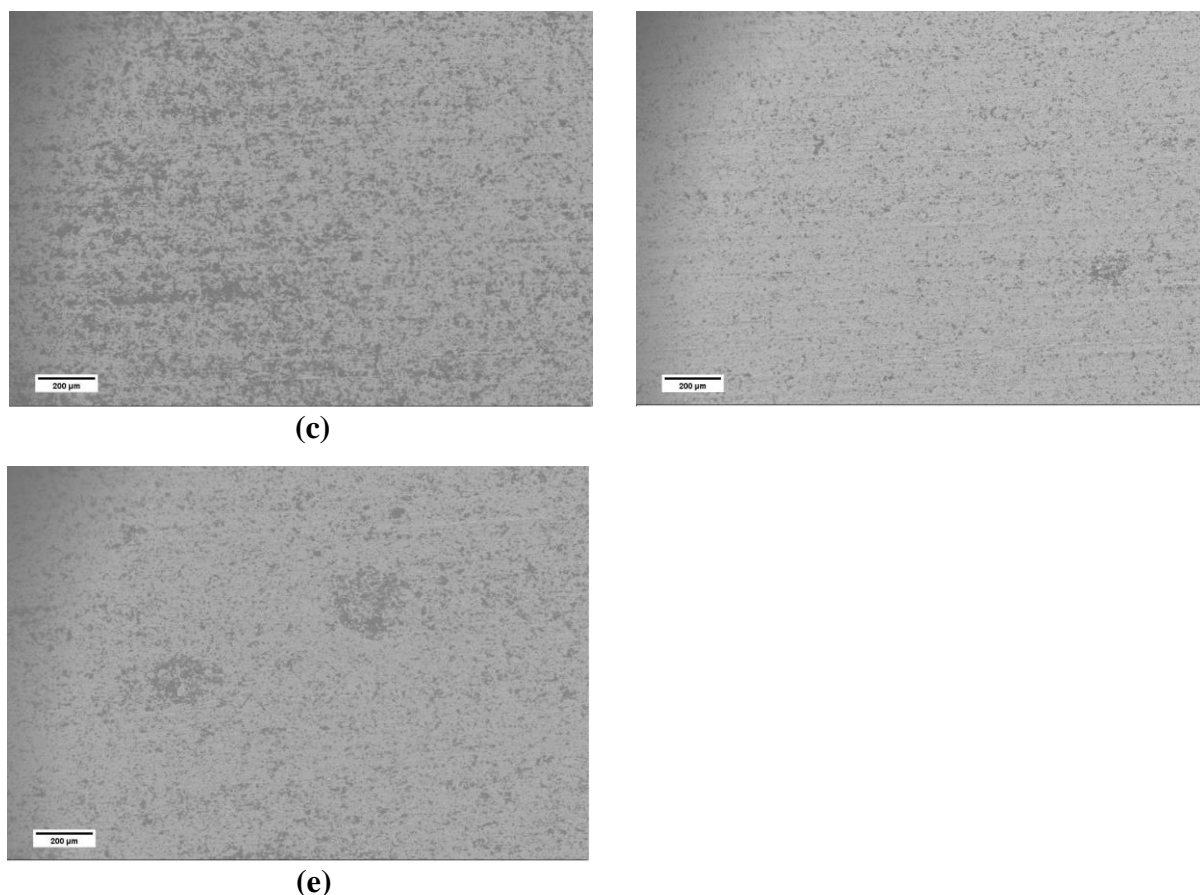


Figure 5.16 SEM images of deposition times variation trials (a) DP1066 (0.5 min) (b) DP1067 (1 min) (c) DP1068 (1.5 mins) (d) DP1069 (2 mins) (e) DP10610 (2.5 mins) (scale bar: 200 μm)

With prolonged deposition time, the thickness of coating layer increase. The case in carbon based particle may be different. Figure 5.16 shows the SEM image of the samples in time variation trial. Sample DP1067 and DP1068 have larger particles coverage compared to other samples in this trial. The Particles in the suspension need enough deposition time to cover the whole area of the steel substrate and the deposited mass on a substrate has a linear relationship with deposition time. In the trial, the reason why sample DP1069 and DP10610 has less particles coverage is not quite clear. This may relate to the iodine concentration variation during the EPD process.

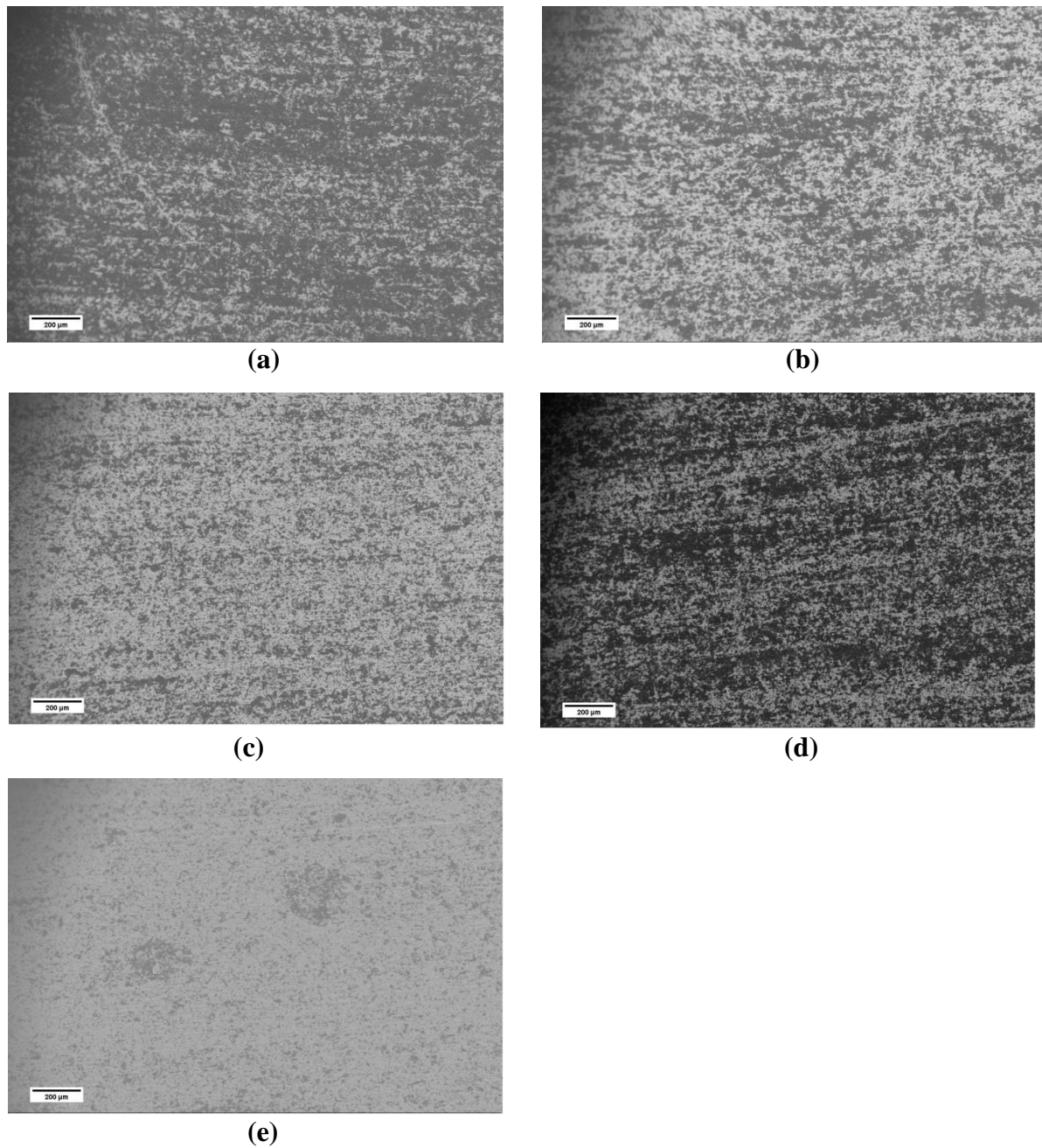


Figure 5.17 SEM images of SEM images of voltage variation trials (a) DP1866 (20V) (b) DP1867 (30V) (c) DP1868 (40V) (d) DP1869 (50V) (e) DP18610 (60V) (scale bar:200 μm)

From Figure 5.17, the particle coverage of sample DP1866 is the best. The particle coverage reduces with increased voltage and it increases again after the voltage is higher than 40V. As mentioned before, high voltage may cause turbulence that affect the morphology of the coating layer. However, from the result of voltage variation, the influence of turbulence raised by high voltage might be overcome if the particles can deposit on to the substrate fast enough. Another possible reason is that, due to the turbulence caused by high voltage, the

quality of the coating is not controllable and irregular.

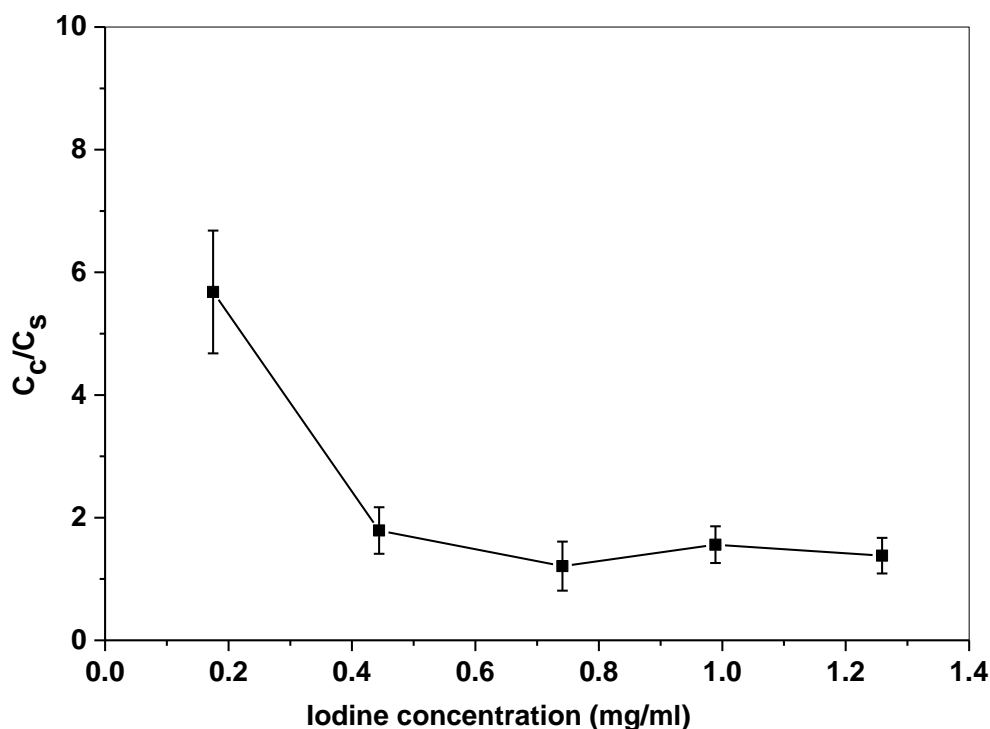


Figure 5.18: Plot of electrical conductivity ratios *versus* iodine concentrations

Figure 5.18 shows the plots of the relative conductivity versus iodine concentration in acetone. The electrical conductivity of coated samples decreases with increased iodine concentration. Iodine concentration in suspension relates to the deposition speed of particle directly and can affect the packing behaviour of the coating layer. When the same voltage is applied, higher iodine concentration means high as-generated current. Higher current may cause turbulent in the suspension and the coating layer may be disturbed during its deposition. Hence, lower iodine concentration is beneficial to produce a coating layer with good quality. The thickness of as-deposited coating layer also increases with the increase of iodine concentration in suspension. However, if the iodine concentration is too low, the particles movement in the suspension cannot be activated and a coating layer is not able to be formed from the particles.

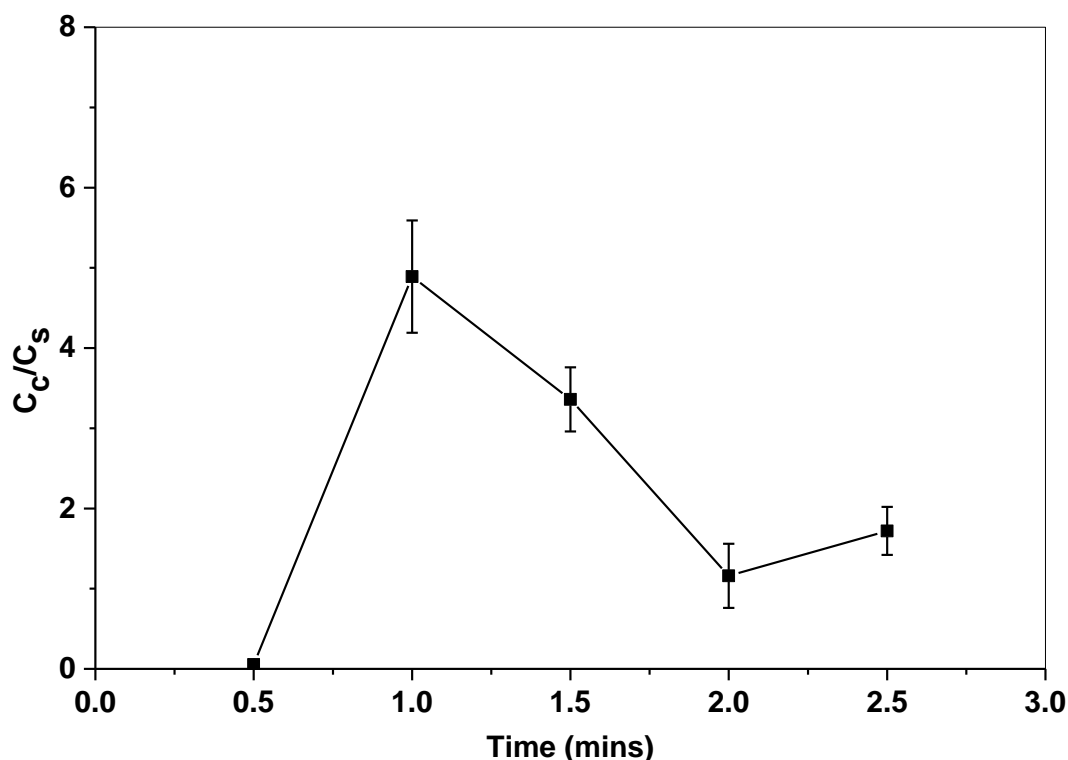


Figure 5.19: Plot of electrical conductivity ratios *versus* deposition times

As shown in Figure 5.19, 1 minute deposition time seems to be the best deposition time for the system to achieve a coating layer with good conductivity. With prolonged deposition time, the thickness of EPD coating layer increases. The deposition rate will be decreased with prolonged deposition time because the coating layer generated may act as insulating layer, especially for ceramic particles. The particles in the suspension need enough deposition time to cover the whole area of the steel substrate and the deposited mass on a substrate has a linear relationship with deposition time [40]. The variation in the electrical conductivity of the coated samples may relate to the deposition pattern of the carbon based particle on the steel substrate. As the hydrogen ions escaped in the form of hydrogen gas, prolonged deposition time may lead to increased porosity of the EPD coating layer. Therefore, the tunnelling resistant of the coating layer is increased.

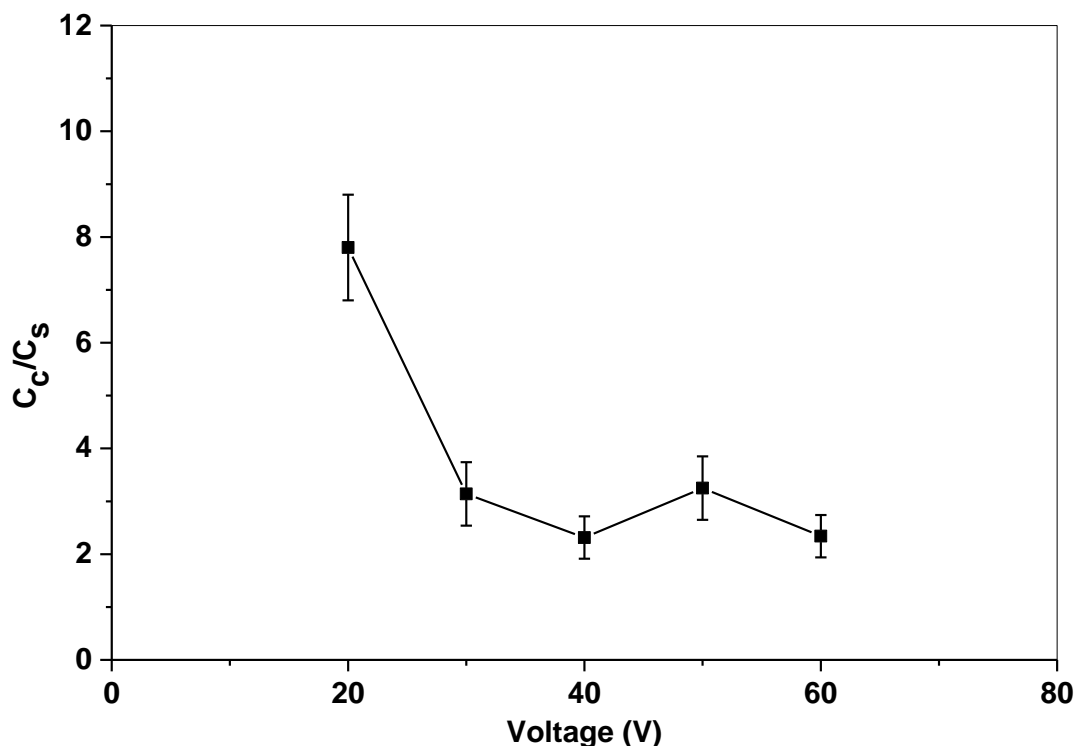


Figure 5.20: Plot of electrical conductivity ratios *versus* voltages

For the effect of voltage to the electrical conductivity shown in Figure 5.20, a conclusion can be drawn that 20V and 40 V both can produce coated samples with higher electrical conductivity. High voltage may cause turbulence that affects the morphology of the coating layer. However, from the result of voltage variation, the influence of turbulent raised by high voltage might be overcome if the particles can deposit onto the substrate fast enough because particles under high voltage also move faster than low voltage. Another possible reason is that, due to the turbulence caused by high voltage, the quality of the coating is irregular and cannot be controlled.

The change of the electrical conductivity of the coating layer mainly contributes to the change of tunnelling resistance and contact resistance between electrical conducted components (carbon based particles). The tunnelling resistance will be reduced significantly if more graphite or graphene particles cover the surface and they are near each other. As a result, a fine control of oxide scale layer growth and EPD process to produce a surface fully covered by graphite or graphene particles is important to the electrical conductivity of the coated samples.

5.3.3 Comparison of the electrical conductivity of the coating on different steel substrates

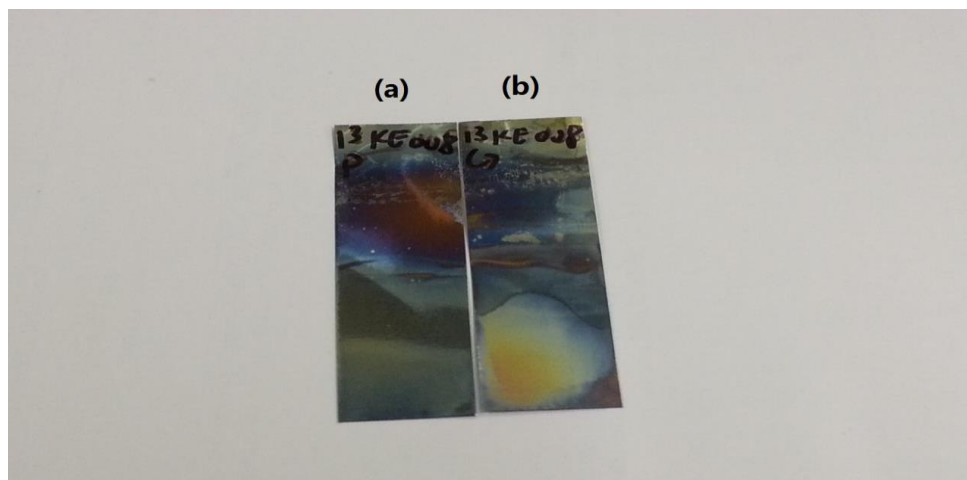


Figure 5.21 Images of 13KE008 (a) graphene coated (b) graphite coated

The sample images of the different substrates after EPD and heat treatment are shown in Figure 5.21 to Figure 5.24. From the images, it seems that graphite and graphene were only successfully coated on to 13KE21 substrate. The success of coating relate to the surface treatment of the steel substrates in TATA steel. The binding of particles after heat treatment is contributed from the generation of thin layer iron oxides. The oxidation in this temperature highly depends on the surface treatment of the steel surfaces, such as polishing, and the steel types. The surface roughness seems to be a critical factor. 13KE008 samples were not able to bind graphite or graphene particles after heat treatment. The surface roughness and the

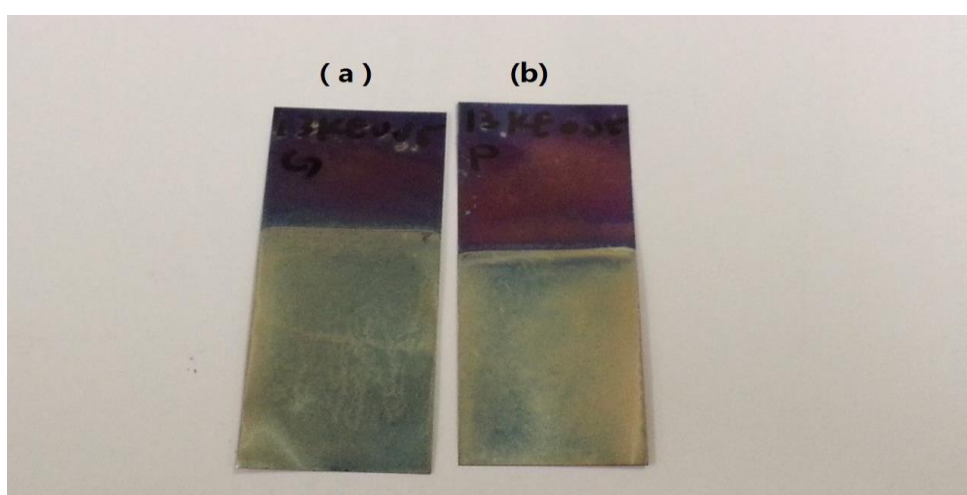


Figure 5.22 Images of 13KE005 (a) graphite coated (b) graphene coated

anti-oxidation property of 13KE008 are much better than the surface roughness of normal Black Plate. In the case of 13KE005, the chromium oxides on the surface can retard the

oxidation of iron under high temperature. This is the reason why graphite and graphene particles were not bound on to the 13KE005 surface. For 13KE009 samples, the heat treatment time and temperature were not able to form a thick enough scale on nickel layer to bind graphite and graphene particles onto its surface. Although 13KE21 samples can bind some graphite or graphene particles, only small amount of particles were bounded onto the surfaces.

SEM was used to characterize the surface of 13KE21 samples and their electrical conductivity was also measured. The SEM images are shown in Figure 5.25 and the electrical conductivity ratios toward 13KE21 substrates are shown in Table 5.2. From Figure 5.25, only a very small amount of graphite and graphene particles were bound onto the steel substrates. Some of the bound particles are optically transparent and this phenomenon indicates that few layer graphene particles were bound on graphite coated and graphene coated samples. The

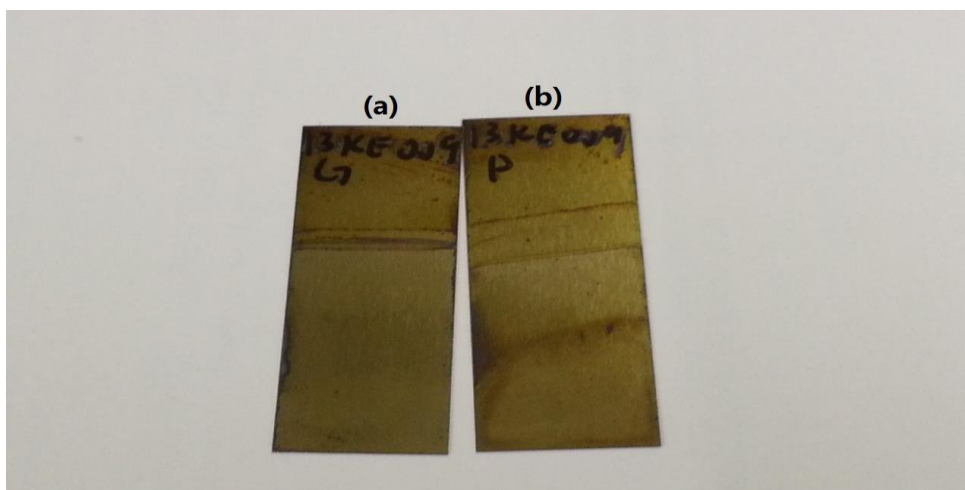


Figure 5.23 Images of 13KE009 (a) graphene coated (b) graphite coated

electrical conductivity of the coated samples are both lower than the 13KE21 substrate. Although few layer graphene was bound, the electrical conductivity of 13KE21 was not improved because the amount of bound graphite or graphene particles was small that the tunnelling resistant between each particle is very high. The thin scale layer contributes more than the bound graphite or graphene particles. From the results, graphene or graphite particle coverage on steel substrates is a critical factor that affects the electrical conductivity of the coated samples.

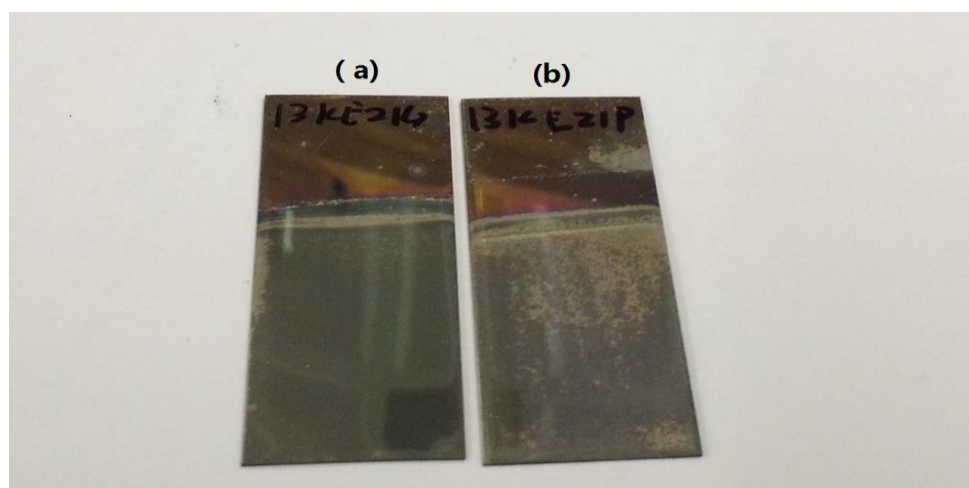


Figure 5.24 Images of 13KE21 (a) graphene coated (b) graphite coated

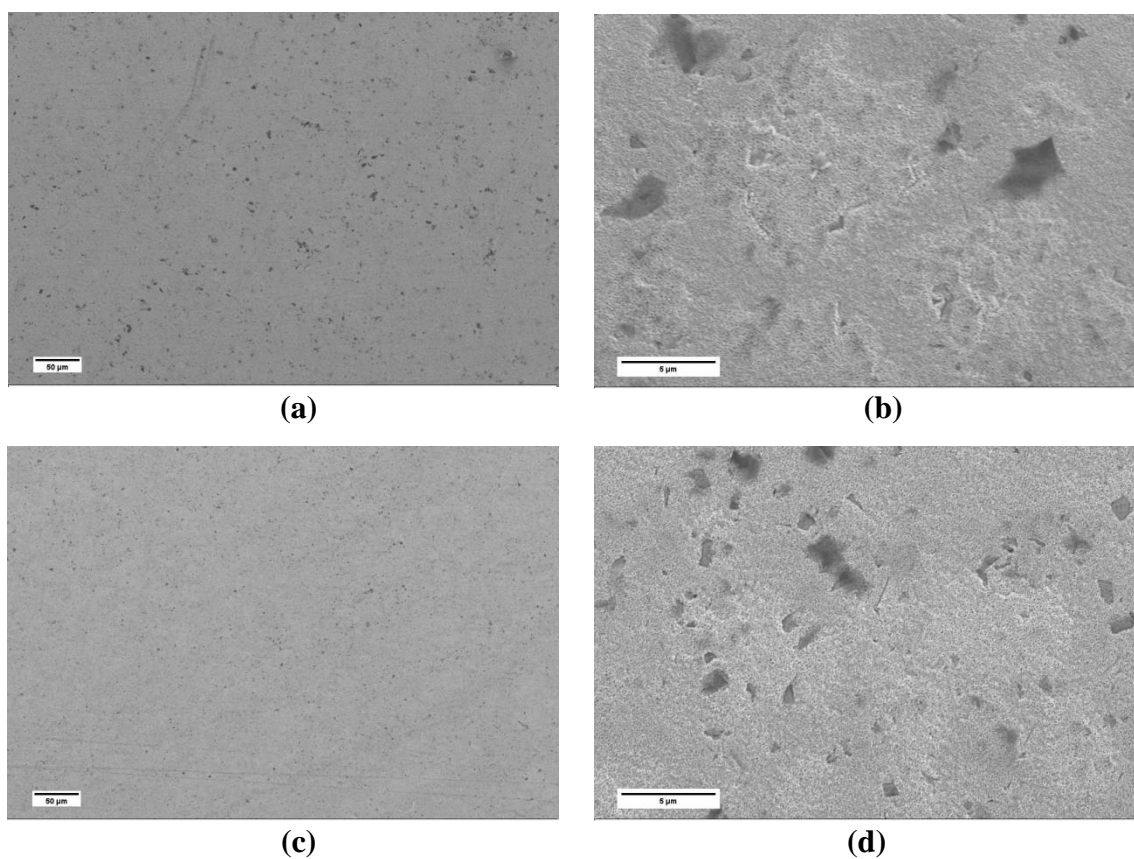


Figure 5.25 SEM images of (a)(b) graphite coated 13KE21 samples and (c)(d) graphene coated 13 KE21 samples

Table 5.2 Electrical conductivity of coated 13KE21 samples

Sample Code	Relative conductivity
Graphite coated 13KE21	0.854
Graphene coated 13KE21	0.198

Surface scan and depth profiling were performed onto the samples with three different coating materials. The XPS results of PP10 coated samples are shown in Figure 5.26 and Table 5.3. From the results, the surface of PP10 coated sample contains NiO, Ni_2O_3 , Fe_2O_3 and PP10 graphite. The amount of Ni_2O_3 is much less than NiO and this may result from oxidation conditions. Peak binding energy 862.1 eV stands for both NiO and Ni_2O_3 , and their atomic percentage is 4.15. The precise amount of Ni_2O_3 cannot be identified from the result. 13KE21 steel is a steel special treated with nickel coating on top. The presence of Fe_2O_3 is resulted from the outward metal diffusion and inward oxygen diffusion.

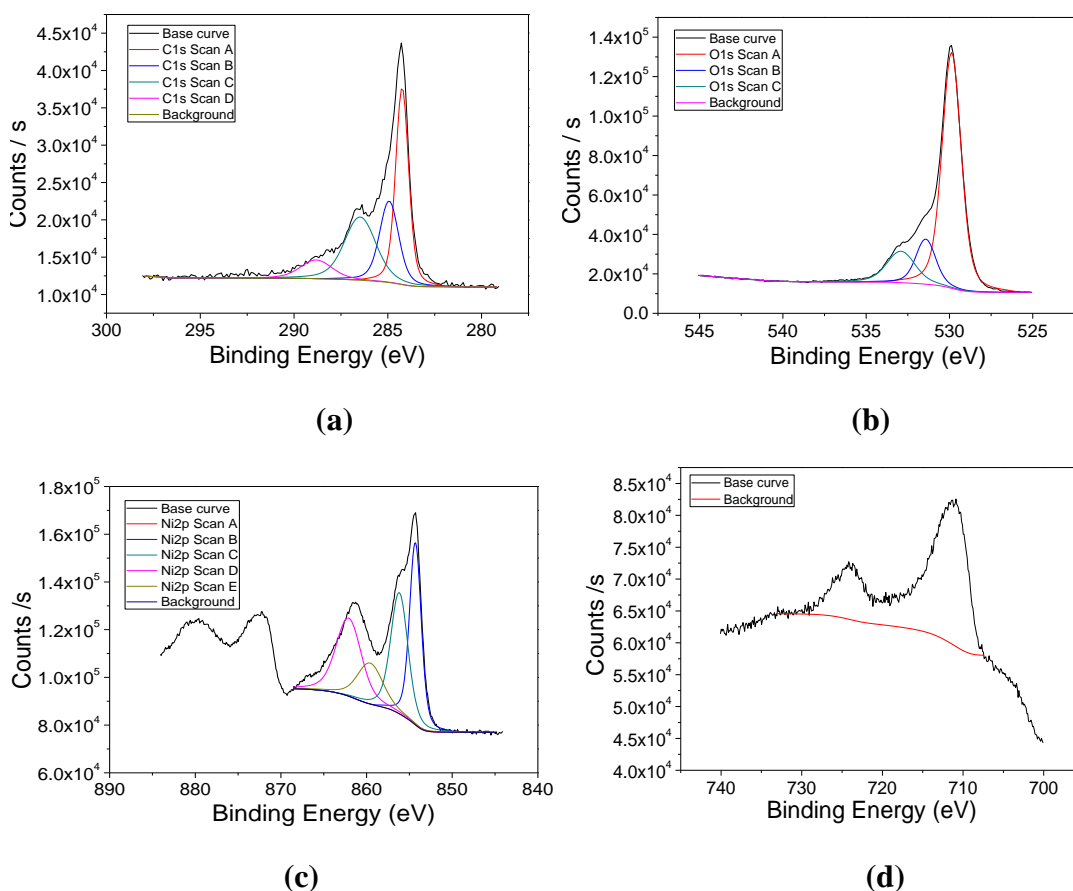
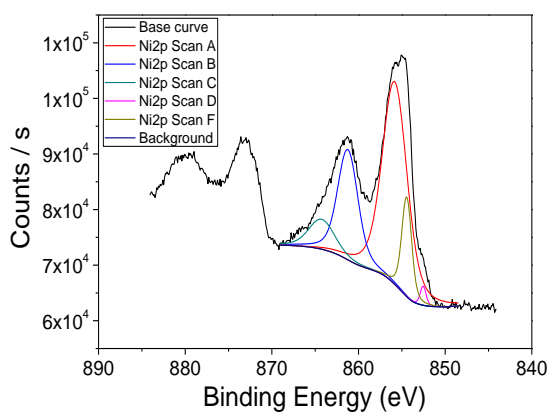
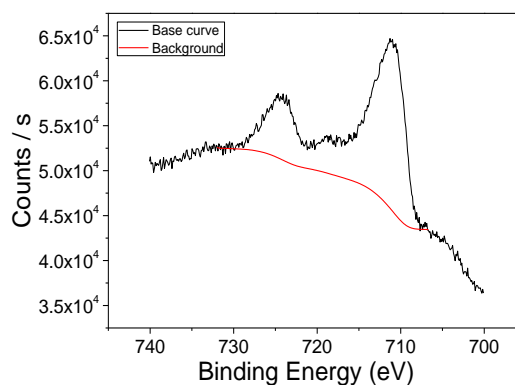


Figure 5.26 XPS surface scan of PP10 coated sample (a) Carbon element scan (b) Oxygen element scan (c) Nickel element scan (d) Iron element scan

Table 5.3 XPS data of the PP10 coated sample treated at 580^o C for 5 minutes

Name	C1s Scan A	C1s Scan B	C1s Scan C	C1s Scan D	O1s Scan A	O1s Scan B	O1s Scan C	Ni2p Scan B	Ni2p Scan C	Ni2p Scan D	Ni2p Scan E	Fe2p
Peak Binding Energy (eV)	284.2	284.9	286.4	288.8	529.8	531.4	532.9	854.3	856.1	862.1	859.6	71.3
Atomic %	11.63	7.11	9.08	2.72	34.15	6.81	6.78	4.44	4.33	4.15	2.17	6.63

The XPS results of PPG coated samples are shown in Figure 5.27 and Table 5.4. The compound appeared in the PPG coated samples after thermal treatment were NiO, Ni₂O₃ and Fe₂O₃. PPG particles did not react with oxygen during the thermal treatment. The peak binding energy 855.8 eV represents both NiO and Ni₂O₃. In the PPG coated surface, the amount of Ni₂O₃ is more than NiO and this indicate that the size of the carbon based particles could affect oxidation behaviour of 13KE21 steel during thermal treatment because the oxygen transportation was affected.

**(a)****(b)**

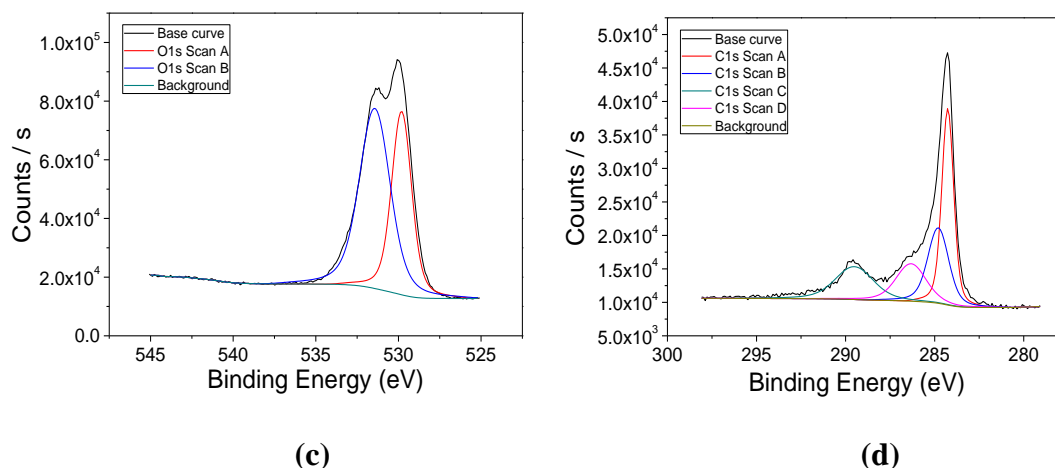


Figure 5.27 XPS surface scan of the PPG coated sample (a) Nickel element scan (b) Iron element scan (c) Oxygen element scan (d) Carbon element scan

Table 5.4 XPS data of the PPG coated sample treated at 580^o C for 5 minutes

Name	Ni2p Scan A	Ni2p Scan B	Ni2p Scan C	Ni2p Scan D	Ni2p Scan F	Fe2p 3	O1s Scan A	O1s Scan B	C1s Scan A	C1s Scan B	C1s Scan C	C1s Scan D
Peak Binding Energy (eV)	855.8	861.2	864.3	852.5	854.4	711.1	529.8	531.4	284.3	284.8	289.5	286.3
Atomic %	4.54	2.58	0.7	0.1	0.89	7.98	19.32	29.34	12.79	8.67	6.91	6.18

The XPS results of the graphene coated samples are shown in Figure 5.27 and Table 5.4. The compound appeared in the coated samples after thermal treatment were the same. The peak binding energy 856.2 eV represents both NiO and Ni₂O₃. In the graphene coated surface, the amount of Ni₂O₃ is different from the other two coated samples. Again, this indicates the oxidation behaviour was changed by the carbon based particles size and dimensions. The metal outward diffusion still took place no matter what the coating materials was as Fe₂O₃ appeared in these three types of coated

samples. In addition, the nickel top coating on steel could not act as the protection layer against oxidation. During thermal treatment, oxygen reacted with the nickel layer first and diffused through the layer to react with iron. At the same time, the iron and nickel diffused outward through the micro-tunnel to react with oxygen as well.

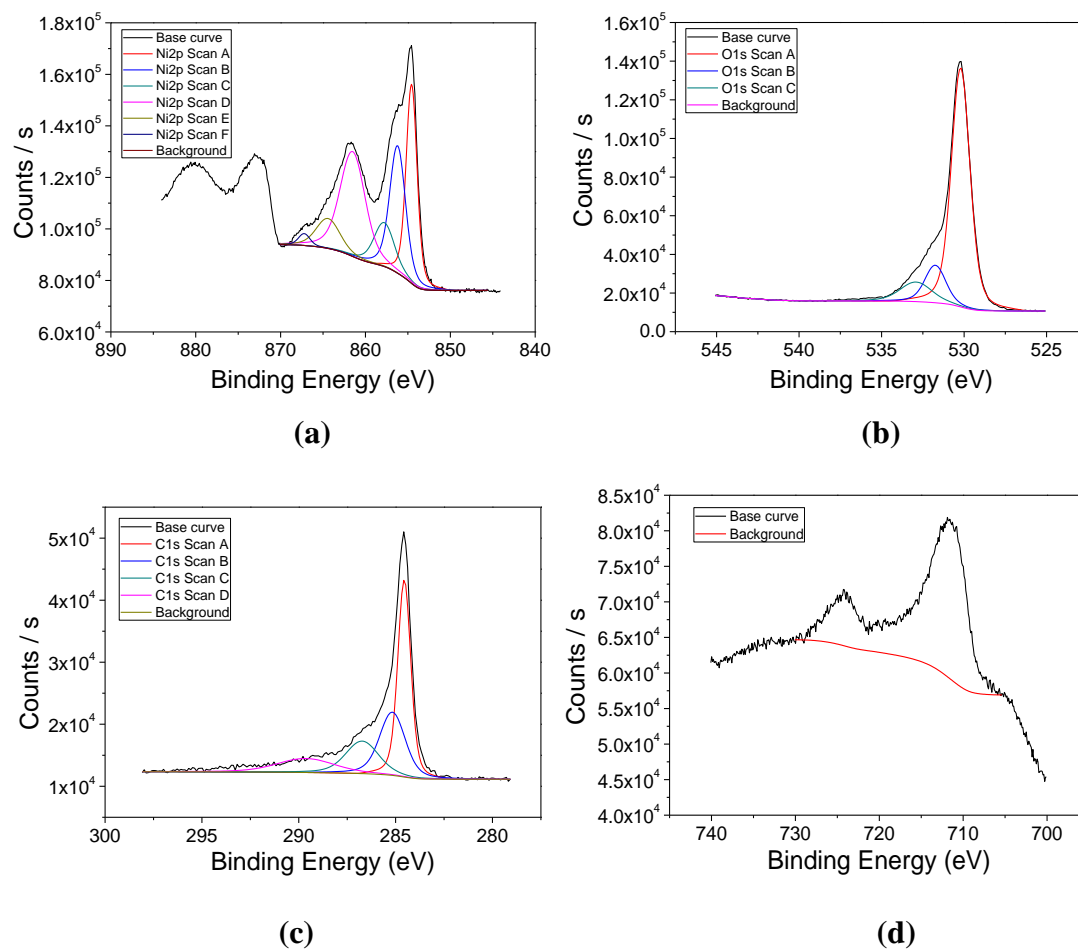


Figure 5.27 XPS surface scan of the graphene coated sample (a) nickel element scan (b) oxygen element scan (c) carbon element scan (d) iron element scan

Table 5.4 XPS data of the graphene coated sample treated at 580^o C for 5 minutes

Name	Ni2p Scan A	Ni2p Scan B	Ni2p Scan C	Ni2p Scan D	Ni2p Scan E	Ni2p Scan F	O1s Scan A	O1s Scan B	O1s Scan C	C1s Scan A	C1s Scan B	C1s Scan C	Fe2p3
Peak Binding Energy (eV)	854.7	856.2	857.8	861.5	864.4	567. 2	530.2	531.7	532.9	284.6	285.2	286.7	711.6
Atomic %	4.16	3.88	1.71	5.1	1.38	0.27	34.36	6.09	4.83	13.39	8.56	5.63	6.42

The XPS depth profiling result of PP10 coated sample is shown in Figure 5.28(a). The depth etching speed is about 1nm/s. The depth profiling depth is about 600nm for PP10 coated sample. From Figure 5.28(a), the nickel and oxygen are the major component of this layer. Oxygen still exist at 600nm and this means that the oxygen diffused inwardly deeper than 600nm after the thermal treatment. The inward diffusion depth can be estimated to about 1 micron. However, the layer at 600nm depth may consist of both pure nickel and nickel oxides because the amount of oxygen at 600nm is not enough to react with nickel. The atomic percent of carbon reduces steadily from 15% to 5% through the coating layer. For the PPG coated samples (Figure 5.28 (b)), the depth profile is different from the PP10 coated sample. The atomic percent of nickel is very low at the surface and increases gradually along with the etching depth. The atomic percent of oxygen is a little higher initially and reduces to about 20% along with the etching depth, which is similar to the PP10 coated sample. The trend of iron atomic percent is also similar to PP10 coated sample. However, the trend of carbon atomic percent is distinguished from the PP10 coated sample. The atomic percent of carbon is high at the initial and drops significantly to 15% within a short etching depth. At the deepest spot, carbon atomic percent is about 5% which is similar to PP10 coated sample.

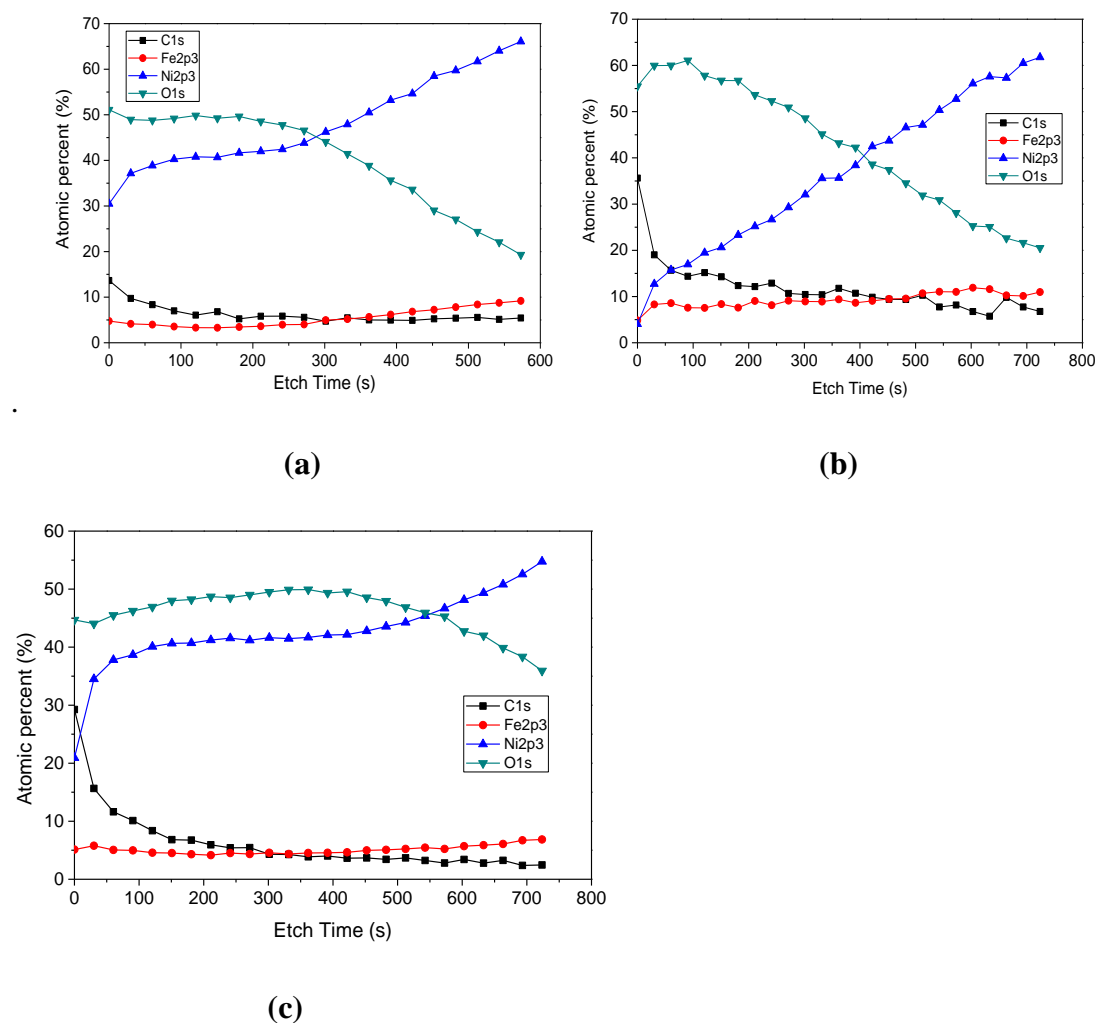


Figure 5.28 XPS depth profiling of (a) PP10 coated sample (b) PPG coated sample (c) the graphene coated sample

From Figure 5.28(c), the trends of atomic percent of carbon and iron are similar to PPG coated sample. The trend of nickel atomic percent is similar to PP10 coated sample but the initial atomic percent is 10% lower. Oxygen atomic percent changes differently from the other two coated samples. It is also high initially but it increases first and then reduces to 35% instead of 20%. The layer at about 750nm deep still contains large quantity of oxygen element.

From the XPS depth profiling results, the three coated samples have some similar features and this may be resulted from same substrate is used and all the coated particles are carbon based. The differences between these three samples may

because of the size and thickness of the coating carbon based particles used. However, the carbon based particles coated on 13KE21 substrate are not distributed uniformly and, therefore, the randomness of the selected site of the XPS depth profiling analysis needs to be considered. As a result, solid conclusion about the relationship between different types of carbon based particles and the surface composition of the coated samples still cannot be drawn.

5.4 Conclusions

Graphite and graphene particles were deposited on to steel substrates successfully by EPD and thermal treatment after EPD coating was adopted to improve the adhesion. Graphite and graphene particle were bound on to the steel substrates successfully. The electrical conductivity of the steel was improved significantly with improved EPD and thermal treatment conditions. The best electrical conductivity of the coated steel is 10 times higher than that of the steel substrate. The best thermal temperature is about 580°C and the best thermal treatment time is about two minute. The optimum EPD conditions are 0.175 mg/ml iodine concentration, 20 or 40V EPD voltage and 1 minute deposition time. The binding mechanism of thermal treatment is a simple mechanical binding.

The steel substrate used initially was Black Plate. Different steel susbtrates were used to investigate the possibility of duplicate the coating process on other steel substrates. Only 13KE21 steel can bind graphite and graphene particles after thermal treatment and other types of steel were not able bind the particles. The surface treatment of the steel susbtrates has a significant effect on the EPD process and steel oxidation. Any surface treatment that can retard steel oxidation has a detrimental effect on the binding of graphite and graphene particles on steel during thermal treatment. Higher temperature and longer treatment time can progress steel oxidation and bind the particles on the steel susbtrates. However, the process will require more energy and

become time inefficient, which is bad for future industrial scale-up. The porous structure of the iron oxides layer has a detrimental effect on the corrosion resistant of the coated steel substrates. The conditions and different solvent systems of EPD process need to be investigated to further identify the optimized conditions and system for carbon based EPD coatings. In addition, a protective coating can be applied onto the thermal treated samples to improve its corrosion resistant without compromising the electrical conductivity significantly to achieve a coating system with good conductivity and good corrosion resistant. In this case, PU/graphene anti-corrosion coating can be used as the protective layer. However, thermal treatment is one of the route that can improve the adhesion between carbon based particles and steel. Other routes can be developed to solve the adhesion problems and achieve an adherent and high electrical conductivity coating layer on steel

References

- [1] Honeycombe RWK, Bhadeshia HKDH. Steels : microstructure and properties. 2nd ed. London : Edward Arnold; 1995.
- [2] Chevalier S, Caboche G, Przybylski K, Brylewski T. Effect of nano-layered ceramic coatings on the electrical conductivity of oxide scale grown on ferritic steels. *J Appl Electrochem* 2008;39:529–34.
- [3] Zhang D, Duan L, Guo L, Tuan WH. Corrosion behavior of TiN-coated stainless steel as bipolar plate for proton exchange membrane fuel cell. *Int J Hydrogen Energy* 2010;35:3721–6.
- [4] Bonastre J, Garc ía P, Galv án JC, Cases F. Characterisation and corrosion studies of steel electrodes covered by polypyrrole/phosphotungstate using Electrochemical Impedance Spectroscopy. *Prog Org Coatings* 2009;66:235–41.

- [5] Show Y, Nakashima T, Fukami Y. Anticorrosion coating of carbon nanotube / polytetrafluoroethylene composite film on the stainless steel bipolar plate for proton exchange membrane fuel cells. *J Nanomater* 2013;2013:1–7.
- [6] Lee YB, Lim DS. Electrical and corrosion properties of stainless steel bipolar plates coated with a conduction polymer composite. *Curr Appl Phys* 2010;10:S18–21.
- [7] Wang Y, Northwood DO. An investigation into polypyrrole-coated 316L stainless steel as a bipolar plate material for PEM fuel cells. *J Power Sources* 2006;163:500–8.
- [8] Gannon PE, Tripp CT, Knospe AK, Ramana CV, Deibert M, Smith RJ, et al. High-temperature oxidation resistance and surface electrical conductivity of stainless steels with filtered arc Cr–Al–N multilayer and/or superlattice coatings. *Surf Coatings Technol* 2004;188-189:55–61.
- [9] Ho WY, Pan H, Chang CL, Wang DY, Hwang JJ. Corrosion and electrical properties of multi-layered coatings on stainless steel for PEMFC bipolar plate applications. *Surf Coatings Technol* 2007;202:1297–301.
- [10] Wei P, Deng X, Bateni MR, Petric A. oxidation behaviour and conductivity of UNS 430 stainless steel and crofer 22 APU with spinel coatings. *ECS Trans* 2007;7:2135–43.
- [11] Rashtchi H, Sani MAF, Dayaghi AM. Effect of Sr and Ca dopants on oxidation and electrical properties of lanthanum chromite-coated AISI 430 stainless steel for solid oxide fuel cell interconnect application. *Ceram Int* 2013;39:8123–31.
- [12] Singh V, Joung D, Zhai L, Das S, Khondaker SI, Seal S. Graphene based materials: past, present and future. *Prog Mater Sci* 2011;56:1178–271.

- [13] Lee C, Wei X, Kysar JW, Hone J. Measurement of the elastic properties and intrinsic strength of monolayer graphene. *Science* 2008;321:385–8.
- [14] Lee C, Wei X, Li Q, Carpick R, Kysar JW, Hone J. Elastic and frictional properties of graphene. *Phys Status Solidi* 2009;246:2562–7.
- [15] Kirkland NT, Schiller T, Medhekar N, Birbilis N. Exploring graphene as a corrosion protection barrier. *Corros Sci* 2012;56:1–4.
- [16] Ferrari AC, Bonaccorso F, Falko V, Novoselov KS, Roche S, Bøggild P, et al. Science and technology roadmap for graphene, related two-dimensional crystals, and hybrid systems. *Nanoscale* 2014.
- [17] Akhavan O, Ghaderi E. Toxicity of graphene and graphene oxide nanowalls against bacteria. *ACS Nano* 2010;4:5731–6.
- [18] Ishikawa R, Ko PJ, Kurokawa Y, Konagai M, Sandhu A. Electrophoretic deposition of high quality transparent conductive graphene films on insulating glass substrates. *J Phys Conf Ser* 2012;352:012003.
- [19] Chavez-Valdez A, Shaffer MSP, Boccaccini AR. Applications of graphene electrophoretic deposition. A review. *J Phys Chem B* 2013;117:1502–15.
- [20] Poirier D, Grandmaison EW, Matovic MD, Barnes KR, Nelson BD. High temperature oxidation of steel in an oxygen-enriched low NO_x furnace environment. *IFRF Combust J* 2006.
- [21] Rahmel A, Tobolski J. Influence of water vapor and carbon dioxide on the oxidation of iron in oxygen at high temperatures. *Corros Sci* 1965;5:333–4.
- [22] Sachs BK, Tuck CW. Scale growth during reheating cycles. *Mater Corros* 1970;21:945–54.

- [23] Cook EA, Rasmussen KE. Scale-free heating of slabs and billets. *IRON STEEL ENG* 1970;47:63–9.
- [24] Caplan D, Cohen M. Effect of cold work on the oxidation iron from 400-650 °C. *Corros Sci* 1966;6:321–35.
- [25] Leslie WC. The physical metallurgy of steels. Hemisphere Publ., Washington; 1981.
- [26] Atkinson A. Transport processes during the growth of oxide films at elevated temperature. *Rev Mod Phys* 1985;57:437–70.
- [27] Tylecote RF, Mitchell TE. Marker movements in the oxidation of iron and some other metals. *J Iron Steel Inst* 1960;196:445.
- [28] Baud J, Ferrier A, Manenc J, Benard J. The oxidation and decarburizing of Fe-C alloys in air and the influence of relative humidity. *Oxid Met* 1975;9:69–97.
- [29] Chen RY, Yuen W. YD. Review of the high-temperature oxidation of iron and carbon steels in air or oxygen. *Oxid Met* 2003;59:433–68.
- [30] Birks N, Meier GH, Pettit FS. Introduction to the high temperature oxidation of metals. Cambridge University Press; 2006.
- [31] Kofstad P. On the formation of porosity and microchannels in growing scales. *Oxid Met* 1985;24:265–76.
- [32] Rahmel A, Tobolski J. Einfluss von wasserdampf UND kohlendioxid auf die oxidation von eisen in sauerstoff bei hohen temperaturen. *Corros Sci* 1965;5:333–46.

- [33] Caplan D, Sproule GI, Hussey RJ, Graham MJ. Oxidation of Fe-C alloys at 700 °C. *Oxid Met* 1979;13:255–72.
- [34] Meyer JC, Geim AK, Katsnelson MI, Novoselov KS, Obergfell D, Roth S, et al. On the roughness of single- and bi-layer graphene membranes. *Solid State Commun* 2007;143:101–9.
- [35] Meyer JC, Geim AK, Katsnelson MI, Novoselov KS, Booth TJ, Roth S. The structure of suspended graphene sheets. *Nature* 2007;446:60–3.
- [36] Definition: Hematite. Webster's Online Dict 2013.
- [37] Qiu H, Hu X, Chen S, Fang F. Study on growth of oxide scale on high carbon steel at high temperature. *Appl Mech Mater* 2012;149:34–7.
- [38] Sun X, Song M. Highly Conductive carbon nanotube/polymer nanocomposites achievable? *Macromol Theory Simulations* 2009;18:155–61.
- [39] Jin J, Lin Y, Song M, Gui C, Leesirisan S. Enhancing the electrical conductivity of polymer composites. *Eur Polym J* 2013;49:1066–72.
- [40] Besra L, Liu M. A review on fundamentals and applications of electrophoretic deposition (EPD). *Prog Mater Sci* 2007;52:1–61.

Chapter 6 Electrical conductivity and anti-corrosion capacity of PU/graphene nanocomposite coatings

6.1. Introduction

Electricity Energy Storage (EES) is a process that converts electrical energy from generating plants into other forms that can be stored and convert back to electrical energy when needed. The EES technologies are widely used for either potable (mobile phone batteries) or stationary energy resources (pump hydroelectric storage) [1,2]. The technologies development is very fast which urge the EES industries to revolve. Apart from the traditional applications in utility and consumer use, there are a lot of new applications arisen such as renewable energy generation, smart house and electrical vehicles [3]. The future market potential of EES, driven by the extended utilization of renewable energy and the transformation of the energy sector, expands rapidly and will be much larger than the existing market which requires the EES industries to advance their technologies and products very fast. The general properties of EES are energy capacity, power, discharge time, lifetime and unit sizes. The electrical conductivity of the components in the EES devices relates to the energy capacity, power, discharge time and even unit sizes while the corrosion resistance of the components is one of the factors that determine the lifetime of EES devices [3,4].

When EESs are in service, the materials of the EES contact different environments, some of which are very corrosive (i.e. metal panels in fuel cell). The reactions between the materials and the environments will destroy or deteriorate the materials and this process is defined as corrosion [5]. Corrosion causes tremendous economic loss and it is a significant part of the gross national production every year in USA [6]. and the estimated annual cost is about 2000-3000 dollars per inhabitant in 1985 [7]. The protection against corrosion is vital to reduce the cost of the products. There are several methods to protect the materials against corrosion (metals substrate in EES devices. The use of coating is the most popular one and about 90% of all metal

surfaces are covered with protective coatings. The protection efficiency of the organic coating is magnificent due to the fact that they are very thin (thickness ranges from 5 microns to 250 microns depend on the applications) [8]. There are three mechanisms of organic coating systems against corrosion: the physicochemical (barrier) mechanism, the electrochemical mechanism (inhibition or cathodic protection) and the adhesion mechanism [9]. Although organic coatings are ideal to protect metal substrates from corrosion, they may not be suitable for the protection of EES devices as their electrical conductivities are very low which will affect the performance of the devices. The protective coatings used for EES should possess good electrical conductivity and anti-corrosion properties [10]. Although the organic coatings have excellent anti-corrosion properties, they do not possess acceptable electrical conductivity. In terms of EIS measurement, the electrical resistance of the coating is used as the indication of its efficiency to block the ions that damage the metal substrates [8]. Therefore, an organic coating with excellent anti-corrosion properties may not have good electrical conductivity.

It is not easy to develop an organic coating with excellent electrical conductivity and anti-corrosion properties at the same time. The coating industry has been undergoing a continual change in technology in the last few decades. With the discovery of new materials and the change in international legislation, the formulation of coatings has been changed significantly. Graphene is a promising material and its potential use in coating is huge. The excellent properties of graphene and graphene based composites used as electrical conductive and anti-corrosion materials have been discussed in Chapter 2. The wide utilisation and excellent properties of PU make it an excellent candidate as anti-corrosion coatings. The combination of graphene and PU may be able to produce a coating with good electrical conductivity and anti-corrosion properties. The porous surface of the EPD coated metal substrates shown in Chapter 5 can be covered by PU/graphene nanocomposite coatings. The multi-layers coating system

will be discussed in this chapter as well. The coated samples will be characterised by EIS and four point probe test for anti-corrosion property and electrical conductivity respectively. The coating resistance obtained with different technique will be discussed.

6.2. Application of EIS in coating evaluation

6.2.1 Fundamentals of EIS

In an ideal circuit, the ability of a circuit element to resist the flow of electrical current can be defined according to Ohm's law. The resistance is the ratio between voltage E and current I ($R=E/I$). The resistor defined by Ohm's law is ideal resistor and it follows three simplifying properties: (1) the resistor always follows Ohm's Law no matter how current and voltage change; (2) frequency does not affect the value of resistance; (3) AC current and voltage signals through a resistor are in phase with each other [11]. However, the circuit element in reality exhibit more complex behaviour. Therefore, impedance is introduced to replace. Impedance is also a measure of the resistance against the flow of electrical current but not limited by the simplified properties mentioned above. The impedance of an electrochemical system is studied as a function of the frequency under an applied AC wave in electrochemical impedance spectroscopy. AC wave is the perturbation of the system. After the application of AC wave, a new steady-state will be reached after a certain time. The required time is known as the time constant, τ , and it is equal to $R \times C$ where R is the resistance in ohms and C is the capacitance in farads of the system. The ratio between the response and the perturbation is the transfer function. If the perturbation is AC potential, the response is current and the transfer function is impedance. In order to simplify the calculation, Laplace transformation is used to transfer the response and perturbation from a time domain into frequency domain. Therefore, fast processes can be studied in high frequencies region while slow processes can be investigated at low

frequencies region. As a result, the data at high frequencies may reveal dipolar properties, intermediate frequencies for bulk properties and low frequencies for surface properties [8].

When the perturbation is AC potential, impedance can be expressed as $Z = E/I$, where E is the potential and I is the current. There are two components contribute to impedance. They are resistors (resistive/real component) and AC circuit elements such as capacitors, inductors and so on (reactive/imaginary component). The reactive component affects not only the magnitude of the AC wave but also its phase (time dependent characteristic). For example, the resulted current waveform will not in phase with the applied voltage (for example, leads 90 °) when alternating voltage wave is applied to a capacitor. Hence, it would be convenient to use complex notation by incorporating the complex number j where $j^2 = -1$. Therefore, if a sinusoidal potential varying with time t is applied in a system as

$$E(t) = E_0 \exp(j\omega t) \quad (1)$$

Its response would be

$$I(t) = I_0 \exp(j\omega t - \theta) \quad (2)$$

$E(t)$ and $I(t)$ are the instantaneous values while E^0 and I^0 are the maximum values of the potential and current wave forms, respectively. Θ is the phase angle difference and ω is the angular frequency in radians given by $\omega = 2\pi f$. In order to keep the system linear, a low AC voltage of about 10 mV is usually applied [8,12].

Complex notation allows the impedance relationships to be understood and presented as Argand diagrams (Figure 6.1 (a)) in both polar coordinates (θ and $|Z|$) and Cartesian (Z' and Z''). The θ and $|Z|$ can be used to form the Bode impedance spectrum where those two are plotted against frequencies (Figure 6.1 (b) and (c) [13]) while the Z'' is plotted against Z' in Nyquist plot (Figure 6.1 (d) [14]). The use of Bode plots is recommended by Mansfeld because: (1) the measured points are

displayed equally while in Nyquist the majority of are cluster at both ends of the spectrum; (2) it is burdensome to label the curves in Nyquist plot with frequency marks; (3) resistor and capacitor regions can be distinguished clearly and the information provided by the change of phase angle as a function of frequency is an excellent indicator of small changes in the spectrum [15]. The degradation stages of a coating can be told from Bode plot as shown in Figure 6.1 (c). Combining the information obtained from Bode and Nyquist plots can understand the coating behaviour under corrosion.

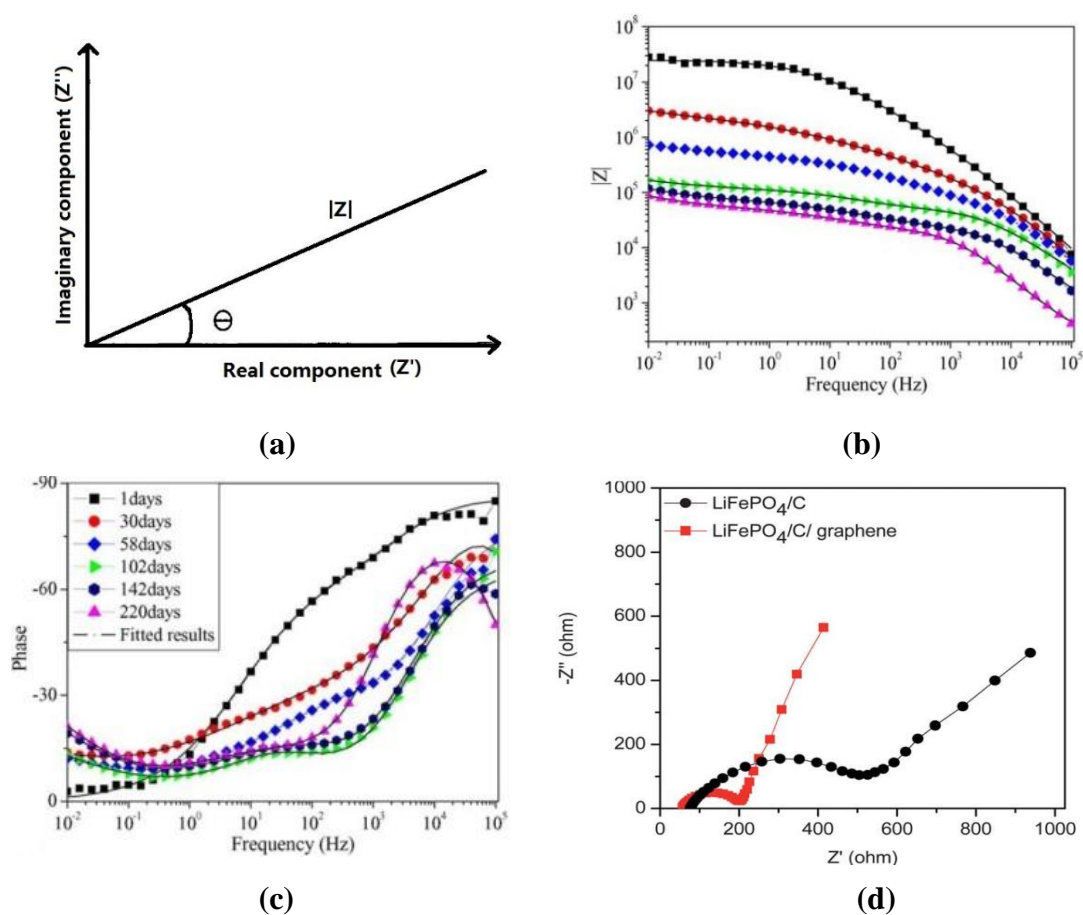


Figure 6.1 Images of (a) impedance vector (b) example Bode plot (c) example Bode plot with phase angle as Y axis (d) example Nyquist plot

6.2.1 Application of EIS in coatings

EIS is a very useful tool to investigate the coating behaviours under corrosion environment. Prediction of the lifetime of corrosion protection [16], comparison of

coatings systems [17], measurement of water uptake [18], the detection of changes due to exposure [19], identification of the corrosion mechanisms that lead to failure [20] and the build-up of models for coating system performance [21]. The coating has a tendency to memorize the past exposure event where each exposure to water and temperature damage the coating layer. As the exposure continues, the transport pathways with the coating are enlarged or created and water/electrolytes start to accumulate at the coating/substrate interphase where small-scale corrosion begins. The initiation of corrosion is the start of corrosion failure of the system but this only takes places when the barrier properties of coating layer begin to be weakened. The development of EIS data interpretation, modelling and test methodologies become more mature nowadays. Coating scientists are working hard to assimilate the data of EIS from different coating systems under different situation to develop meaningful understanding for the molecular level changes that happen during exposure processes. The effort that has done can be used to rank and predict the performance of a coating product. EIS is an excellent technique that offers the paths to understand the anti-corrosion properties, thermal properties and water solubility. Combining the technique with other testing protocols, the performance of the coating systems can be evaluated effectively [22]. In addition, EIS can provide accurate quantitative results of the behaviour of the coatings. However, there are some limitations in the utilisation of EIS: (1) the poor reproducibility of data with a variation in magnitude of up to three orders between repeated tests due to the heterogeneity of the coating; (2) it is difficult to derive a complete transfer function from the knowledge of reaction mechanisms due to the overlapped time constants; (3) the various coatings (topcoat, primer etc.) applied on the substrates cannot be distinguished by EIS [8]. Therefore, EIS is a powerful tool but not the only tool to investigate the corrosion behaviour of coatings.

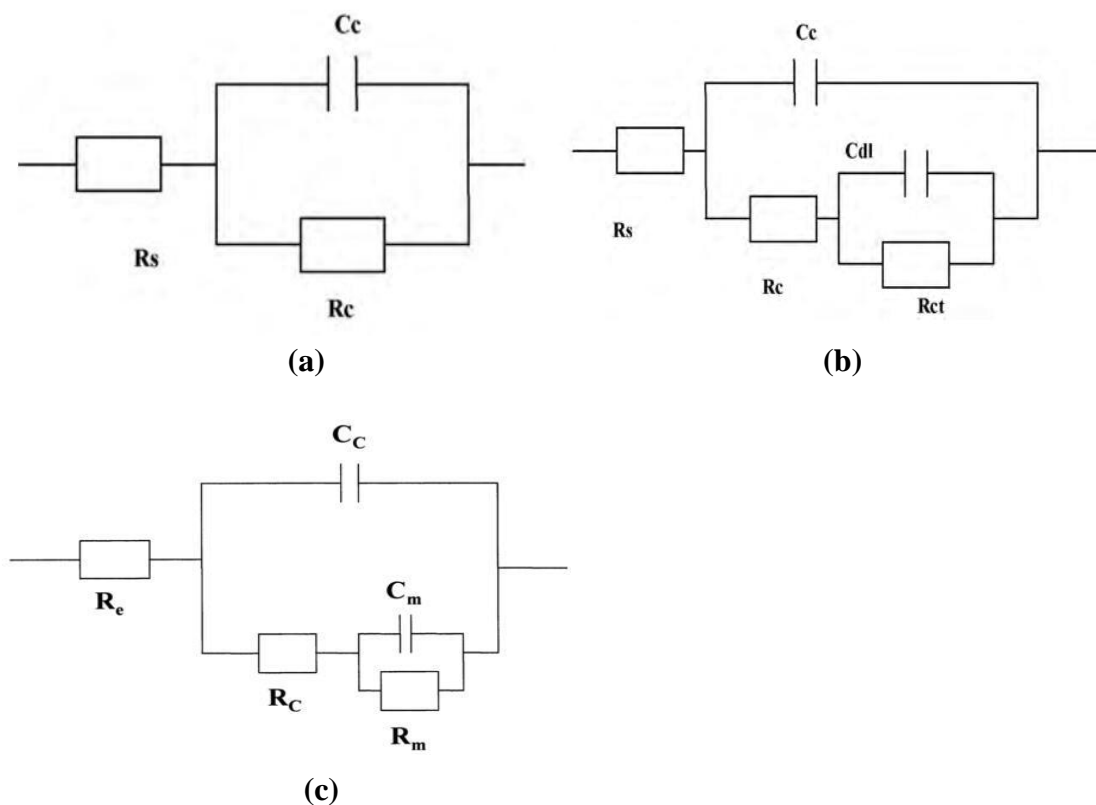


Figure 6.2 Images of equivalent circuits (a) simple Randles Circuit (b) coatings in the middle or at the end of degradation (c) coatings contain defects

Different models have been used to stimulate the coating in different situation. In the case of an undamaged coating, a simple parallel Randles Circuit (RC) (Figure 6.2 (a)) is good enough to interpret the data, but it is not sufficient to model complex systems. When the corrosive medium reaches coating/substrate interface, the EIS result obtained can be stimulated by the equivalent circuit shown in Figure 6.2 (b) [20]. When the coating contains defects, it is a damaged coating and, hence, an equivalent circuit other than RC should be used (Figure 6.2 (c)) [19]. Comparing Figure 6.2 (b) and (c), coating containing defect is similar to the coating in the middle or at the end of degradation. The presence of defects accelerates corrosion. In this project, EIS is used to predict the anti-corrosion properties of the prepared coatings and reveal the effect of graphene on the anti-corrosion properties. The equivalent circuits mentioned will be used to stimulate the results obtained.

6.3. The electrical conductivity of the nanocomposite coatings

6.3.1 PU conductivity

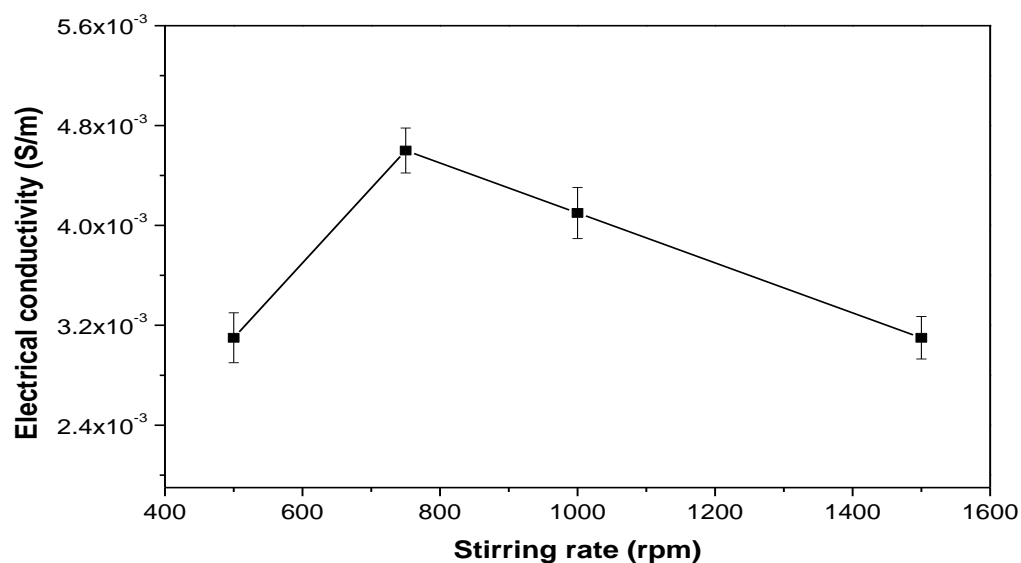


Figure 6.3 Plot of electrical conductivity versus stirring rate (topcoat trials)

Figure 6.3 shows the electrical conductivity versus stirring rate of 8 wt% PP10 filled PU topcoat. The stirring rates are selected according to general stirring rates used in TATA Steel. It seems that 750 rpm stirring rate is an ideal stirring rate to achieve higher conductivity. However, the conductivity only changed from 0.0032 to 0.0046 which indicates that stirring rate does not affect the electrical conductivity significantly. In addition, the electrical conductivity may actually near the same when the standard deviation is considered. Therefore, stirring rate did not have a profound effect on the electrical conductivity and the function of stirring is to disperse the particles uniformly in the coating.

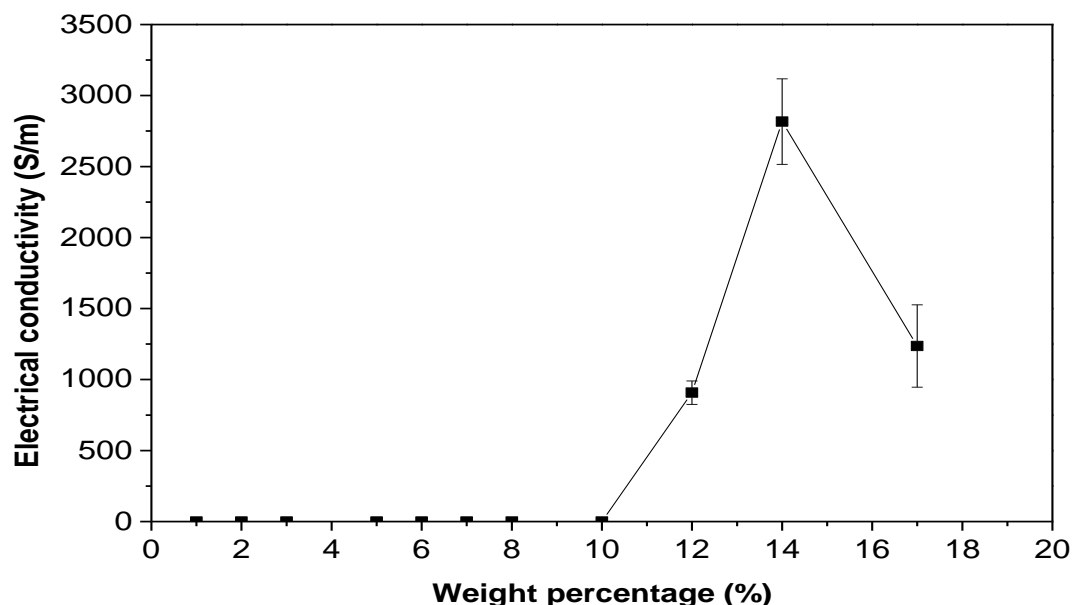


Figure 6.4 Plot of electrical conductivity *versus* PP10 weight percent for PPPU trials

Table 6.1 Electrical conductivity values of PPPU system

Code name	PPPU7500	PPPU8500	PPPU10500	PPPU12500	PPPU14500	PPPU17500
Electrical conductivity (S/m)	7.42E-4 ± 1E-4	3.2E-3 ± 3E-4	0.21 ± 0.01	907.75 ± 82	2816.9 ± 201.3	1336.2 ± 290.6

Figure 6.4 and Table 6.1 show the electrical conductivity of the coatings in PPPU trial. From the results, 14 wt% PP10/PU coating has the highest conductivity and the percolation threshold of this system is 7 wt%. The reason why 14 wt% PP10/PU coating has best conductivity is that the contact resistance and tunnelling resistance between the PP10 particles are the lowest. The distance between the dispersed PP10 particles in the PU matrix is the key factor that affects the electrical conductivity. A polymer composite can only be conductive when the distance between two conductive filler particles less than 2~3 nm [23]. With more PP10 particles added into the matrix, current can pass through the coating layer with less resistance which lead to higher electrical conductivity. However, if excessive amount of PP10 is added, the contact resistance between PP10 particles has a detrimental effect on the resulted coating's

conductivity. This is the reason why the electrical conductivity begins to drop when the PP10 loading is larger than 14 wt%.

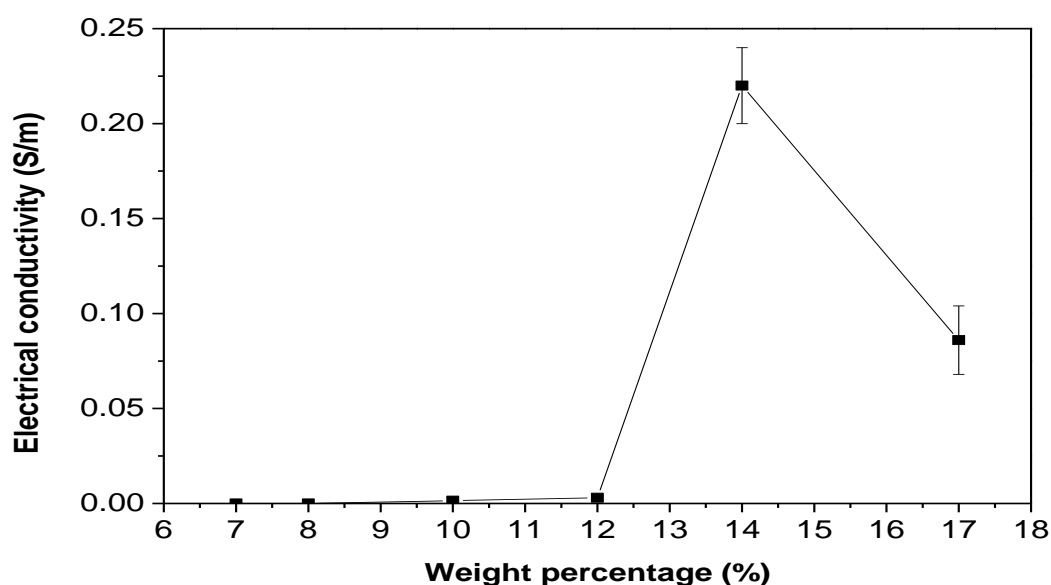


Figure 6.5 Plot of electrical conductivity *versus* PP10 weight percent for EPPPU trials

Table 6.2 Table 2 Electrical conductivity values of EPPPU system

Code name	EPPPU7500	EPPPU8500	EPPPU10500	EPPPU12500	EPPPU14500	EPPPU17500
Electrical conductivity (S/m)	0	0	$7\text{E-}4 \pm 1.2\text{E-}4$	$3.4\text{E-}3 \pm 1.9\text{E-}3$	0.22 ± 0.056	0.086 ± 0.019

Figure 6.4 and Table 6.2 show the electrical conductivity of EPPPU coating systems. EPPPU system is a two layers coating system where primer is underneath the top coating. Compared to PPPU system, similar trend of electrical conductivity *versus* PP10 weight percent is observed. In addition, the electrical conductivity of EPPPU coated samples are much lower than PPPU coated samples which indicate that the application of primer significantly reduce the electrical conductivity due to the insulation effect.

Table 6.3 Electrical conductivity of PPPU topcoat

Coating system	PU top coat	EPD + PU top coat
Electrical conductivity (S/m)	0.0032 \pm 0.0003	0.31 \pm 0.02

From Table 6.3, the application of EPD coating layer prior to PU topcoat can significantly enhance the electrical conductivity of the coating system. PU topcoat acts as barrier layer in this system. As a result of the deposited graphite layer has very high electrical conductivity, the electrical conductivity of the topcoat is improved because more electrical conductance is presented in the system. In addition, the distance between the EPD layer and the PU topcoat is very close and, therefore, the tunnelling resistance is very low.

6.3.2 Primer conductivity

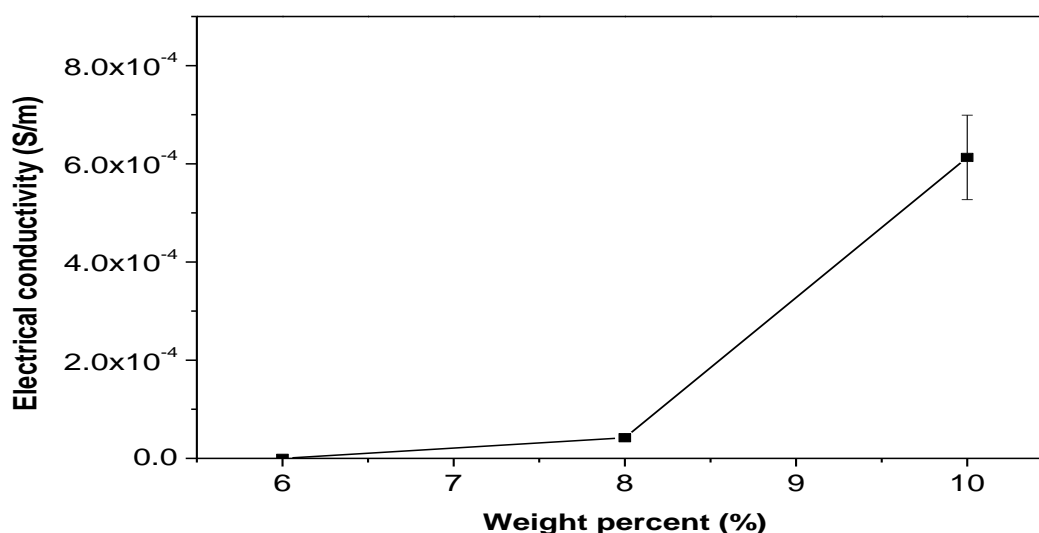
**Figure 6.6 Plot of electrical conductivity *versus* PP10 weight percent for EPP primer trials**

Table 6.4 Electrical conductivity EPP system

Code name	EPP6500	EPP8500	EPP10500
Electrical conductivity (S/m)	0	$4.21\text{E-}5 \pm 7.4\text{E-}6$	$6.13\text{E-}4 \pm 2.16\text{E-}4$

Figure 6.6 and Table 6.4 show the electrical conductivity of the coatings in EPP trial. From the results, the percolation threshold of this system is 8wt%. Compared to the electrical conductivity of conductive top coat, the electrical conductivity values of primer/PP10 composite coating are generally lower. The reason is that the primer has higher viscosity than PU top coat. Agglomerates of PP10 particles were formed during stirring and the particles could not be dispersed effectively. As discussed before, the distance between the dispersed PP10 particles in the coating is the key factor that affects the electrical conductivity. With agglomerates of PP10 particles formed, the distance between each particle will be larger and the tunnelling resistance will be increased. Higher viscosity of primer system leads to poorer electrical conductivity performance than PU top coat system.

6.3.3 Hybrid filler system and multi-layer coating

Table 6.5 Electrical conductivity of hybrid filler PU topcoat system

Code name	HIPU81000	HIIPU81000	HIIPU81000
Electrical conductivity (S/m)	0.14 ± 0.01	2567.4 ± 235	$2\text{E-}3 \pm 2.8\text{E-}4$

In hybrid filler system, the addition of CNTs can improve the electrical conductivity of the system significantly as shown in Table 6.5. The tube shape CNT can act as a bridge between PP10 particles to form a conductive network. Therefore, the tunnelling resistance of this coating system is reduced significantly and the resistance of this system is mainly the contact resistance between filler particles. The addition of graphene does not show obvious enhancing effect. The addition of CNT can improve

the electrical conductivity of the coating significantly. The role of PP10 particles act as the island of the conductive network. Therefore, the combination of these bridges and islands allow the current to flow without high resistance.

Table 6.6 Electrical conductivity of hybrid filler primer system

Coating system	HIIIPP4500	HIIIPP8500
Electrical conductivity (S/m)	$4.2\text{E-}3 \pm 5\text{E-}4$	0.4 ± 0.12

From Table 6.6, the addition of MWCNTs into the system can significantly improve the electrical conductivity of primer system. However, the electrical conductivity hybrid filler epoxy primer is poorer than hybrid filler PU top coat with the same weight percent of hybrid filler incorporated. The results are as expected. With the addition of MWCNTs, the percolation threshold of epoxy primer system was much lower than the system where only PP10 was added. The high aspect ratios and tube shape of MECNTs can facilitate the formation of conductive network in the coating system. As a result of MWCNTs' structure, the tunnelling resistance in the coating system is reduced significantly.

Table 6.6 Electrical conductivity of hybrid filler primer system

Code name	MI(1)	MI(2)	MII(1)	MII(2)
Electrical conductivity (S/m)	4.92 ± 0.78	1.71 ± 0.28	2.54 ± 0.29	1.14 ± 0.18

After the trials of hybrid filler system, the produced coatings were used to investigate the performance of multi-layers coating. The electrical conductivity of the multi-layer coating systems are shown in Table 6.6. From both trials, the systems (MI(1) and MII(2)) containing EPP8500 primer have higher conductivity. Comparing the three layers and two layers coatings (MII), the three layers coating systems (MI) have

higher conductivity due to the EPD coating layer. However, multi-layers coating systems have much lower electrical conductivity than single layer coating system. With the application of second coating layer, the tunnelling resistant and contact resistance of the whole system will be increased because the addition of extra insulation polymeric component in the system. In addition, the interface between two coatings may act as insulated layer because they polymers near the interface act as barrier to separate the conductive particles between the two coatings. The tunnelling resistance of the whole system will be increase significantly as the conductive particles are not close enough to each other to let the current pass through without much resistance. The application of EPD layer can only improve the electrical conductivity of the whole coating system a little because the insulation effect resulted from the polymeric component is too significant.

Table 6.7 Electrical conductivity of second set of hybrid filler primer

Code name	HIVE 21000	HVE21000	HVIE21000
Electrical conductivity (S/m)	1.96E-3 ± 3.6E-4	4.8E-4 ± 7.2E-4	2.26E-3 ± 5.34E-4

In order to improve the electrical conductivity of the coating further, a new filler TEG was utilized. Table 6.7 shows the electrical conductivity of coating contained different ratios of hybrid fillers. From the results, the sample with the TEG to MWCNTs ratios of 2:1 (HIVE21000) has the lowest electrical conductivity while the electrical conductivity of HIVE21000 and HVIE21000 is the nearly same. MWCNTs could act as bridge between TEG particles so the current can pass through the sample with less resistance and, therefore, the electrical conductivity of the samples increases with more MWCNTs in the hybrid filler. However, the bridging effect of MWCNTs becomes less profound when MWCNTs to TEG ratio is bigger than 1. Hence, the effect of weight percent on electrical conductivity was investigated by fabricating

HIVE samples with different weight percent of hybrid fillers.

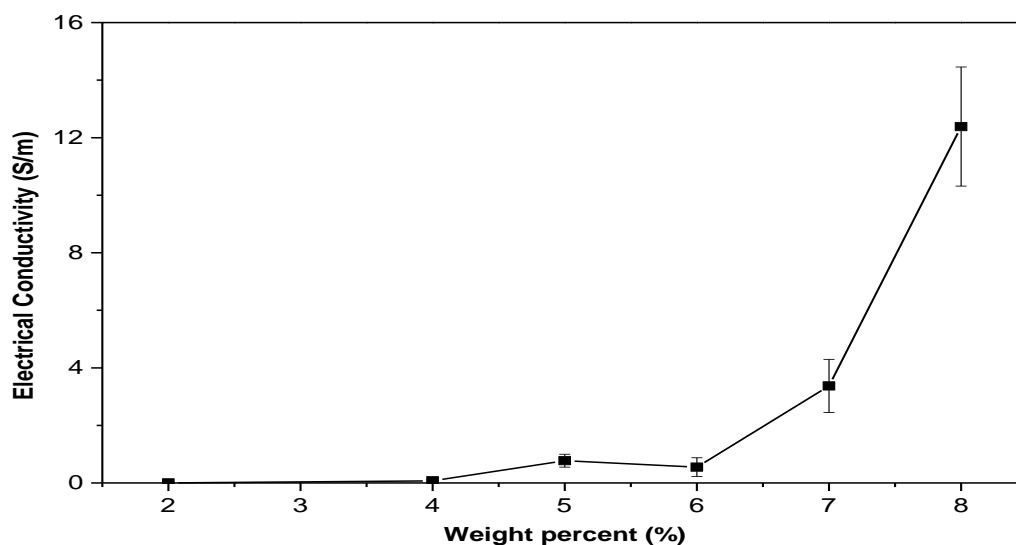


Figure 6.7 Plot of electrical conductivity *versus* hybrid filler weight percent of HIVE

Table 6.8 Electrical conductivity, resistance, conductivity ratios of hybrid filler filled primer samples primer system

Code name	HIVE21000	HIVE41000	HIVE51000	HIVE61000	HIVE7000	HIVE81000
Electrical conductivity (S/m)	1.96E-3 ± 3.6E-4	0.073 ±0.013	0.77 ±0.22	0.54 ±0.32	3.37±0.93	12.37±2.1
Resistance (Ω)	1.16E6 ± 2E5	30849 ±581	3116 ± 465	5167 ±577	701±188	183±30
Conductivity ratios C_c/C_s	6.67E-7 ± 1.2E-7	2.51E-5 ±4.4E-6	2.62E-4 ± 7.6E-5	1.87E-4 ±1.1E-5	1.2E-3 ±3.15E-4	4.21E-3 ±7.04E-4

Figure 6.7 shows the electrical conductivity of HIVE samples contained different weight percent of hybrid fillers. The values of electrical conductivity resistance and conductivity ratios of HIVE samples are shown in Table 6.8. With the addition of hybrid filler, the electrical conductivity of primer increase significantly. The resistance of HIVE samples was lower than 1000 Ω when the hybrid filler weight percent was higher than 7 wt%. The percolation threshold of HIVE system was significantly

lower than the systems in the reports before. The addition of TEG provided superior electrical conductivity than the materials used before.

Table 6.9 Electrical conductivity comparison of the samples with and without salt

Code name	Electrical conductivity (S/m)	Resistance (Ω)	Conductivity ratios C_c/C_s
HVIE61000	0.2 \pm 0.04	11314 \pm 1047	6.85E-5 \pm 1.3E-5
HVIE61000 + salt	0.29 \pm 0.05	7905 \pm 1072	9.83E-5 \pm 2.03E-5

Salt (NaCl) addition can improve the electrical conductivity of the conductive primer systems as shown in Table 6.9. The sample with intermediate electrical conductivity of the hybrid filler primer was selected. Ions will be formed when salt dissolve in the epoxy primer system to act as electrical conductive island to reduce the tunnelling resistance further of the system. The concentration selected was according to the study of Song *et al* [23]. Excessive salt will reduce the electrical conductivity and might weaken the performance of the coating. In terms of anti-corrosion properties, the addition of salt might accelerate the corrosion process. The ions in the environment (electrolyte such as NaCl) need to migrate into the coating and react with the metal substrate. In the coating containing salt, the migration of ions from the environment to substrate might be easier and the failure of coating might be initiated earlier.

6.3.4 The Mechanisms of electrical conductivity

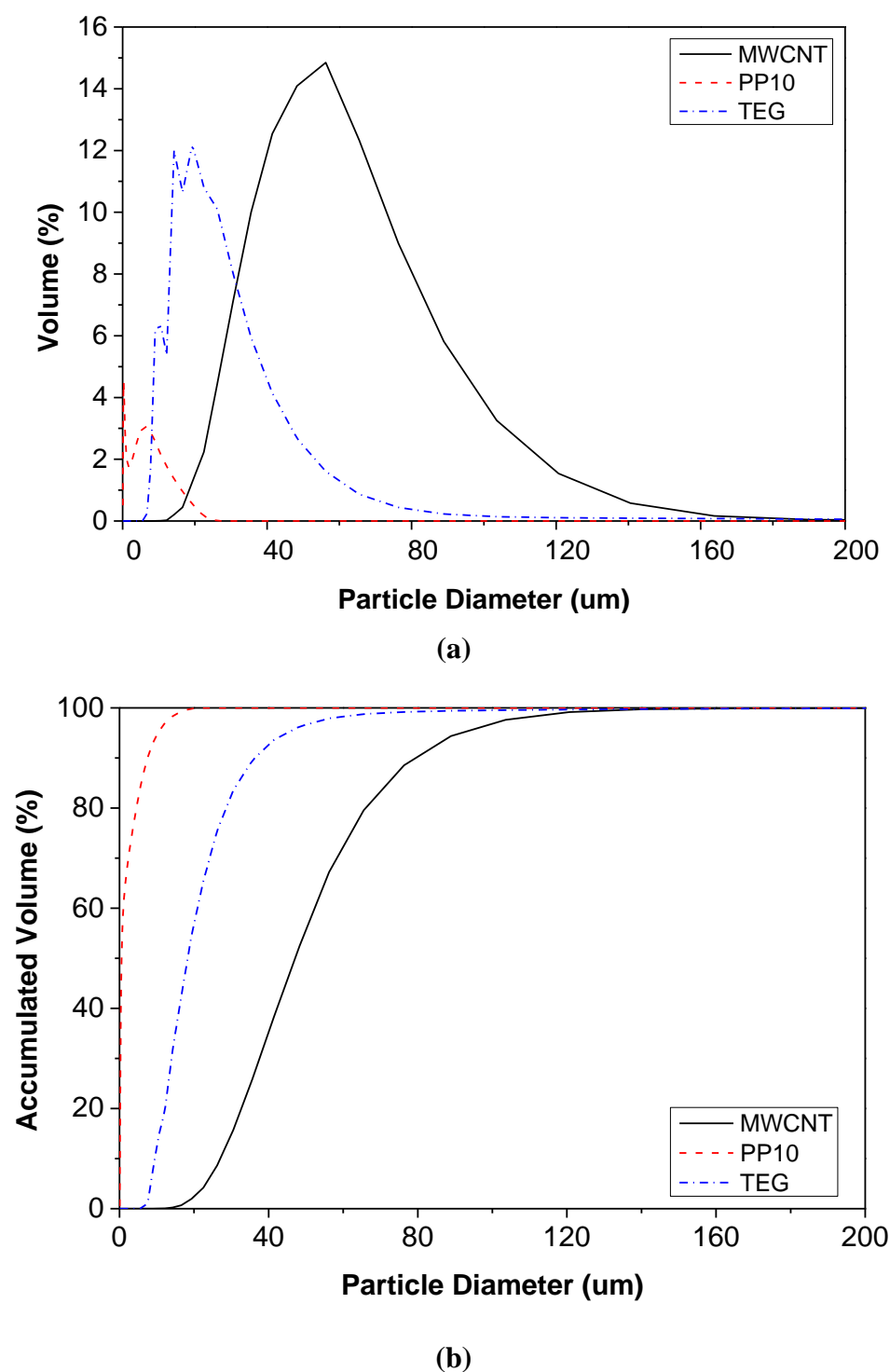


Figure 6.8 Plots of (a) particle size distribution of three different fillers (b) Accumulated volume versus particle diameter of three different fillers

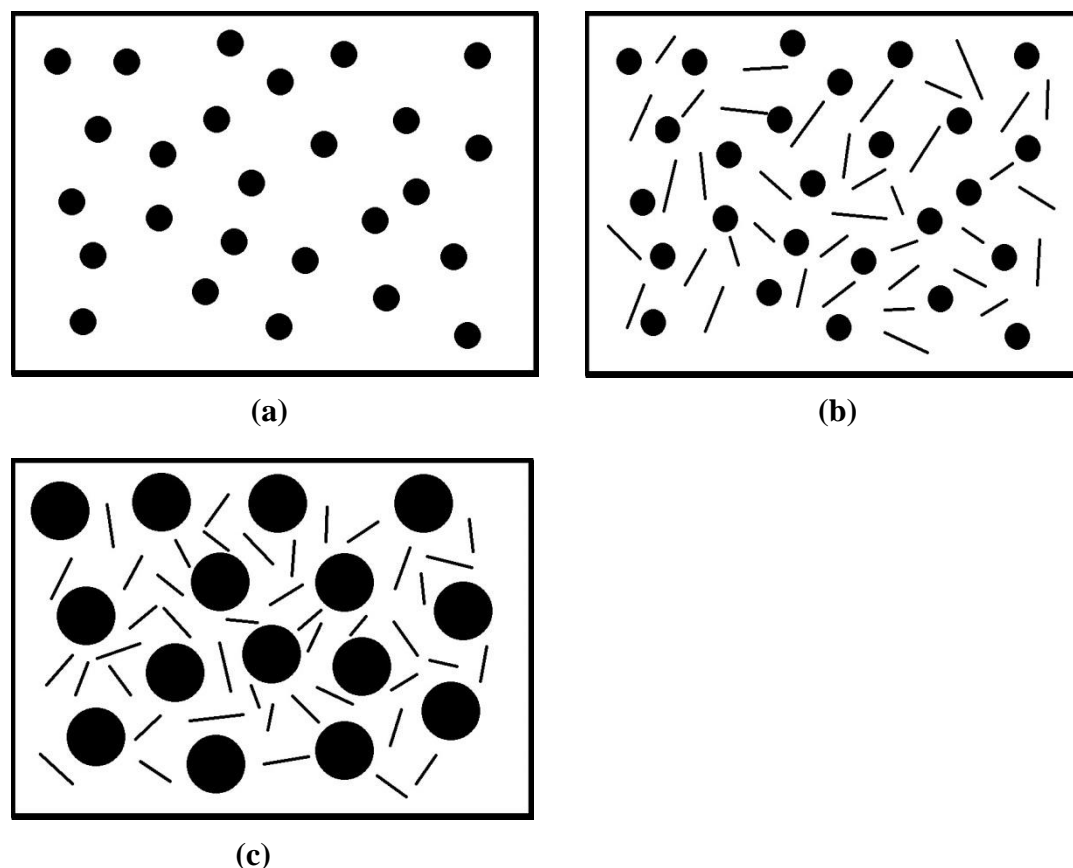


Figure 6.9 Scheme of the filler reinforced coating (a) PP10 (b) PP10 + MWCNT (c) TEG + MWCNT

The key of achieving high electrical conductivity in composite is to reduce the distance between the conductive particles. Increasing the weight percent of the conductive fillers is one of the effective methods. However, the cost of the filler and the reduction in coating properties are the major drawbacks. Hence, increasing the diameter of the filler particles is an alternative way to increase the electrical conductivity without increasing the cost and weakening the coating performance. Figure 6.8 show the particle size distribution and particle diameter of PP10, TEG and MWCNT. According to the previous result, the hybrid filler system using TEG and MWCNT had higher electrical conductivity. Hence, the bigger size particle can facilitate the formation of conductive network. Owing to the reduced distance between the conductive fillers in the system (as shown in Figure 6.9), the tunnelling resistance of the system is reduced significantly. As a result, the percolation threshold is reduced significantly and the electrical conductivity of the system is improved

remarkably. The selection of the filler is vital for the electrical conductivity enhancement.

6.4 The anti-corrosion property of the nanocomposite coatings

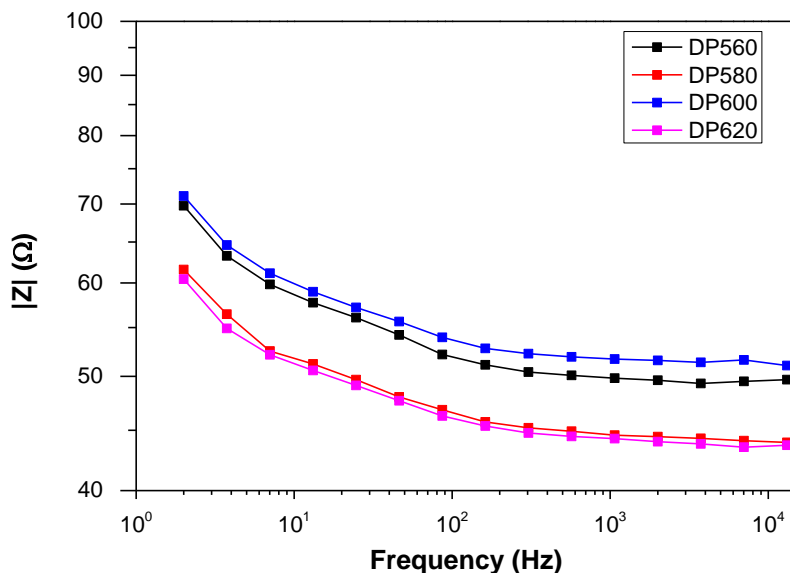
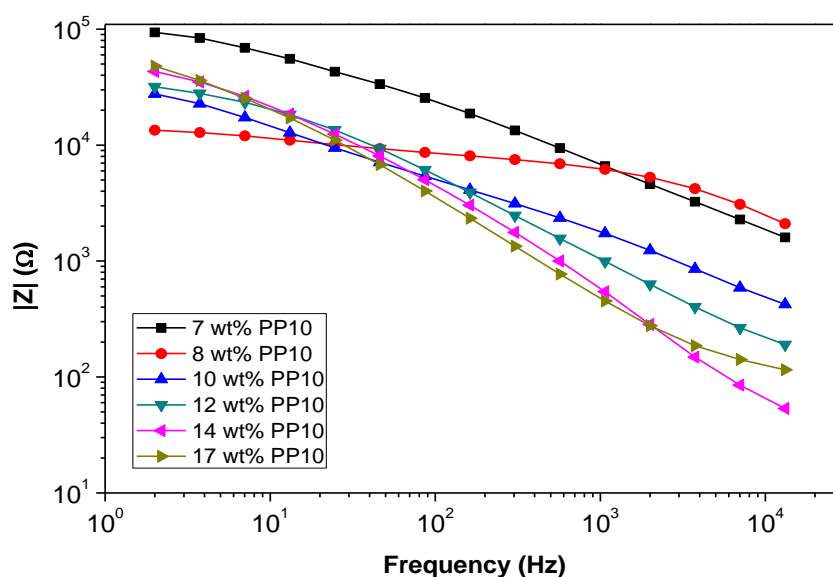


Figure 6.10 Bode plot of the samples with EPD coating (after heat treatment)

Figure 6.10 show the impedance *versus* frequency for some EPD samples after heat treatment. The maximum impedance in Bode plot is a good indication of the coating protection against corrosion [24]. In terms of steel substrate, a good protective organic coating should have the maximum impedance value above $10^6 \Omega$ [25]. The results shown in Figure 6.10 are much lower than the standard. Owing to the porous nature of the EPD coating, it cannot act as an effective coating against corrosion.



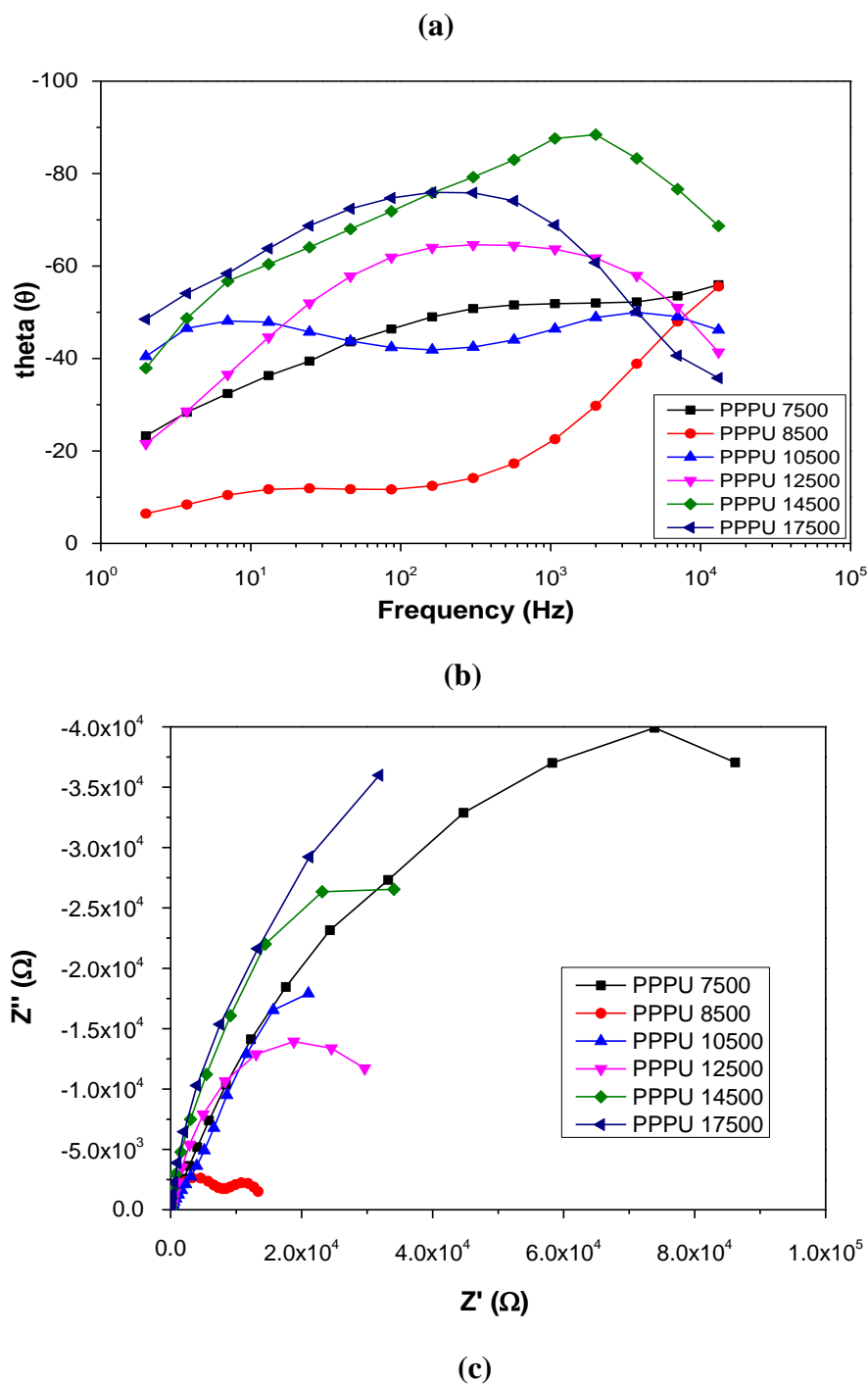
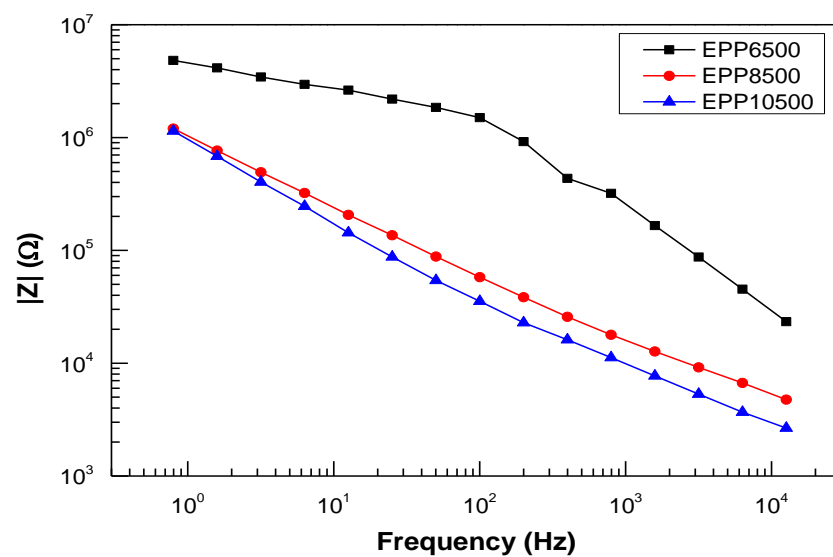


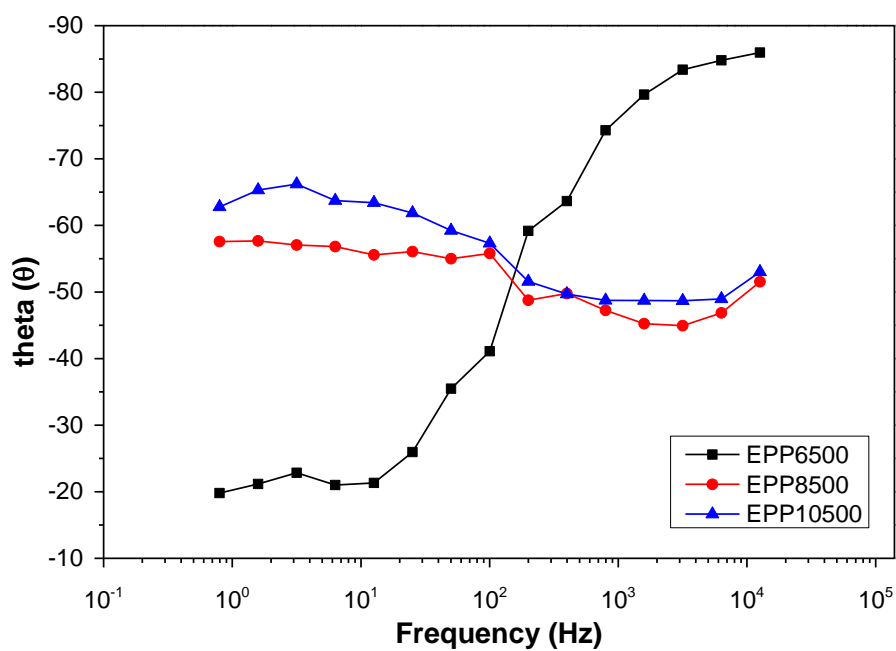
Figure 6.11 EIS results of PPPU trial (a) Bode plot (b) Bode phase angle plot (c) Nyquist plot

The EIS results of PPPU trial are shown in Figure 6.11. The maximum impedance in this frequency range decreases with filler weight percent first and then increases with filler weight percent but the impedance of the sample with 17 wt% PP10 is lower than

that with 7 wt% PP10. PU/7 wt% PP10 topcoat has the highest maximum impedance while PU/8 wt% has the lowest maximum impedance. Although, most of the samples display characteristic of effective barrier film in Nyquist plot, the maximum impedances of all the samples are below $10^6 \Omega$ which indicate that they cannot serve as a good protective coating while maintaining high electrical conductivity. With the increase of PP10 loading, the coating structure was damaged but the diffusion pathways for the corrosive medium was prolonged. That is the reason why the maximum impedance decreases with filler loading first and then increase. The appearance of second semi-circle in Nyquist plot (Figure 6.11 (c)) suggests that the barrier effect of the film is partially lost and the metal substrate can contact the corrosive medium. All the coatings are tested without any long time exposure to corrosive environment. Therefore, the heterogeneity and the defects induced during preparation are accounted for this phenomenon. The Bode phase angle plot can be used to evaluate the degradation stages of a coating. From Figure 6.11 (b), PPPU 12500, 14500 and 17500 are approaching to the phase 2 of degradation where the corrosion starts. PPPU 7500 and 10500 are in the phase 1 of degradation where water start to penetrate the coating layer. PPPU 8500 is in the phase 3 of degradation where severe corrosion occurs [19]. Although PPPU 10500 has lower impedance, the lifetime may be longer than PPPU 12500, 14500 and 17500.



(a)



(b)

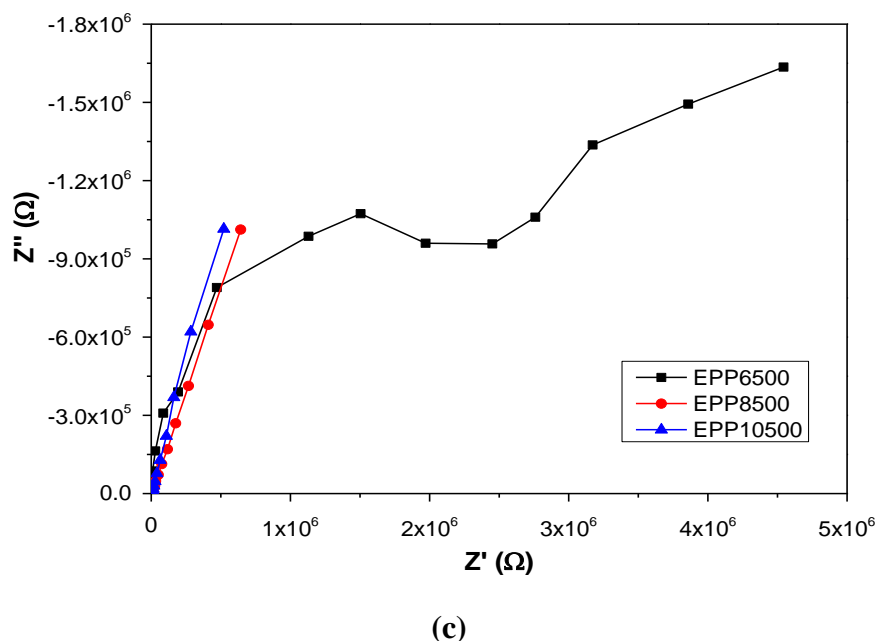
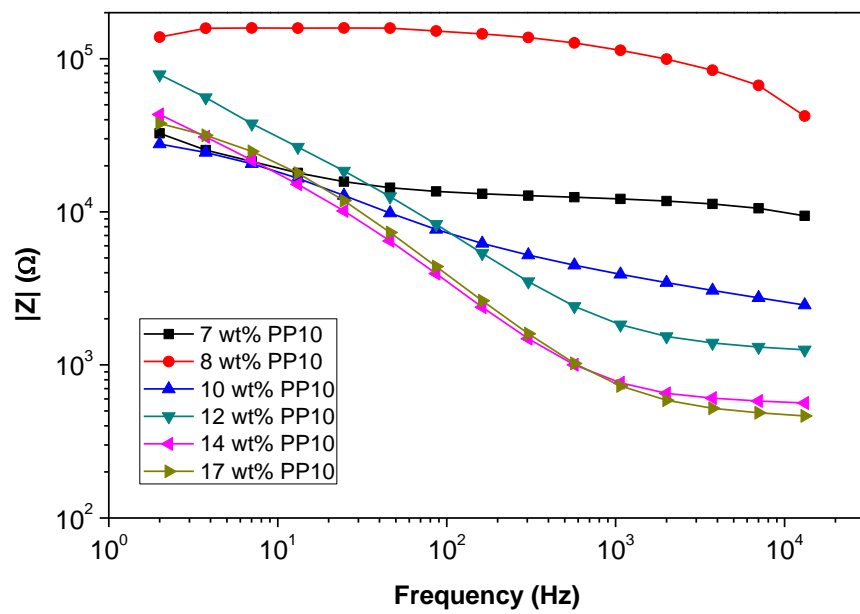
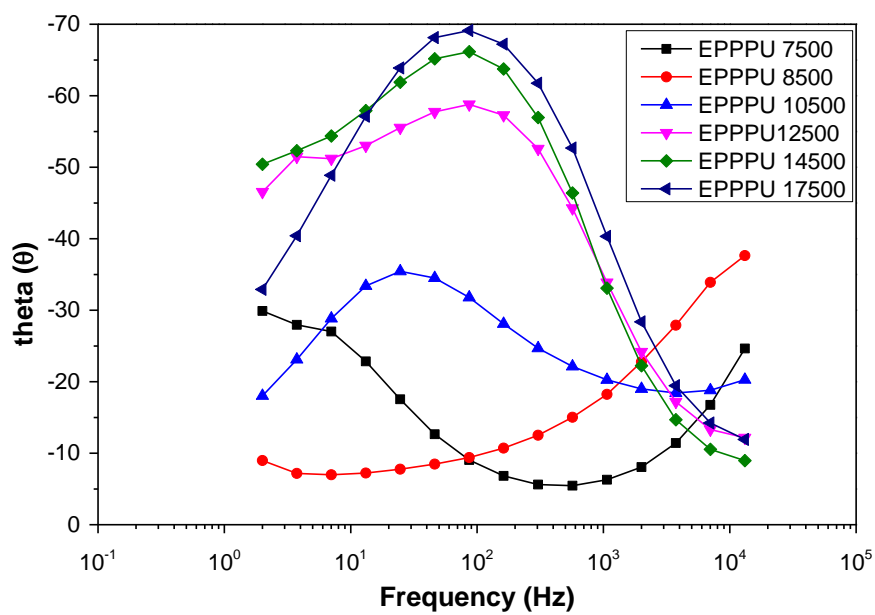


Figure 6.12 EIS results of EPP trials (a) Bode plot (b) Bode phase angle plot (c) Nyquist

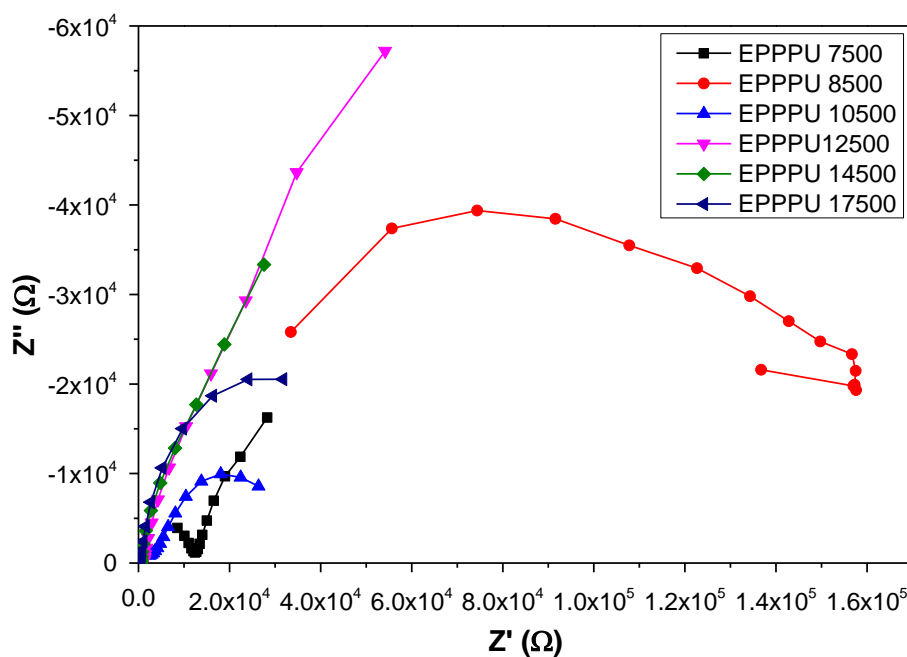
Compared to PU topcoat, the primer with same weight percent of PP10 has higher maximum impedance and, thus, the anti-corrosion property of primer is better than topcoat. All the coatings in EPP series can act as good protective coating for steel. The maximum impedance of the composite coating decreases with increasing PP10 weight percent. Hence, excessive filler is detrimental to the anti-corrosion property. From Figure 6.12 (b), all the coatings are in the phase 1 of degradation and EPP6500 has the best anti-corrosion property and lifetime. One time constant is identified in each curve of different samples in the Nyquist plot. The curve of EPP 6500 is unusual and the reason is still unknown.



(a)



(b)

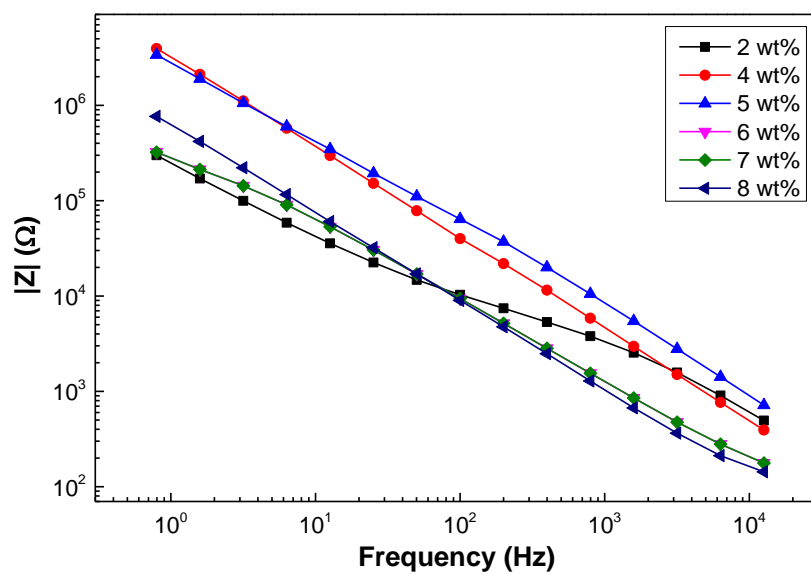


(c)

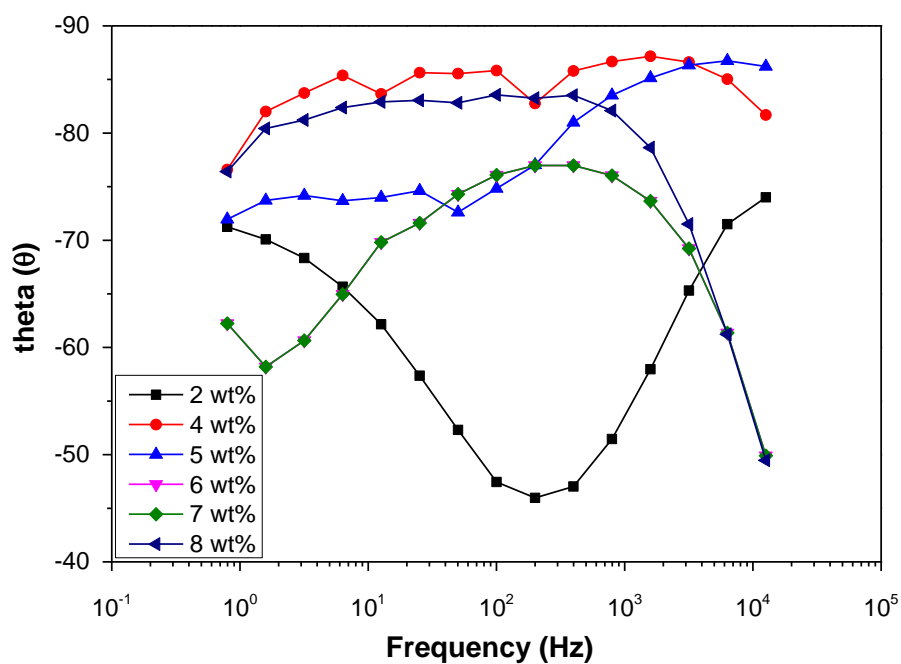
Figure 6.13 EIS results of EPPU trials (a) Bode plot (b) Bode phase angle plot (c) Nyquist

EPPPU series is a two-layers coating series where primer was applied on the substrate before topcoat. The results show that the maximum impedance of EPPPU is similar to PPPU. In theory, two-layer coating should have better anti-corrosion property than one-layer coating. Therefore, the quality of the two-layer coating is not good enough due to facility limitation. The produced coatings may be heterogeneous and contain defects. From the Nyquist, only EPP7500 has two semi-circles which indicate the loss of barrier property. The quality of EPP7500 is the worst. From the phase angle plot, EPP the quality of EPP12500, 14500 and 17500 seem to be worse than the other as they seem to be in the phase 2 of degradation. Their curves are quite similar to the curves of coatings exposed to corrosive environment for a period of time [13]. The results of the two-layer system are not reliable as the facility to prepare the coating is not ideal.

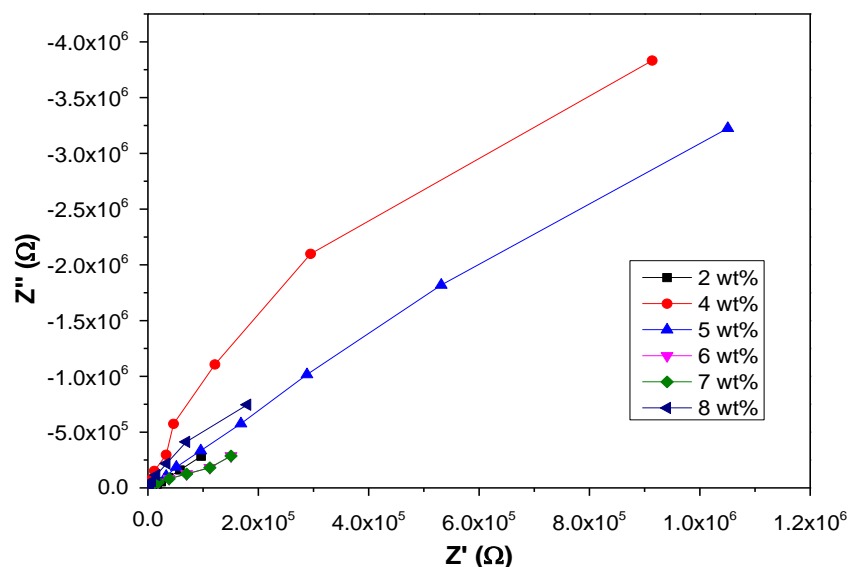
Hybrid filler system



(a)



(b)



(c)

Figure 6.14 EIS results of HIVE hybrid filler trials (a) Bode plot (b) Bode phase angle plot (c) Nyquist plot

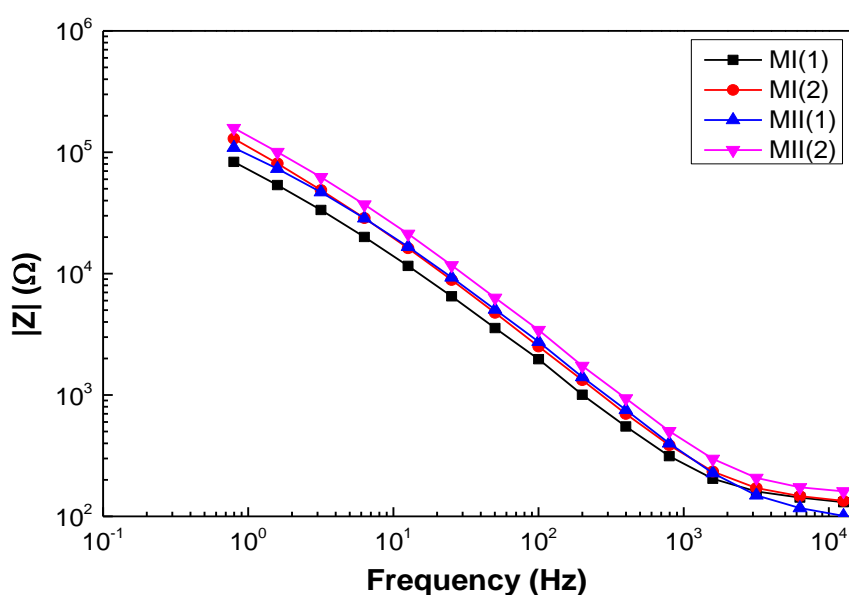
The EIS results of the hybrid filler primer trial are shown in Figure 6.14. The anti-corrosion property is better than PPPU series and worse than EPP series. The incorporation of hybrid filler actually weakens the anti-corrosion properties due to the high electrical conductivity. The maximum impedance increase with filler loading and then decrease after the loading is greater than 5 wt%. In this frequency range, only the coatings with 4 wt% and 5wt% filler meet the standard of good protective coating. From Figure 6.12 (b), all the coatings exhibit good protective effect except the 2 wt% and 7 wt%. The area selected for characterisation may be very heterogeneous where corrosive substance can penetrate through the coating easier. The results from Nyquist plot suggest that all the coatings have good barrier effect.

Table 6.10 Fit results of hybrid filler series from Randel

Filler weight percent (%)	$R_s(\Omega)$	R_s Error(%)	$C_c(F)$	C_c Error (%)	$R_c(\Omega)$	R_c Error (%)
2	2875	26.314	3.89E-07	21.331	2.70E+05	38.81

4	64.29	48.354	3.84E-08	2.7903	1.47E+07	27.323
5	72.31	57.096	4.67E-08	4.4497	1.07E+07	38.949
6	75.82	168.93	2.53E-08	7.6864	5.16E+06	25.54
7	143.2	25.074	1.74E-07	8.8187	3.42E+05	19.476
8	105.4	13.839	1.81E-07	4.1225	2.47E+06	30.837

The fit results from equivalent circuit are shown in Table 6.10. The results are used to compare the results of electrical conductivity to distinguish the concept of coating resistance in electrical conductivity and EIS. The equivalent circuits shown in Figure 6.2 are used for fitting. Randel cell has lower error percentage so the results from that are adopted. However, the two circuits used are not perfect for the system. Development of a more suitable circuit is necessary. In the table, R_s stands for the resistance of the substrate, C_c is the capacitance of the coating and R_c represent the resistance of the coating. Comparing the values of resistance in the electrical conductivity and EIS, the values are very different. Therefore, the coating resistance in EIS is an indication of coating resistance against ions but not the current resistance in the electrical conductivity. The coating resistance from EIS cannot be used to represent the electrical conductivity of a coating.



(a)

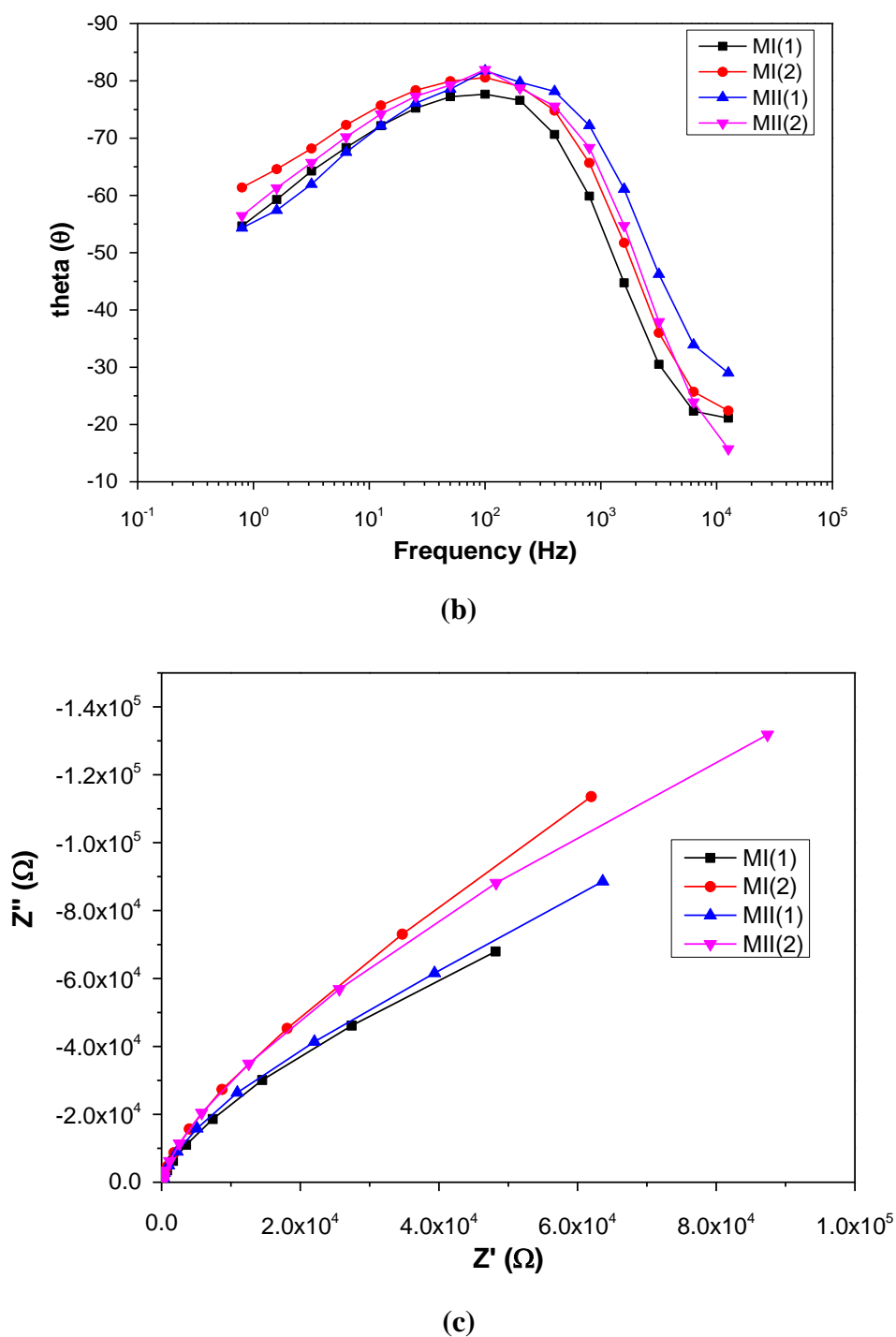


Figure 6.15 EIS results of HIVE hybrid filler trials (a) Bode plot (b) Bode phase angle plot (c) Nyquist plot

The EIS results of multi-layer coating are shown in Figure 6.12. The maximum impedance value obtained is similar to the two-layer coating system. However, the phase of degradation is different. Owing to the existence of porous EPD coating, the

anti-corrosion property is weakened compared to the system without EPD coating. All the coatings are in the phase 2 of degradation and the lifetime is shorter than usual coating. In addition, the defects and heterogeneity induced during preparation account for the weakened anti-corrosion properties as well.

6.5 The surface characterisation of the coated surfaces

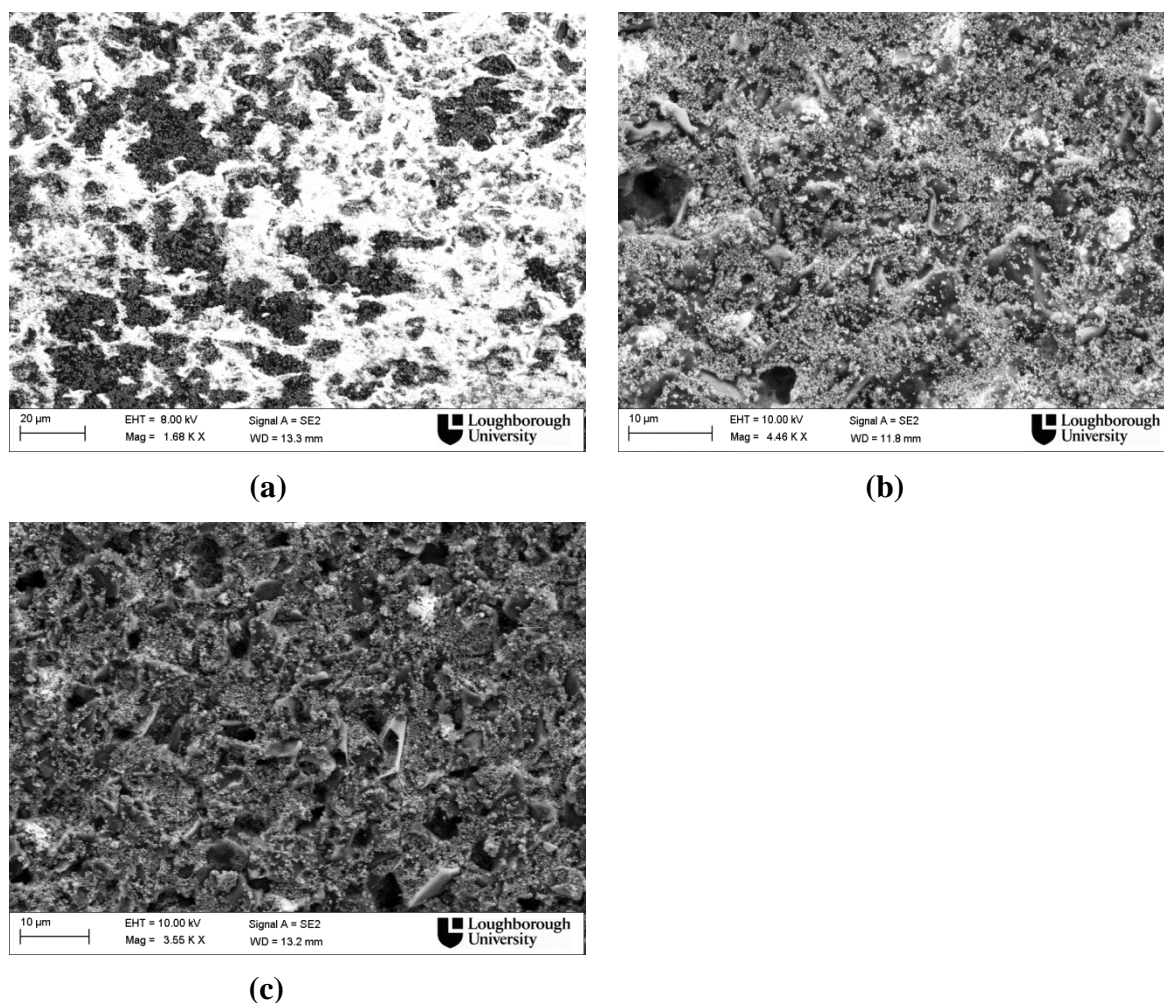


Figure 6.16 Example FEGSEM images of (a) PPPU 6500 (b) PPPU 10500 (c) PPU14500

FEGSEM is used to characterize the surface of the coating. From the images, coatings with higher weight percent of filler have less polymer coverage on the surface. Therefore, the porous nature of the coating surface leads to poor anti-corrosion capacity. Although polymer may present between the gaps of the fillers, the corrosive medium can still penetrate through the coating easier than the coating with proper

polymer coverage. The presence of high percentage of filler may affect the cure of the coating to hinder the polymer chains to react with each other for the formation of polymer network. Hence, the cure kinetic of reinforced PU coating needs to be investigated to reveal the effect of filler on the cure of coating.

6.6. Conclusions

Hybrid filler system has the best electrical conductivity and acceptable anti-corrosion capacity. The best filler ratios is TEG:MWCNT=1:1. Multi-layer coating system consist of EPD coating, conductive primer and conductive topcoat has superior electrical conductivity than single layer primer or topcoat. However, the anti-corrosion capacity is worse than single layer system due to the limited facility of coating preparation. The key to improve electrical conductivity is to reduce the distance between the conductive particles. The strategy of using particles with larger diameter and high aspect ratios to form conductive network is recommend. The cure of the coating may be affected significantly by the fillers. The study of cure kinetic of the composite is necessary.

References

- [1] Chen H, Cong TN, Yang W, Tan C, Li Y, Ding Y. Progress in electrical energy storage system: A critical review. *Prog Nat Sci* 2009;19:291–312.
- [2] Mclarnon F, Cairns E. Energy storage. *Ann Rev Energy* 1989;14.
- [3] Electrical Energy Storage project team. Electrical energy storage white paper. 2009.
- [4] EA Technology. Review of electrical energy storage technologies and systems and of their potential for the UK 2004.
- [5] Mattsson E. Basic corrosion technology for scientists and engineers. Ellis Horwood. Halsted Press; 1989.
- [6] Koch GH, Brongers MP, Thompson NG, Virmani YP, Payer JH. Corrosion

- cost and preventive strategies in the United States. 2002.
- [7] Wranglen G. An Introduction to corrosion and protection of metals. London: Chapman and Hall; 1985.
- [8] Amirudin A, Thierry D. Application of electrochemical impedance spectroscopy to study the degradation of polymer-coated metals. *Prog Org Coatings* 1995;26:1–28.
- [9] Funke W. Polymeric materials for corrosion control. In: Dickie RA, Floyd FL, editors. *Am. Chem. Soc. Symp., USA*; 1986, p. 222.
- [10] Woodman AS, Anderson EB, Jayne KD, Kimble MC. Development of corrosion-resistant coatings for fuel cell bipolar plates. *Proc AESF Annu Tech Conf* 1999:717–25.
- [11] AJ B, LR F, J L, CG Z. *Electrochemical methods: fundamentals and applications*. New York: Wiley; 1980.
- [12] Loveday D, Peterson P, Rodgers B. Evaluation of Organic Coatings with Electrochemical Impedance Spectroscopy Part 1: Fundamentals of Electrochemical Impedance Spectroscopy EQUIVALENT. *JCT Coatings Tech* 2004:46–52.
- [13] Jianguo L, Gaoping G, Chuanwei Y. EIS study of corrosion behaviour of organic coating/Dacromet composite systems. *Electrochim Acta* 2005;50:3320–32.
- [14] Shi Y, Chou S, Wang J, Wexler D, Li H, Liu H, et al. Graphene wrapped LiFePO₄/C composites as cathode materials for Li-ion batteries with enhanced rate capability. *J Mater Chem* 2012;22:16465–70.
- [15] Mansfeld F. Technical Note: Concerning the Display of Impedance. *Corrosion* 1988;44:558–9.
- [16] Hinderliter BR, Croll SG, Tallman DE, Su Q, Bierwagen GP. Interpretation of EIS data from accelerated exposure of coated metals based on modeling of coating physical properties. *Electrochim Acta* 2006;51:4505–15.

- [17] Mansfeld F. Use of electrochemical impedance spectroscopy for the study of corrosion protection by polymer coatings I ---I I. J Appl Electrochem 1995;25:187–202.
- [18] van Westing EPM, Ferrari GM, de Wit JHW. The determination of coating performance with impedance measurements-II. Water uptake of coatings. Corros Sci 1994;36:957–77.
- [19] Lavaert V, Moors M, Wettinck E. An EIS study of the influence of imperfections on the corrosion behaviour of an organic coated steel system. J Appl Electrochem 2002;32:853–7.
- [20] Zhu Y, Xiong J, Tang Y, Zuo Y. EIS study on failure process of two polyurethane composite coatings. Prog Org Coatings 2010;69:7–11.
- [21] Grundmeier G, Schmidt W, Stratmann M. Corrosion protection by organic coatings: electrochemical mechanism and novel methods of investigation. Electrochim Acta 2000;45:2515–33.
- [22] Bierwagen G, Tallman D, Li J, He L, Jeffcoate C. EIS studies of coated metals in accelerated exposure. Prog Org Coatings 2003;46:148–57.
- [23] Jin J, Lin Y, Song M, Gui C, Leesirisan S. Enhancing the electrical conductivity of polymer composites. Eur Polym J 2013;49:1066–72.
- [24] Costa JM, Mercer AD. Progress in the Understanding and Prevention of Corrosion. The Institute of Materials, London, UK; 1993.
- [25] Scully JR, Hensley ST. Corrosion, New Orleans, LA, USA: National Association of Corrosion Engineers; Paper No. 359.

Chapter 7 Cure dynamics of PU/graphene nanocomposites

7.1 Introduction

Thermoset materials are the materials that formed by pre-polymer *via* curing. In the industry, thermoset materials occupy a large portion of the market of the polymer products in the industry. The typical forming techniques for thermoset materials are reactive injection moulding, compression moulding and extrusion. The properties of the thermoset materials are highly dependent on the crosslinked-density, the extent of cure, polymer types and processing methods. The cure of thermoset materials usually triggered by heat and there are different stages of cure which allow the extent of cure can be controlled via adapting the cure temperature etc. [1]. It is important to study the factors that affect the cure and cure density of thermoset materials to maintain good control of the final products. Cure dynamics offers a microscopic view about the curing process of a thermoset material which can provide the information of cure time, cure temperatures, activation energy and so on [2]. In industry, the objective of manufacturing thermoset products is to produce a product with good green strength to resist deformation of damage during the process in a minimized time. Therefore, the information obtained from cure dynamics can help to gain better understanding of structure-property relations and to optimise the process conditions to achieve good results. In addition, the understanding of cure dynamic is significant to evaluate the feasibility and design of commercial polyurethane processing.

A number of characterization techniques can be used to study the cure dynamics and the cure reactions of thermoset materials including refractive index [3], electrical resistivity [4], density [5], FTIR [6] and DSC [7]. The polyurethane system consist of one part system (pre-polymer contains -OH and -NCO groups) and two-parts (each pre-polymer contains one reactive group). DSC and FTIR will be more suitable to monitor the chemical reaction of polyurethane. The trace of cure can be monitored

via the changes in concentration of reactive functional groups or the production of new chemical bonds during reaction. It has been widely adopted to monitor the cure dynamic and the development of polymer structure during the thermoset materials formation [8–10]. The specific absorption peak of the NCO groups (around 2280 cm^{-1}) is used as the variable during the process and C-H peak is used as a reference peak to compensate the effect of sample thickness and the background. The heat generated from the chemical reaction can be detected by DSC. In addition, the reaction heat release rate (reaction rate) can be monitored as well. Due to the simplicity and the ability to obtain thermal transition information, it is an effective characterisation technique to study the cure dynamic of polyurethane reaction. The reaction parameters can be calculated according to mathematic models fitting which will be discussed afterward.

Theoretically, the reaction rate of polyurethane reaction relates to the active hydrogen groups, the concentration of isocyanate groups and the catalyst. According to some researchers, the reaction mechanism of PU reaction is second order mechanism where the concentrations of hydrogen group and isocyanate group control the rate of reaction. The situation would be more complicated in reality and with the presence of filler. In addition, autocatalytic and diffusion effects exist during the polymerisation and phase separation of two reactants may takes place during reaction [16]. The incorporation of fillers can affect the degree of cure, reaction rate and the properties of the final composites. The effect of the graphene based materials on polyurethane was limitedly investigated while the effect of graphene based materials on epoxy resin was widely reported. Graphene had UV-shielding effect when low irradiation intensity was used to cure epoxy resin and the final product had a slightly decreased conversion. The shielding effect on high irradiation intensity was not identified [11]. The cure behaviour and thermal stability of graphene oxide (GO) reinforced on the two-parts epoxy resin (tetrafunctional tetraglycidyl-4, 4'-diaminodiphenylmethane with

4,4'-diaminodiphenylsulfone) was investigated by Qiu *et al* [12]. The enthalpies of the cure reaction of the composites were increased and the activation energies were lower than pure epoxy resin. Therefore, the presence of GO had catalyst effect and the effect was more profound with the increase of GO loading. The activation energies increased with GO loading in the initial stage while they decrease with GO loading in the latter stage. This phenomenon suggested that the addition of GO hindered the vitrification of the nanocomposites. Their results also suggested that the addition of GO decreased the thermal stability of the epoxy resin. Galpaya and his co-workers summarized the effects of graphene based materials in the epoxy resins [13]. The addition of GO might have catalytic effect and retardation effect on the cure of epoxy resin while graphene had retardation effect, catalytic effect and steric hindrance. Wang and his co-workers reported that GO had catalytic effect on the initial cyclomerization stage to PT30 ester polyurethane resin which reduced the cure temperature dramatically. In addition, GO had the steric hindrance effect which led to the elevated activation energy with the increase of GO content. 1 wt% GO was the most effective GO loading [14].

The reports of the cure dynamics of Graphene based materials/PU nanocomposites are limited. From the previous chapter, the network formation of PU coating was hindered with increasing graphene loadings. The addition of graphene or graphite had a significant effect on the cure of PU coatings. In this chapter, the effect of graphite, graphene and graphene oxide on the cure dynamic of two-part PU coating by Modulated Temperature DSC and FTIR.

7.2 Theories of the cure dynamic monitored by MDSC and FTIR

7.2.1 MDSC

Modulated temperature differential scanning calorimetry (MTDSC) is an extension version DSC where a modulated temperature input signal is used. This technique is

proved to be very useful for characterising many materials especially polymers [15,16]. The simultaneous measurement of the amplitude (modulus) of the complex heat capacity, the heat flow and the phase angle between heat flow and heating rate (heat flow phase) enables a more detailed study of complicated materials systems, both in quasi-isothermal and non-isothermal conditions. The thermal change and the transition took place during reaction can be detected by MTDSC. During the transition of a polymerisation, the heat flow increases first and then decrease after reaching a maximum value. In terms of heat capacity, it decrease slightly and then a step change will be observed. This step change is corresponded to the transformation from liquid to solid [17]. The time at half of the change in heat capacity $t_{1/2}$ can be used to determine the time of vitrification where half of the materials has transformed to the solid state. Isothermal DSC is preferred for the fundamental dynamic studies because parallel reactions with different activation energy take place with temperature change during non-isothermal DSC. The relative reaction rates change with temperature variation. Although non-isothermal DSC can provide all the dynamic information that several isothermal DSC contain, the reaction parameters derived from the analysis of non-isothermal DSC are often inaccurate in practice. The activation energy and the pre-exponential factor are usually overestimated. In terms of the temperature selection for isothermal DSC, non-isothermal DSC is necessary to provide the heat flow profile during cure. If the cure temperature is too low, the reaction time is too long and the corresponded heat flow is too low to exceed the baseline noise. If the cure temperature is too high, the reaction time is too short to allow the whole conversion process to be recorded. Therefore, the combination of isothermal and non-isothermal DSC to study cure dynamic is preferred.

In the characterisation of cure dynamic with DSC, the basic assumption is that the heat generated during cure reaction is proportional to the rate of conversion and the relationship is shown below [18]:

$$\Delta H = \frac{da}{dt} \times \Delta H_{tol} \quad \text{Equation 7.1}$$

Where ΔH is the heat generated at time t , da/dt is the reaction rate and ΔH is the total heat generated. The basic cure dynamic equation to calculate reaction rate of MTDSC is shown below [18]:

$$\frac{da}{dt} = Ae^{-x}f(a) \quad \text{Equation 7.2}$$

Where da/dt is the rate of conversion, A is the pre-exponential factor, $x=E_a/RT$ (E_a is the activation energy, R is the gas constant and T is the cure temperature), and $f(a)$ is the cure dynamic model function. The general cure dynamic model applied is the reaction order model which is also called n^{th} order model [18]:

$$f(a) = (1 - a)^n \quad \text{Equation 7.3}$$

For this general model, it is difficult to explain the detailed mechanism in all cure conditions and thermoset systems. Therefore, an empirical approach model is preferred to model the cure process of a thermoset system under certain conditions. An auto-catalysed model was proposed to analyse the cure dynamic of two-part polyurethane network formation [19]. The model is expressed as the equation below:

$$\frac{da}{dt} = ka^m(1 - a)^n \quad \text{Equation 7.4}$$

Where $m + n$ is the order of the reaction, a is the conversion and k is the reaction rate. The rate constant k mainly depends on cure temperature and it can be determined via Arrhenius equation:

$$k = A \times e^{\frac{E_a}{RT}} \quad \text{Equation 7.5}$$

The parameters in this equation are the same as those in equation 7.2. The pre-exponential factor A relates the number of reaction sites required to trigger a reaction. The reaction rate increase with increasing cure temperature. According to the classical collision theory, the number of reaction sites with high kinetic energy increases with increasing cure temperature which can accelerate the reaction [20]. With the aid of this dynamic model, the reaction rate, the order of the reaction, conversion and the activation energy can be obtained to fully investigate the cure

dynamic of graphene based materials/PU nanocomposites. This model is more accurate than n^{th} order model.

7.2.2 FTIR

The basic principle of utilising FTIR to monitor the cure of polyurethane is widely reported in literature [21]. FTIR method is simple and fast to characterise the cure process of PU. Calibration is necessary for each sample and it can be done via using a reference peak whose concentration remains constant through the whole reaction. The conversion of the cure reaction can be determined via the equations as followed. A_{NCO} is the absorbance of the isocyanate and A_{ref} is the absorbance of the reference bond in FTIR experiment. In this project, C-H bond was selected as the reference bond (3124 cm^{-1} to 2524 cm^{-1}). The calibrated area under each peak can be calculated according to equation 7.5.

$$A = \frac{A_{\text{NCO}}}{A_{\text{ref}}} \quad \text{Equation 7.6}$$

Therefore, the conversion (a) of the reaction can be calculated from equation 7.6

$$a = 1 - \frac{A(t)}{A_0} \quad \text{Equation 7.7}$$

Where $A(t)$ is the calibrated area of NCO peak at time t and A_0 is the initial calibrated area of NCO peak.

The 2280 cm^{-1} peak of NCO group was selected to monitor the cure process and the absorbance area of the NCO peak was integrated from 2171 cm^{-1} to 2389 cm^{-1} . With the reaction proceeds, the concentration of NCO group was reduced and the conversion of the reaction can be monitored via the depletion of NCO group.

7.3 Results of cure dynamic from FTIR and MDSC

7.3.1 MDSC characterisation

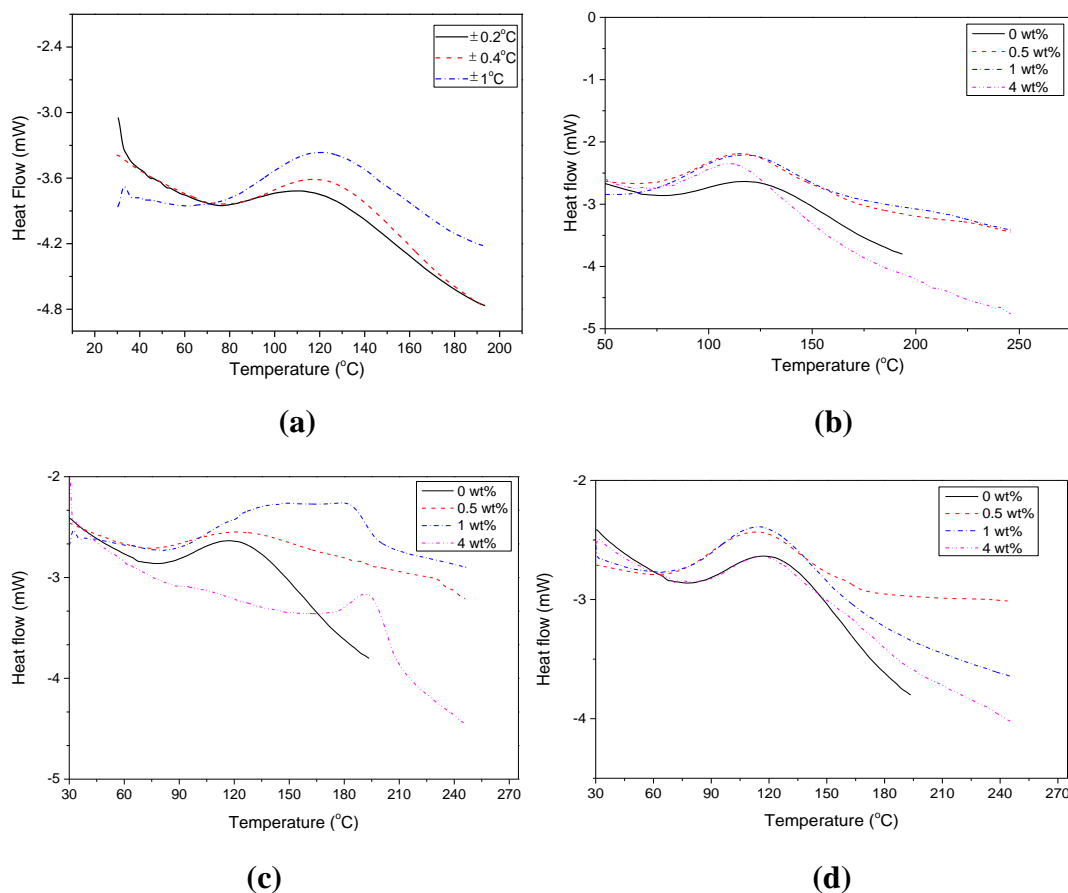


Figure 7.1 Non-isothermal DSC curves of (a) pure PU resin with different modulation amplitude and PU nanocomposites with different filler loadings (b) G (c) GO (d) TEG

The non-isothermal DSC curves of pure PU and PU nanocomposites are shown in Figure 7.1. The effect of modulation amplitude was compared in Figure 7.1 (a). From the figure, the initiation temperature of cure is around 77 °C and the peak temperature is around 122 °C. The peak temperature of the curve with $\pm 0.2^\circ\text{C}$ amplitude is lower than the other two amplitudes. The selection of amplitude must be big enough to allow all the information can be recorded and small enough to prevent cooling from happening. The typical amplitudes range is 0.1 to 1 °C [17]. The curve using 0.2 °C amplitude may not sufficient to identify the cure temperature. In order to prevent cooling, 0.4 °C modulation amplitude was selected. From Figure 7.1 (b), the addition

of graphene reduces the initiation temperature and peak temperature slightly indicates that graphene has catalytic effect on the cure of two-part PU resin. In terms of GO, the initiation temperature and the peak temperature increased slightly at low GO loading and increased significantly at 4 wt% GO loading. From the results, the addition of GO seems to have retarding effect on the cure of PU resin. TEG is also graphene but it has bigger particle size and better degree of exfoliation than G. From Figure 7.1 (d), the initiation temperature and peak temperature are reduced by the addition of TEG but the catalytic effect is not obvious when the TEG loading is 4 wt%. Therefore, the catalytic effect of TEG is only effective at low TEG loading. The non-isothermal results provide an initial insight of the cure dynamic of PU nanocomposites. Isothermal results will reveal more details. The temperatures selected for isothermal studies are between the initiation temperature and peak temperature of the PU nanocomposites.

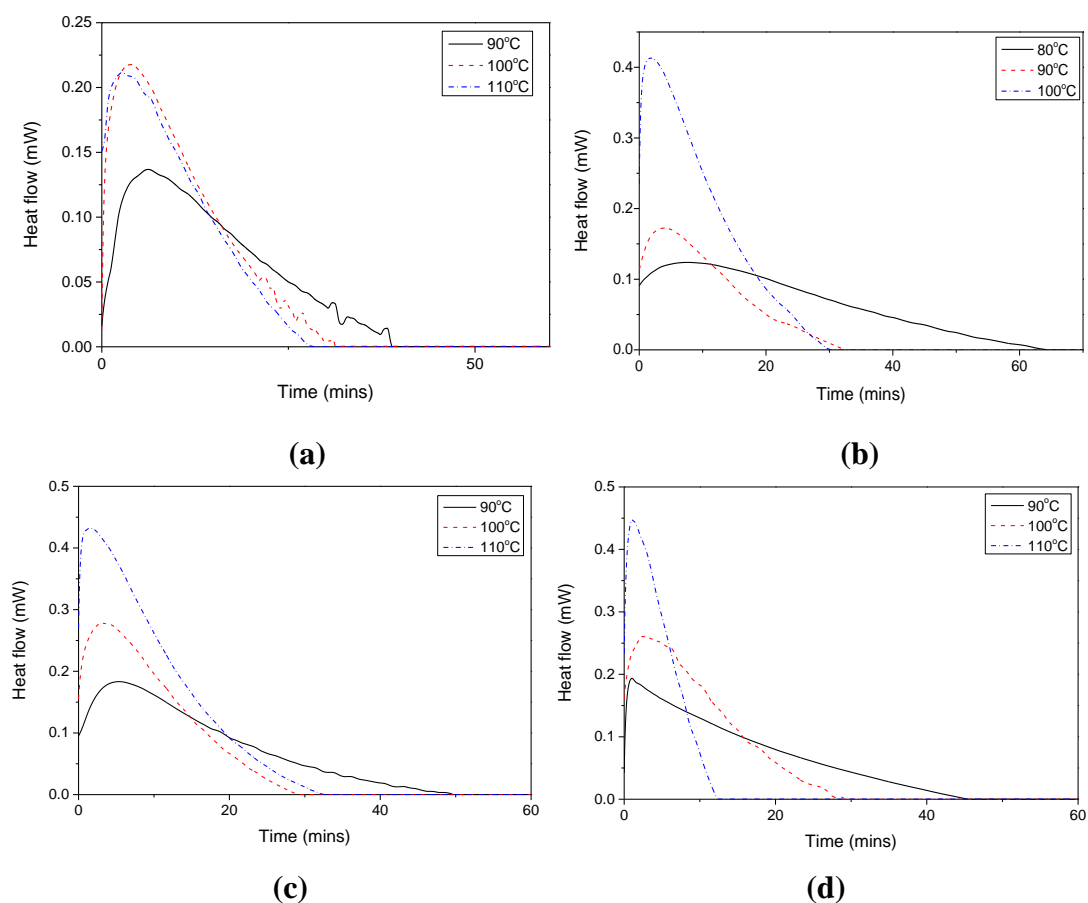


Figure 7.2 Isothermal DSC curves of PU/G nanocomposites with different G loadings (a) 0 wt% (b) 0.5wt% (c) 1 wt% (d) 4 wt%

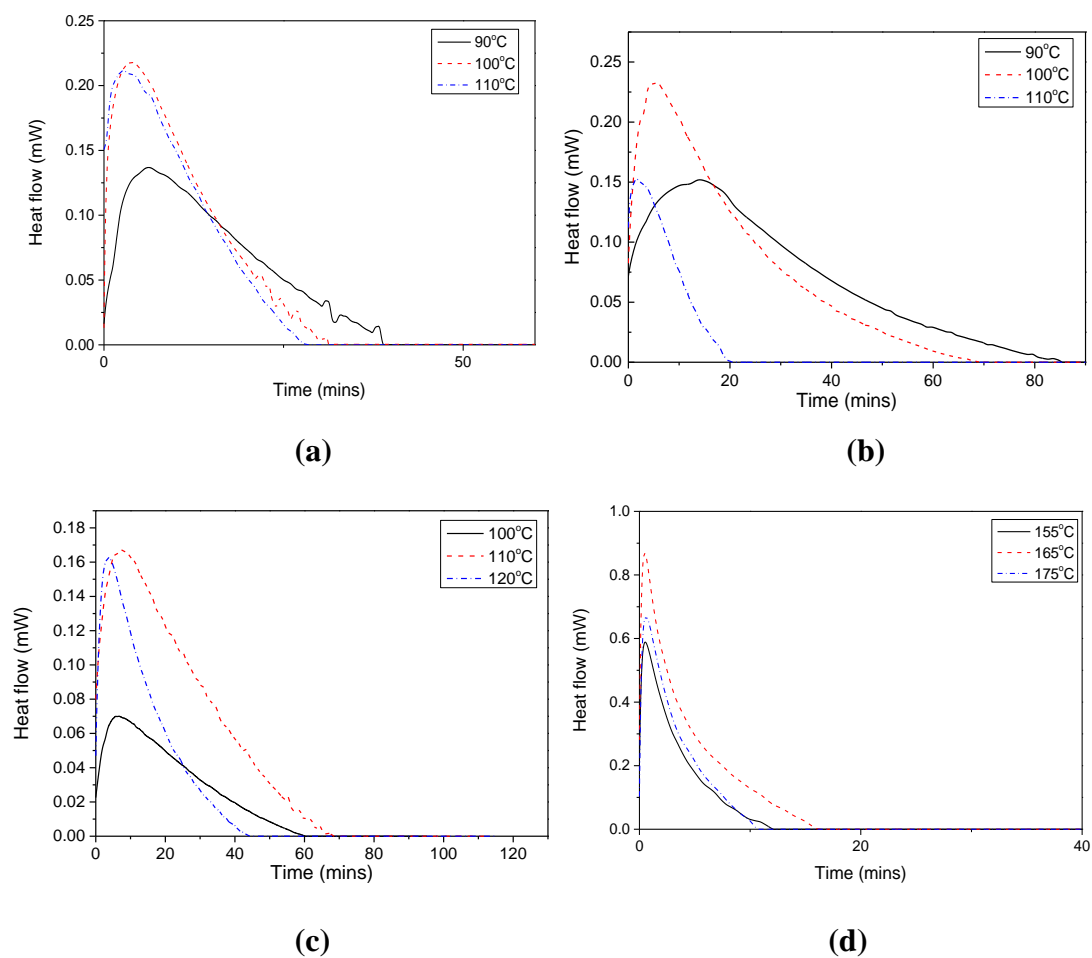
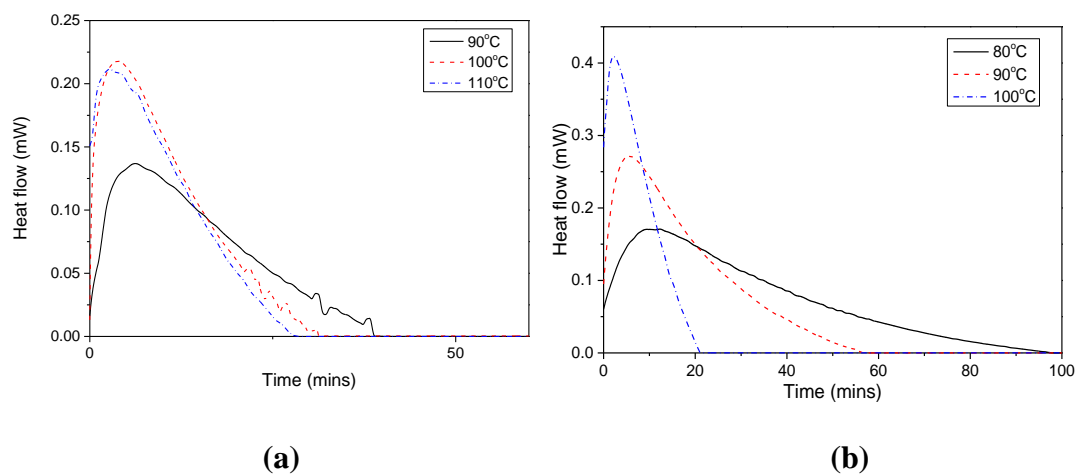


Figure 7.3 Isothermal DSC curves of PU/GO nanocomposites with different GO loadings (a) 0 wt% (b) 0.5wt% (c) 1 wt% (d) 4 wt%



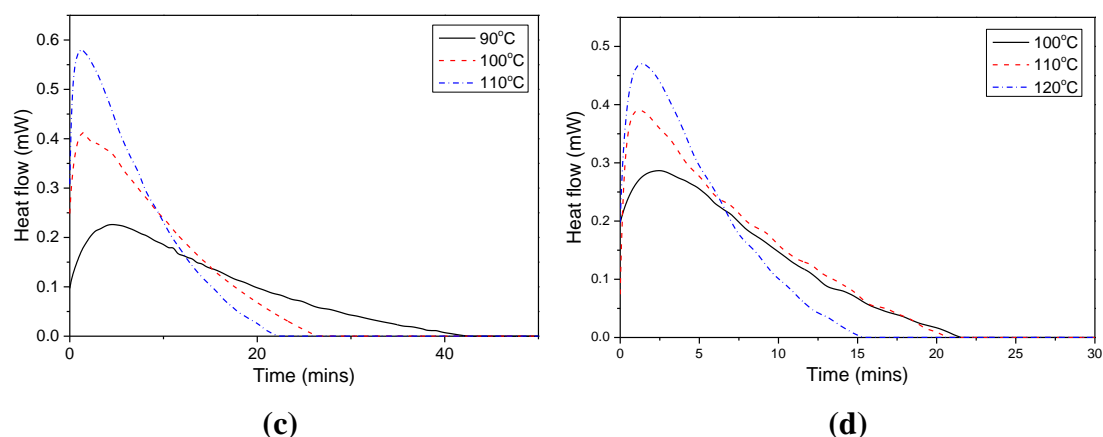


Figure 7.4 Isothermal DSC curves of PU/TEG nanocomposites with different TEG loadings (a) 0 wt% (b) 0.5wt% (c) 1 wt% (d) 4 wt%

The isothermal DSC curves of all the PU nanocomposites are shown in Figure 7.2 to Figure 7.4. From the results, the nanocomposites cured at higher temperature generally reach their maximum conversion faster, which indicated that higher temperature led to higher reaction rate. Comparing the results in Figure 7.2, the addition of 0.5 wt% G reduces the initiation temperature and cure temperature of PU slightly, which proves the existence of a catalytic effect, but the catalytic effect was not obvious in 1 wt% and 4 wt% G. In terms of PU/GO nanocomposites, the addition of GO increases the initiation temperature and peak temperature of PU significantly at high GO loading. The initiation of reaction was retarded significantly. The existence of $-\text{COOH}$ and $-\text{OH}$ functional groups on GO sheets may have a profound effect on the reaction mechanisms and the initiation of the reaction. Graphene and graphene oxide have the ability to absorb organic molecules [22]. Excessive amount of graphene oxide may absorb the reactants and catalyst, and reduces the contact between the isocyanates and polyols. At the same time, the trapped isocyanate and polyol may only react with the functional groups on the GO sheets. In the case of graphene, excessive amount may retard the reaction a bit because some reactants and catalyst are trapped. The mobility of the reactants and catalyst is restricted. Hence, the reaction is retarded. The isothermal DSC curves of TEG reinforced PU nanocomposites are

similar to those of G reinforced PU nanocomposites. They had similar catalytic effect at low filler loading. However, the initiation temperature and peak temperature of 4 wt% TEG/PU nanocomposite was higher than 4 wt% G/PU nanocomposite because the larger size TEG exhibit steric hindrance effect at lower filler loading than G.

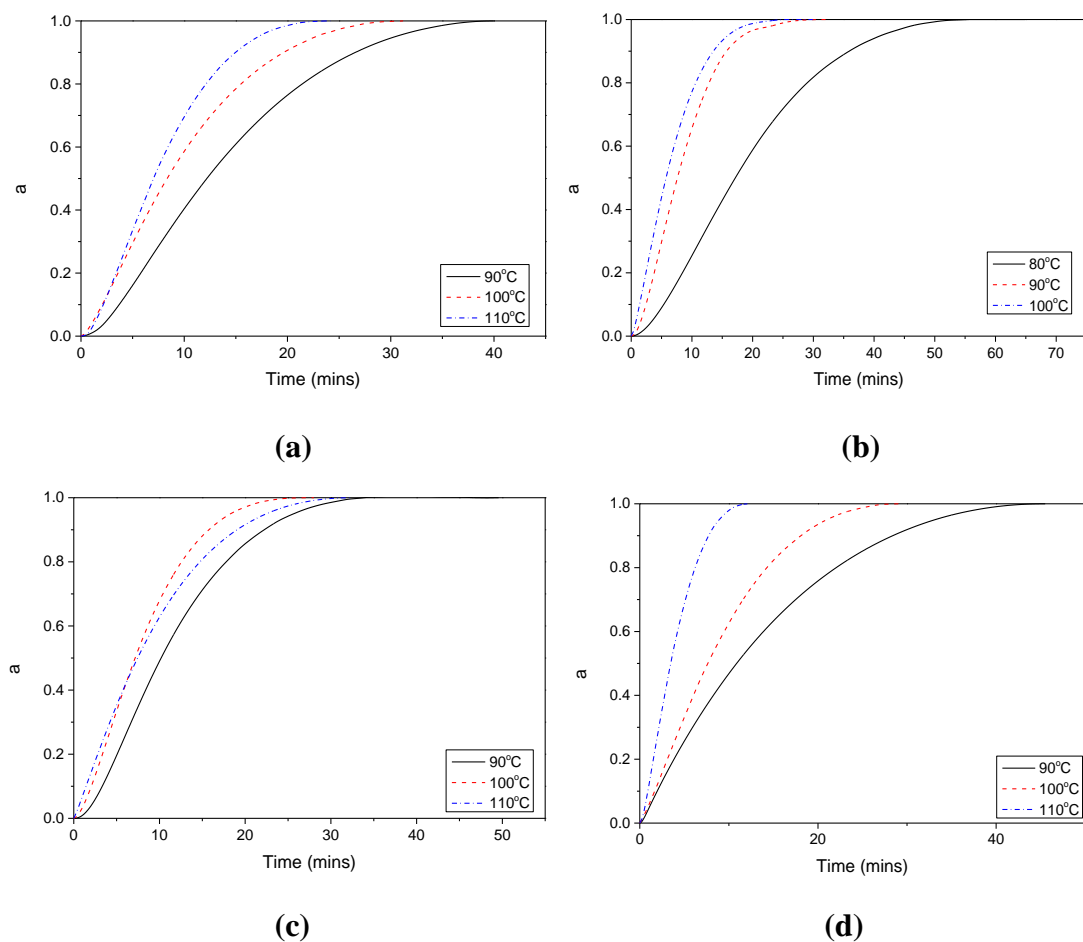
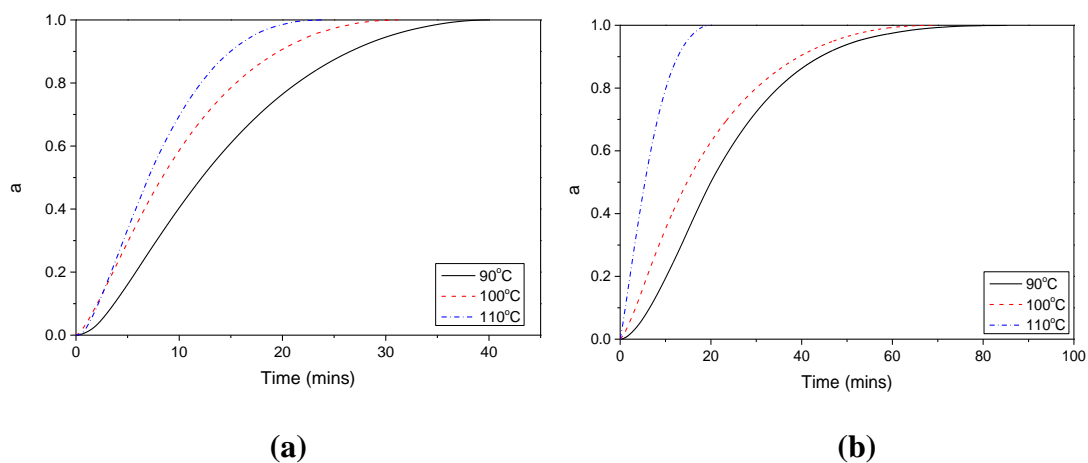


Figure 7.5 Plots of conversion (a) against reaction time of PU/G nanocomposites with different G loadings (a) 0 wt% (b) 0.5wt% (c) 1 wt% (d) 4 wt%



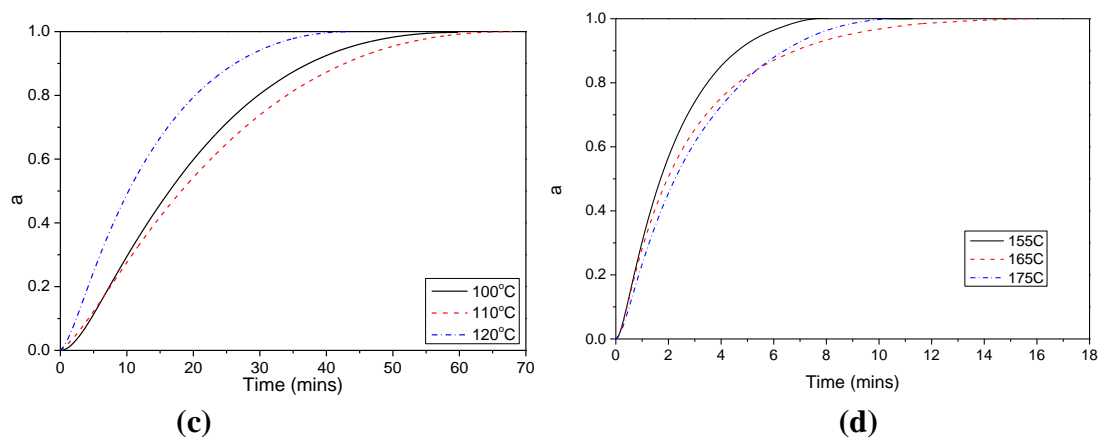


Figure 7.6 Plots of conversion (a) against reaction time of PU/GO nanocomposites with different GO loadings (a) 0 wt% (b) 0.5wt% (c) 1 wt% (d) 4 wt%

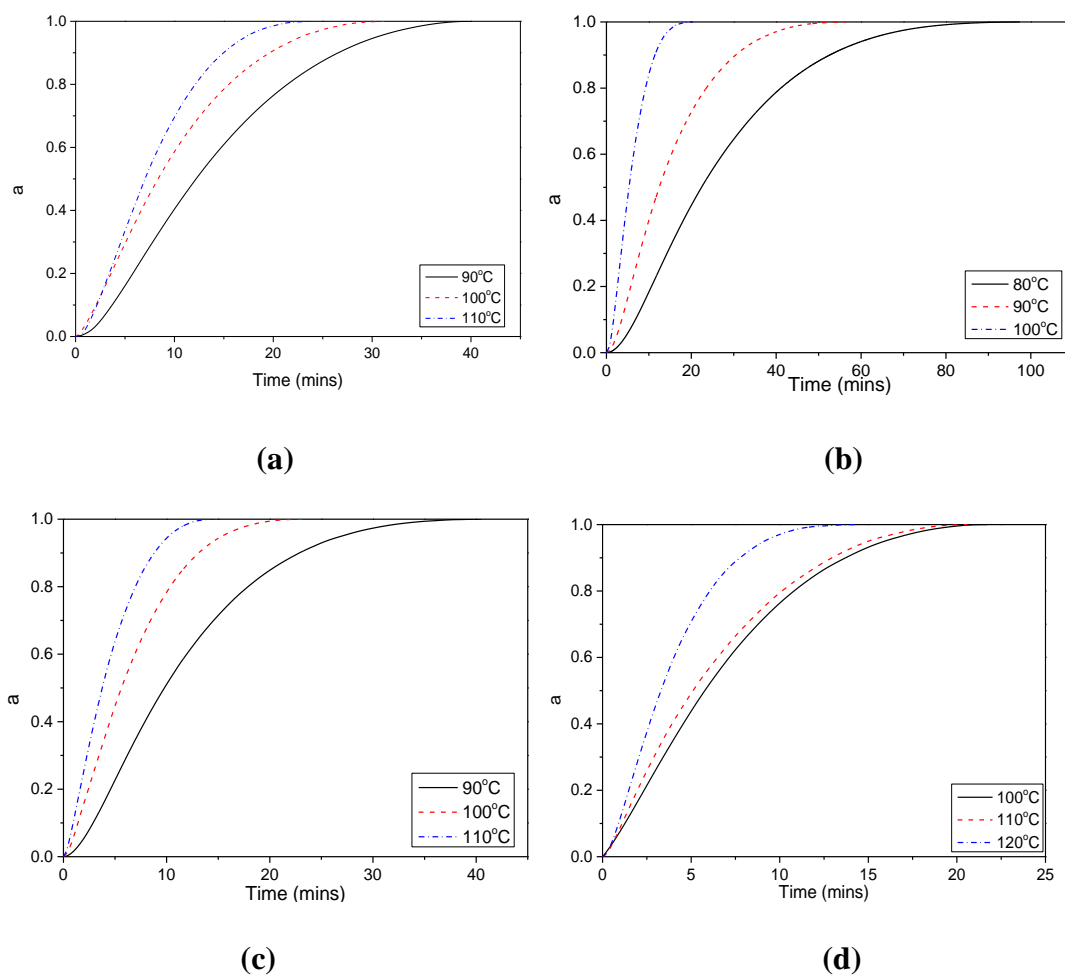
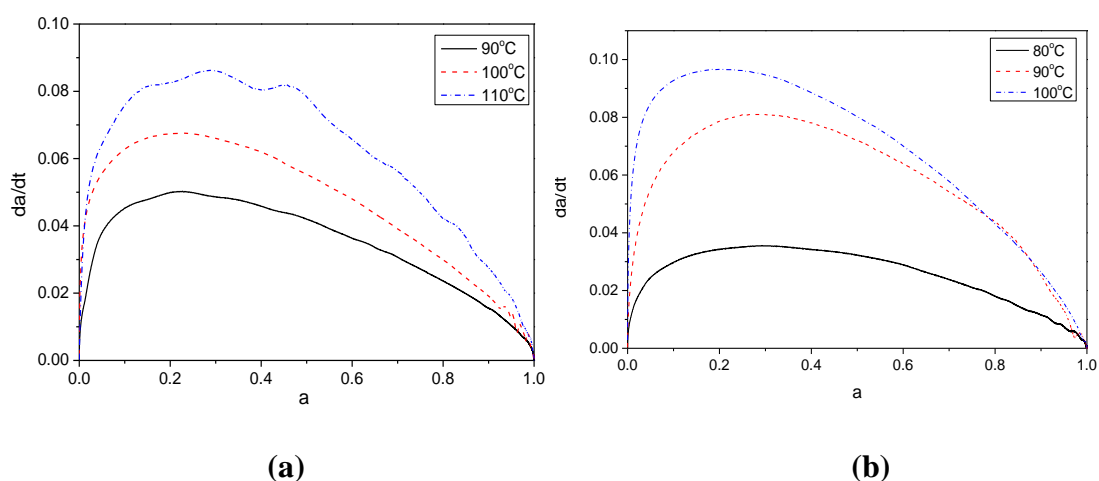


Figure 7.7 Plots of conversion (a) against reaction time of PU/TEG nanocomposites with different TEG loadings (a) 0 wt% (b) 0.5wt% (c) 1 wt% (d) 4 wt%

The plots of conversion *versus* reaction time of the nanocomposites are shown in Figure 7.5 to Figure 7.7. From Figure 7.5 (b) to (a), (c) and (d), the nanocomposite

cured at 90 °C had the fastest reaction rate which indicate 0.5 wt% G had catalytic effect while the nanocomposites with higher filler loading did not. From Figure 7.6, the addition of GO in the system had retarded effect on the cure reaction and the reaction mechanism seemed to be altered by the addition of GO. The reaction rates at higher cure temperature were slower with high filler loading. The reaction of two-part PU resin and GO seem to be very different from others. Compared the nanocomposites reacted at the same temperature in Figure 7.7, similar conclusions to the isothermal DSC results can be drawn. So far, the addition of graphene has catalytic effect on the cure reaction but the steric hindrance effect became more profound in high filler loading. In terms of GO, the cure of PU was altered significantly. All the conversion versus time curves are slow initially and then become more rapid. Afterwards, they slow down again before it reach the maximum conversion. The curves look like an 'S' shape which is the characteristic feature of autocatalytic behaviour [23]. This behaviour is more notable in the curves with lower cure temperature. The behaviour of 4 wt% PU/GO nanocomposite exhibited near autocatalytic model but the initial stage was much rapid than others. The phenomenon can be a valid evident of the theory mentioned in literature. The behaviour of PU/TEG nanocomposites is similar to PU/G nanocomposites.



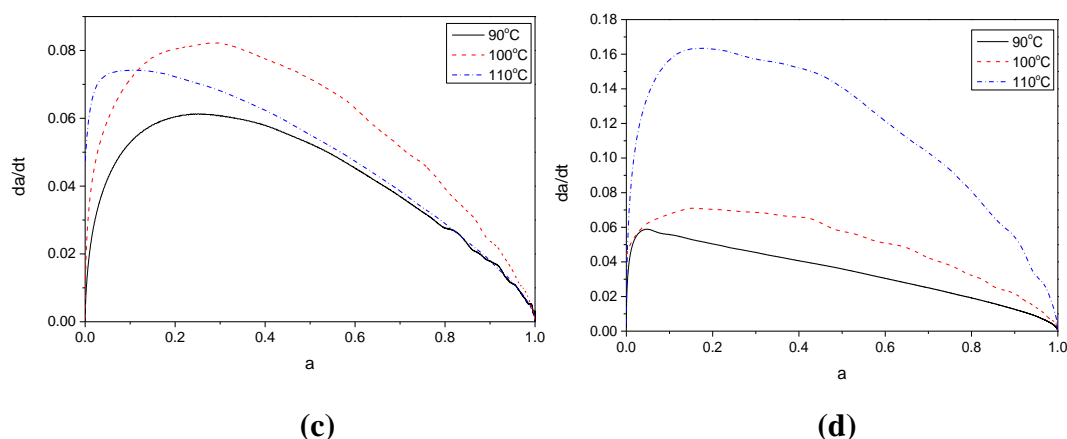


Figure 7.8 Plots of conversion rate (da/dt) against conversion (a) of PU/G nanocomposites with different G loadings (a) 0 wt% (b) 0.5wt% (c) 1 wt% (d) 4 wt%

Figure 7.8 shows the plots of conversion rate against conversion of PU/G nanocomposites. The conversion rates of all the PU/G composites reached their maximum at intermediate conversion and this indicated that all the reactions followed auto-catalytic model. The conversion rate of the reactions follow n^{th} order model is the highest at the beginning of the reaction. The conversion rate increased faster with higher cure temperature. Comparing the results of the nanocomposites cured at 90 °C, 0.5 wt% G had the best catalytic effect where the maximum conversion rate reached about 0.08. Although the conversion rate of 4 wt% PU/G cured at 110 °C, it did not mean the catalytic effect of 4 wt% graphene is the best because the conversion rate at lower cure temperatures are lower than other PU/G nanocomposites. The reason why is that the steric hindrance of graphene trap the reactants in a small area and the reactants are facilitated to react with each other at early stage. In addition, the high cure temperature leads to high mobility of the reactants which accelerate the reaction further.

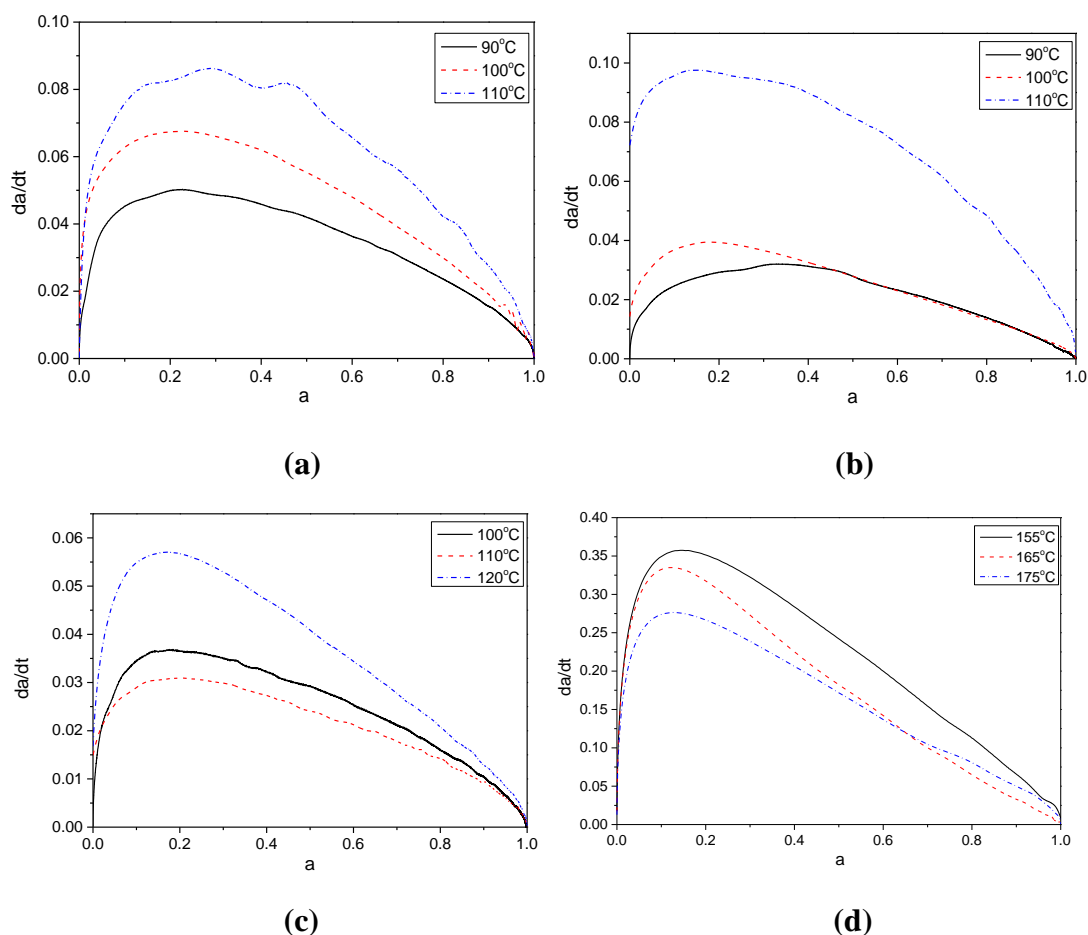


Figure 7.9 Plots of conversion rate (da/dt) against conversion (a) of PU/GO nanocomposites with different GO loadings (a) 0 wt% (b) 0.5wt% (c) 1 wt% (d) 4 wt%

Figure 7.9 shows the plots of conversion rate *versus* conversion of PU/GO nanocomposites. Comparing the results of pure PU and 0.5 wt% PU/GO nanocomposite, the conversion rates of the nanocomposite at 90 °C and 100 °C are lower while the conversion rate at 110 °C is the same as pure PU. With more GO was added, the conversion rates decreased with the increase of cure temperature. Combined the results to the isothermal DSC curve of PU/GO nanocomposites, the nanocomposites did not react completely at lower temperature. Therefore, the conversion rates at high cure temperatures are low relatively. Higher cure temperature could extend the degree of cure and increase the cure density of the nanocomposites. The excessive amount of GO trapped the reactants in a small area and the viscosity might increase dramatically which restrain the reaction to proceed. Higher cure

temperature can provide more energy to activate the reaction to a more completed state and increase the mobility of the reactants. Although the reaction rates were lower in 165 °C and 175 °C, the extent of reactions are higher with the increase of cure temperature. The presence of oxidative groups on GO sheets may retard the reaction and increase the temperature required to activate the reaction. The cure behaviours of the PU/GO nanocomposites follow autocatalytic models where the maximum conversion rate appears at the intermediate conversion range.

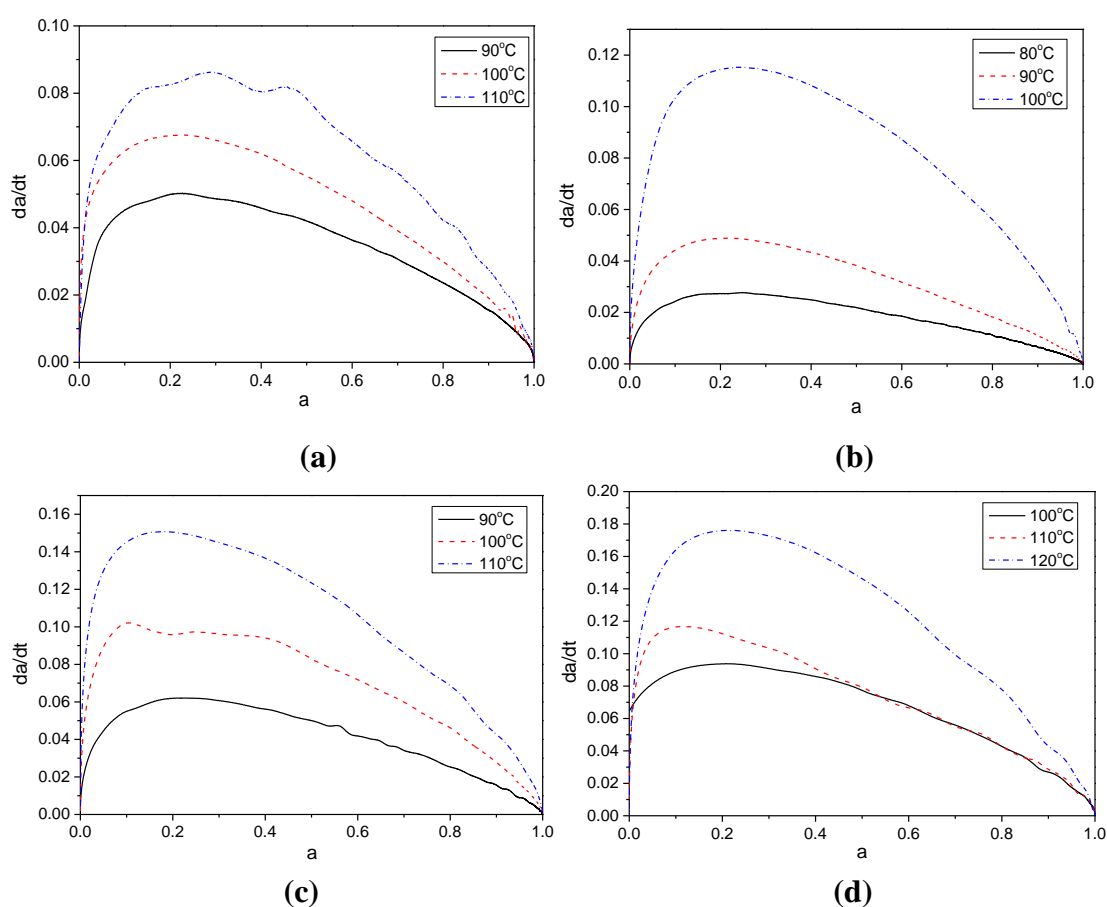


Figure 7.10 Plots of conversion rate (da/dt) against conversion (a) of PU/TEG nanocomposites with different TEG loadings (a) 0 wt% (b) 0.5wt% (c) 1 wt% (d) 4 wt%

The plots of conversion rate change with conversion of PU/TEG nanocomposites are shown in Figure 7.10. The conversion rates increase with elevated cure temperatures and the cure behaviours follow autocatalytic model. All the results of conversion rate against conversion are well corresponded to the results reported before. The

conversion rates of the nanocomposites at 90 °C are lower than pure PU while the conversion rates at 100 °C are higher than pure PU. The highest conversion rate could reach 0.12. The catalytic effect of graphene still exists although the initiation temperature and peak cure temperatures are increased. The presence of graphene can accelerate the reaction of the nanocomposites. There is competition between catalytic effect and steric hindrance of graphene sheets. The catalytic effect is more dominated when the cure temperature is higher (higher mobility of the reactants). At the same cure temperature, the steric hindrance effect will be more dominated when the filler loading increases. The increase of initiation temperature and cure temperature may be resulted from the increase of activation energy which is essential for a reaction to happen. The activation energy and other reaction parameters can be calculated from autocatalytic modelling. The cure behaviours can be understood extensively.

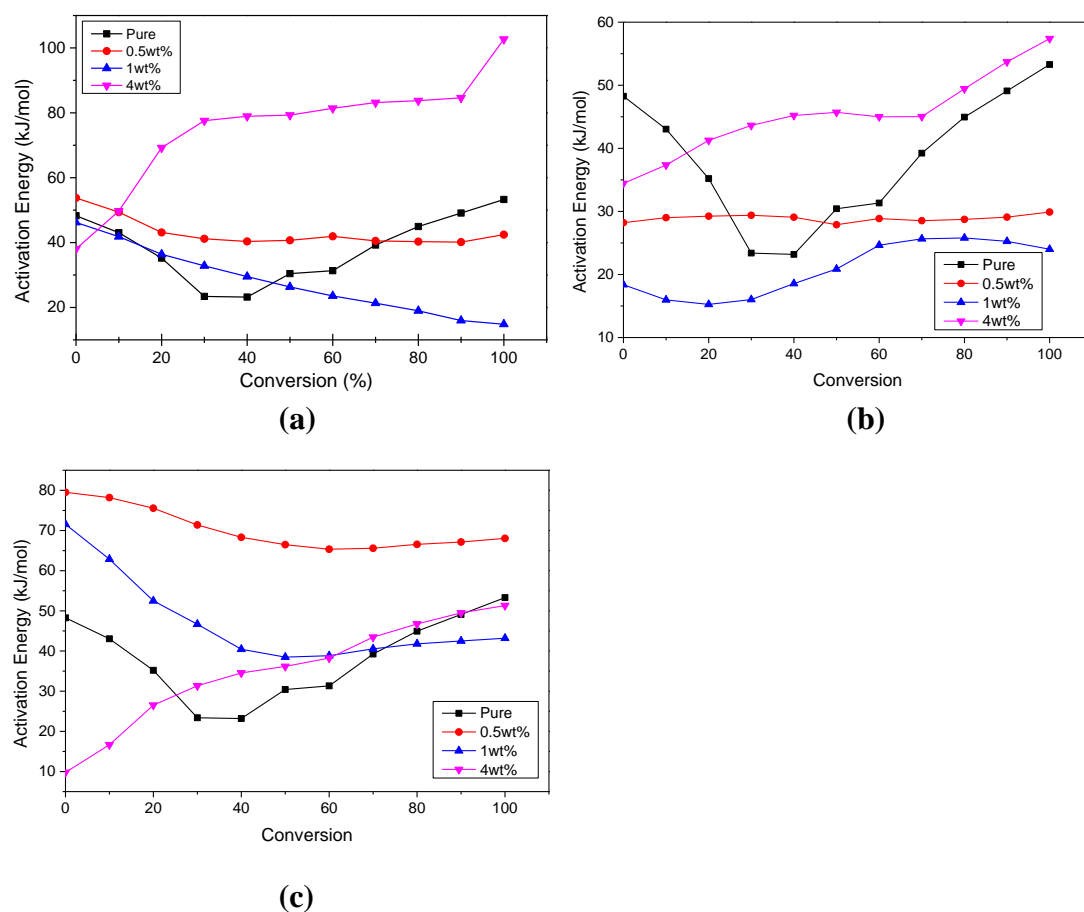


Figure 7.11 Plots of activation energy *versus* conversion of PU nanocomposites with different filler loadings (a) G (b) GO (c) TEG

The activation energy results of all the nanocomposites are shown in Figure 7.11. For the pure PU, the activation energy is high initially and then decrease due to the presence of catalyst which facilitates the propagation of the thermoset network. However, the activation energy increase after the conversion reaches 40% because the reaction proceeds towards to diffusion control as a result of the increase of viscosity. With the addition of G, the initial activation energy increases with filler loading first and then decrease. 4 wt% PU/G nanocomposite has the lowest initial activation energy. The catalytic effect of graphene on the initial activation energy is more profound with increasing graphene weight percent. However, the activation energy increased dramatically as the reaction proceeded. This may be resulted from the increase of viscosity which makes the steric hindrance effect of graphene more profound. In terms of the 0.5 wt% and 1 wt% PU/G nanocomposites, the activation energy decreased with the increase of conversion. Hence, graphene can facilitate the reaction to 100% complete efficiently. The addition of graphene can improve the cure efficiency of PU and reduce the cost of processing because less the energy is required to cure PU. From the results, the addition of 1 wt% G is most efficient. The TEG/PU nanocomposites had similar trends of activation energy change with filler loading and conversion. The initial activation energy of 0.5 wt% and 1wt% PU/TEG nanocomposites are much higher than pure PU while the initial activation energy of 4 wt% PU/TEG nanocomposite is much lower. With increasing the size of the graphene sheets and higher extent of graphene exfoliation, the steric hindrance effect is more significant which retard the cure and network formation of PU. The results can explain why the polymer coverage is low with increasing TEG loading. High TEG loading can significantly affect the network formation of PU which is detrimental to the anti-corrosion properties of the coating. The efficient loading of TEG for curing may be about 1 wt% to 3 wt%. All the PU/GO nanocomposites had lower initial activation energy than pure PU and they reduce with filler loading first and then increase. Steric hindrance effect is more dominant than catalytic effect in high filler

loading area (above 1 wt %). Compared the initial activation energy of 0.5 wt% PU nanocomposites, GO has the best catalytic effect which may be owing to the presence of the oxidative debris on the surface of GO sheets [24].

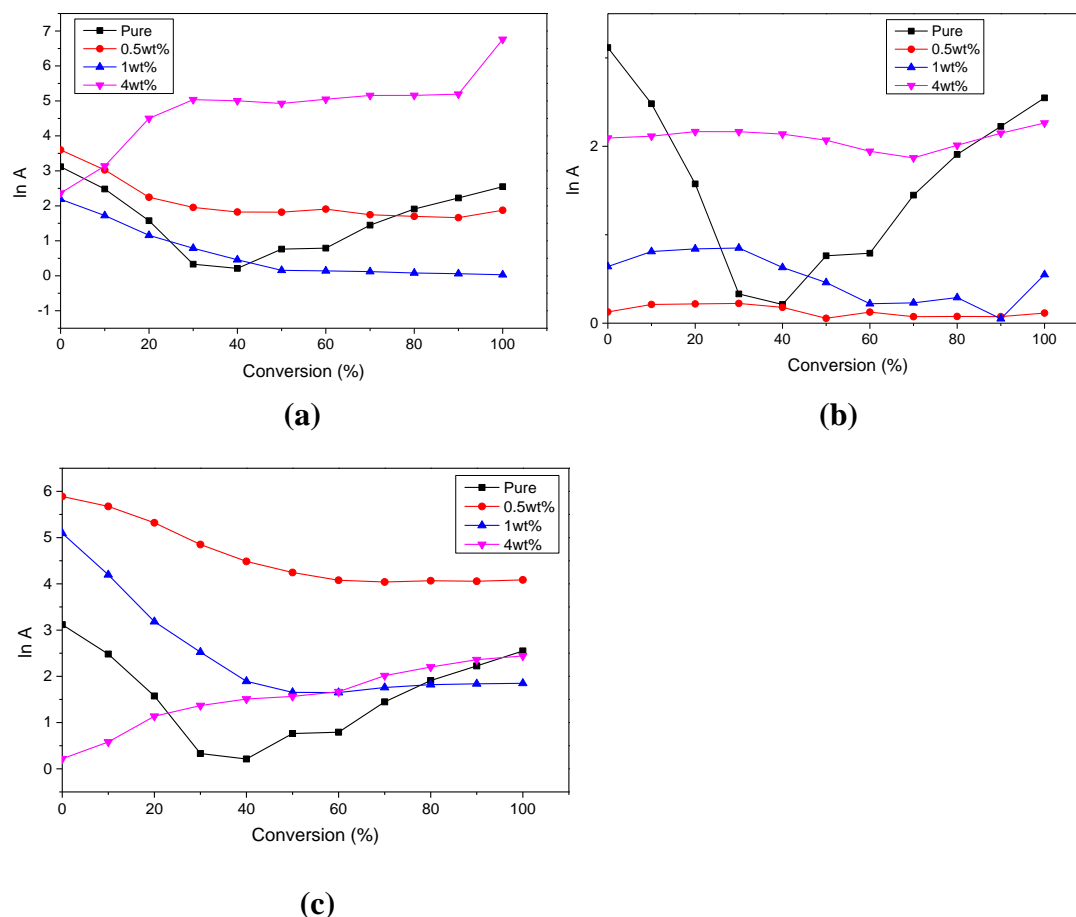


Figure 7.12 Plots of pre-exponential factor *versus* conversion of PU nanocomposites with different filler loadings (a) G (b) GO (c) TEG

The results of pre-exponential factor change with conversion are shown in Figure 7.12. The trends of pre-exponential factor change with filler loading are similar to the activation energy results of graphene based PU nanocomposites. In terms of PU/GO nanocomposites, the trends of initial pre-exponential factor are similar but the pre-exponential factor kept nearly constant with increasing conversion. This phenomenon may be ascribed to the surface functional groups of the GO sheets which increases the potential reaction sites and reduce the sites required from isocyanate and polyol. Table 7.1 show the reaction parameters from autocatalytic model. The reaction order of pure PU is about 2 which means that the reaction rate is controlled by the

concentration of isocyanate and polyol. With the addition of graphene, the reaction order did not change a lot and it was still about 2. However, the addition of 4 wt% GO made the reaction order reach nearly 3 and 0.5 wt% G and GO reduced the reaction order to nearly 1. The function groups on GO sheets allow the isocyanate and polyol can react with them. The addition of excessive amount of GO will change the reaction order where the reaction rate depends on the concentration of isocyanate, polyol and GO. In terms of 0.5 wt% G and 0.5 wt% GO, the possible reason is the strong catalytic effect induced. However, it is also possible that the results obtained from autocatalytic model are not accurate although the correlation coefficient is greater than 0.99

Table 7.1 The reaction parameters obtained from the modelling of the MDSC results

Filler Type	Weight percent	Temperature (°C)	k	m	n	Reaction order	lnA	E _a (kJ/mol)
Pure PU	0	90	0.27	0.82	1.62	2.44	3.12	48.26
		100	0.38	0.72	1.39	2.11		
		110	0.60	0.86	1.44	2.30		
TEG	0.5	80	0.10	0.60	1.42	2.03	5.89	79.52
		90	0.19	0.62	1.53	2.14		
		100	0.54	0.75	1.47	2.22		
	1	90	0.19	0.52	1.25	1.77	5.09	71.55
		100	0.59	0.83	1.75	2.58		
		110	0.61	0.63	1.46	2.09		
	4	100	0.55	0.68	1.88	2.56	0.22	9.78
		110	0.59	0.87	1.91	2.78		
		120	0.63	0.58	1.36	1.94		
G	0.5	80	0.12	0.23	0.63	0.86	3.60	53.74
		90	0.33	0.54	1.31	1.85		

		100	0.36	0.72	1.42	2.13		
	1	90	0.13	0.35	0.87	1.22	2.19	46.20
		100	0.22	0.47	1.04	1.51		
		110	0.26	0.53	1.50	2.03		
	4	90	0.32	0.78	2.14	2.91	2.37	38.05
		100	0.46	0.88	1.82	2.70		
		110	0.60	0.60	1.29	1.89		
	GO	0.5	90	0.09	0.50	1.08	0.13	28.21
			100	0.10	0.41	1.31		
			110	0.14	0.13	0.65		
		1	100	0.12	0.56	1.32	0.64	18.38
			110	0.14	0.69	1.56		
			120	0.15	0.43	1.30		
		4	155	1.25	0.53	1.65	2.09	34.44
			165	1.50	0.59	2.29		
			175	1.54	0.72	2.25		

7.3.2 FTIR characterisation

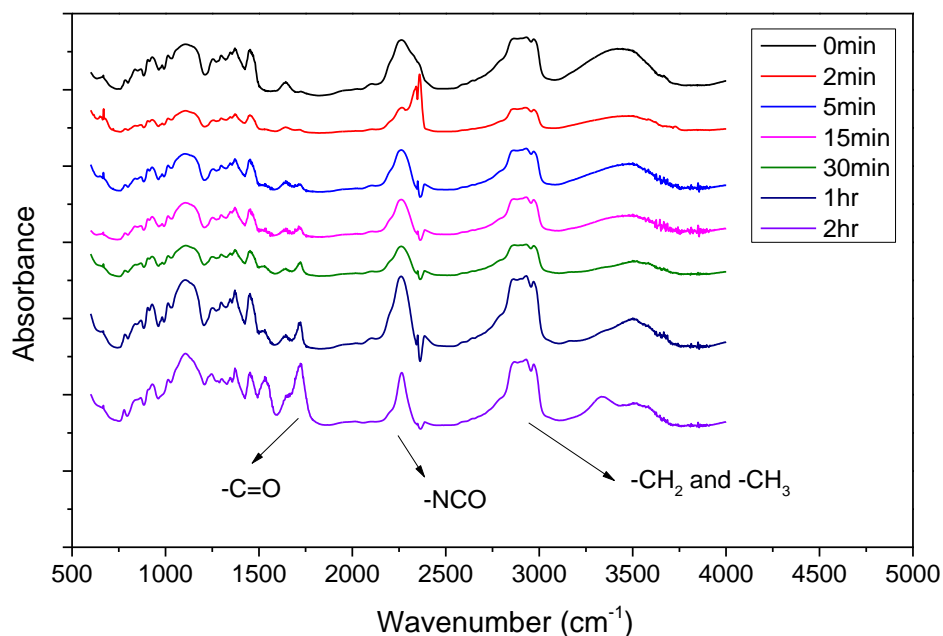
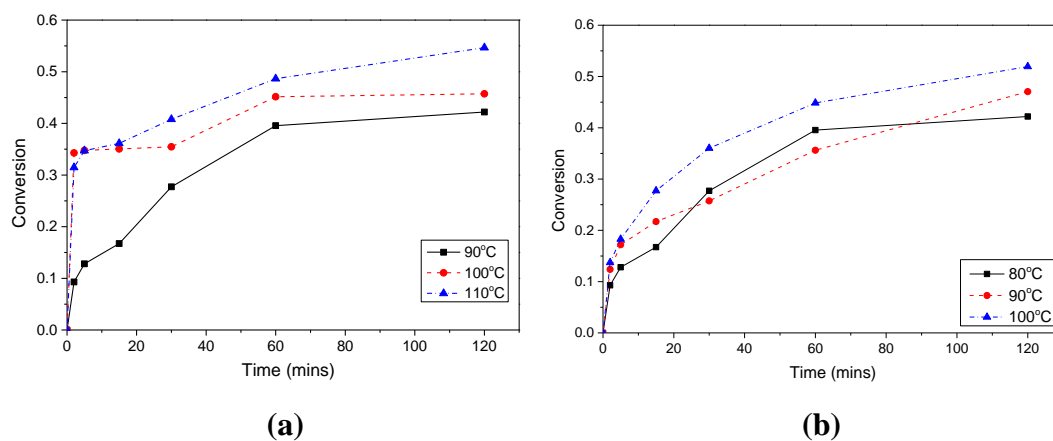


Figure 7.12 Example FTIR spectra of PU nanocomposites (PU/G) cured with different time (without calibration)

An example FTIR spectrum of PU nanocomposites is shown in Figure 7.12. Although they were not calibrated, it still can be seen that the intensity of -NCO peak reduced with increasing reaction time and the intensity of -C=O group peak increased with increasing reaction time. The intensity of -CH_2 and -CH_3 peak is main constant which means the -CH_2 and -CH_3 peak can be used as reference peak.



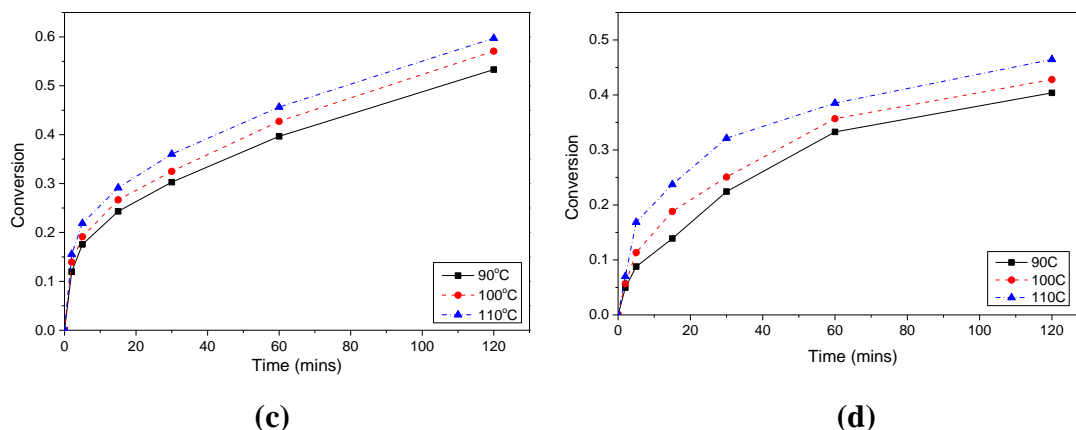
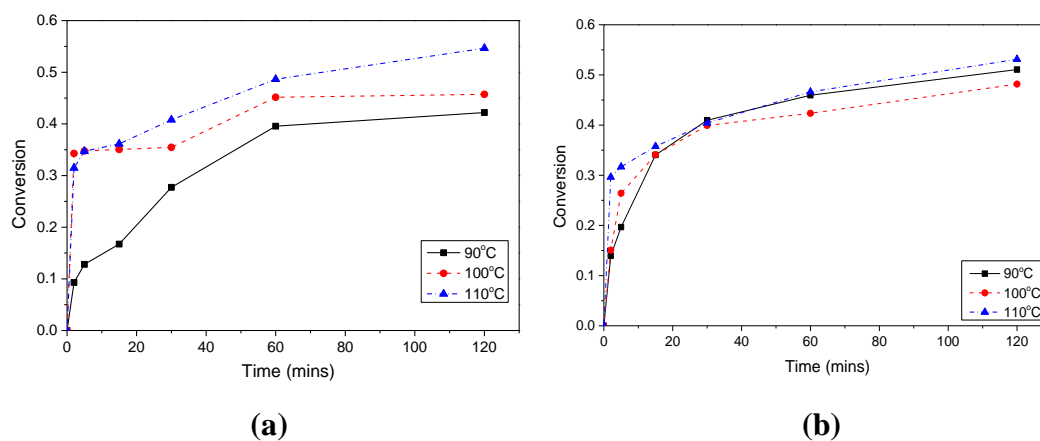


Figure 7.13 Plots of conversion versus reaction time of PU/G nanocomposites with different G loadings obtained from FTIR characterisation (a) 0 wt% (b) 0.5wt% (c) 1 wt% (d) 4 wt%

The plots conversion versus reaction time of PU/G obtained from FTIR were shown in Figure 7.13. The PU nanocomposite resin was put on a KBr disk and then reacted in isothermal condition in MDSC chamber for constant heating. Afterwards, the cured resin was characterized by FTIR. The extent of cure and the reaction rate increased with cure temperatures and decreased with increasing G content. The results exhibited a near autocatalytic behaviour. The highest reaction rate appears in the intermediate conversion. Although the shape of the curves are not similar to ‘S’ shape, the conversion increased rapidly with reaction time and then reached a plateau which also follows the autocatalytic model. The reaction took place in an open environment lead to a reduce reaction rate [25].



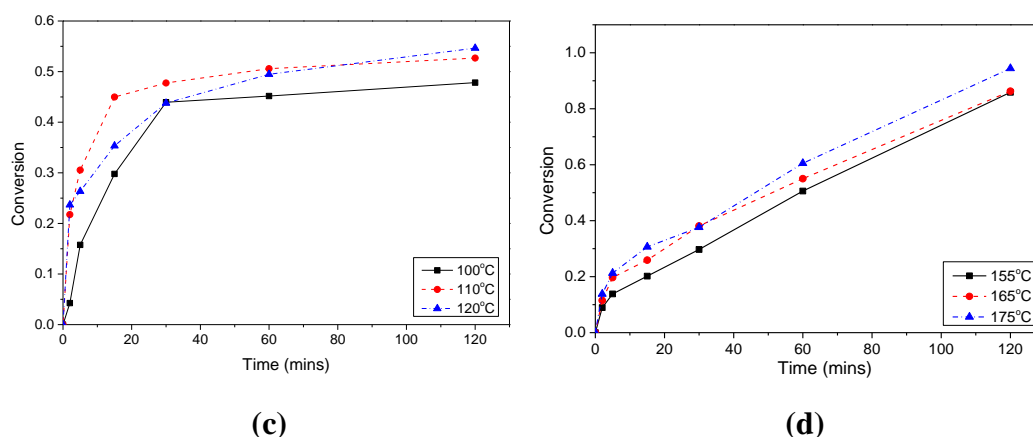
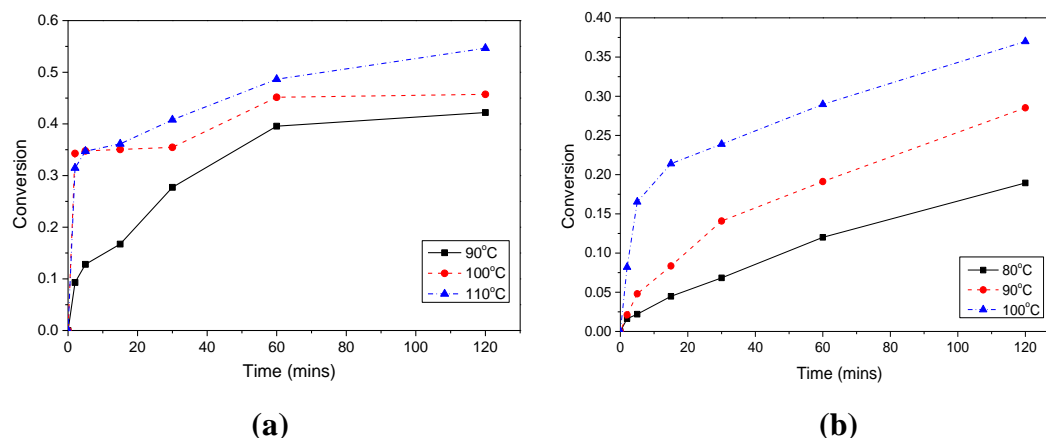


Figure 7.14 Plots of conversion versus reaction time of PU/GO nanocomposites with different GO loadings obtained from FTIR characterisation (a) 0 wt% (b) 0.5wt% (c) 1 wt% (d) 4 wt%

The degree of cure decreased with increasing GO loading and then increased as shown in Figure 7.14. With more GO was added, the resin could reach higher conversion. However, the initiation temperature and peak cure temperature were increased significantly. Therefore, the increase of degree of cure and reaction rate might be due to the increase of cure temperature. The addition of GO significantly alter the reaction mechanism of two-part PU. Comparing the results from Figure 7.15 to Figure 7.14, the degree of cure decreased with TEG loading and then increased. The reaction rate and the degree of cure were more sensitive to cure temperature. The catalytic effect of TEG was more effective at high cure temperature while the steric hindrance effect was more dominated at low cure temperature.



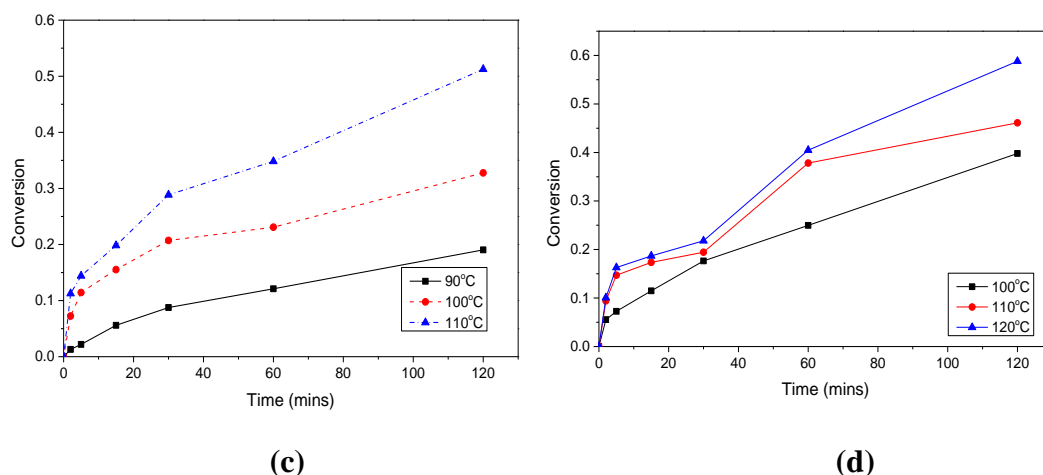


Figure 7.15 Plots of conversion versus reaction time of PU/TEG nanocomposites with different TEG loadings obtained from FTIR characterisation (a) 0 wt% (b) 0.5wt% (c) 1 wt% (d) 4 wt%

7.4 Conclusions

FTIR and MDSC were used to investigate the cure dynamic of PU and graphene based PU composites. Graphene had catalytic effect and steric hindrance effect on the cure of PU where catalytic effect was more dominated at higher cure temperature. With graphene was added, the steric hindrance will be more dominated. In terms of GO, it also exhibited catalytic effect and steric hindrance effect but the surface oxidative debris on GO sheets allow GO participated in the reaction as well. The presence of GO can alter the reaction mechanism of two-part PU. The excessive amount of GO, G and TEG can significantly affect the network formation of PU. The cure density of PU may be weakened with excessive amount of G or TEG. This conclusion can supported the SEM results in last chapter. The most efficient filler loading was 0.5 wt% which can improve the cure efficiency and properties of the nanocomposites. Conductive and anti-corrosive coating can still be produced from high filler loading nanocomposites if the requirement of mechanical properties is not essential.

References

- [1] Dodiuk H, Sydney HG. Handbook of thermoset plastics. William Andrew

- Publishing; 2013.
- [2] Steinfeld JI, Francisco JS, Hase WL. Chemical kinetics and dynamics. 2nd ed. Prentice Hall; 1989.
 - [3] Dannenberg H. Refractive index method for determining cure rates of epoxy resins. Soc Pet Eng Journa 1959;15:875–80.
 - [4] Acitelli MA, Prime RB, Sacher E. Kinetics of epoxy cure: (1) The system bisphenol-A diglycidyl ether/m-phenylene diamine. Polymer (Guildf) 1971;12:335–43.
 - [5] CUTHREIJ KE. Epoxy polymers. III: factors affecting the cure. J Appl Polym Sci 1968;12:1128–33.
 - [6] Elwell MJ, Ryan AJ, Grunbauer HJM, VanLieshout HC. An FTIR study of reaction kinetics and structure development in model flexible polyurethane foam systems. Polymer 1996;37:1353–61.
 - [7] Jin J, Chen L, Song M, Yao K. An Analysis on Enhancement of Fatigue Durability of Polyurethane by Incorporating Organoclay Nanofillers. Macromol Mater Eng 2006;291:1414–21.
 - [8] Hardis R. Cure kinetics characterization and monitoring of an epoxy resin for thick composite structures 2012.
 - [9] Shi Z, Yu D, Wang Y, Xu R. Nonisothermal cure kinetics in the synthesis of polybenzoxazine – clay nanocomposites 2002.
 - [10] Prime RB, Michalski C, Neag CM. Kinetic analysis of a fast reacting thermoset system. Thermochim Acta 2005;429:213–7.
 - [11] Martin-Gallego M, Verdejo R, Lopez-Manchado MA., Sangermano M. Epoxy-graphene UV-cured nanocomposites. Polymer 2011;52:4664–9.
 - [12] Qiu SL, Wang CS, Wang YT, Liu CG, Chen XY, Xie HF, et al. Effects of graphene oxides on the cure behaviors of a tetrafunctional epoxy resin. Express Polym Lett 2011;5:809–18.
 - [13] Galpaya DGD, Fernando JFS, Rintoul L, Motta N, Waclawik ER, Yan C, *et al.*

- The effect of graphene oxide and its oxidized debris on the cure chemistry and interphase structure of epoxy nanocomposites. *Polymer (Guildf)* 2015;71:122–34.
- [14] Wang X, Jin J, Song M. Cyanate ester resin/graphene nanocomposite: Curing dynamics and network formation. *Eur Polym J* 2012;48:1034–41.
- [15] Verdonck E, Schaap K, Thomas LC. A discussion of the principles and applications of Modulated Temperature DSC (MTDSC). *Int J Pharm* 1999;192:3–20.
- [16] Simon SL. Temperature-modulated differential scanning calorimetry: theory and application. *Thermochim Acta* 2001;374:55–71.
- [17] Reading M, Hourston DJ. Modulated temperature differential scanning calorimetry theoretical and practical applications in polymer characterisation. Dordrecht ; [Great Britain] : Springer,; 2006.
- [18] Montserrat S, Flaque C, Page P, Malek J. No Title. *J Appl Polym Sci* 1994;56:1413.
- [19] Harper DP, Wolcott MP, Rials TG. Evaluation of the cure kinetics of the wood / PMDI bondline. *Int J Adhes Adhes* 2001;21:137–44.
- [20] Pilling MJ, Seakins PW. *Reaction Kinetics*. Oxford: Oxford University Press; 1995.
- [21] Rego JM, Pastor M a., Campo JJ, Katime I. Influence of the catalyst on the kinetics of a RIM formulation. *J Appl Polym Sci* 1989;38:237–48.
- [22] Wu T, Chen M, Zhang L, Xu X, Liu Y, Yan J, et al. Three-dimensional graphene-based aerogels prepared by a self-assembly process and its excellent catalytic and absorbing performance. *J Mater Chem A* 2013;1:7612.
- [23] Zhao L, Hu X. Autocatalytic curing kinetics of thermosetting polymers: a new model based on temperature dependent reaction orders. *Polymer* 2010;51:3814–20.
- [24] Ryu SH, Sin JH, Shanmugharaj AM. Study on the effect of hexamethylene

diamine functionalized graphene oxide on the curing kinetics of epoxy nanocomposites. *Eur Polym J* 2014;52:88–97.

- [25] Yao K. High Performance Polyurethane-organoclay nanocomposites. Loughborough University, 2005.

Chapter 8 Conclusions and Future Work

8.1 Conclusions

Since the discovery of graphene, it has been utilized in many applications. The application of graphene in composites is very common to reinforce the properties and manufacture different functional nanocomposites. Graphene based polymeric nanocomposites exhibited improved mechanical, thermal, electrical and barrier properties with very low percolation threshold. In this project, electrical conductive and anti-corrosion coatings were developed based on the application of graphene. In addition, the fabrication of graphene was also investigated.

A proposed mechanical-chemical approach was used to prepared graphene and it was both cost effective and suitable for large-scale production. Simple equipment was required and the procedure was not complicated. The most effective conditions are 1:1 graphite to melamine ratios, 1000R ball milling revolutions and 1 hour ultrasonication time. XRD results indicated that the graphite layers were exfoliated efficiently and TEM results confirmed the existence of graphene.

EPD was used to deposit graphene and PP10 graphite on steel substrates. With fine control of the EPD conditions and thermal treatment, electrical conductive coatings on steel substrates were produced successfully. The best electrical conductivity was 10 times higher than the electrical conductivity than steel substrate. The best thermal treatment temperature is about 580°C and the best thermal treatment time is about five minutes. The optimized EPD conditions so far are 0.175 mg/ml iodine concentration, 20 or 40V EPD voltage and 1 minute deposition time. The binding mechanism of thermal treatment is a simple mechanical binding. The anticorrosion properties of the EPD coatings were not good due to their porous nature. Therefore, a polymeric protective coating is needed to improve the anti-corrosion properties.

Electrical conductive and anti-corrosion PU/graphene nanocomposites were developed. Hybrid filler system was adopted and it showed the best electrical conductivity and acceptable anti-corrosion property. The best filler ratio is TEG:MWCNT = 1:1. Multi-layer coating system consists of EPD coating, conductive

primer and conductive topcoat has superior electrical conductivity than single layer primer or topcoat. However, the anti-corrosion property is worse than single layer system due to the limited facility of coating preparation. The key to improve electrical conductivity is to reduce the distance between the conductive particles. The strategy of using particles with larger diameter and high aspect ratios to form conductive network is recommend. However, the cure of the coating was affected with the incorporation of excessive amount of filler. The mechanical properties of the coating may be weakened.

FTIR and MDSC were used to understand the cure dynamic of model PU and graphene based PU nanocomposites. Graphene had catalytic effect and steric hindrance effect on the cure of PU where catalytic effect was more obvious at high cure temperature and steric hindrance effect was more dominated with high graphene loading. GO also showed catalytic effect and steric hindrance effect. In addition, the functional groups on the GO surface can participate in the reaction with PU. Therefore, the reaction mechanism was altered. From the results, the addition of excessive amount of filler can significantly affect the cure behaviour of two-part PU and even reduce the crosslink density and weaken its mechanical properties. The most efficient filler loading was 0.5 wt% which can improve the cure efficiency and properties of the nanocomposites.

The development of PU/graphene based conductive and anti-corrosion coating was successful. The addition of graphene can enhance the electrical property and anti-corrosion property. A procedure was developed to fabricate graphene and the optimized conditions to produce EPD coating and PU coating were discussed.

8.2 Future work

The time and equipment limited the further investigation of graphene fabrication. The amount of melamine added to penetrate the graphite galleries were found to be excessive. To prevent the wasting of material, more specimens with different graphite to melamine ratios could be tested to confirm the minimum amount of melamine required for effective exfoliation. The average layer number of the graphene sheets was not defined precisely. XRD scans do not indicate the number of layers; TEM

images cannot display the full nature of the whole specimen. Additional Raman spectroscopy could help to identify the number of layers for each specimen on average, providing a precise and more intuitive view on the quality of the prepared graphene. Additional testing with varying length of sonication could be done to find the optimal length of sonication which gives a good balance between layer number and flake size. Exfoliation could be further promoted, possibly by adding additional spacers during exfoliation.

The conditions and different solvent systems of EPD process need to be investigated to further identify the optimized conditions and system for carbon based EPD coatings. PU/Graphene based nanocomposite coatings were developed to improve the anti-corrosion property of the surface with EPD coating. Hybrid filler system was found to exhibit best electrical conductivity and anti-corrosion property. However, the coating application method was still lab based and may induced non-uniform coating quality. In addition, the technique to produce multi-layer coating was not perfect. Extra more work should be done to investigate a good method to apply coating. The cure of the PU coating may be improved with a better technique to apply coating. The surfaces of the steel substrates were not modified in order to see whether a good coating with good adhesion could be produced. The answer was yes but future work about surface modification for improved properties and adhesion can be done. Model PU was used for cure dynamic investigation because the PU coatings supplied by TATA Steel were full of additives and pigments. The addition of excessive amount of filler can significantly affect the cure behaviour of two-part PU which may decrease the cure density and cure efficiency. Other model PUs can be used to investigate the cure dynamic further and different size of graphene sheets and graphene oxide sheets can be used as well.

Publications

1. Tong, Yao, Siva Bohm, and Mo Song. "Graphene based materials and their composites as coatings." *Austin J Nanomed Nanotechnol* 1.1 (2013): 1003.
2. Y. Tong, Y. Lin, S.Wang and M.Song. "A study of crystallisation of poly (ethylene oxide) and polypropylene on graphene surface." *Polymer* 73 (2015): 52-61.
- 3 Y. Tong, M.Song, " Role of nanofillers in PU based blends and interpenetration networks ", Book chapter in *Polyurethane Volume 1- Blends And IPNs*, Elseviers Publishers, Submitted for press
4. TONG, Y., BOHM, S. and SONG, M., 2015. Carbon based coating on steel with improved electrical conductivity. *Austin Journal of Nanomedicine & Nanotechnology*, 3(1), pp. 1041 - 1047